Halogen Oxide Studies in the Boundary Layer by Multi Axis Differential Optical Absorption Spectroscopy and Active Longpath-DOAS

Gerd Hönninger

Dissertation
submitted to the
Combined Faculties for the Natural Sciences and for Mathematics
of the Ruperto Carola University of Heidelberg, Germany
for the degree of
Doctor of Natural Sciences

presented by
Diplom-Physicist: Gerd Hönninger
born in: Bad Mergentheim

Oral examination: 14.02.2002

Halogen Oxide Studies in the Boundary Layer by Multi Axis Differential Optical Absorption Spectroscopy and Active Longpath-DOAS

Referees: Prof. Dr. Ulrich Platt
Prof. Dr. Konrad Mauersberger

Untersuchungen von Halogenoxiden in der Grenzschicht mit Multi-Axis-DOAS und Landpfad-DOAS

Reaktive Halogenverbindungen (insbesondere Halogenoxide) sind wegen ihres großen Einflusses auf Ozon von großer Bedeutung für die Chemie der Troposphäre. Dies wurde zum ersten Mal während Episoden von völligem Abbau des bodennahen Ozons nach Sonnenaufgang im polaren Frühjahr durch Bromoxid (BrO) entdeckt. Halogenoxidvorkommen wurden zwischenzeitlich auch in mittleren Breiten an Küsten (Jodoxid, IO und Joddioxid, OIO) und im Toten Meer Becken (BrO) gefunden. Neue Ergebnisse von Feldmessungen, die im Rahmen dieser Arbeit an Meßorten in der Arktis und in mittleren Breiten durchgeführt wurden, werden hier vorgestellt. BrO und seine vertikale Verteilung in Bodennähe wurden während Ozonverlustereignissen in arktischen Gebieten Kanadas in hohen und mittleren geographischen Breiten beobachtet. Die ersten gleichzeitigen Messungen von BrO und IO in der arktischen bodennahen Grenzschicht wurden mit bodengestützter MAX-DOAS gemacht, die im Rahmen dieser Arbeit entwickelt wurde. Die Messungen an der Hudson Bay stellen die südlichsten und ersten direkten Messungen von bodennahem Ozonverlust in der Arktis durch BrO dar und erlaubten zum ersten Mal, die Tag- und Nachtchemie von Bromoxid zeitlich hochaufgelöst zu untersuchen. Molekulares Brom wurde als eine wichtige nächtliche Reservoirsubstanz identifiziert, die bei Sonnenaufgang nach ihrem photolytischen Abbau Ozonverluste startet. Die ersten gleichzeitigen, zeitlich hochaufgelösten Messungen von BrO und elementarem Quecksilber in der Gasphase in der kanadischen Arktis stützen die vorgeschlagene Schlüsselrolle von BrO als Oxidationsmittel von elementarem Quecksilber in der Gasphase während des polaren Frühjahrs. Weitere Messungen von Halogenoxiden an Reinluft- und mäßig verschmutzten Meßstationen ergaben zusätzliche Konzentrationsdaten und Obergrenzen für Halogenoxide.

Halogen Oxide Studies in the Boundary Layer by Multi Axis Differential Optical Absorption Spectroscopy and Active Longpath DOAS

The importance of reactive halogen species (particularly halogen oxides) in the troposphere is due to their strong effect on tropospheric ozone levels, which has been first discovered during surface ozone depletion episodes in the polar boundary layer after polar sunrise (bromine oxide, BrO). Halogen oxides have also been reported from mid-latitude coastal sites (iodine oxide, IO and iodine dioxide, OIO) and from the Dead Sea basin (BrO). Results from the field studies performed in framework of this thesis at Arctic and mid-latitude locations are presented here. BrO and its vertical profile near the ground has been observed during surface ozone destruction in the Canadian high and low Arctic. First simultaneous measurements of BrO and IO in the Arctic boundary layer were performed by ground-based MAX-DOAS, which was developed within this work. The measurements at the Hudson Bay represent the southernmost and first direct observations of Arctic surface ozone losses due to BrO and allowed for the first time to study the day and nighttime chemistry of BrO at high time resolution. Molecular bromine was inferred to be a major reservoir compound during the night, initiating sunrise ozone destruction upon photolysis. The first simultaneous measurements of BrO and gas phase elemental mercury at high time resolution in the Canadian Arctic support the proposed key role of BrO as oxidant for mercury in the gas phase during polar springtime. Further measurements of halogen oxides at clean and moderately polluted mid-latitude coastal sites yielded new field data on halogen oxide concentrations and upper limits at different pollution levels.

Contents

1 Introduction **1**

2 The Atmospheric Chemistry of Halogens **5**

2.1 Ozone in the Atmosphere 5

2.1.1 Stratospheric Ozone 7

2.1.2 Tropospheric Ozone 10

2.2 Reactive Halogen Species in the Troposphere 13

2.2.1 Reaction Pathways of RHS 14

2.2.2 Sources of RHS 22

2.2.3 Sinks of RHS 26

2.3 Tropospheric Bromine Chemistry 27

2.3.1 Sources and Reaction Cycles of Reactive Bromine 31

2.3.2 The Lifetime of Bromine Oxide Radicals in the Boundary Layer . . 34

2.3.3 Sinks of Reactive Bromine 36

2.4 Tropospheric Iodine Chemistry 36

2.4.1 Sources and Reaction cycles of Reactive Iodine 36

2.4.2 Fate of Reactive Iodine 37

2.5 Mercury in the Atmosphere 39

2.5.1 Sources and Partitioning of Mercury in the Atmosphere 40

2.5.2 Sinks of Atmospheric Mercury and the Role of Halogens 43

3 From DOAS to MAX-DOAS **47**

3.1 DOAS Overview 47

3.1.1 The Measurement Principle 48

3.1.2 The Analysis Procedure 52

3.1.3 Corrections to the Measured Spectra 54

3.1.4 Error Estimation 56

3.1.5 The Effects of Residual Structures 56

3.1.6 Differential Cross Sections 57

3.1.7 Example for a DOAS Evaluation 57

3.2 Active and Passive DOAS . . . 60
3.2.1 The Quartz Fiber Mode Mixer . . . 60
3.2.2 Fraunhofer Structures . . . 61
3.2.3 The Ring Effect . . . 62
3.2.4 The Solar I_0 Effect . . . 64
3.3 Scattering Processes in the Atmosphere . . . 65
3.3.1 Rayleigh Scattering . . . 65
3.3.2 Raman Scattering . . . 66
3.3.3 Mie Scattering . . . 67
3.4 Radiative Transfer in the Atmosphere . . . 69
3.4.1 The Airmass Factor Concept . . . 69
3.4.2 An Improved Airmass Factor Concept . . . 72
3.5 Multi-Axis-DOAS . . . 77
3.5.1 Off Axis DOAS . . . 78
3.5.2 Multi-Axis-DOAS Observations from the Ground . . . 80
3.5.3 MAX-DOAS Airmass Factors . . . 84
3.5.4 Airborne MAX-DOAS (AMAX-DOAS) . . . 90
3.5.5 Multi-Axis-DOAS Instruments . . . 91
3.5.6 Other Possible MAX-DOAS Applications . . . 94

4 Instrumental Setups 99
4.1 The MAX-DOAS Instrument . . . 99
4.1.1 Entrance Optics . . . 99
4.1.2 Spectrograph and Detector Unit . . . 100
4.2 The Active Long Path-DOAS System . . . 102
4.2.1 The LP-DOAS Telescope . . . 102
4.2.2 The Light Source . . . 103
4.3 New Miniature DOAS Instruments . . . 104
4.3.1 The Mini-MAX-DOAS System . . . 104
4.3.2 The Portable Active LP-DOAS System . . . 109

5 Field Measurements 111
5.1 Preparatory Field Studies . . . 111
5.1.1 Zugspitze MAX-DOAS Measurements . . . 111
5.1.2 Indian Ocean Field Study . . . 120
5.2 ALERT2000 Field Study . . . 127
5.2.1 Measurement Sites . . . 129
5.2.2 Meteorological Parameters . . . 130
5.2.3 MAX-DOAS BrO Measurements . . . 132
5.2.4 MAX-DOAS IO Measurements . . . 138

5.2.5 Ozone Measurements during ALERT2000 . . . 138
5.2.6 Mercury Measurements during ALERT2000 . . . 142
5.3 LP-DOAS Measurements on Crete . . . 143
5.3.1 Measurement Site . . . 143
5.3.2 Meteorological Parameters . . . 144
5.3.3 Active LP-DOAS BrO, IO, OIO Measurements . . . 144
5.3.4 Nitrogen Compounds at Finokalia . . . 147
5.4 Hudson Bay Campaign . . . 149
5.4.1 Measurement Site . . . 149
5.4.2 Meteorological Parameters . . . 149
5.4.3 First LP-DOAS Measurements at the Hudson Bay . . . 151
5.4.4 Etalon Structures . . . 156
5.4.5 Local Pollution . . . 160
5.4.6 MAX-DOAS BrO Measurements . . . 161
5.4.7 Ozone Measurements at Kuujjuarapik . . . 163
5.4.8 Mercury Measurements at Kuujjuarapik . . . 166

6 Results **167**
6.1 BrO in the Free Troposphere . . . 167
6.2 Halogen Oxides in the Southern Indian Ocean . . . 167
6.3 Results from ALERT2000 . . . 168
6.3.1 Time Series of BrO during ALERT2000 . . . 168
6.3.2 The Vertical Extent of the BrO Layer . . . 170
6.3.3 BrO during Ozone Depletion . . . 171
6.3.4 Comparison with GOME Vertical Column Densities . . . 180
6.3.5 Iodine Chemistry in the Arctic Boundary Layer . . . 182
6.4 Results from Crete2000 . . . 183
6.4.1 Upper Limits of Halogen Oxides in the Mediterranean Region . . . 183
6.4.2 Results from MOCCA Model Simulation . . . 184
6.5 Results from the Hudson Bay Measurements . . . 187
6.5.1 First Halogen Oxide Measurements at Hudson Bay . . . 188
6.5.2 Day/Nighttime Chemistry of Bromine Oxide . . . 190
6.5.3 Upper Limits of the Halogen Oxides IO, OIO, OBrO and OClO . . . 197
6.5.4 Comparison of LP-DOAS and MAX-DOAS Results . . . 198
6.5.5 Comparison of Boundary Layer BrO Data with GOME Maps . . . 200
6.5.6 Model Results of Day/Nighttime Chemistry at Kuujjuarapik . . . 204
6.6 The Role of BrO as Oxidant for Gas Phase Mercury . . . 207
6.6.1 Reactive Bromine - Mercury - Interaction . . . 209

7 Summary and Outlook **211**

Appendix **215**

A The Etalon-Effect **215**

B UFS Zugspitze Data Winter 1999/2000 **217**

C Data from Marion Dufresne, December 2000 **223**

D 5 day Back Trajectories Overview for ALERT2000 **225**

E MOCCA Simulation Results for Crete2000 **227**

List of Figures **239**

List of Tables **241**

References **260**

Acknowledgements **262**

Chapter 1

Introduction

Atmospheric ozone has become a major concern since the discovery of the ozone hole by *Farman et al.* [1985]. This observation proved, to what extent anthropogenic activities can influence environmental conditions in the atmosphere. At that time total atmospheric ozone above Antarctica during spring was found to have decreased to below 200 Dobson Units[1], which was only about 70% of the values observed in the years before. In the following years springtime ozone columns fell even below 100 DU. This observation was very important, since the ozone layer protects life on Earth against the harmful ultraviolet radiation of the sun. A slight decrease in the stratospheric ozone concentration could be explained by the suggestions of *Molina and Rowland* [1974] and *Stolarski and Cicerone* [1974] that reactive chlorine compounds could be involved in catalytic ozone destruction cycles. The predicted global ozone loss due to anthropogenic emissions of CFCs (chlorofluorocarbons) and halons (brominated organic compounds) into the atmosphere was estimated to 10-20% over the next 50-100 years. However, they could not explain the observation of the *Antarctic ozone hole* reported by *Farman et al.* [1985]. In 1986, *Solomon et al.* suggested that chlorine compounds might react on the surfaces of *polar stratospheric clouds* (PSCs) which occur at the low temperatures in the Antarctic stratosphere during polar night. *McElroy et al.* [1986] proposed additional ozone destruction cycles involving combined chemistry of reactive chlorine and bromine. These theories were confirmed by many studies in the following years, which proved the key role of reactive halogen compounds (chlorine and bromine) in stratospheric ozone chemistry.
In the mid 1980s sudden depletion events of ozone in the planetary boundary layer[2] were reported during springtime from several Arctic sites [*Oltmans and Komhyr* 1986;

[1]One Dobson Unit (DU) corresponds to an O_3 column of 0.01 mm at standard pressure and temperature

[2]The *Planetary Boundary Layer* (PBL) is the lowermost region of the troposphere which is directly influenced by friction on the earth's surface. Vertical mixing of trace gases and momentum is usually fast, leading to a generally well-mixed boundary layer of about 1 km vertical extent, depending on the stability conditions.

Bottenheim et al. 1986]. Within hours to days ozone levels at the surface frequently dropped to unmeasurable values in the weeks and months following polar sunrise. It turned out that also in the planetary boundary layer reactive halogen compounds (mainly bromine) are involved in catalytic ozone destruction during Arctic spring [*Barrie et al.* 1988; *Barrie and Platt* 1997]. Most recently, indications and direct measurements of the presence of reactive bromine in the free troposphere have been reported as well [*Harder et al.* 1998; *Frieß et al.* 1999; *McElroy et al.* 1999; *van Roozendael et al.* 2000; *Fitzenberger et al.* 2000]. Halogen species are therefore assumed to have an influence on the ozone chemistry of the atmosphere on a global scale. Ground-based measurements have subsequently discovered the reactive halogen species bromine monoxide [*Hausmann and Platt* 1994], iodine monoxide [*Alicke et al.* 1999] and iodine dioxide [*Hebestreit* 2001; *Allan et al.* 2001] by Longpath-DOAS measurements in the boundary layer. However, many open questions still remained:

- What is the global distribution of reactive halogen species in the boundary layer?
- What are the release processes for the reactive halogen compounds observed at different locations?
- What are the levels of reactive halogens in the free troposphere?
- How can reactive halogen species influence the ozone budget in the troposphere on a global scale?
- What are the consequences for the oxidizing capacity of the atmosphere and the global radiation budget?

In this PhD thesis field studies on reactive halogen species were carried out at various coastal sites yielding highly interesting results which have not been reported in the literature so far.

Outline of the thesis

First an overview of the relevant atmospheric chemistry of ozone and reactive halogen species is given in the *second chapter*. Both reactive bromine and iodine chemistry is described in detail. An additional section is included on atmospheric mercury, which is supposed to be strongly influenced by reactive bromine in polar regions. The *third chapter* introduces the measurement technique and related concepts used in this study. The central technique applied in this work is the differential optical absorption spectroscopy (DOAS) method. An overview is given on the principles and details of the DOAS analysis procedure. Special aspects of active and passive DOAS instruments, which were both applied in this work are also described. For passive DOAS of scattered sunlight the understanding of the processes which determine the radiative transfer in the atmosphere is essential. Therefore

the basic atmospheric processes and the airmass factor concept used for modelling the radiative transfer is described in this chapter. After a brief overview of the off axis DOAS method, the MAX-DOAS[3] technique is introduced, which was developed in this work based on off axis DOAS. Since MAX-DOAS represents a significant new development and opens a wide field of future applications, the method is described in detail and possible applications are discussed. The *fourth chapter* presents the employed hardware for the measurements. The custom built MAX-DOAS system as well as a state of the art Longpath-DOAS system are described and the main components are characterized. Additionally, the new mini-DOAS instruments tested during this thesis are briefly shown. The *fifth chapter* presents two preparatory and the three main field campaigns carried out as major experimental part of this work. The respective measurement location and climatology as well as the performed DOAS and related measurements are characterized in detail. Finally the results of the field measurements of halogen oxide radicals are presented in the *sixth chapter*, together with interpretation of the data and comparison with previous findings and model studies, which have been performed in this work to simulate the situations encountered during the field studies. The main results of this work are summarized in the final *chapter seven* and a short outlook is given on the future of this research field.

[3] **M**ulti-**Ax**is-DOAS

Chapter 2

The Atmospheric Chemistry of Halogens

In this chapter the atmospheric chemistry of halogens species, their impact on ozone chemistry, relevant radicals and their role as oxidants in the atmosphere is discussed. A brief introduction on atmospheric ozone is given in section 2.1. An overview of the main reaction pathways of halogen species in the atmosphere and in particular in the troposphere is given in section 2.2. The sources and sinks of bromine compounds in the troposphere and their impact on tropospheric ozone, particularly in the boundary layer, is subject of section 2.3. Section 2.4 deals with the sources, recycling and sinks of iodine compounds in the marine boundary layer. The possible involvement of reactive halogens in the atmospheric cycling of mercury species is addressed in section 2.5.

2.1 Ozone in the Atmosphere

Ozone was first proposed as an atmospheric constituent by [*Schönbein* 1840]. Its existence in the troposphere was then established in 1858 by chemical means [*Houzeau* 1858]. In the late 19^{th} century subsequent spectroscopic studies in the visible and ultraviolet regions showed, that ozone is present at a higher mixing ratio in the upper atmosphere than near the ground [*Hartley* 1881]. The presence of ozone in the stratosphere, with a maximum concentration between 15 and 30 km altitude, the so-called ozone layer, protects life from harmful UV radiation, which can affect the health of humans, animals and plants. In 1930 the first theory on the photochemical formation of ozone in the stratosphere predicting a maximum concentration around 20 km was proposed by *Chapman* [1930] (see Figure 2.2). The much lower actual ozone levels measured were subsequently explained by numerous chemical species present in the stratosphere, such as hydrogen and nitrogen compounds [*Bates and Nicolet* 1950; *Crutzen* 1970; *Johnston* 1971]. A possible role of halogen compounds in stratosphere was already proposed by *Crutzen* [1973]. In 1985 the discovery of

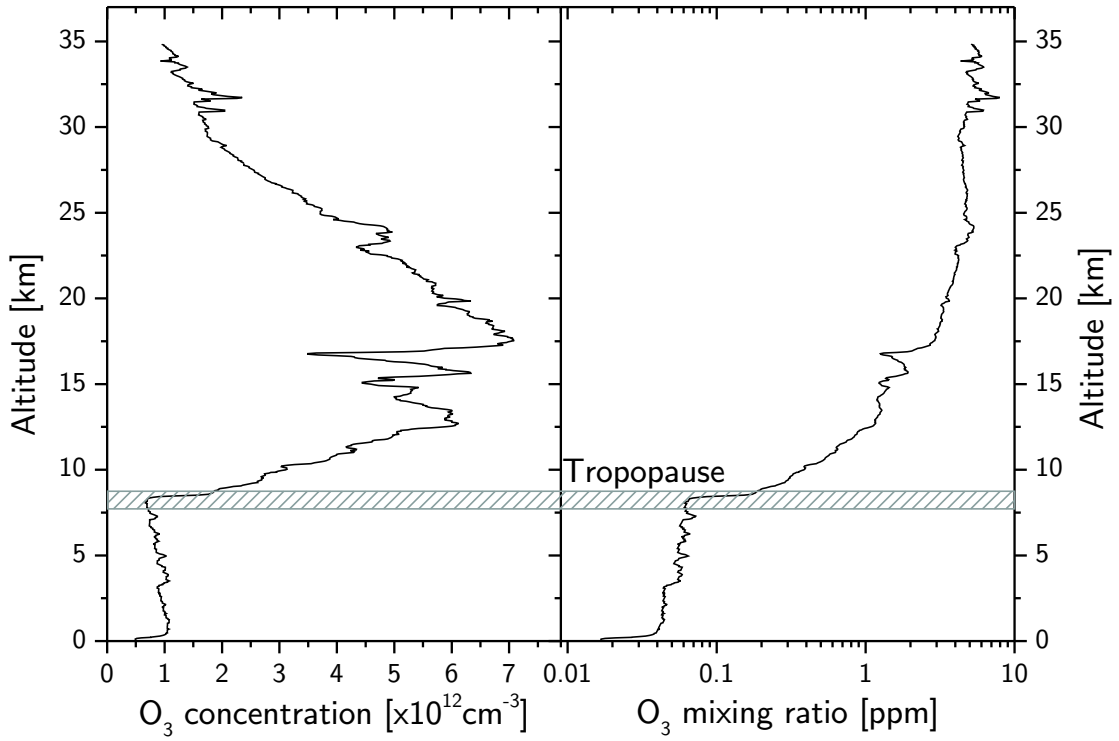

Figure 2.1: *Typical ozone sonde profile from the ground to 35 km measured during the ALERT2000 field campaign*

the *Antarctic ozone hole* by *Farman et al.* [1985] lead to a growing interest in stratospheric ozone chemistry.

Only about 10% of the total ozone column is located in the troposphere. However, also in the troposphere ozone is a key component being the most important precursor of hydroxyl radicals (OH). The OH radical is the most important oxidizing species in the daytime atmosphere (see e.g. review by *Crutzen and Zimmermann* [1991]) and therefore the key component in the degradation and removal of pollutants from the atmosphere. It is also the central compound in the formation of ozone in both, polluted and clean areas and contributes to the radiative forcing as a greenhouse gas.

Figure 2.1 shows a typical ozone vertical profile with the concentration and mixing ratio of ozone in the atmosphere as a function of altitude. The ozone sonde profile was measured during the ALERT2000 field campaign and represents typical background levels. In the following two sections the sources and sinks of stratospheric and tropospheric ozone will be explained.

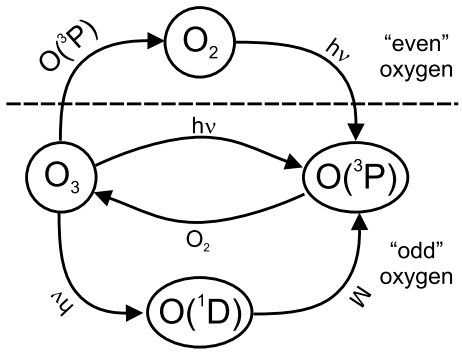

Figure 2.2: *The Chapman cycle*

2.1.1 Stratospheric Ozone

Since ozone is a strong absorber in the ultraviolet spectral region (see cross section in Figure 3.2), it is one of the key species in the earth's atmosphere. The formation and destruction of ozone in the stratosphere can be described by the so-called odd-oxygen chemistry. The production of ozone is initiated by the photolysis of molecular oxygen [*Chapman* 1930]:

$$O_2 + h\nu \longrightarrow 2O(^3P) \qquad \lambda \leq 242\,nm \qquad (2.1a)$$

$$O(^3P) + O_2 + M \longrightarrow O_3 + M \qquad (2.1b)$$

Ozone is formed via the reaction (2.1b) of O + O_2 with a collision partner M. The following reactions lead to destruction of ozone:

$$O_3 + h\nu \longrightarrow O_2 + O(^1D) \qquad \lambda \leq 320\,nm \qquad (2.2a)$$

$$O(^1D) + M \longrightarrow O(^3P) + M \qquad (2.2b)$$

$$O_3 + h\nu \longrightarrow O_2 + O(^3P) \qquad \lambda \leq 1180\,nm \qquad (2.2c)$$

$$2O(^3P) + M \longrightarrow O_2 + M \qquad (2.2d)$$

$$O(^3P) + O_3 \longrightarrow 2O_2 \qquad (2.2e)$$

Reactions (2.1b) and the photolysis of ozone ((2.2a) and (2.2c)) rapidly interconvert O and O_3, which provides the rationale for the concept of *odd oxygen* (O and O_3). *Even oxygen* is defined as O_2. Since reaction (2.2d) is known to be too slow for it to play a part in stratospheric chemistry, (2.2e) represents the only loss process for odd oxygen in the chapman cycle. The reaction scheme is shown in Figure 2.2.

Soon it became clear that the observed ozone profiles cannot be explained by the Chapman cycle alone, but that other ozone destroying mechanisms must exist. Model calculations including only oxygen chemistry strongly overestimated the stratospheric ozone abundance by more than a factor of two. Therefore additional sinks for ozone must be important. A

set of ozone destroying reaction cycles, involving hydrogen oxides, was first proposed by *Bates and Nicolet* [1950]:
Cycle a)

$$O + OH \longrightarrow O_2 + H \tag{2.3a}$$
$$H + O_2 + M \longrightarrow HO_2 + M \tag{2.3b}$$
$$O_3 + HO_2 \longrightarrow 2O_2 + OH \tag{2.3c}$$

net: $O + O_3 \longrightarrow O_2$

Cycle b)

$$O + OH \longrightarrow O_2 + H \tag{2.4a}$$
$$H + O_3 + M \longrightarrow OH + O_2 + M \tag{2.4b}$$

net: $O + O_3 \longrightarrow 2O_2$

Cycle c)

$$O_3 + OH \longrightarrow O_2 + HO_2 \tag{2.5a}$$
$$O + HO_2 \longrightarrow OH + O_2 \tag{2.5b}$$

net: $O + O_3 \longrightarrow 2O_2$

OH is produced in the stratosphere by the reaction of oxygen atoms with water vapor or methane (CH_4). The stratosphere appears to be very dry since the tropopause acts as a cold trap and therefore prevents tropospheric water vapor from mixing into the stratosphere. Instead, water vapor is produced in the stratosphere by the following reactions:

$$CH_4 + O(^1D) \longrightarrow OH + CH_3 \tag{2.6a}$$
$$CH_4 + OH \longrightarrow H_2O + CH_3 \tag{2.6b}$$
$$O(^1D) + H_2O \longrightarrow 2OH \tag{2.6c}$$

The reaction chains (2.3) to (2.5) were the first of numerous *catalytic reaction cycles* proposed for the destruction of ozone: the compound responsible for the conversion of ozone to molecular oxygen (OH) is not consumed during the reaction cycles but only acts as a catalyst. It therefore remains available for the destruction of ozone unless it is removed by other sinks. Catalytic species have a strong impact on the ozone budget even at very low concentrations. The class of odd hydrogen compounds, i.e. OH and HO_2, can be summarized as HO_x.

Similar catalytic ozone destruction cycles involve nitrogen oxides [*Crutzen* 1970; *Johnston* 1971]:

$$O_3 + NO \longrightarrow O_2 + NO_2 \tag{2.7a}$$
$$O + NO_2 \longrightarrow NO + O_2 \tag{2.7b}$$

net: $O + O_3 \longrightarrow 2O_2$

$$O_3 + NO \longrightarrow O_2 + NO_2 \tag{2.8a}$$
$$NO_2 + O_3 \longrightarrow NO_3 + O_2 \tag{2.8b}$$
$$NO_3 + h\nu \longrightarrow NO + O_2 \tag{2.8c}$$

net: $2O_3 + h\nu \longrightarrow 3O_2$

Nitrogen oxides are produced in the stratosphere mainly by oxidation of N_2O, which is a stable, well-mixed constituent of the atmosphere with a mixing ratio of ≈306 ppb. It is biogenically emitted from soils or the oceans and destroyed in the stratosphere:

$$N_2O + O(^1D) \rightarrow 2NO \tag{2.9}$$

As for hydrogen compounds NO_x denotes the family of the reactive nitrogen compounds NO, NO_2 and NO_3, while all inorganic nitrogen species are summarized as NO_y.

Together with the following catalytic cycles involving chlorine and combined chlorine-bromine chemistry, the consideration of the catalytic cycles described above leads to an ozone budget in the stratosphere which is consistent with the observations [*Molina and Rowland* 1974; *Molina and Molina* 1987; *McElroy et al.* 1986].

$$Cl + O_3 \longrightarrow ClO + O_2 \tag{2.10a}$$
$$ClO + O \longrightarrow Cl + O_2 \tag{2.10b}$$

net: $O + O_3 \longrightarrow 2O_2$

$$Cl + O_3 \longrightarrow ClO + O_2 \tag{2.11a}$$
$$Cl + O_3 \longrightarrow ClO + O_2 \tag{2.11b}$$
$$ClO + ClO + M \longrightarrow Cl_2O_2 + M \tag{2.11c}$$
$$Cl_2O_2 + h\nu \longrightarrow Cl + ClO_2 \tag{2.11d}$$
$$ClO_2 + M \longrightarrow Cl + O_2 + M \tag{2.11e}$$

net: $2O_3 \longrightarrow 3O_2$

$$Cl + O_3 \longrightarrow ClO + O_2 \tag{2.12a}$$
$$Br + O_3 \longrightarrow BrO + O_2 \tag{2.12b}$$
$$BrO + ClO \longrightarrow Br + ClO_2 \tag{2.12c}$$
$$ClO_2 + M \longrightarrow Cl + O_2 + M \tag{2.12d}$$
$$\text{net:} \quad 2O_3 \longrightarrow 3O_2$$

Under normal conditions most of the chlorine in the stratosphere is usually bound up in the reservoir species hydrogen chloride (HCl) and chlorine nitrate ($ClONO_2$) formed in the reactions

$$Cl + CH_4 \longrightarrow HCl + CH_3 \tag{2.13}$$
$$ClO + NO_2 + M \longrightarrow ClONO_2 + M \tag{2.14}$$

Under the special conditions in the polar winter stratosphere (darkness, cold temperatures, stable polar vortex), heterogeneous reactions on the surface of *Polar Stratospheric Clouds* (PSCs) can transform a huge fraction of chlorine into activated forms, e.g. into Cl_2 by the reaction:

$$ClONO_2 + HCl \xrightarrow{het} Cl_2 + HNO_3 \tag{2.15}$$

As a result during polar winter molecular chlorine can accumulate inside the polar vortex. As soon as sunlight is present the photolysis of Cl_2

$$Cl_2 + h\nu \longrightarrow Cl + Cl \tag{2.16}$$

produces chlorine atoms which can efficiently destroy ozone in the catalytic cycles 2.10, 2.11 and - if bromine is present - 2.12. During polar spring these processes lead to the *Stratospheric ozone hole*, which was first discovered by *Farman et al.* [1985] over Antarctica.

2.1.2 Tropospheric Ozone

The production of ozone by the reaction sequence 2.1 is not possible in the troposphere, since UV light below 240 nm necessary to photolyze O_2 cannot penetrate into the troposphere due to complete absorption by O_2 ($\lambda < 242\,nm$) and O_3 ($240\,nm < \lambda < 290\,nm$) in the stratosphere. Therefore, except for the urban areas during pollution episodes, it was commonly assumed until the late 1970s that tropospheric ozone has its origin in the stratosphere (e.g. [*Junge* 1963]). It was believed that stratospheric ozone was mixed through the tropopause region exhibiting a gradient towards the earth's surface which was thought to

be the dominant sink. *Fishman and Crutzen* [1978] compared tropospheric ozone concentrations in the two hemispheres with the then known source and sink mechanisms. It turned out that only about 50% of the tropospheric ozone has its origin in the stratosphere and is transported through the tropopause. Instead, as proposed by *Fishman and Crutzen* [1978], the production of ozone in the troposphere is driven by NO_x chemistry and reactions involving methane or higher hydrocarbons. A key sequence for the formation and destruction of tropospheric ozone are reactions involving NO_x:

$$NO_2 + h\nu \longrightarrow NO + O(^3P) \qquad \lambda \leq 420\,nm \tag{2.17a}$$

$$O(^3P) + O_2 + M \longrightarrow O_3 + M \qquad k_1 = 1.5 \cdot 10^{-14} \tag{2.17b}$$

$$NO + O_3 \longrightarrow NO_2 + O_2 \qquad k_2 = 1.8 \cdot 10^{-12} \tag{2.17c}$$

with the rate constants given in units of cm^3 $molec^{-1}$ s^{-1}. The ozone concentration is then determined by the photo stationary steady state of reactions (2.17), which can be expressed as the so-called *Leighton ratio L*:

$$L \equiv \frac{[NO]}{[NO_2]} = \frac{J(NO_2)}{[O_3] \cdot k_2} \tag{2.18}$$

Remote regions are, in contrast to areas with anthropogenic influence, generally characterized by low NO_x with mixing ratios as low as 5-10 ppt e.g. in the Antarctic boundary layer [*Jones et al.* 1999]. Similarly, in the arctic boundary layer NO_x mixing ratios typically range between 10 and 20 ppt ([*Beine et al.* 2001], see also section 5.4). Under these conditions, nitrogen and hydrogen oxides are able to produce ozone during the degradation of methane or higher hydrocarbons in the following reaction sequence:

$$CH_4 + OH \longrightarrow CH_3 + H_2O \tag{2.19a}$$

$$CH_3 + O_2 + M \longrightarrow CH_3O_2 + M \tag{2.19b}$$

$$CH_3O_2 + NO \longrightarrow CH_3O + NO_2 \tag{2.19c}$$

$$CH_3O + O_2 \longrightarrow CH_2O + HO_2 \tag{2.19d}$$

$$CH_2O + h\nu \xrightarrow{50\%} HCO + H \tag{2.19e}$$

$$CH_2O + h\nu \xrightarrow{50\%} H_2 + CO \tag{2.19f}$$

$$HCO + O_2 + M \longrightarrow CO + HO_2 + M \tag{2.19g}$$

$$H + O_2 + M \longrightarrow HO_2 + M \tag{2.19h}$$

$$HO_2 + NO \longrightarrow OH + NO_2 \tag{2.19i}$$

$$NO_2 + h\nu \longrightarrow NO + O \tag{2.19j}$$

$$O + O_2 + M \longrightarrow O_3 + M \tag{2.19k}$$

$$\text{net:} \qquad CH_4 + xO_2 \longrightarrow CO + 2H_2O + yO_3$$

The number of ozone molecules produced by the degradation of one methane molecule is y≈2.5. Ozone producing reaction schemes similar to (2.19) can also involve higher hydrocarbons. Besides the production of ozone, this reaction mechanism is an important source of carbon monoxide (CO) in the troposphere.

Carbon monoxide can produce additional ozone according to the following reactions [*Fishman and Crutzen* 1978]:

$$CO + OH \longrightarrow CO_2 + H \tag{2.20a}$$
$$H + O_2 + M \longrightarrow HO_2 + M \tag{2.20b}$$
$$HO_2 + NO \longrightarrow OH + NO_2 \tag{2.20c}$$
$$NO_2 + h\nu \longrightarrow NO + O \tag{2.20d}$$
$$O_2 + O + M \longrightarrow O_3 + M \tag{2.20e}$$
$$\text{net:} \quad CO + 2O_2 \longrightarrow CO_2 + O_3$$

Carbon monoxide, like CH_4, however, only produces ozone if the NO_x concentrations are above a threshold value. This is not the case for low NO_x conditions of remote areas with background conditions of typically 10 ppt. Instead, CO and hydrocarbons lead to destruction of ozone under low NO_x conditions:

$$CO + OH \longrightarrow CO_2 + H \tag{2.21a}$$
$$H + O_2 + M \longrightarrow HO_2 + M \tag{2.21b}$$
$$HO_2 + O_3 \longrightarrow OH + 2O_2 \tag{2.21c}$$
$$\text{net:} \quad CO + O_3 \longrightarrow CO_2 + O_2$$

The ozone mixing ratios in the unpolluted marine boundary (e.g. in the southern Indian ocean) range from ≈ 13 ppb during summer to ≈ 30 ppb during winter [*Gros et al.* 1998]. This pronounced seasonal variation of ozone is partly due to the seasonal variation of O_3 input from the stratosphere and by long range transport of ozone producing pollutants from biomass burning. The summer minimum of ozone can be explained by photochemical O_3 depletion which is controlled by the availability of OH radicals. The concentration of OH depends on the solar flux since OH is generated by the photolysis of O_3 to $O(^1D)$, followed by its reaction with water vapor:

$$O_3 + h\nu \longrightarrow O_2 + O(^1D) \qquad \lambda \leq 320\,nm \tag{2.22a}$$
$$O(^1D) + H_2O \longrightarrow 2OH \tag{2.22b}$$

The removal of OH occurs via the reaction with CO (reactions (2.20a) and (2.21a)), with CH_4 (reactions (2.19a) and (2.19b)) or reactions with other hydrocarbons.
The classical picture of the O_3 chemistry in the troposphere is, however, incomplete and

far from being completely understood.
In the weeks and months after polar sunrise, the ozone budget in the polar marine boundary layer is strongly affected by halogen chemistry. The mechanisms leading to the sometimes complete depletion of surface ozone during such periods, the *polar tropospheric ozone hole*, are described in the next section and the role of bromine is explained in section 2.3. There are also several field studies at mid-latitudes showing a behavior of ozone mixing ratios which could not be explained by standard OH and NO_x chemistry. Recent measurements by *Nagao et al.* [1999] and *Dickerson et al.* [1999] suggest that ozone destruction by halogen chemistry could play a significant role in the remote marine boundary layer at mid- and low latitudes. *Nagao et al.* [1999] proposed that the observed *sunrise ozone destruction* may be due to reactive halogens released from nighttime reservoir species which are rapidly photolyzed during sunrise.

2.2 Reactive Halogen Species in the Troposphere

Reactive **H**alogen **S**pecies (RHS) comprise the halogen atoms X, their monoxides XO, higher oxides X_nO_m, the hypohalous acids HOX, the halogen molecules X_2 and interhalogen compounds XY (X,Y = F, Cl, Br, I). In contrast to RHS the reactivity of reservoir species like halogen-NO_x compounds (XNO_x) or hydrogen halides (HX) are comparably slow. As will be described in this section, there are two main catalytic reaction cycles involving halogens which can destroy ozone in the troposphere, particularly in the marine boundary layer: Cycle (I) is based on the XO-self- or XO-YO-cross-reaction, cycle (II) on the reaction of XO with HO_x radicals.
Over the past decade significant amounts of XO were found in the marine boundary layer (MBL) of various coastal areas. Strong and sudden increases in the BrO mixing ratio during spring were found both in the Arctic [*Hausmann and Platt* 1994; *Tuckermann et al.* 1997; *Martinez et al.* 1999; *McElroy et al.* 1999] and in the Antarctic [*Kreher et al.* 1997; *Frieß* 1997; *Frieß* 2001] boundary layer. Recently a study suggesting a free tropospheric background of 1-3 ppt of BrO based on multi-platform observations of BrO has been presented by *van Roozendael et al.* [2000]. Huge clouds of highly elevated BrO amounts over the polar sea ice of both hemispheres, with areas spanning several thousand square kilometers, were observed from satellite [*Wagner and Platt* 1998; *Richter et al.* 1998; *Hegels et al.* 1998]. It has been proposed that these boundary layer BrO clouds may also contribute to BrO in the free troposphere [*McElroy et al.* 1999; *Roscoe et al.* 2001]. These events of highly elevated BrO in polar regions, ground-based measurements showed levels of up to 30 ppt, were always coincident with the destruction of ozone in the boundary layer, indicating that reactive bromine is responsible for catalytic ozone destruction. Enhanced BrO in the boundary layer associated with ozone destruction was also detected over the Caspian Sea [*Wagner et al.* 2001] and in the Dead Sea basin

[*Hebestreit et al.* 1999].
Iodine oxide (IO) was first observed at Mace Head, Ireland by *Alicke et al.* [1999] at levels of up to 6 ppt. Recently IO and also OIO were found at various coastal sites with mixing ratios in the ppt range: on Tenerife, Canary Islands and Cape Grim, Tasmania [*Allan et al.* 2000; *Allan et al.* 2001], at Mace Head, Ireland [*Allan et al.* 2000; *Hebestreit* 2001], in the European Arctic [*Wittrock et al.* 2000] and in Antarctica [*Frieß et al.* 2001; *Frieß* 2001]. Figure 2.3 shows the regions where tropospheric reactive halogen species were measured. Besides DOAS measurements of halogen oxides photolyzable bromine species (mostly HOBr, BrO) have been detected by *Impey et al.* [1999] using a Photolyzable Halogen Detector (PHD, conversion of reactive halogens to chloroacetone and bromoacetone and subsequent GC analysis). Hydrocarbon Clock measurements to derive chlorine and bromine atom concentrations have been reported from various locations, which are not all shown on the map [*Jobson et al.* 1994; *Ramacher et al.* 1997; *Ramacher et al.* 1999; *Solberg et al.* 1996; *Ariya et al.* 1999]. Additionally, chemical amplifier measurements by *Perner et al.* [1999] suggest that ClO is present in the Arctic boundary layer during ozone depletion periods.

2.2.1 Reaction Pathways of Reactive Halogen Species in the Troposphere

The main reaction schemes of the halogens Cl, Br and I are very similar regarding tropospheric chemistry[1]. As will be discussed later, there are differences in the rate constants and different quantum yields concerning their photochemical reaction channels (see e.g. Table 2.1). Therefore, if the reactions given are similar for the different halogens involved, X and Y will be used instead of the chemical symbols Cl, Br or I. Several rate constants and photolysis frequencies of RHS, which are important with regard to the two different ozone destruction cycles involving halogens, are listed in Table 2.1. Halogen atoms (X, Y) and their monoxides (XO, YO) are the key species in the ozone destruction cycles [*Hausmann and Platt* 1994; *LeBras and Platt* 1995; *Platt and Janssen* 1995]. Halogen oxides are formed in reaction with ozone (see reactions 2.23a and 2.23b below). Halogen atoms in the troposphere have a very short lifetime in the troposphere against their reaction with ozone (lifetime τ=0.08 s, 0.8 s, 0.8 s for Cl, Br, I). The typical reaction scheme for the first catalytic ozone destruction cycle involving reactive halogen species is

[1] As will be discussed at the end of this section, fluorine atoms mainly react with H_2O or hydrocarbons to HF, which is rapidly removed from the atmosphere.

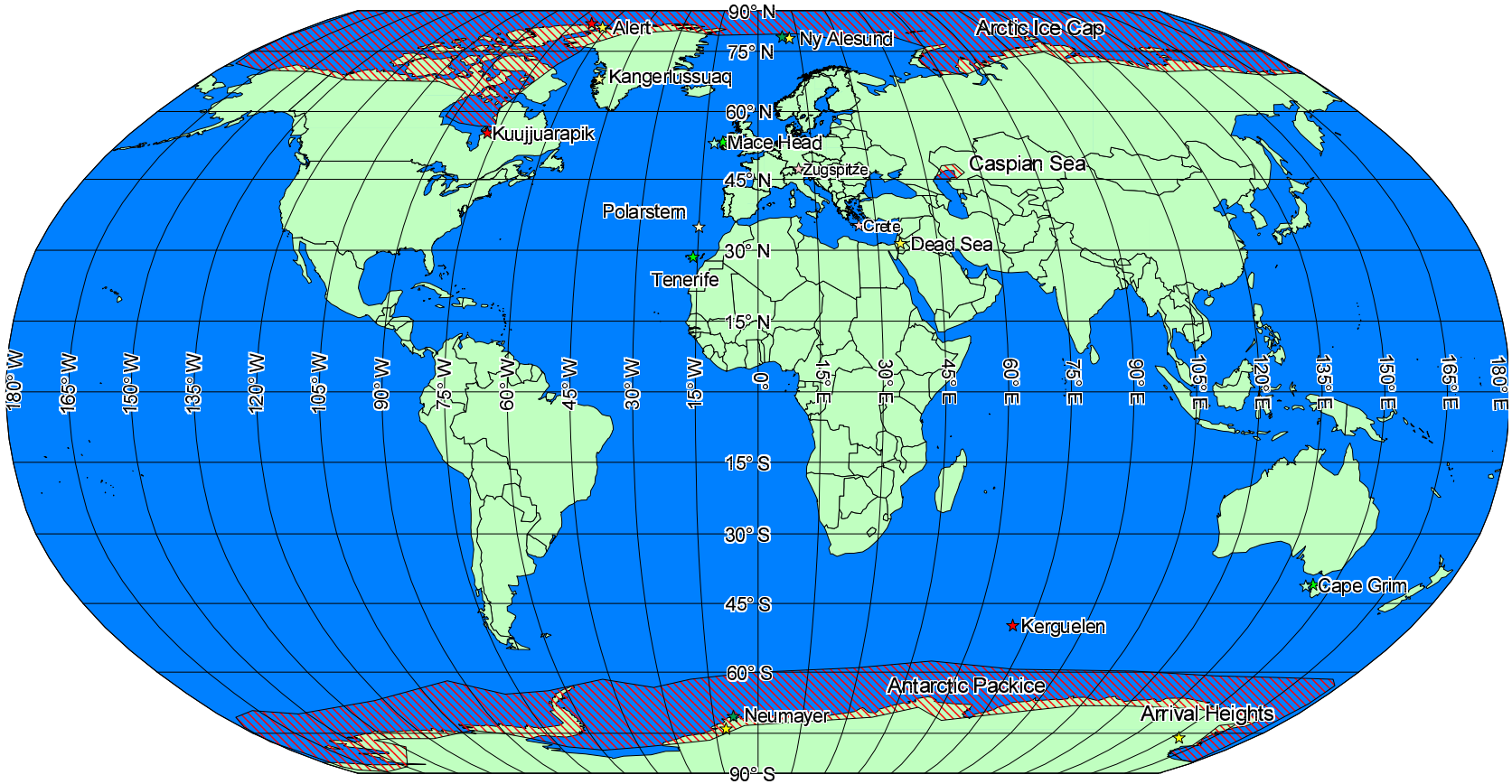

Figure 2.3: *Overview of Locations, where Measurements of Reactive Halogen Species in the troposphere have been reported: yellow symbols indicate reactive bromine (mostly BrO), green symbols reactive iodine (dark: IO, light: OIO) compounds. GOME satellite measurements are indicated as red hashed areas. The red symbols mark the locations, where measurements of halogen oxides were performed in this work: Alert (BrO, IO), Kuujjuarapik (BrO, upper limits for IO, OIO, OBrO, OClO) and Kerguelen (IO). The light red symbols represent upper limits derived in this work.*

Reaction			rate constant k $[\frac{cm^3}{molec \cdot s}]$ photolysis frequency j $[\frac{1}{s}]$	Reference
ClO + ClO	$\longrightarrow$	Products[a]	k=$1.6 \cdot 10^{-14}$	[*DeMore et al.* 1997]
BrO + ClO	$\longrightarrow$	Products	k=$1.4 \cdot 10^{-11}$	[*DeMore et al.* 1997]
IO + ClO	$\longrightarrow$	Products	k=$1.3 \cdot 10^{-11}$	[*DeMore et al.* 1997]
BrO + BrO	$\longrightarrow$	Products	k=$3.2 \cdot 10^{-12}$	[*DeMore et al.* 1997]
BrO + IO	$\longrightarrow$	Products	k=$6.9 \cdot 10^{-11}$	[*DeMore et al.* 1997]
IO + IO	$\longrightarrow$	Products	k=$8.0 \cdot 10^{-11}$	[*DeMore et al.* 1997]
$Cl + O_3$	$\longrightarrow$	$ClO + O_2$	k=$1.2 \cdot 10^{-11}$	[*DeMore et al.* 1997]
$Br + O_3$	$\longrightarrow$	$BrO + O_2$	k=$1.2 \cdot 10^{-12}$	[*DeMore et al.* 1997]
$I + O_3$	$\longrightarrow$	$IO + O_2$	k=$1.2 \cdot 10^{-12}$	[*DeMore et al.* 1997]
$ClO + HO_2$	$\longrightarrow$	$HOCl + O_2$	k=$5.0 \cdot 10^{-12}$	[*DeMore et al.* 1997]
$BrO + HO_2$	$\longrightarrow$	$HOBr + O_2$	k=$2.1 \cdot 10^{-11}$	[*DeMore et al.* 1997]
$IO + HO_2$	$\longrightarrow$	$HOI + O_2$	k=$8.4 \cdot 10^{-11}$	[*DeMore et al.* 1997]
$Cl_2 + h\nu$	$\longrightarrow$	2Cl	j=0.0021	[*Röth et al.* 1996]
$BrCl + h\nu$	$\longrightarrow$	Br+Cl	j=0.012	[*Röth et al.* 1996]
$Br_2 + h\nu$	$\longrightarrow$	2Br	j=0.044	[*Röth et al.* 1996]
$I_2 + h\nu$	$\longrightarrow$	2I	j=0.26	[*Tellinghuisen* 1973]
$ClO + h\nu$	$\longrightarrow$	Cl+O	j=$4.2 \cdot 10^{-6}$	[*Röth et al.* 1996]
$BrO + h\nu$	$\longrightarrow$	Br+O	j=0.035	[*Röth et al.* 1996]
$IO + h\nu$	$\longrightarrow$	I+O	j=0.35	[*Lazlo et al.* 1995]
$HOCl + h\nu$	$\longrightarrow$	Cl + OH	j=$1.8 \cdot 10^{-4}$	[*Röth et al.* 1996]
$HOBr + h\nu$	$\longrightarrow$	Br + OH	j=$7.6 \cdot 10^{-4}$	[*Röth et al.* 1996]
$HOI + h\nu$	$\longrightarrow$	I + OH	j=$5.9 \cdot 10^{-3}$	[*Bauer et al.* 1998]

[a]See reactions 2.23c, 2.23d, 2.23e and Table 2.2 for the possible products. Branching ratios vary strongly for different halogens.

Table 2.1: *List of rate constants and photolysis frequencies. Photolysis frequencies are calculated for 70° SZA at 80°N and surface albedo of 0.9*

Cycle I:

$$X + O_3 \longrightarrow XO + O_2 \tag{2.23a}$$
$$Y + O_3 \longrightarrow YO + O_2 \tag{2.23b}$$
$$XO + YO \longrightarrow X + Y + O_2 \tag{2.23c}$$
$$\longrightarrow XY + O_2 \tag{2.23d}$$
$$\longrightarrow OXO + Y \tag{2.23e}$$

net: $2O_3 \longrightarrow 3O_2$

where X and Y denote the halogen atoms (Cl, Br, or I). An overview of the possible reaction products and the respective branching ratios for the halogen oxide self- and cross reactions is given in Table 2.2. The halogen or interhalogen molecules XY (e.g. Br_2 or

	ClO	k_{XO+YO} $[10^{-12}\frac{cm^3}{molec\cdot s}]$	BrO	k_{XO+YO} $[10^{-12}\frac{cm^3}{molec\cdot s}]$	IO	k_{XO+YO} $[10^{-12}\frac{cm^3}{molec\cdot s}]$
ClO	$\longrightarrow$ $Cl_2O_2^a$ $\xrightarrow{29\%}$ Cl_2+O_2 $\xrightarrow{50\%}$ $Cl+ClOO$ $\xrightarrow{21\%}$ $Cl+OClO$	1.6×10^{-2}[b]	$\xrightarrow{44\%}$ $Br+Cl+O_2$ $\xrightarrow{7\%}$ $BrCl+O_2$ $\xrightarrow{49\%}$ $OClO+Br$	13.9[b]	$\xrightarrow{55\%}$ $I+OClO$ $\xrightarrow{25\%}$ $I+Cl+O_2$ $\xrightarrow{20\%}$ $ICl+O_2$	6.1[c]
BrO	———		$\xrightarrow{85\%}$ $Br+Br+O_2$ $\xrightarrow{15\%}$ Br_2+O_2	3.2[b]	$\xrightarrow{\leq30\%}$ $I+Br+O_2$ $\xrightarrow{\leq5\%}$ $IBr+O_2$ $\xrightarrow{65-93\%}$ $OIO+Br$ $\xrightarrow{\leq15\%}$ $OBrO+I$ $\xrightarrow{\sim0\%}$ $IBrO_2+M$	85[d]
IO	———		———		$\xrightarrow{7-15\%}$ $2I+O_2$ $\xrightarrow{\leq5\%}$ I_2+O_2 $\xrightarrow{30-46\%}$ $OIO+I$ $\xrightarrow{42-45\%}$ I_2O_2+M	82[e]
$\frac{k_{XO+YO}}{k_{BrO+BrO}}$	$\frac{k_{ClO+ClO}}{k_{BrO+BrO}}=5\times10^{-3}$		$\frac{k_{ClO+BrO}}{k_{BrO+BrO}} = 4.3$ $\frac{k_{BrO+BrO}}{k_{BrO+BrO}} = 1$		$\frac{k_{ClO+IO}}{k_{BrO+BrO}} = 1.9$ $\frac{k_{BrO+IO}}{k_{BrO+BrO}} = 27$ $\frac{k_{IO+IO}}{k_{BrO+BrO}} = 26$	

[a] not stable in the troposphere due to thermal decomposition
[b] rate constant and branching ratios taken from [*DeMore et al.* 1997]
[c] [*Bedjanian et al.* 1997]
[d] [*Rowley et al.* 2001]
[e] [*Bloss et al.* 2001]

Table 2.2: *Rate constants and branching ratios of halogen oxide self- and cross-reactions*

BrCl) formed in reaction (2.23d) are rapidly photolyzed during daytime:

$$XY + h\nu \longrightarrow X + Y \tag{2.24}$$

Reaction (2.23e) does not lead to a net destruction of ozone, since photolysis of OXO leads to the formation of oxygen atoms which recombine quickly with O_2 to form ozone:

$$OXO + h\nu \longrightarrow XO + O \tag{2.25a}$$
$$O + O_2 + M \longrightarrow O_3 + M \tag{2.25b}$$

In case of X=I, however, the photo-dissociation of OIO possibly yields I and O_2, leading to a net ozone destruction [*Plane et al.* 2001; *Hebestreit* 2001]. This will be discussed in section 2.4.

The reaction of XO with YO ((2.23c) and (2.23d)) is the rate limiting step of the reaction cycle. The self reactions (X=Y=Br, X=Y=Cl) are usually slower than the cross reactions (X=Br, Y=Cl). Particularly reactions involving iodine (X=I, Y=Br or Cl) are very efficient in destroying ozone. The second catalytic cycle involves HO_x radicals:
Cycle II:

$$X + O_3 \longrightarrow XO + O_2 \tag{2.26a}$$
$$OH + O_3 \longrightarrow HO_2 + O_2 \tag{2.26b}$$
$$XO + HO_2 \longrightarrow HOX + O_2 \tag{2.26c}$$
$$HOX + h\nu \longrightarrow OH + X \tag{2.26d}$$

net: $2O_3 + h\nu \longrightarrow 3O_2$

In the troposphere, reactive bromine is most important for catalytic ozone destruction. For the example of bromine, at 15 ppt BrO the net effect of the HO_x cycle (cycle II) is comparable to that of cycle I (at a typical level of 1 ppt HO_2). Note that the efficiency of cycle II is linearly dependent on the XO concentration, whereas the XO dependence of cycle I is quadratic. Thus at high XO levels cycle I will dominate, at low XO cycle II. At 30 ppt BrO, which are frequently observed during ozone depletion in the Arctic boundary layer, 66% of the ozone destruction will take place by cycle I. In addition the efficiency of cycles I and II can be enhanced by the presence of other halogen oxide species (i.e. IO, ClO) due to cross reactions (e.g. reaction 2.23c for BrO + IO) when reaction 2.23b occurs with IO or ClO instead of BrO.
An important loss channel for the halogen oxide formed in reaction (2.23a) is its photolysis and the reaction with NO:

$$XO + h\nu \longrightarrow X + O \tag{2.27}$$
$$XO + NO \longrightarrow X + NO_2 \tag{2.28}$$

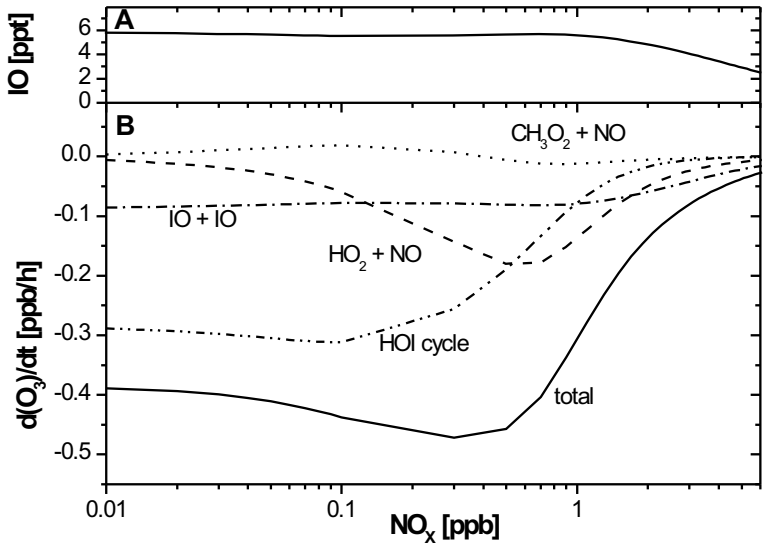

Figure 2.4: *Ozone destruction rates of the different catalytic reaction cycles for the case of iodine, as a function of the NO_x concentration. Adapted from Stutz et al. [1999].*

The photolysis of halogen oxides 2.27 leads to a null cycle with respect to ozone destruction since the oxygen atom formed quickly recombines with O_2 to yield ozone (reaction 2.25b).

Stutz et al. [1999] calculated the importance of the different cycles for the ozone destruction rate $\frac{d[O_3]}{dt}$ as a function of the NO_x mixing ratio (see Figure 2.4) for given 6 ppt iodine oxide. Assuming no loss of reactive halogens and all self and cross reactions leading to O_3 destruction channels, an upper limit of the ozone loss rate as a function of XO concentration can be expressed as:

$$-\frac{d[O_3]}{dt} = 2 \cdot \sum_{i,j} k_{X_iO+Y_jO}[X_iO][Y_jO] + \sum_i k_{X_iO+HO_2}[X_iO][HO_2] \tag{2.29}$$

where the combined effects of the cycles I (including all self and cross reactions) and cycle II are taken into account.
At high NO_x concentrations, e.g. in the polluted marine boundary layer the exchange reactions with the reservoir species XNO_3 can significantly alter the partitioning of reactive halogen species.

$$XO + NO_2 \longrightarrow XNO_3 \tag{2.30a}$$

$$XNO_3 + h\nu \longrightarrow XO + NO_2 \tag{2.30b}$$

However, these reactions represent a null cycle with no net chemistry as long as the photolysis of XNO_3 takes place in the XO + NO_2 channel. If X + NO_3 were formed

instead, additional O_3 loss would result.
Apart from its importance for the destruction of ozone the reaction of halogen oxides with hydroperoxy radicals (2.26c) followed by the photolysis of the product from this reaction, the hypohalous acids HOX (2.26d), also have a strong influence on the ratio of OH/HO_2 [*Stutz et al.* 1999; *Hebestreit* 2001]. In analogy to reaction 2.26c, XO can also react with organic peroxy radicals (RO_2, R = organic group), e.g. the methyl peroxy radical, CH_3O_2, instead of HO_2. It has been shown in laboratory experiments that this reaction is very efficient for X = Br [*Aranda et al.* 1997]. HOBr was formed in about 80 % of the reactions. The efficiency of the catalytic ozone destruction cycles involving halogen radicals strongly depends on the number of cycles that the reactive compounds X and XO can pass before being lost to a reservoir species. Regarding the halogen group from fluorine over chlorine and bromine to iodine, the reactivity of the halogen atoms decreases strongly. To assess the role of a halogen species in ozone destruction the branching ratio for the reaction of X with ozone (2.23a) and the reactions with hydrocarbons RH has to be considered. For bromine and iodine the reactions with HO_x are also important branching reactions:

$$X + RH \longrightarrow HX + R \tag{2.31}$$

$$X + HO_2 \longrightarrow HX + O_2 \tag{2.32}$$

$$XO + HO_2 \longrightarrow HOX + O_2 \tag{2.33}$$

- *Fluorine* atoms released in the troposphere react very quickly with atmospheric water vapor, which is much more abundant than hydrocarbons (e.g. CH_4). HF is stable against photolysis or reaction with OH. Therefore fluorine will always remain in this passive form and has no effect on ozone chemistry [*Wayne et al.* 1995].

- *Chlorine* atoms react rapidly with CH_4 and other hydrocarbons to form HCl. However, Cl can be in principle be activated by reaction of HCl with OH, and under certain circumstances it is released as a byproduct of autocatalytic bromine release (see section 2.3).

- *Bromine* atoms only react with unsaturated hydrocarbons and already oxidized compounds like aldehydes.

- *Iodine* atoms almost exclusively react with ozone or other radicals.

The relative reaction rate $\frac{R_{O_3}}{R_{O_3}+\sum R_{RH}+R_{HO_2}}$ is a measure of the probability of the reaction of a halogen atom with ozone. In Table 2.3 the situation for the four halogens is listed.
Table 2.3 shows, that fluorine is of no importance in the atmosphere since conversion to HF is very fast. Therefore, as reactive halogen species in the troposphere only chlorine, bromine and iodine are considered. In the case of chlorine about half of it is consumed by the reaction with hydrocarbons. For bromine, however, the probability for reaction with

X	RH	k^*_{X+RH} (k_{X+O_3}) $[cm^3s^{-1}]$	$typ[RH]$ ($typ[O_3]$) $[cm^{-3}]$	$R_{RH} = k_{X+RH}[RH]$ ($R_{O_3} = k_{X+0_3}[O_3]$) $[s^{-1}]$	$\frac{R_{O_3}}{R_{O_3}+\sum R_{RH}+R_{HO_2}}$	$\frac{R_{O_3}}{\sum R_{RH}+R_{HO_2}}$
F	H_2O	$1.4 \cdot 10^{-11}$	$7 \cdot 10^{16}$	$2.8 \cdot 10^6$	$3.5 \cdot 10^{-6}$	$3.5 \cdot 10^{-6}$
	CH_4	$6.4 \cdot 10^{-11}$	$4.0 \cdot 10^{13}$	$2.6 \cdot 10^3$		
				$\sum R_{RH} = 2.8 \cdot 10^6$		
	(O_3	$1.0 \cdot 10^{-11}$	$1.0 \cdot 10^{12}$	10.0)		
Cl	CH_4	$1.0 \cdot 10^{-13}$	$4.0 \cdot 10^{13}$	4.0	0.52	0.92
	C_2H_6	$5.7 \cdot 10^{-11}$	$3.0 \cdot 10^{10}$	1.7		
	C_3H_8	$1.4 \cdot 10^{-10}$	$1.0 \cdot 10^{10}$	1.4		
	CH_2O	$7.3 \cdot 10^{-11}$	$1.0 \cdot 10^{10}$	0.73		
	C_2H_2	$2.1 \cdot 10^{-10}$	$1.0 \cdot 10^{10}$	2.1		
	C_2H_4	$3.1 \cdot 10^{-10}$	$5.0 \cdot 10^9$	1.5		
				$\sum R_{RH} = 11$		
	(O_3	$1.2 \cdot 10^{-11}$	$1.0 \cdot 10^{12}$	12.0)		
Br	CH_2O	$1.1 \cdot 10^{-12}$	$1.0 \cdot 10^{10}$	0.01	0.984	60
	HO_2	$2.0 \cdot 10^{-12}$	$1.0 \cdot 10^8$	$2.0 \cdot 10^{-4}$		
				$\sum R_{RH} = 2.0 \cdot 10^{-2}$		
	(O_3	$1.2 \cdot 10^{-12}$	$1.0 \cdot 10^{12}$	1.2)		
I	HO_2	$3.8 \cdot 10^{-13}$	$1.0 \cdot 10^8$	$3.8 \cdot 10^{-5}$	0.99997	$3.1 \cdot 10^4$
	(O_3	$1.2 \cdot 10^{-12}$	$1.0 \cdot 10^{12}$	1.2)		

*$rate\ constants\ taken\ from$ [*DeMore et al.* 1997]

Table 2.3: *Comparison of the branching between reaction 2.31, 2.32 and 2.23a. The 6th column is a measure of the probability of the reaction with ozone, the last column can be seen as a zero order approximation for the number of ozone destruction cycles a halogen atom can pass before being lost to the reservoir.*

ozone is 98 % and even higher with almost unity for iodine.
Assuming that all XO radicals formed in the reaction of X with O_3 are 100 % reconverted to X atoms by self and cross reactions, the fraction of the rates R_{O_3} of reaction 2.23a and the sum of the rates $R_{RH} + R_{HO_2}$ of reactions 2.31 and 2.32, $\frac{R_{O_3}}{\sum R_{RH}+R_{HO_2}}$ is an approximation of the mean number of catalytic ozone destruction cycles that a halogen atom can pass. From the last column in Table 2.3 one can see that Br and especially I are much more efficient in destroying ozone than Cl.

To describe the partitioning between the main RHS X and XO the ratio of the halogen oxide concentration [XO] and the corresponding halogen atom [X] is determined by the relative rates of the reactions which convert X into XO (the halogen reaction with ozone 2.23a and the reaction with hydrocarbons RH and HO_x (2.31, 2.32) and the reactions transforming XO to X (NO reaction, self- or cross-reaction and photolysis (2.28, 2.23c, 2.27)):

$$\frac{[XO]}{[X]} = \frac{k_{X+O_3}[O_3] + k_{X+RH}[RH]}{k_{XO+NO}[NO] + 2 \cdot k_{XO+XO}[XO] + k_{XO+YO}[YO] + J(XO)} \tag{2.34}$$

Due to the fast photolysis of the IO radical the IO/I ratio is between 1 and 10 for typical NO_x and O_3 levels (e.g. [*Platt and Janssen* 1995; *Vogt et al.* 1996]). This is significantly lower than that of the other halogens. BrO/Br and ClO/Cl are of the order of 100 and 1000 respectively [*Barrie et al.* 1988]. Figure 2.5 shows a schematic overview of the halogen

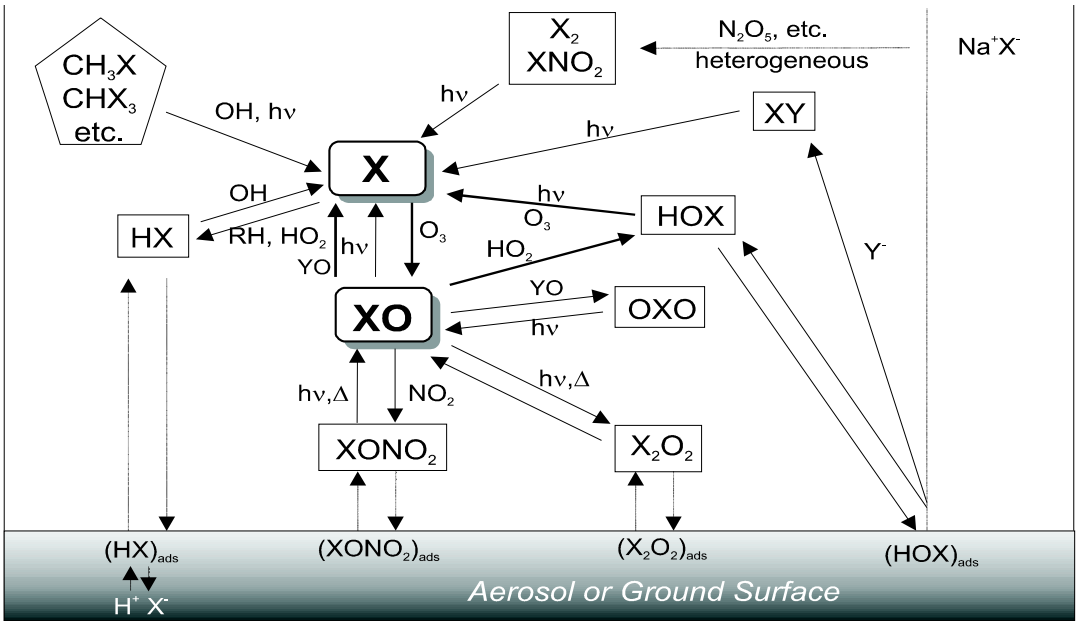

Figure 2.5: *Schematic overview of tropospheric halogen chemistry (X = Cl, Br, I), adapted from Platt and Janssen [1995]. Heavy lines indicate ozone-destruction sequences. Sources of RHS are the release from sea salt and the photolysis of halocarbons.*

chemistry in the troposphere adapted from *Platt and Janssen* [1995].

2.2.2 Sources of Reactive Halogen Species in the Troposphere

Halogen release mechanisms have been the subject of a number of model, laboratory and field investigations. Despite some still unresolved details, two main sources can been identified: Halogen release from sea salt and the photolysis of photolabile organohalogens. Both processes will be described in this section.

Halogen Release from Sea Salt

The release of halogens from sea salt via heterogeneous reactions was introduced by *Holland* [1978] two decades ago. In the early 1990s the first release mechanisms were described by *Fan and Jacob* [1992], *Mozurkewich* [1995], *Platt and Lehrer* [1996], *Sander and Crutzen* [1996] and *Vogt et al.* [1996]. Evidence from laboratory measurements was reported by *Oum et al.* [1998], *Behnke et al.* [1997], *Fickert et al.* [1999] and *Kirchner et al.* [1997] in the past years. By weight sea salt contains 55.7% Cl^-, 0.19% Br^- and $2 \cdot 10^{-5}$% I^- *Holland* [1978]. As sea ice surfaces, salt deposits on snow and aerosol particles sea salt is in contact with the atmosphere. It represents a large reservoir of halogens, is available at almost every coastline and - in form of aerosols - present over the open

sea. However, the absolute atmospheric halogen input from sea salt remains uncertain [*Platt and Lehrer* 1996; *Wennberg* 1999; *Platt and Stutz* 1998].

- **Autocatalytic or Halogen-catalyzed RHS Liberation From (Sea) Salt**
  This very important process is based on the uptake of gaseous HOX (e.g. produced by reactions 2.26c or 2.33) on acidic salt surfaces [*Fan and Jacob* 1992; *Tang and McConnel* 1996; *Vogt et al.* 1996] followed by the formation of an (inter-) halogen molecule in the aqueous phase:

$$X + O_3 \longrightarrow XO + O_2 \tag{2.35a}$$
$$XO + HO_2 \longrightarrow HOX + O_2 \tag{2.35b}$$
$$(HOX)_g \longrightarrow (HOX)_{aq} \tag{2.35c}$$
$$(HOX)_{aq} + (Y^-)_{aq} + (H^+)_{aq} \longrightarrow (XY)_{aq} + H_2O \tag{2.35d}$$
$$(XY)_{aq} \longrightarrow (XY)_g \tag{2.35e}$$
$$XY + h\nu \longrightarrow X + Y \tag{2.35f}$$

net: $X + HO_2 + (Y^-)_{aq} + (H^+)_{aq} + O_3 \xrightarrow{h\nu} X + Y + H_2O + 2O_2$

XY (e.g. Br_2 or BrCl) is highly volatile and quickly released to the gas phase. There it is readily photolyzed during daytime (see e.g. Table 2.1) and reacts with ozone to XO or YO (2.23a or 2.23b) again. Br_2 and BrCl have been measured in the atmosphere for the first time during the ALERT2000 field study by *Foster et al.* [2001]. *Platt and Lehrer* [1996] introduced the name 'bromine explosion' for this mechanism (cf. section 2.3.1), since it can lead to an exponential growth in the BrO concentration in the gas phase. The halogen atom X acts as a catalyst promoting the oxidation of Br^- to Br by O_3. This reaction sequence has been demonstrated in laboratory [*Fickert et al.* 1999] and modelling (see e.g. [*Lehrer* 1999]) investigations. The current understanding is that bromine is mainly released by the autocatalytic process, while chlorine is a by-product since bromine release is preferred to chlorine, even though it is much less abundant in a sea salt solution [*Fickert et al.* 1999]. However, the simultaneous release of small amounts of BrCl leads to a 'bromine-catalyzed liberation of chlorine'. A 'chlorine explosion' is much less probable due to very inefficient gas-phase conversion of Cl to HOCl. An 'iodine explosion' is not expected to occur since the concentration of iodine in sea salt is too small. However, previous reactive iodine chemistry (see section 2.4) can lead to strong enrichments in particulate iodine, which are known to occur [*Gäbler and Heumann* 1993]. Additionally reactive iodine can accelerate the release of Br and Cl from the sea salt due to faster gas phase reactions [*Vogt et al.* 1999]. The required acidity (reaction 2.35d only occurs at pH<6.5 [*Fickert et al.* 1999]) for the autocatalytic release processes is supplied by HCl or other strong acids, such as HNO_3 and H_2SO_4 (see below).

- **Halogen release via the attack of strong acids on halides**
  The attack of strong acids such as H_2SO_4 on sea salt aerosols is known to release gaseous halogen compounds as e.g. HX:

$$H_2SO_4 + 2(NaX)_{aerosol} \longrightarrow 2HX + Na_2SO_4 \tag{2.36}$$

  A recycling of gaseous HX via heterogeneous reactions is possible and is supposed to be of major importance in polar regions [*McFiggans et al.* 2000; *Sander et al.* 1999; *Vogt et al.* 1999] and in the remote marine boundary layer [*Seisel and Rossi* 1997]. On the surface of sea salt aerosols the reaction of HOX with HX is followed by the release of X_2 to the gas phase [*Abbatt* 1994; *Abbatt* 1995; *Abbatt and Nowak* 1997], as originally suggested by *Fan and Jacob* [1992]. Afterwards the (inter)halogen molecule is rapidly photolyzed (Table 2.1):

$$HOX + HX \longrightarrow X_2 + H_2O \tag{2.37}$$

  Seisel and Rossi [1997] discovered a reaction that requires cold and acidified aerosol surfaces. Therefore this reaction of nitrous acid (HONO) and HBr

$$HONO + HBr \longrightarrow BrNO + H_2O \tag{2.38}$$

  could be of importance in polar regions but not at mid latitudes. During the ALERT2000 field campaign (see section 5.2) significant HONO production from the snowpack by photochemical reactions was found by *Zhou et al.* [2001].

- **Halogen release via NO_y species**
  Antropogenically emitted species like NO_2 and N_2O_5 have been found to release halogens from sea salt [*Finlayson-Pitts and Johnson* 1988; *Finlayson-Pitts et al.* 1989; *Mozurkewich* 1995]. In the presence of nitrogen oxides heterogeneous reactions on aerosol surfaces like (2.39) are known to produce halogenated nitrogen oxides which are photolabile (2.40) or which may also react directly with sea salt (2.41) [*Schweizer et al.* 1999]:

$$(N_2O_5)_g + (NaX)_s \longrightarrow (XNO_2)_g + (NaNO_3)_s \tag{2.39}$$

$$XNO_2 + h\nu \longrightarrow X + NO_2 \tag{2.40}$$

$$(XNO_2)_g + (NaX)_s \longrightarrow (NaNO_2)_s + (X_2)_g \tag{2.41}$$

  Under atmospheric conditions reaction 2.39 is very slow [*Mozurkewich* 1995]. However, in contrast to the other halogen release mechanisms described at the beginning of this section, the formation of XNO_2 and X_2 can proceed without light, leading to an accumulation of these photolabile species before sunrise ('dark source' of RHS). *Nagao et al.* [1999] observed O_3 depletion events in the sub-tropical marine boundary layer and proposed night-time halogen release followed by photolysis at sunrise

for these events. Nevertheless, this source is the more effective the higher the NO_x values are, i.e. the more polluted the atmosphere is. Therefore it cannot be expected to be the dominant process of halogen release in the remote marine boundary layer. The uptake of NO_3 by aqueous solutions of NaX leads to another night-time mechanism [*Gershenzon et al.* 1999]:

$$(NO_3)_g + (NaX)_s \longleftrightarrow (NO_3 - NaX)_s;\ (NO_3 - NaX)_s \longrightarrow NaNO_3 + (X)_s \quad (2.42)$$

The uptake coefficient was found to be near 0.01 for sea water by *Rudich et al.* [1996], while *Seisel and Rossi* [1997] found 0.05 for dry NaCl.

Halogen Release from Degradation of Organohalogens

Organohalogens or halocarbons are emitted by a number of natural and anthropogenic sources. The most important natural source is the emission from algae in the oceans [*Schall and Heumann* 1993]. In total the source strength of methyl halides CH_3X is about $(100 - 400) \cdot 10^9$ g CH_3Br and $4 \cdot 10^9$ g CH_3I/year. In addition, there are emissions of polyhalogenated hydrocarbons like bromoform (tribromomethane, $CHBr_3$) or iodoform (triiodomethane, CHI_3), dibromo- and diiodomethane (CH_2Br_2, CH_2I_2) of a short photolytic lifetime (order of seconds in the marine boundary layer, see e.g. [*Carpenter et al.* 1999]). Also, short-chained organic halogens including different halogen species such as CH_2ClI or CH_2IBr [*Wayne et al.* 1995] have been detected in the atmosphere in significant amounts (see Table 2.4). Recently the global total source strength of bromoform has been reassessed to $2.2 \cdot 10^{11}$ g $CHBr_3$/year [*Carpenter and Liss* 2000]. Especially in the tropics biomass burning is another important anthropogenic source of halogenated hydrocarbons. *Manø and Andreae* [1994] estimate the man-made amount of methyl bromide to be $(10 - 50) \cdot 10^9$ g CH_3Br/year.
In contrast to CFCs, which are photostable in the troposphere, most brominated and iodinated halocarbons can be photolyzed even at low UV intensity in the planetary boundary layer or the free troposphere. Table 2.4 shows the typical mixing ratios and photolytic lifetimes in the troposphere for several halogenated hydrocarbons of importance for the tropospheric halogen budget.

The comparatively short lifetimes of the iodinated hydrocarbons are particularly striking. Especially as the iodide content of sea salt is only of the order of 10^{-5} % [*Holland* 1978], iodocarbon photolysis deserves more attention as RHS source than the iodine release from sea salt. As an example the photolytic lifetime of CH_3I is about hundred times shorter than its lifetime with respect to the reaction with OH [*DeMore et al.* 1997] and photolysis of the alkyl iodides occurs on a much shorter timescale than for the equivalent bromine or chlorine compounds [*Carpenter et al.* 1999].

Compound	typ. mixing ratio [ppt]	approx. lifetime
CH_3Br	10^a	8 months^a
CH_2Br_2	$< 1.5^c$	4 months^b
CH_2BrCl	$< 0.5^c$	5 months^d
$CHBr_2Cl$	0.8^h	1.2 months^d
$CHBr_3$	6^h	1.2 months^e
$CHBrCl_2$	$< 0.5^c$	1.2 months^d
CH_3I	2.4^g	5 days^f
C_2H_5I	0.1^h	40 hours^f
CH_2ClI	0.11^h	5 hours^f
CH_2BrI	0.3^h	45 minutes^f
CH_2I_2	0.4^h	5 minutes^f

[a] [*Yvon and Butler* 1996] [b] [*Mellouki et al.* 1992]
[c] [*Schall and Heumann* 1993] [d] [*Bilde et al.* 1998]
[e] [*Moortgat et al.* 1993] [f] [*Vogt et al.* 1999]
[g] [*Reifenhäuser and Heumann* 1992] [h] [*Carpenter et al.* 1999]

Table 2.4: *Lifetime and typical tropospheric mixing ratio of brominated and iodinated hydrocarbons. Adapted from Schauffler et al. [1999], Carpenter et al. [1999] and Vogt et al. [1999].*

2.2.3 Sinks of Reactive Halogen Species in the Troposphere

The first step in the loss process of RHS in the troposphere is their reaction with hydrocarbons (RH, e.g. CH_4, see reaction 2.31) or peroxy radicals (HO_2 and organic peroxy radicals RO_2, see reaction 2.32) to form hydrogen halides HX. The final loss of these compounds from the atmosphere is due to wet (after uptake on water-droplets of clouds or fog or on aerosol surfaces) and/or dry deposition (by sedimentation or surface reaction) on the earth's surface, including snow and ice surfaces, vegetation, buildings etc. As a result gaseous species are removed, at least temporarily, from the atmosphere. HX are readily soluble in water, which leads to efficient wet deposition on the ground or on aerosol surfaces and thus - at least temporarily - to a removal of RHS from the atmosphere. The different halogens show different behavior concerning their reaction with hydrocarbons (cf. Table 2.3. Cl reacts fast with all hydrocarbons, Br only with unsaturated hydrocarbons or oxidized species like aldehydes and carbonyls leading to the formation of HX. Iodine atoms cannot react with saturated or unsaturated hydrocarbons [*Miyake and Tsnogai* 1963]. Additionally, Br atoms can add to the C=C double bond of olefins leading to brominated organic compounds. The lifetime of the respective compound with respect to photolysis determines the efficiency of Br loss. For a detailed description cf. the reviews of *DeMore et al.* [1997] and *Atkinson et al.* [1997]. For chlorine the most important sink is the reaction with hydrocarbons by reaction 2.31. For more details concerning loss processes of bromine and iodine species see sections 2.3 and 2.4, respectively.

In principle, the reactivation of halogen atoms from the reservoir compound HX is possible by the reaction with OH

$$HX + OH \longrightarrow X + H_2O \tag{2.43}$$

However, as can be seen from Table 2.5 the reaction is endothermic and therefore negligible for fluorine. For chlorine, bromine and iodine the production rates of X atoms by reaction 2.43 is of the order of 1 atom per second and therefore also negligible under typical circumstances.

Halogen	reaction enthalpy ΔH in $[\frac{\text{kcal}}{\text{mol}}]$
F	15.0
Cl	-18.2
Br	-33.7
I	-49.9

Table 2.5: *Enthalpy of reaction (2.43) DeMore et al. [1994].*

2.3 Tropospheric Bromine Chemistry

Since the 1980s sudden ozone depletions - low ozone events - in the polar boundary layer after sunrise have been reported from various Arctic sites [*Oltmans and Komhyr* 1986; *Bottenheim et al.* 1986; *Barrie et al.* 1988; *Barrie et al.* 1994; *Sturges et al.* 1993; *Solberg et al.* 1996; *Rasmussen et al.* 1997]. Soon theories about an involvement of bromine compounds were discussed [*Barrie et al.* 1988; *Bottenheim et al.* 1990; *Finlayson-Pitts et al.* 1990; *LeBras and Platt* 1995] after *Barrie et al.* [1988] reported high filterable bromine concentrations during ozone depletion events (see Figure 2.6). In the following studies the key role of bromine was confirmed by DOAS measurements of BrO during the Polar Sunrise Experiment PSE92 [*Hausmann and Platt* 1994] and ARCTOC95/96 [*Tuckermann et al.* 1997; *Martinez et al.* 1999]. Recently, the same phenomenon was also reported from various Antarctic stations [*Wessel* 1996; *Kreher et al.* 1997; *Lehrer* 1999; *Frieß* 2001]. Observed BrO levels near the ground ranged from 10 to 30 ppt during ozone depletion events leading to a high efficiency of the ozone destruction cycles 2.23 and 2.26. Observations from the GOME (Global Ozone Monitoring Experiment) satellite instrument showed that these episodes of very high BrO in the boundary layer are frequent during polar spring in the Arctic and around Antarctica [*Wagner and Platt* 1998; *Richter et al.* 1998; *Hegels et al.* 1998; *Wagner* 1999]. Besides the polar regions GOME maps also show enhanced BrO vertical column densities (VCDs) in the lower Canadian Arctic (especially Hudson Bay [*Richter et al.* 1998; *Wagner et al.* 2001]) and also at the northern part of the Caspian

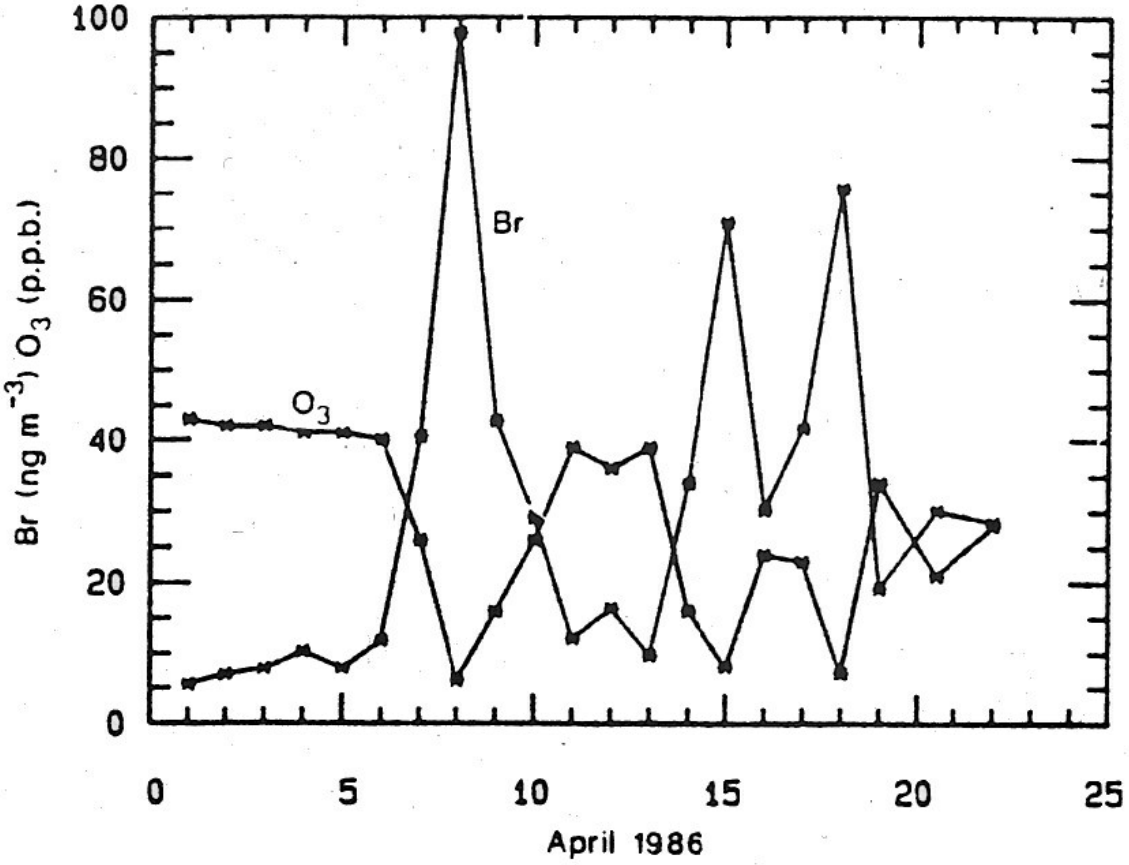

Figure 2.6: *Filterable bromine and ozone mixing ratios measured in April 1986 in the Canadian high arctic at Alert. Taken from Barrie et al. [1988].*

Sea [*Wagner et al.* 2001].

Within the framework of this thesis ground-based measurements of bromine oxide were performed in the polar boundary layer during the ALERT2000 campaign at Alert, Canada and for the first time in the Canadian low arctic at Kuujjuarapik on the east coast of Hudson Bay. Several low ozone events correlated to high values of bromine monoxide of up to 30 ppt were observed (see sections 5.2 and 5.4). During the ALERT2000 polar sunrise experiment also the first direct measurements of Br_2 (up to 25 ppt) and BrCl (up to 35 ppt) by atmospheric pressure chemical-ionization mass spectrometry (APCIMS) were reported by *Foster et al.* [2001] (see Figure 2.7). Recently the highest BrO mixing ratios ever detected in the atmosphere (up to 180 ppt) were found at the Dead Sea, Israel, correlated to ozone depletion in the Dead Sea valley [*Hebestreit et al.* 1999; *Matveev et al.* 2001; *Hebestreit* 2001].

Airborne measurements performed in April 1997 after polar sunrise showed BrO VCDs of $1 - 3 \cdot 10^{14} molec \cdot cm^{-2}$ in the North American Arctic [*McElroy et al.* 1999]. Since there was no correlation with altitude, solar zenith angle (SZA) and latitude the

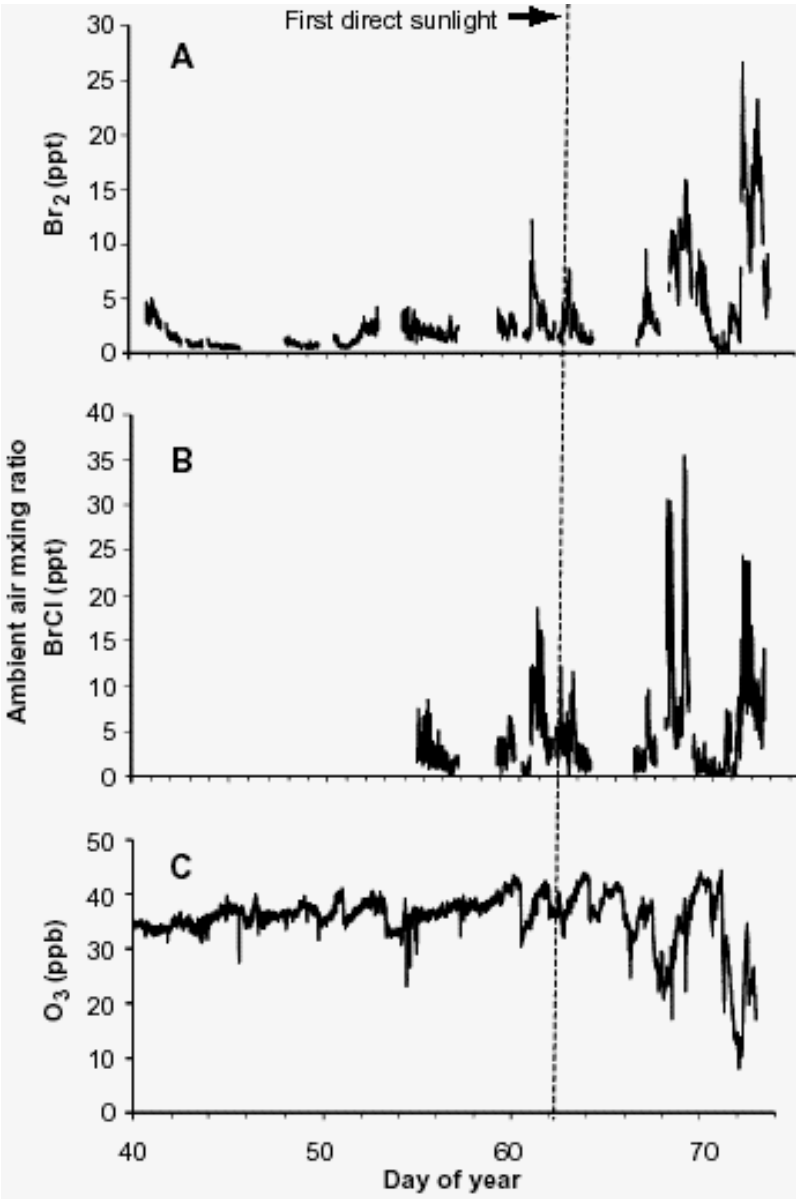

Figure 2.7: *Br_2, BrCl and ozone mixing ratios measured during polar sunrise 2000 at Alert. Taken from Foster et al. [2001].*

interpretation of McElroy and co-workers was that most of the BrO was present below a height of 8 km and therefore in the troposphere. Assuming that all of the BrO was located in the boundary layer they calculated a mixing ratio of 50 - 100 ppt, which was a factor of 2 to 3 higher than the ground-based measurements performed during polar sunrise in the boundary layer (e.g. [*Hausmann and Platt* 1994; *Tuckermann et al.* 1997; *Martinez et al.* 1999]). They concluded that a fraction of the bromine monoxide was present in the free troposphere, leading to mixing ratios of 10 - 30 ppt depending on

the vertical distribution during the measurements. Reactive bromine compounds being present at these levels sustained by efficient recycling processes would have a strong effect on the ozone budget of the free troposphere. *McElroy et al.* [1999] assumed open leads (cracks) in the arctic pack-ice and strong convective transport processes to be responsible for the large input of reactive bromine into the free troposphere (see Figure 2.8). *Wennberg* [1999] proposed heterogeneous processes on background sulphur aerosols

Figure 2.8: *Open leads in the arctic can cause strong convective transport. Photograph taken on April 12, 2000 on the flight to Alert.*

to be responsible for significant reactive bromine release.
Comparison of balloon borne measurements using direct sunlight (sensitive only to the atmospheric column above the flight altitude) with simultaneous measurements from the GOME satellite instrument or ground-based zenith scattered sunlight instruments (sensitive for the total atmospheric column) concurrently show a difference in the VCD which can only be explained by a contribution from the troposphere. 1 - 2 ppt BrO background values are found in the free troposphere, as a result of balloon-borne measurements [*Harder et al.* 1998; *Frieß et al.* 1999]. *Fitzenberger et al.* [2000] reported the first direct profile measurements of BrO in the free troposphere by balloon borne differential optical absorption spectroscopy with mixing ratios of 0.6-2.0 ppt.
The abundance of reactive bromine over the oceans is still an open question of importance since even reactive bromine mixing ratios in the ppt range can have a significant effect on the tropospheric ozone budget [*Sander and Crutzen* 1996] and the oxidation capacity of the remote marine boundary layer [*Vogt et al.* 1996]. During a cruise of the German research vessel FS Polarstern in October 2000 the MAX-DOAS approach developed within this thesis (cf. section 3.5) was applied to measure BrO in the marine boundary layer in the range between 0 and 2 ppt [*Leser* 2001].

This overview shows that a considerable number of measurements of reactive bromine have been carried out. On the other hand, there are still many open questions concerning tropospheric bromine chemistry. Especially the source and sink mechanisms and the influence of reactive Br on a global scale, are still not entirely solved. This section gives a detailed description of the sources and sinks of reactive Br, recycling processes and reaction cycles of bromine species in the troposphere.

2.3.1 Sources and Reaction Cycles of Reactive Bromine

Organobromine compounds

As described in general already in section 2.2.2 halocarbons emitted from natural sources are potential precursors for reactive bromine compounds in the troposphere. Typical mixing ratios and tropospheric lifetimes of brominated hydrocarbons known to be emitted from the oceans are given in Table 2.4. Macroalgae and phytoplankton are responsible for a part of the total production of volatile brominated organic substances in the oceans and therefore for their release to the atmosphere. The surface layer of the ocean is supersaturated of these compounds most of the time, so the ocean atmosphere exchange leads to a source mechanism for bromo-hydrocarbons [*Reifenhäuser and Heumann* 1992]. Besides the natural sources methyl bromide (CH_3Br) also has anthropogenic sources like fumigation of soils, burning of leaded gasoline (which contains ethylene dibromide ($C_2H_4Br_2$), EDB, as an antiknock compound [*Thomas et al.* 1997]) and biomass burning. The lifetime of organobromine compounds is of the order of a month up to one year (see Table 2.4). Methyl bromide (CH_3Br) is by far the most abundant bromocarbon in the troposphere, but has a relatively long lifetime of approximately 8 months. Apart from the fact that methyl bromide is one of the most important source gases for reactive bromine in the lower stratosphere [*Butler and Rodriguez* 1996], its degradation in the upper troposphere possibly contributes to a global BrO background in the free troposphere [*Frieß et al.* 1999; *Fitzenberger et al.* 2000]. However, during algae blooms with strongly increased emission, methyl bromide might be important as a precursor for reactive bromine in the marine boundary layer. Also, due to its shorter photolytic lifetime bromoform ($CHBr_3$) could be an important precursor of reactive bromine.

Autocatalytic bromine release - the bromine explosion

The atmospheric abundances and degradation rates of organobromine compounds mentioned above can clearly not sustain sudden increases of reactive bromine of up to 10 ppt/h as observed in the arctic boundary layer during polar spring. Also, the observation of up to 180 ppt BrO in the Dead Sea valley suggests that a much more efficient process must exist which releases reactive bromine from salt surfaces, a huge bromine reservoir that is present both in the Arctic as salt covered sea ice surface as well as in the Dead Sea valley

as large salt pans.
The mechanism suggested to cause the observed sudden BrO enhancements in the boundary layer is the autocatalytic release of bromine involving heterogeneous reactions on sea salt surfaces [*Fan and Jacob* 1992; *Tang and McConnel* 1996; *Vogt et al.* 1996]. The release of reactive halogens from acidic sea salt surfaces occurs via the uptake of gaseous HOBr:

$$(HOBr)_g \longrightarrow (HOBr)_{aq} \tag{2.44a}$$
$$(HOBr)_{aq} + (Cl^-)_{aq} + (H^+)_{aq} \longrightarrow (BrCl)_{aq} + H_2O \tag{2.44b}$$
$$(BrCl)_{aq} + (Br^-)_{aq} \longrightarrow (Br_2Cl^-)_{aq} \tag{2.44c}$$
$$(Br_2Cl^-)_{aq} \longrightarrow (Br_2)_{aq} + (Cl^-)_{aq} \tag{2.44d}$$
$$(Br_2)_{aq} \longrightarrow (Br_2)_g \tag{2.44e}$$
$$Br_2 + h\nu \longrightarrow 2Br \tag{2.44f}$$
$$2(Br + O_3) \longrightarrow 2(BrO + O_2) \tag{2.44g}$$
$$2(BrO + HO_2) \longrightarrow 2(HOBr + O_2) \tag{2.44h}$$

net: $HOBr + (Br^-)_{aq} + (H^+)_{aq} + 2HO_2 + 2O_3 \xrightarrow{h\nu} 2HOBr + H_2O + 4O_2$

Here, (aq) denotes the aqueous phase, i.e. reactions on deliquescent sea salt aerosol or the surface layer of freshly frozen sea ice[2]. This bromine release mechanism is also illustrated in Figure 2.9. The oxidation of Br^- to Br by O_3 leads to the release of two halogen atoms for each halogen atom taken up by the sea salt surface as HOBr. This leads to an exponential growth of gaseous reactive bromine, the *bromine explosion* [*Platt and Lehrer* 1996]. The release of Br_2 is preferred to BrCl, even if Br is much less abundant in a sea salt solution [*Fickert et al.* 1999]. The principal mechanisms involved in the autocatalytic bromine release could also be reproduced by *Lehrer* [1999] using a 1D model including the above described gas phase and heterogeneous reactions (on the sea ice surface as well as on the aerosol) and turbulent vertical mixing in the boundary layer. The following prerequisites are necessary for a bromine explosion to take place:

1. The bromine release from sea salt only occurs for pH < 6.5. The necessary acidity of the salt surface can be supplied by uptake of gaseous HCl or strong acids, such as HNO_3 and H_2SO_4 [*Keene et al.* 1998; *Lehrer* 1999].

2. The heterogeneous processes only lead to an exponential increase in gaseous reactive bromine if more than one bromine atom is produced for each scavenged HOBr molecule. This is the case as long as the release of Br_2 is preferred to that of BrCl as e.g. reported by *Fickert et al.* [1999].

[2]Sea salt aerosol appears to be (partly) liquid down to T≈230 K, therefore heterogeneous reactions are fast [*Koop et al.* 2000]

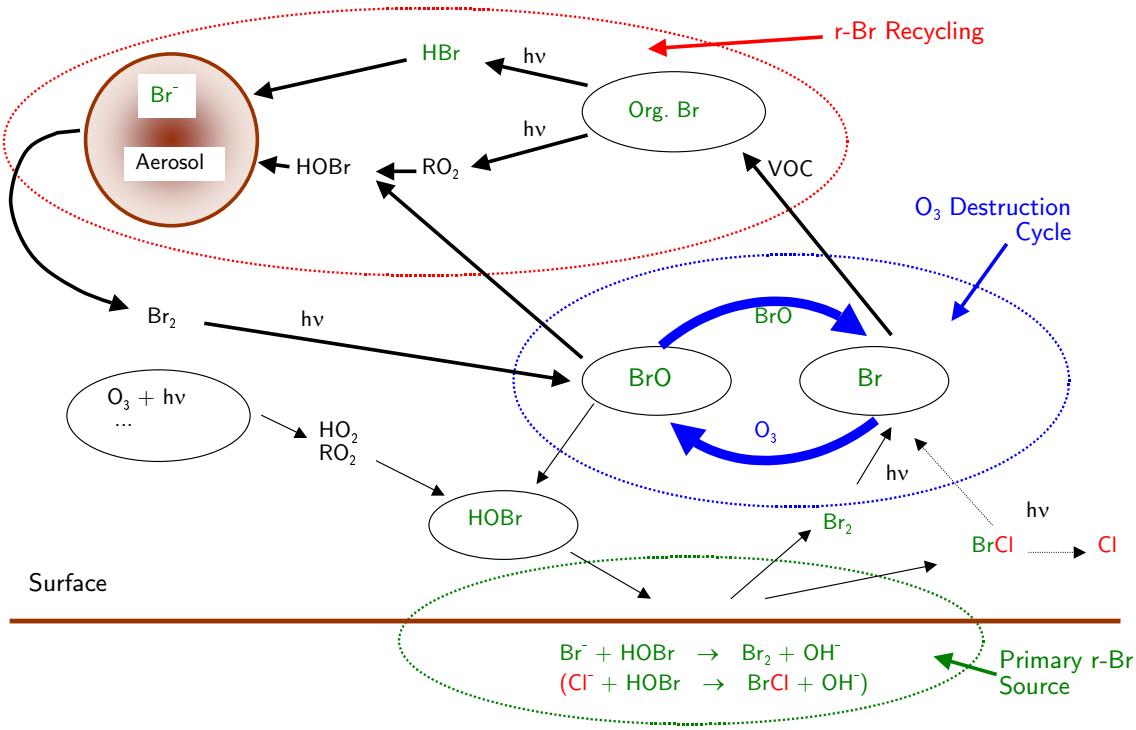

Figure 2.9: *Overview of the tropospheric bromine chemistry including the bromine explosion mechanism.*

3. To sustain the high concentrations of the reactive bromine, the meteorological conditions must prevent boundary layer air from mixing with free tropospheric air. During late winter and early spring, strong inversion layers in the lowermost 1000 m of the polar atmosphere effectively prevent upward mixing of boundary layer air.

4. Since the aerosol usually cannot provide enough surface area to release the observed amounts of reactive bromine sea ice surfaces strongly enriched in sea salt are needed. These are present as surface brines (a liquid layer with a high salinity on the frozen sea ice) and frost flowers on freshly frozen sea ice (see Figure 2.10).

5. The autocatalytic bromine release and the subsequent destruction of ozone requires light, so bromine explosions only occur after polar sunrise.

6. An initial small amount of reactive bromine is needed to start the heterogeneous bromine release on these sea salt surfaces.

7. The released bromine causes the destruction of ozone in the marine boundary layer. When all ozone is consumed, reactive Br is converted to HBr and either taken up by the aerosol or deposited at the surface as bromide (Br^-). It can re-enter the gas phase during another bromine explosion.

8. After the inversion layer breaks up ozone is mixed in from higher altitudes.

9. This cycle can be passed several times during polar spring.

Because especially the prerequisites of sunlight and a strong inversion layer are only present simultaneously during polar spring, episodes of bromine catalyzed ozone destruction are only observed during springtime.

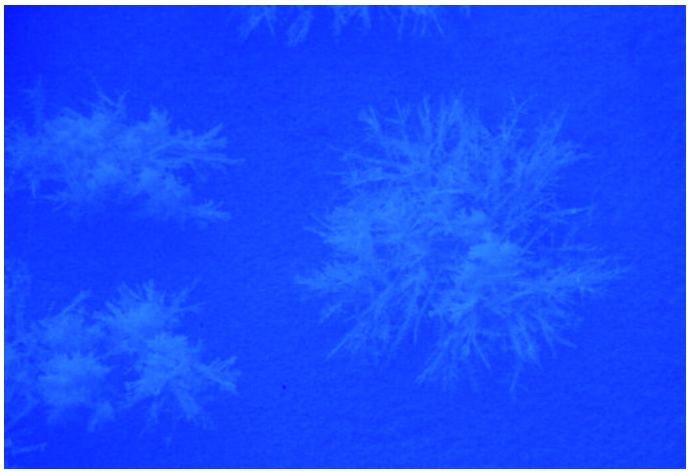

Figure 2.10: *Frost flowers on freshly frozen sea ice. Picture taken close to the Ice Camp during the Alert2000 field campaign*

2.3.2 The Lifetime of Bromine Oxide Radicals in the Boundary Layer

Since BrO radicals are one of the major atmospheric species investigated in this work, the lifetime of BrO in the boundary layer with respect to different loss processes has to be known. Since in this work also the first studies of the day and nighttime chemistry of BrO were possible at high time resolution (see Section 6.5.2), the important differences for the BrO reaction pathways during day and night should also be noted.
The photolytic lifetime of BrO at a solar zenith angle of 70° ranges between 30 s and 100 s depending on surface albedo, etc.

$$BrO + h\nu \longrightarrow Br + O \tag{2.45}$$

The only other important reaction channel of BrO besides the photolysis reaction 2.45 are the BrO self reaction and cross reactions with other halogen oxides (see Table 2.2):

$$BrO + BrO \xrightarrow{85\%} Br + Br + O_2 \tag{2.46}$$

$$\xrightarrow{15\%} Br_2 + O_2 \tag{2.47}$$

The BrO lifetime with respect to the self reaction is given by:

$$\tau_{BrO} = \frac{1}{[BrO] \cdot k_{BrO+BrO}} \tag{2.48}$$

At 10 ppt (2.6×10^8 molec/cm^3) this leads to a lifetime of τ_{BrO} of 1200 s. This lifetime of BrO, however, is inversely proportional to the BrO concentration, therefore at 40 ppt the BrO lifetime would be only 300 s. During daytime, the Br_2 produced with a quantum yield of ≈0.15 is rapidly photolyzed (τ_{Br_2} ≈30 s-1 min) to yield Br atoms.
Bromine atoms can react with oxidized or unsaturated hydrocarbons (e.g. formaldehyde HCHO, olefines), HO_2 radicals or ozone in the following pathways:

$$Br + RH \xrightarrow{2\%} HBr + R \tag{2.49}$$

$$Br + O_3 \xrightarrow{98\%} BrO + O_2 \tag{2.50}$$

Here, RH denotes the sum of HO_2, HCHO and olefines which react with Br atoms. As long as ozone is not completely depleted ([O_3]>several ppb), almost all Br atoms (>98%) react with ozone leading to no net BrO loss. For the branching ratio see also column 6 in Table 2.3. Depending on RH levels the effective conversion time of BrO to HBr can be up to ≈5000 s. Since the BrO self reaction is significantly faster, it leads to efficient ozone destruction. As it takes about one day to completely destroy e.g. 40 ppb O_3 HBr (Br^-) and HOBr have to be recycled to reactive bromine in reactions 2.44 to explain the ozone losses described at the beginning of this section. In summary, during daytime the BrO lifetime is determined by the reaction of Br atoms with RH to HBr ranging between 1 and 2 hours.
During nighttime, however, the photolysis frequency of BrO is zero. Therefore the BrO self reaction (and possible cross reactions with other halogen oxides) is the only important reaction pathway of BrO radicals. However, at nighttime also the photolysis of Br_2 is not possible, therefore only 85% of the Br atoms can react with O_3 back to BrO. The 15% path to Br_2 therefore leads to an accumulation of Br_2 at night, which acts as a nighttime reservoir species and photolyzes to Br atoms rapidly during sunrise. In summary the lifetime of BrO radicals during nighttime is determined by the branching ratio of the reaction of Br atoms with RH and O_3 on the one hand and by the branching ratio of the BrO self reaction to yield atomic or molecular bromine on the other side. At high BrO levels of 40 ppt the lifetime with respect to Br_2 formation is of the order of 2000 s and therefore significantly shorter than with respect to HBr formation (∼15000 s). At lower BrO levels (e.g. 10 ppt) the lifetime with respect to Br_2 formation is of the order of 8000 s. The loss to HBr in this case is negligible with a BrO lifetime of >12 hours. The different lifetimes are discussed in section 6.5.2 in the context of the day and nighttime measurements performed at the Hudson Bay as one of the major parts presented in this work.
In case of other species present in the boundary layer which can react with BrO, in particular the halogen oxides ClO and IO, and NO_2 but also DMS, Hg^0, etc. the BrO lifetime

can be significantly shorter, especially during nighttime, due to formation of reservoir compounds like BrCl, IBr, $BrONO_2$, etc.

2.3.3 Sinks of Reactive Bromine

The most important sink for reactive bromine are the reaction with hydrocarbons (especially HCHO and alkenes, 2.31) and the reaction with HO_2 (2.32) which yield HBr [*Bedjanian et al.* 1998]. The lifetime of HBr with respect to reaction with OH is about one day, therefore it can undergo wet and dry deposition at the surface, especially in the planetary boundary layer where mixing is fast.
The reaction of BrO with dimethyl sulfide (DMS)

$$BrO + DMS \longrightarrow Br + DMSO \qquad k = 2.6 \cdot 10^{-13} \frac{cm^3}{molec \cdot s} \tag{2.51}$$

might be important in the unpolluted remote marine boundary layer where the only other sink for DMS is the reaction with OH radicals [*Toumi* 1994]. No BrO has been reported from measurements in the marine boundary layer at mid-latitudes, however, the measurements performed by *Leser* [2001] suggest BrO to be present in the north Atlantic marine boundary layer at mixing ratios of ≈1 ppt which could make the reaction with BrO a major loss mechanism for DMS.

2.4 Tropospheric Iodine Chemistry

2.4.1 Sources and Reaction cycles of Reactive Iodine

While the major source for reactive bromine in the MBL is thought to be the autocatalytic release on sea salt surfaces described in the previous section, the main source for reactive iodine in coastal regions are iodo-hydrocarbons biogenically produced in the oceans and released to the atmosphere. Iodocarbons are rapidly destroyed by photolysis or degradation with OH, with lifetimes between 5 days for methyl iodide (CH_3I) and only 5 minutes for diiodomethane (CH_2I_2) (cf. Table 2.4). Therefore organic iodine compounds are rapidly destroyed to form reactive iodine (I, IO) which potentially has a strong impact on the boundary layer ozone chemistry. To a minor extent, catalytic processes corresponding to reactions (2.35) involving HOI can lead to an additional release of reactive halogens from aerosols and sea ice surfaces. However, the presence of reactive iodine in the MBL is expected to have no 'event-like' character as it is the case for bromine. Instead, the abundance of inorganic iodine is mainly linked to the biogenic activity in the ocean and to the distance from coastlines or the open sea as the source regions for iodocarbons.
The main reaction path for reactive iodine is cycle (2.26) involving HO_x radicals which is

more efficient in destroying ozone at the observed iodine levels than the cycle involving the IO self reaction (2.23). Model calculations have shown that the IO/HO_x cycle accounts for up to 75% of the ozone destruction if 6 ppt of inorganic iodine are present in the MBL [*Stutz et al.* 1999] (see Figure 2.4). The importance of reactive iodine on the tropospheric ozone budget could thus be comparable to the photolytic ozone loss processes involving HO_x if only a few ppt of reactive iodine are present.

2.4.2 Fate of Reactive Iodine

In contrast to the other halogens I atoms do not react with hydrocarbons to form HI. However, HI is formed in the reaction of iodine with HO_2,

$$I + HO_2 \longrightarrow HI + O_2 \tag{2.52}$$

In case of iodine the reactivation of I from the HI reservoir via the reaction

$$HI + OH \longrightarrow I + H_2O \qquad\qquad k = 7 \cdot 10^{-11} cm^3 molec^{-1} s^{-1} \tag{2.53}$$

can take place, because the lifetime of HI due to reaction with OH is only 3 to 4 hours (at typical OH concentrations of 1×10^6molec/cm^3). Also, the iodine compounds $IONO_2$, I_2O_2 and INO_2 with photolytic lifetimes of less than 1 hour act only as temporary reservoir species and not as a sink for reactive iodine.
The fate of reactive iodine is presently not completely understood, however, since large aerosols are usually enriched in iodine (in the form of iodate IO_3^-), irreversible uptake of inorganic iodine on aerosols seems to be an important loss mechanism for reactive iodine. *Vogt et al.* [1999] have suggested the uptake of the IO dimer I_2O_2 on aqueous aerosol surfaces or the self- reaction of IO in the aqueous phase, followed by a hydrolysis reaction:

$$IO + IO \longrightarrow I_2O_2 \tag{2.54a}$$
$$I_2O_2 + (H_2O)_{aq} \longrightarrow (HOI)_{aq} + (IO_2)^-_{aq} + (H^+)_{aq} \tag{2.54b}$$
$$IO + IO + H_2O \longrightarrow (HOI)_{aq} + (IO_2)^-_{aq} + (H^+)_{aq} \tag{2.54c}$$
$$(IO_2)^-_{aq} + (H_2O_2)_{aq} \longrightarrow (IO_3)^-_{aq} + H_2O \tag{2.54d}$$

The formation of iodate (IO_3^-) is a possible loss process for reactive iodine since reactions (2.54) lead to an accumulation of this compound in the aerosol. Another possible sink are OIO radicals as products of the IO self reaction (for rate constants and branching ratios see Table 2.2):

$$IO + IO \longrightarrow OIO + I \tag{2.55}$$

In contrast to the homologous OClO and OBrO, which are rapidly photolyzed during daytime, model and laboratory studies suggest that OIO may be photostable since the calculated threshold wavelength for its photo dissociation via

$$OIO + h\nu \longrightarrow IO + O(^3P) \tag{2.56}$$

is 418 nm [*Misra and Marshall* 1998], while the visible absorption spectrum of OIO covers the wavelength region between 480 and 660 nm [*Cox et al.* 1999]. Therefore the absorption cross section of OIO at $\lambda \leq$418 nm is very small. The fate of atmospheric OIO is still uncertain to date. The following reactions with OH and NO possibly lead to a reconversion of OIO into reactive iodine:

$$OIO + NO \longrightarrow IO + NO_2 \tag{2.57a}$$

$$OIO + OH \longrightarrow IO + HO_2 \tag{2.57b}$$

Measurements of *Hebestreit* [2001], who observed OIO for the first time in the boundary layer, suggest that the reaction with NO (2.57a) is the most important loss process for OIO. The estimated lifetime of OIO with respect to this reaction is approximately 20 minutes. The NO mixing ratios during the measurements performed at Mace Head, Ireland, were in the range of 0.25 - 1 ppb. Although OIO photolysis after reaction 2.56 is thought to be negligible, recent laboratory investigations by *Plane et al.* [2001] suggest that the photon induced dissociation reaction

$$OIO + h\nu \longrightarrow I + O_2 \tag{2.58}$$

is important in the atmosphere. This reaction would lead to a lifetime of OIO during daytime of ≈1 s, which is in agreement with observations of OIO only after sunset [*Allan et al.* 2001; *Hebestreit* 2001; *Plane et al.* 2001]. Moreover, this reaction would also enhance ozone destruction by reactive iodine since 2 ozone molecules can be destroyed during each IO self reaction cycle.

Hoffmann et al. [2001] point out that another possible fate of OIO and IO is the polymerization of IO and OIO to higher iodine oxides I_xO_y forming aerosols as reported from laboratory experiments [*Cox and Coker* 1983; *Harwood et al.* 1997; *Hönninger* 1999]. *Hoffmann et al.* [2001] argue that this process could be responsible for bursts of new particles frequently observed in the coastal environment during low tide [*O'Dowd* 2001]. Furthermore it could explain the enrichment of iodate in marine aerosols, although the detailed mechanisms are completely unclear to date.

As a result the formation of OIO can possibly be an important sink for reactive iodine, particularly under low NO_x conditions. Figure 2.11 summarizes the current knowledge of iodine chemistry in the troposphere.

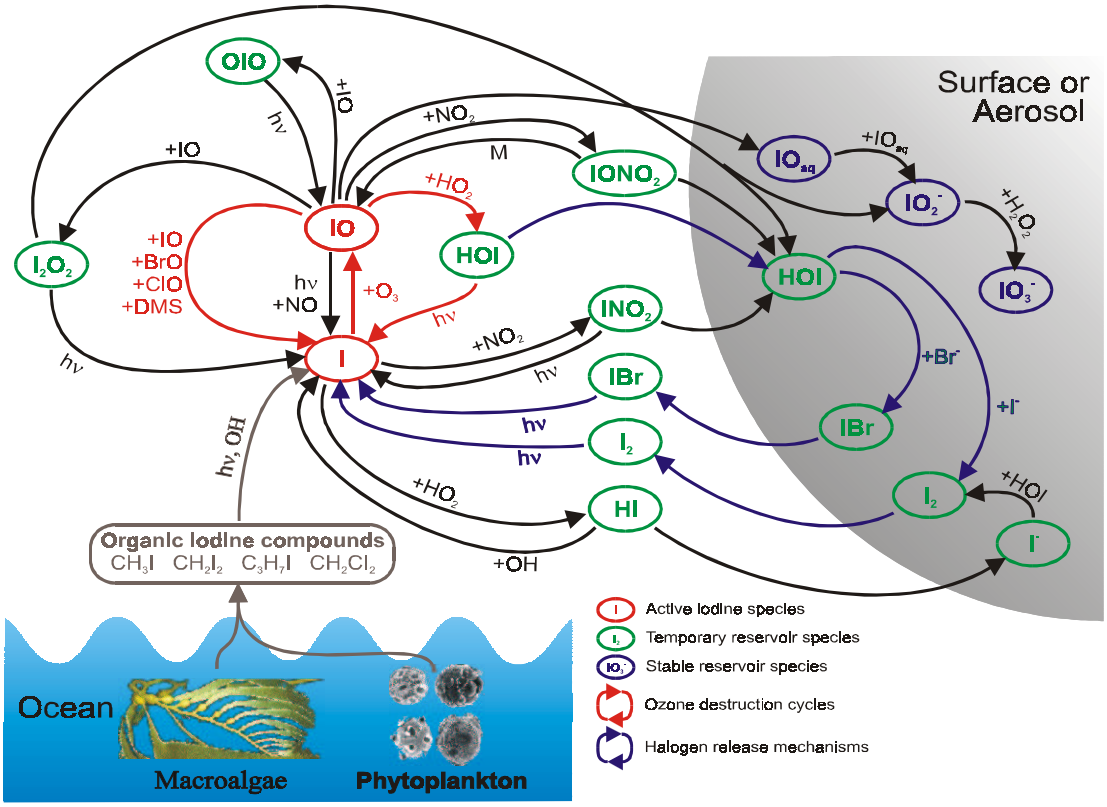

Figure 2.11: *Overview of the tropospheric iodine chemistry: Source gases are shown in brown, red arrows indicate ozone depleting catalytic reaction cycles, and blue arrows indicate heterogeneous release processes. Adapted from Platt and Janssen [1995] and Vogt et al. [1999]*

2.5 Mercury in the Atmosphere

In order to understand the atmospheric chemistry of Mercury (Hg), its basic chemical properties have to be known. Mercury is a transition element (Atomic number Z=80, atomic mass 200.6 amu). Compared to its neighbors Zinc and Cadmium in the Periodic Table it has a positive oxidation potential of E^0=+0.854 V, therefore it is chemically relatively inert. With noble metals (Au, Ag, Pt) elemental mercury (Hg^0) readily forms alloys ('amalgams'). Amalgamation with gold is also used for pre-concentration of Hg in ambient air samples prior to quantitative analysis. Hg is also the only liquid metal at ambient temperatures. Mercury can exist in three oxidation states: 0 (Hg^0), +1 (e.g. HgCl and the dimer Hg_2Cl_2) and +2 (e.g. $HgCl_2$). The role of mercury in the atmosphere was recently reviewed by *Schroeder and Munthe* [1998]. In the atmosphere mercury exists predominantly in its elemental form (Hg^0) and in the +2 oxidation state, the +1 oxidation state is very rare. Its importance is due to the toxicity of Hg^0 and other mercury species

in the atmosphere like methyl mercury (MeHg) species, which are classified carcinogens. Table 2.6 lists the main physical/chemical properties of some important mercury species.

Property	Hg^0	$HgCl_2$	HgO	CH_3HgCl	$(CH_3)_2Hg$
Melting Point [°C]	-39	277	decomp. @500	167 (sublim.)	-
Boiling Point [°C]	357	303	-	-	96
Vapor Pressure [Pa]	0.180^a	8.99×10^{-3a}	9.20×10^{-12b}	1.76^b	8.30×10^{3b}
Water solubility [g/l]	49.4×10^{-6a}	66^a	5.3×10^{-2b}	$\sim$5-6^b	2.95^b

^{a} @20°C ^{b} @25°C

Table 2.6: *Physical/chemical properties of important mercury species. Adapted from Schroeder and Munthe [1998]*

2.5.1 Sources and Partitioning of Mercury in the Atmosphere

Unlike most other metals in the atmosphere which are usually associated with aerosols and mineral dust, mercury is predominantly present in the gas phase. Due to its low water solubility (see Table 2.6) and chemical inertness the atmospheric lifetime of elemental mercury is of the order of 1 year [*Slemr et al.* 1985]. Mercury can therefore be considered a global pollutant. Figure 2.12 gives an overview of the atmospheric mercury budget. A very important characteristic of mercury is its tendency to be readily re-emitted to the air once deposited to surfaces, which always has to be considered when describing sources and sinks of Hg.

Sources and Emissions

Hg is released to the atmosphere from many natural and anthropogenic sources.

- emission from natural sources (volatilization from water and soil surfaces, emissions from volcanoes)
- re-emissions from top soil and vegetation
- anthropogenic emissions from industrial and residential sources (fossil fuel combustion, waste treatment, gold mining, chlor-alkali plants, etc.)

Pirrone et al. [1996] estimated the global anthropogenic Hg emissions of 1660-2200 t/year to be responsible for one third of the total Hg emissions. The rest is assumed to be due to natural emissions and re-emission of previously deposited mercury. Recently for Europe detailed studies of the anthropogenic and natural emissions have been performed as part of the 'European Land-Ocean Interaction Study' (ELOISE) [*Pacyna et al.* 2001; *Pirrone et al.* 2001; *Gårdfeld et al.* 2001].

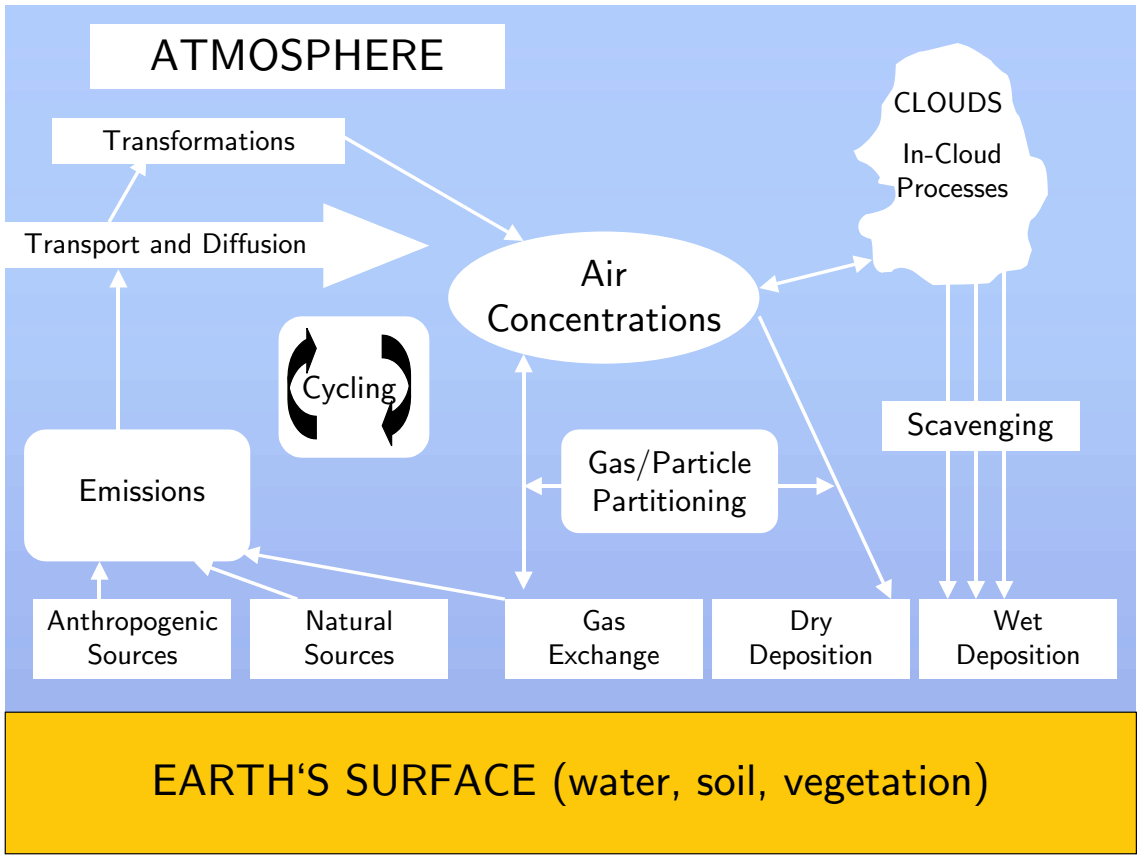

Figure 2.12: *Schematic overview of the atmospheric emissions-to-deposition cycle for mercury. Emissions here also include re-emission of previously deposited Hg, so called 'recycled' mercury. Adapted from [Schroeder and Munthe 1998]*

Physical and chemical speciation of atmospheric mercury

In the atmosphere, the main three forms of Hg are:

- gaseous elemental mercury (GEM) vapor, Hg^0
- reactive gas phase mercury (RGM)
- total particulate phase mercury (TPM)

Of these three species, only Hg^0 has been tentatively identified with spectroscopic methods [*Edner et al.* 1989]. RGM and TPM are so called sum parameters which are operationally defined, i.e. their chemical and physical structure have not been exactly identified by experimental methods but are instead characterized by their properties and capability to be collected by different sampling equipment. RGM is defined as water-soluble mercury species with sufficiently high vapor pressure to exist in the gas phase. The reactive term refers to the capability of stannous chloride ($SnCl_2$) to reduce these species in aqueous

solutions without pretreatment. The most likely candidate for RGM species is $HgCl_2$ and possibly other divalent mercury (Hg(II)) species. The gas phase mercury species Hg^0 (GEM) and RGM are summarized as *Total Gaseous Mercury* (TGM), which is usually measured by commercial mercury analyzers. TGM is an operationally defined fraction defined as species passing through a 0.45 μm filter or some other simple filtration device such as quartz wool plugs and which are collected on gold, or other collection material. TGM is mainly composed of elemental Hg vapor with minor fractions of other volatile species such as $HgCl_2$, CH_3HgCl or $(CH_3)_2Hg$. Another species of particular interest is methyl mercury (MeHg) due to the high capacity of this species to bioaccumulate in aquatic foodchains and to its high toxicity. The presence of MeHg in the atmosphere and its importance in the overall loading of aquatic ecosystems has been demonstrated in a number of publications (e.g. [*Brosset and Lord* 1995]). Since MeHg is only present at low pg/m^3 concentration levels in ambient air, it is not an important species for the overall atmospheric cycling of Hg, but mainly due to its toxicity and capacity for bioaccumulation.
Total particulate mercury (TPM) consists of mercury bound or adsorbed to atmospheric particulate matter. Several different components are possible, e.g. Hg^0 or RGM adsorbed to the particle surface, divalent mercury species chemically bound to the particle or integrated into the particle itself [*Brosset* 1987].
At remote locations, where TPM concentrations are usually low, TGM makes up the main part (>99%) of the total mercury concentration in air. However, in the Arctic boundary layer during spring (see below) TPM can be the major part of atmospheric mercury. The different mercury species are ubiquitous in the troposphere with ambient TGM concentrations averaging about 1.5 ng/m^3 in the background air throughout the world [*Slemr and Langer* 1992]. Higher concentrations are found in industrialized regions and close to emission sources. RGM and TPM vary substantially in concentration typically from 1 to 600 pg/m^3 depending on location [*Keeler et al.* 1995]. In the last few years, new automated and manual methods have been developed to measure TGM, RGM and TPM. Detailed intercomparisons of sampling and analysis methods for atmospheric mercury measurements have been reported by *Ebinghaus et al.* [1999] and *Munthe et al.* [2001].

- TGM is usually measured by Tekran® Gas Phase Mercury Analyzers. The prefiltered sample air stream is passed through gold cartridges where the mercury is collected. The mercury is then thermally desorbed and detected in an integrated CVAFS (cold vapor atomic fluorescence spectrometry) detector. These instruments were also used to measure TGM at Alert and Kuujjuarapik (see section 5.2.6 and 5.4.8).

- RGM is measured using wet chemical techniques. Mist chambers, tubular or annular denuders are used to quantitatively remove RGM from the gas phase. The so collected RGM is subsequently reduced using stannous chloride and analyzed after

amalgamation on gold traps using CVAFS detection.

- For particulate Hg, a variety of different filter methods have been applied such as Teflon or Quartz Fibre filters. Before analysis, these filters undergo a wet chemical digestion usually followed by reduction-volatilization of the mercury to Hg^0 and analysis using cold vapor atomic absorbance spectrometry (CVAAS) or CVAFS.

2.5.2 Sinks of Atmospheric Mercury and the Role of Halogens

Reactive gaseous mercury (mainly $HgCl_2$) is water-soluble (see Table 2.6) and has a high dry deposition rate usually assumed to be comparable to that of nitric acid (e.g. [*Petersen et al.* 1995]). Because RGM compounds are water-soluble, they are efficiently removed from the atmosphere during rain events and have an atmospheric lifetime in the order of days or a few weeks [*Schroeder and Munthe* 1998]. Gaseous elemental mercury (Hg^0) is very unreactive and poorly soluble in water (see Table 2.6) so it has a slow removal rate via deposition and transformation to water-soluble species. Estimates of the atmospheric lifetime of mercury were usually based on the only known atmospheric oxidation process, the very slow reaction with ozone

$$Hg + O_3 \longrightarrow HgO + O_2 \tag{2.59}$$

The rate constant for this reaction is $k_{2.59} = 3\times10^{-20}$cm^3 molec^{-1} s^{-1}[*Hall* 1995] implying a lifetime of Hg with respect to oxidation by 30 ppb ozone of 1.4 yr. Very little is known about gas phase radical reactions as oxidation pathways for Hg^0. The reaction of mercury with chlorine atoms

$$Hg + Cl + M \longrightarrow HgCl + M \tag{2.60}$$

was studied using time resolved flash photolysis studies of Hg/CF_3Cl mixtures. The rate constant $k_{2.60}$ was inferred to $(0.5 - 1.5) \times 10^{-14}$cm^3 molec^{-1} s^{-1}[*Horne et al.* 1968]. Only recently gas phase radical reactions are being investigated in more detail. *Sommar et al.* [2001] studied the reaction of mercury atoms with OH radicals

$$Hg + OH + M \longrightarrow HgOH + M \tag{2.61}$$

$$HgOH + O_2 \longrightarrow HgO + HO_2 \tag{2.62}$$

and reported a rate constant of $k_{2.61}=(8.7\pm2.8)\times10^{-14}$cm^3 molec^{-1} s^{-1}. If this reaction is included in global models a natural lifetime of Hg^0 of 4-7 months can be derived [*Sommar et al.* 2001]. This indicates that gas phase radical reactions may be important as atmospheric sinks for Hg^0. The role of reactive halogen species as oxidants for Hg^0 has also been discussed since mercury depletion events (MDE) have been found, correlated with boundary layer ozone depletion during polar sunrise [*Schroeder et al.* 1998]. Figure

2.13 shows data of TGM and ozone measured at Alert in 1995. During Arctic springtime (March to early June) TGM and ozone are well correlated suggesting that similar processes might be responsible for the depletion of these species. Since the first observation

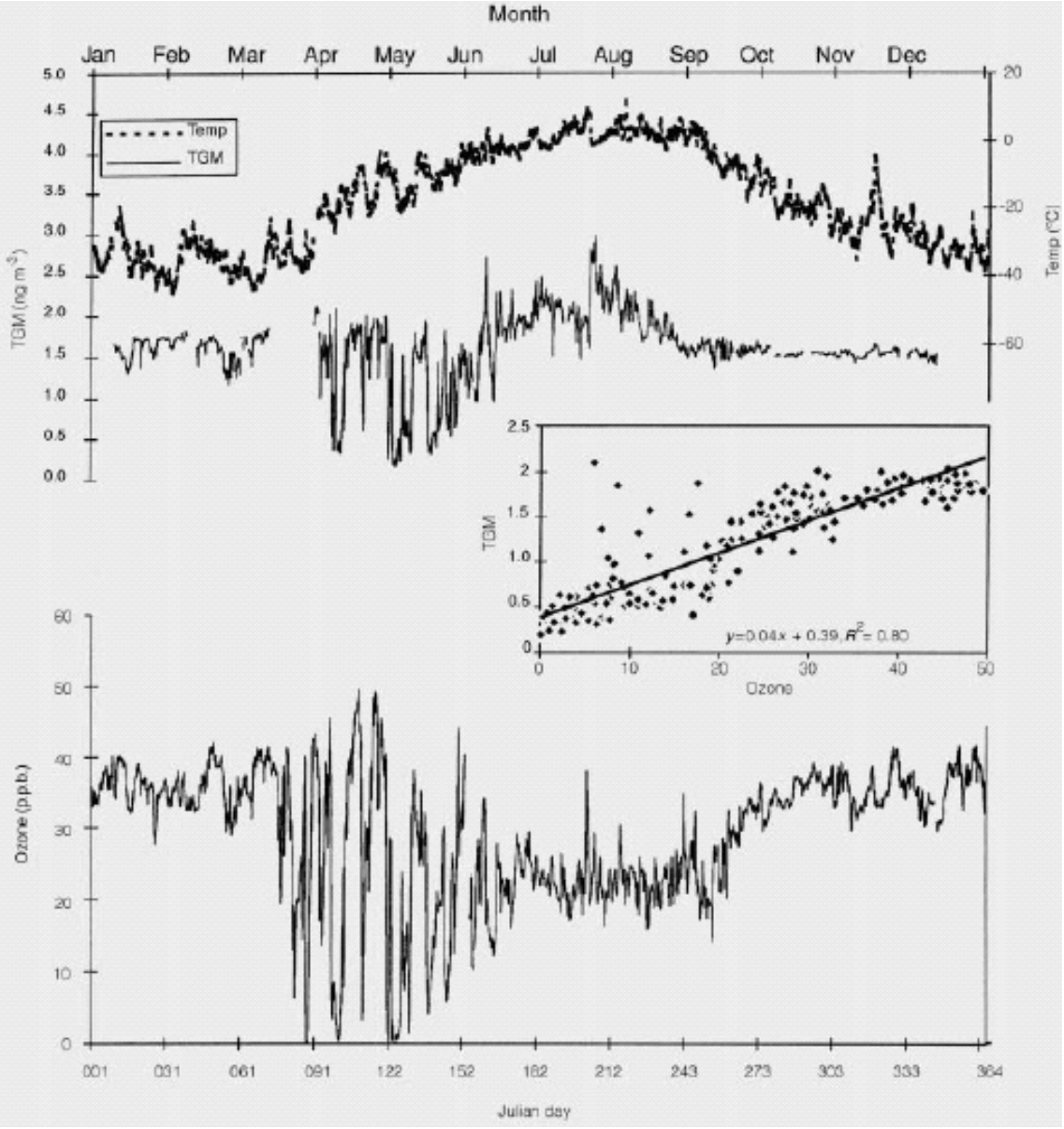

Figure 2.13: *Springtime depletion of total gaseous mercury was first reported by Schroeder et al. [1998]. The time series for 1995 show the strong correlation of ozone and mercury depletion episodes after polar sunrise at Alert, Canada.*

by *Schroeder et al.* the same behavior was found at other Arctic [*Lindberg et al.* 2001] and Antarctic sites [*Frieß* 2001]. *Boudries and Bottenheim* [2000] argue that their hydrocarbon clock measurements indicate that BrO must be responsible for the removal of gaseous

mercury. From the observation that the removal of Hg (like that of propane) stops when ozone is completely depleted whereas the removal of e.g. ethyne continues, they argue that BrO rather than Br is responsible for the oxidation of Hg^0 to Hg(II), since BrO, being produced by reaction of Br with ozone should not be present anymore after ozone is completely depleted. The proposed reaction

$$Hg + BrO \longrightarrow HgO + Br \tag{2.63}$$

was also assumed to be the key reaction for the observed Hg depletions at Alert and at the Hudson Bay (see Sections 5.2.6 and 5.4.8). Using the time dependence of the observed Hg depletion and the measured BrO mixing ratios, the rate constant for reaction 2.63 can be calculated (see Section 6.6). From the data of *Lindberg et al.* [2001] it seems now clear that the Hg depletion mechanism involves oxidation of Hg^0 primarily to some form of RGM followed by both uptake on aerosol surfaces and direct gaseous dry deposition to the local snowpack. *Lu et al.* [2001] reported magnification of atmospheric mercury deposition in polar regions by greatly enhanced wet and dry deposition flux of this toxic heavy metal to the biosphere. The conversion of Hg^0 vapor into one or more much less-volatile Hg(II) species which deposit(s) to frozen surfaces more rapidly than the precursor, and is/are much more water-soluble than Hg^0. Furthermore, oxidized inorganic Hg(II) species can be readily assimilated by polar ecosystems, thus transferring potentially toxic Hg to flora and fauna just as they commence replenishing energy reserves depleted during the long dark polar night. *Lu et al.* [2001] propose that mercury depletions take place whenever the environmental conditions favor the conversion of Hg^0 to Hg(II). Their criteria for mercury depletion are nearly the same as those listed in section 2.3.1 for the bromine explosion:

- marine/maritime location (source of sea-salt halides)
- calm weather, low wind speeds, non-turbulent air flow
- the existence of a temperature inversion
- the presence of sunlight
- sub-zero temperatures (favoring heterogeneous surface chemistry by which sea-salt halides are converted to photolyzable halogen species during and after polar sunrise)

In this thesis the first simultaneous measurements of boundary layer BrO, ozone and mercury species was possible during the ALERT2000 field campaign (see section 5.2) and the measurement campaign at the Hudson Bay in spring 2001 (see section 5.4). These measurements provide the first opportunity to study the rapid transformation of mercury species and the role of reactive bromine compounds during these processes. A detailed understanding of the involved chemical mechanisms can help to quantify and assess the importance of the polar environments as major deposition regions of atmospheric mercury.

Chapter 3

From Differential Optical Absorption Spectroscopy to Multi-Axis-DOAS

This chapter describes the principles of **D**ifferential **O**ptical **A**bsorption **S**pectroscopy (DOAS), the measurement technique used in this thesis. It will also give an overview of the processes determining the radiative transfer in the atmosphere and concepts for numerical retrieval algorithms for the trace gas concentrations and $SCDs$ (Slant Column Densities) from the raw spectra measured with the Longpath- and MAX-DOAS systems, respectively. The new MAX-DOAS technique, which was developed and first employed for ground-based measurements within this thesis, will be described. Several suggestions for possible future applications are also included.

3.1 DOAS Overview

Since the first remote sensing measurements of ozone in the earth's atmosphere by *Dobson and Harrison* [1926] spectroscopic techniques have become an increasingly important branch in the measurement of atmospheric trace gases. In 1975 and 1979 *Noxon* applied absorption spectroscopy of zenith scattered sunlight to measure stratospheric and tropospheric NO_2. In 1979 *Platt et al.* [1979] introduced Differential Optical Absorption Spectroscopy (DOAS) to measure atmospheric trace gas concentrations using an artificial light source. Since then, DOAS has been applied to measure trace-gas concentrations in the troposphere and stratosphere [*Platt* 1994; *Solomon et al.* 1987] as well as under simulated atmospheric conditions [*Etzkorn* 1998]. In fact, several important atmospheric trace gases were measured for the first time using DOAS, e.g. OH [*Perner et al.* 1976], HONO [*Perner and Platt* 1979; *Platt and Perner* 1980], NO_3 [*Platt et al.* 1980], BrO [*Hausmann and Platt* 1994] and IO [*Alicke et al.* 1999] in the troposphere, and OClO

and BrO [*Sanders et al.* 1988] in the stratosphere. A large number of other molecules absorbing light in the UV and the visible wavelength region, e.g. NO_2, NO, NH_3, ClO, O_3, SO_2, CS_2, HCHO can also be detected [*Platt* 1978; *Platt* 1994].

DOAS is a very sensitive measurement technique for these trace gases since they exhibit strong and highly structured absorption cross sections in the UV and visible spectral regions. Because DOAS is capable of measuring ambient air in the open atmosphere it is especially useful in the detection of highly reactive species, such as the free radicals OH, NO_3, halogen oxides (BrO, IO, etc.) or NO_2. The simultaneous determination of the concentration of several trace gases, by analyzing the sum of their absorptions in one wavelength interval, reduces measurement time and allows analysis of the average chemical composition of the observed air mass at high temporal resolution.

3.1.1 The Measurement Principle

In Figure 3.1 the components of a simplified DOAS set-up to measure tropospheric trace gases are shown. Light, with an initial intensity $\mathrm{I}_0(\lambda, L)$, emitted by a suitable light source passes through the observed air mass and is collected by a telescope. Extinction of light on the lightpath, due to absorption processes by different trace gases and scattering by air molecules and aerosol particles, reduces the initial intensity. After the light has travelled a pathlength L, $\mathrm{I}_0(\lambda, L)$ is reduced to $\mathrm{I}(\lambda, L)$ as expressed from Equation 3.1 using Lambert-Beer's law:

$$\mathrm{I}(\lambda, \mathrm{L}) = \mathrm{I}_0(\lambda, \mathrm{L}) \cdot \exp^{\int_{\mathrm{l}=0}^{\mathrm{l}=\mathrm{L}} -\left(\sum_{\mathrm{j}} \sigma_{\mathrm{j}}(\lambda,\mathrm{p},\mathrm{T}) \cdot \mathrm{c_j(l)} + \varepsilon_{\mathrm{R}}(\lambda,\mathrm{l}) + \varepsilon_{\mathrm{M}}(\lambda,\mathrm{l})\right)\mathrm{dl}} + \mathrm{N}(\lambda) \tag{3.1}$$

where for each trace gas species j the parameter $\sigma_j(\lambda,\mathrm{p,T})$ is the absorption cross-section which depends on the wavelength λ, the pressure p and the temperature T, $\mathrm{c}_j(\mathrm{l})$ the number density at the position l along the light path of total length L. The Rayleigh-extinction and Mie-extinction coefficients are described by ε_R and ε_M. $\mathrm{N}(\lambda)$ is the photon noise dependent on $\mathrm{I}(\lambda, L)$. In Figure 3.1a the spectrum of $\mathrm{I}(\lambda, L)$ that results from light that has passed an atmospheric volume with only one absorber (formaldehyde: HCHO) is shown. In the employed DOAS instruments, the light is focused directly onto the entrance slit or into a quartz fiber (bundle) transmitting the light to the entrance slit of a grating spectrograph, with a detector system recording the spectrum of the dispersed light. Due to the limited resolution of the spectrograph, the spectral resolution of spectrum $\mathrm{I}(\lambda, L)$ is degraded. The mathematical description of this process is a convolution of $\mathrm{I}(\lambda, L)$ with the instrument function H of the spectrograph. Figure 3.1b shows the spectrum $\mathrm{I}^*(\lambda,\mathrm{L})$ after a convolution with a typical instrument function H as it is projected by the spectrograph on the detector. By the multi channel detector the wavelength range is mapped into n discrete pixels, numbered i, each integrating the light in a wavelength interval from λ(i)

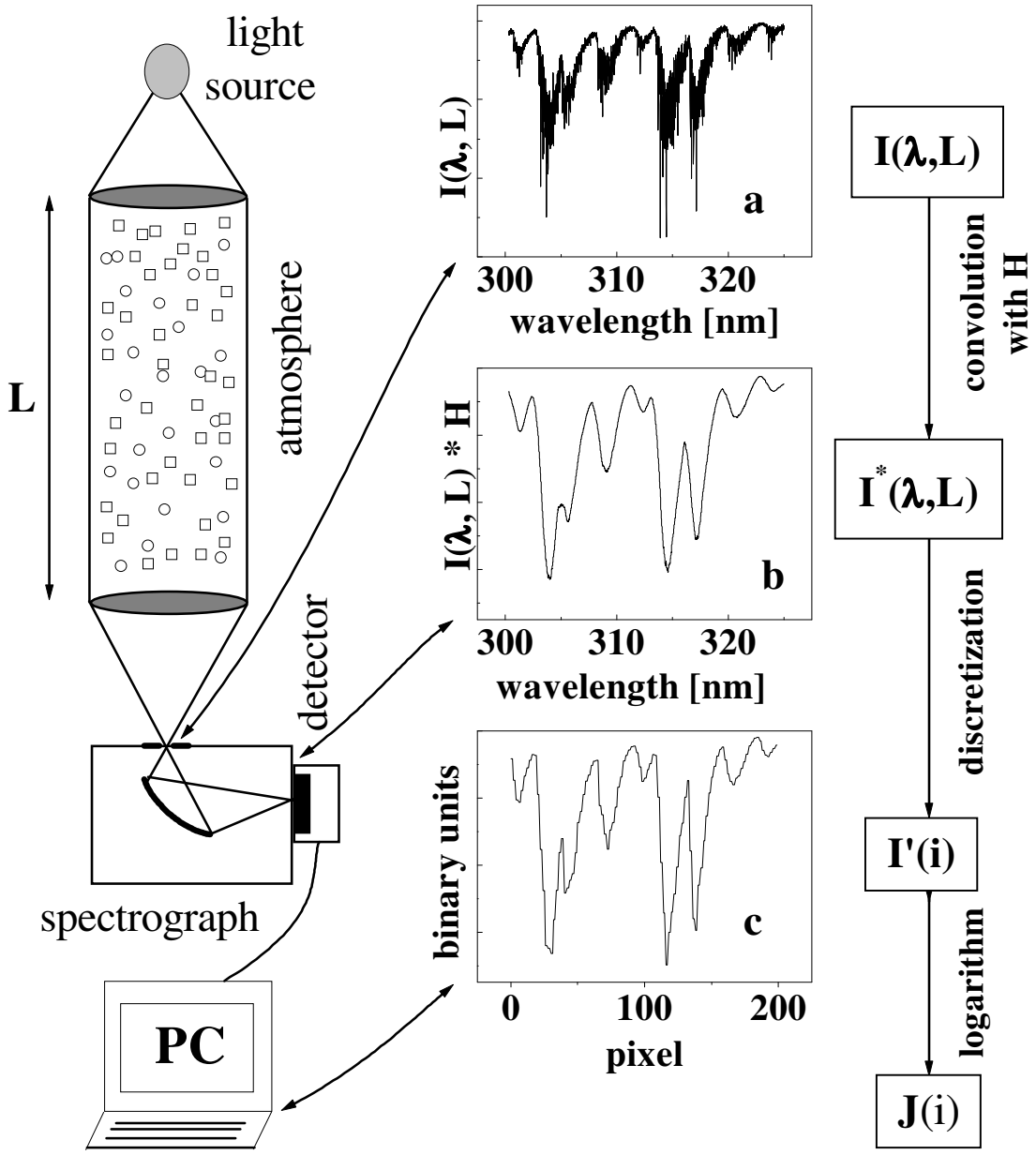

Figure 3.1: *The components of a simplified DOAS set-up. Collimated light undergoes absorption processes on its way through the observed air mass. (a): an example-spectrum of this light entering the spectrograph is shown, assuming only formaldehyde (HCHO) to be present in the observed air mass. This absorption spectrum shows the ro-vibronic structure of HCHO. (b): the same spectrum convoluted by the spectrographs instrumental function reaches the detector. (c): the spectrum after it was mapped by the detector to discrete pixels as it is actually stored to the hard-disk of a PC and can be analyzed numerically.*

to λ(i+1). This interval is given by the wavelength-pixel-mapping Γ_I of the instrument. In the case of a linear dispersion (Γ_I: λ(i)=λ(0)+$\gamma\cdot$ i) the spectral width of a pixel ($\Delta\lambda$(i) = λ(i+1) - λ(i) = γ_0) is constant. The signal I'(i) seen by a pixel i (omitting any instrumental factors, i.e. the response of individual pixels) is given by:

$$\mathrm{I'(i)} = \int_{\lambda(\mathrm{i})}^{\lambda(\mathrm{i+1})} \mathrm{I^*}(\lambda', \mathrm{L})\mathrm{d}\lambda' \tag{3.2}$$

In general the wavelength-pixel-mapping Γ_I of the instrument can be approximated by a polynomial:

$$\Gamma_\mathrm{I} : \lambda(\mathrm{i}) = \sum_{\mathrm{k}=0}^{\mathrm{q}} \gamma_\mathrm{k} \cdot \mathrm{i^k} \tag{3.3}$$

The parameter vector (γ_k) determines the mapping of pixel i to the wavelength λ(i). A change in parameter γ_0 describes a spectral shift of the spectrum. Changing γ_1 squeezes or stretches the spectrum linearly. Parameters γ_k with higher k describe a distortion of the wavelength scale of higher order. Changes in the parameter vector γ_k can be caused by different measurement conditions of the spectra, as the employed grating spectrometers usually show a temperature drift when not thermally stabilized. It is therefore necessary to correct these effects in the analysis procedure. Figure 3.1c shows the discrete spectrum I'(i) as it is recorded and stored in a computer.

The DOAS technique was especially designed to match the needs of absorption spectroscopy in the atmosphere [*Platt* 1994]. In contrary to absorption spectroscopy in the laboratory, the absolute absorption signal of an observed trace gas in the atmosphere can not be accessed due to the lack of information about the measurement light intensity in the absence of the atmosphere. The basic concept behind DOAS allows to bypass this lack of information separating the cross section σ_j into two parts:

$$\sigma_\mathrm{j} = \sigma_\mathrm{j}^\mathrm{b} + \sigma'_\mathrm{j} \tag{3.4}$$

where for a given trace gas j the σ_j^b represents broad spectral features and σ'_j the differential cross-section which represents narrow spectral structures. Considering only σ'_j in the spectra evaluation process avoids interferences from Rayleigh- and Mie-extinction. The separation of the absorption cross-section is illustrated in Figure 3.2 for ozone.

The logarithm of I'(i) (see Figure 3.1c), J(i)= ln(I'(i)), can be described by:

$$\mathrm{J(i)} = \mathrm{J_0(i)} + \sum_{\mathrm{j}=1}^{\mathrm{m}} \mathrm{a'_j} \cdot \mathrm{S'_j(i)} + \mathrm{B'(i)} + \mathrm{R'(i)} + \mathrm{A'(i)} + \mathrm{N'(i)} \tag{3.5}$$

where for each trace gas species j, $\mathrm{S'_j(i)}$ denotes the differential absorption structure. Thus ($\mathrm{S'_j}(\lambda)$=ln(exp(-$\sigma'_j(\lambda)$)$\cdot$H) corresponds to the convolution of the differential

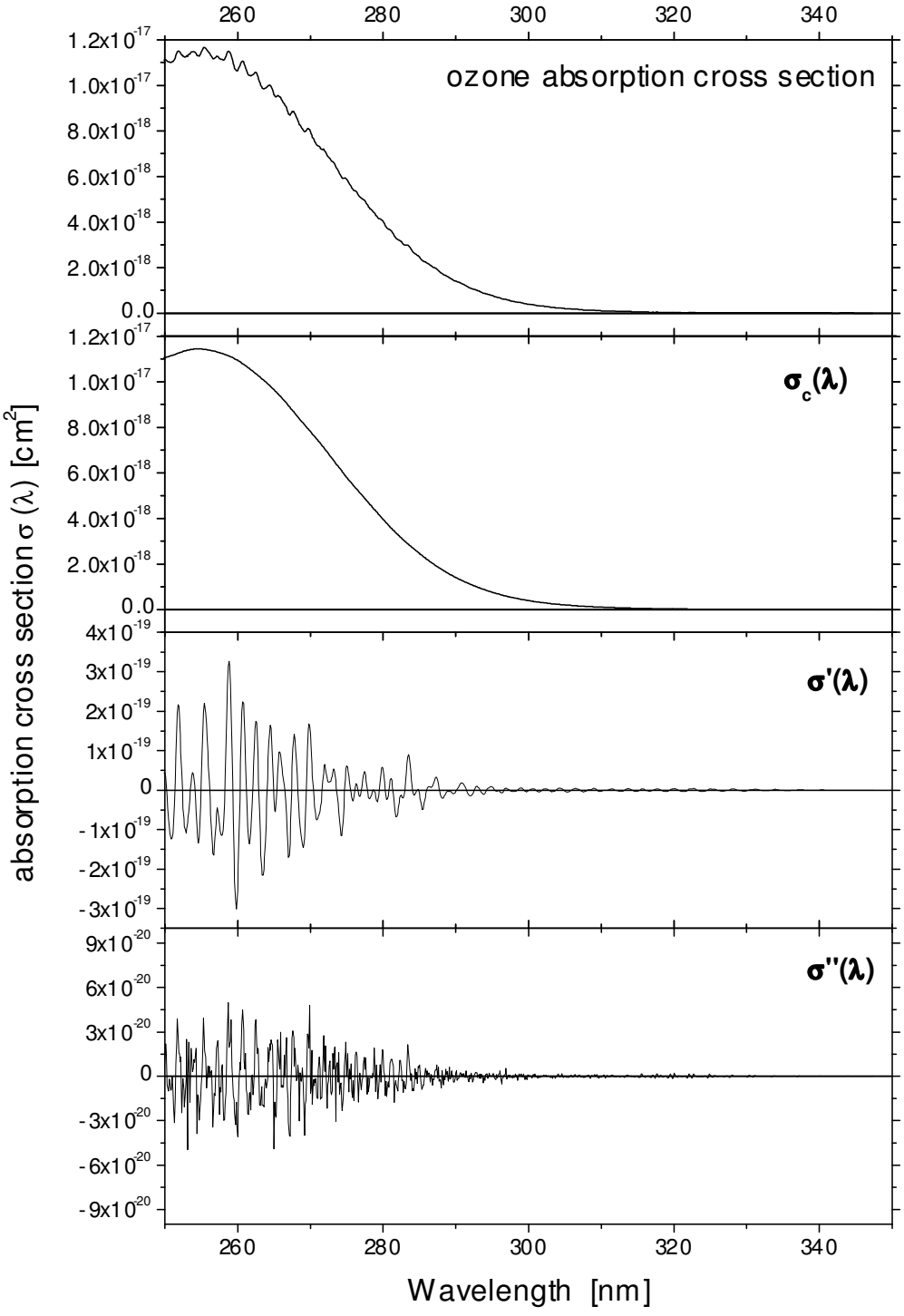

Figure 3.2: *The fundamental DOAS principle is the separation of the absorption cross-section (in this example of ozone, upper part) into 'slowly' varying (broad band, second from top), 'rapidly' varying (narrow band, third from top), and high frequency parts (bottom graph) by applying a numerical band pass filter in the evaluation procedure. Note that O_3 is an extreme case in that $\sigma' \ll \sigma_{tot}$.*

cross-section of the trace gas j with the same instrument function H. $B'(i)$ represents the broad absorption, $R'(i)$ the sum of extinction by Mie- and Rayleigh scattering, $A'(i)$ summarizes any variations in the spectral sensitivity of detector or spectrograph and $N'(i) = \ln(N(\lambda))$ is caused by the detector noise and photon statistics. The scaling factors $a'_j = \bar{c}_j \cdot L$ are then the product of the average number densities over the path-length L.

The overlaying absorption structures of several trace gases are represented by the sum in Equation 3.5. In practice the number of absorbers m can be limited to those trace gases with absorption structures sufficiently strong to be detectable with the used DOAS instrument. As the strength of the absorption structures varies with wavelength, the number of trace gases to be included in Equation 3.5 varies with the observed wavelength interval and the trace gas composition of the probed airmass. Typically $m = 2$ to 10 trace gas absorptions can be identified in a single atmospheric DOAS spectrum [*Platt* 1994]. The concentrations of these trace gases can therefore be measured simultaneously. To retrieve the concentrations, the superimposed absorption structures have to be separated numerically. The task of the evaluation procedure is: (1) to retrieve the parameters a'_j (Equation 3.5) and thus the concentration of the trace gases taking into account all the atmospheric and instrumental effects. (2) to estimate the error $\Delta a'_j$ of the parameters a'_j and therefore of the measured trace gas concentrations. Both tasks can be solved with linear least-squares methods if no instrumental effects are encountered [*Stutz and Platt* 1996].

3.1.2 The Analysis Procedure

The evaluation procedure is based on a model that describes the physical behavior of DOAS spectra according to Equation 3.5. The logarithm of the discrete measured intensity, J(i), is modelled by a function F(i):

$$F(i) = P_r(i) + \sum_{j=1}^{m} a_j \cdot S_j(d_{j,0}, d_{j,1}, ...)(i) \tag{3.6}$$

where the absorption structures of the trace gases S_j, e.g. measured in the laboratory or calculated by convolution of high resolution literature cross section with the instrument function H are input data to the procedure. The polynomial $P_r(i)$ describes the broad spectral structures caused by the characteristics of the lamp $I_0(i)$, the scattering processes $R'(i)$ the spectral sensitivity $A'(i)$ and the broad absorptions by the trace gases $B'(i)$. It can be expressed as:

$$P_r(i) = \sum_{h=0}^{r} c_h \cdot (i - i_c)^h \tag{3.7}$$

where the parameter $i_c = \mathrm{int}(n/2)$ represents the center pixel of the spectral region used for the evaluation. The polynomial refers to i_c to maximize the influence of the

nonlinear terms. The scaling parameters a_j (Equation 3.6) and the polynomial coefficients c_h (Equation 3.7) are found by linearly fitting F to J. The scaling factors a_j are used in the following to calculate the average concentration of the respective trace gases:

$$\overline{c_j} = \frac{a_j}{\sigma'_j \cdot L} \tag{3.8}$$

where σ'_j denotes the differential absorption cross section of trace gas j and L the absorption pathlength.
In order to match the wavelength-pixel-mapping of all spectra, the analysis procedure aligns the reference spectra $S'_j(i)$ (wavelength-pixel-mapping Γ_j) to the spectrum J(i) (wavelength-pixel-mapping Γ_J). The procedure therefore has to recalculate the reference spectrum $S^*_j(i)$ with the wavelength-pixel-mapping Γ_J. This can be approximated as 'shifting and stretching/squeezing' the reference spectrum in wavelength. Since Γ_j (identical to Γ_I in Equation 3.3) is a strongly monotonous function, its inverse also can be described by a polynomial:

$$\Gamma_j^{-1} : x(\lambda) = \sum_{k=0}^{q} \beta_k \cdot \lambda^k \tag{3.9}$$

where $x(\lambda)$ represents the non integer 'pixel number' that results from this inverse transformation. $S_j(\lambda)$ can now be calculated from the continuous spectrum $S_j(x)$. This spectrum has to be approximated using a (e.g. cubic spline) interpolation on the discrete spectrum $S_j(i)$.

$S^*_j(i)$ with the wavelength-pixel-mapping Γ_J can be calculated by deriving $S_j(\lambda)$ with Γ_j^{-1} from $S_j(x)$, which is approximated by a interpolation on $S_j(i)$, and then applying Γ_J:

$$S_j(i) \xrightarrow{\text{interpolation}} S_j(x) \xrightarrow{\Gamma_j^{-1}} S_j(\lambda) \xrightarrow{\Gamma_J} S^*_j(i) \tag{3.10}$$

It is possible to refrain from calculating $S_j(\lambda)$ and combine Γ_j^{-1} and Γ_J to a formula, which links i to x using a polynomial with parameters δ_k:

$$x(i) = x(\lambda(i)) = \sum_{k=0}^{q_s \cdot q_l} \delta_k \cdot i^k \tag{3.11}$$

In the analysis procedure a slightly modified equation equivalent to 3.11 is used, which has the advantage that their spectral alignment parameters $d_{j,k}$, determining the transformation, are zero if the wavelength-pixel-mappings of J and S_j are equal:

$$x = i + f_j(i) \qquad \text{with} \qquad f_j(i) = \sum_{k=0}^{p_j} d_{j,k} \cdot (i - i_c)^k \tag{3.12}$$

The spectrum $S_j(d_{j,0},d_{j,1},...)(i) = S^*_j(i)$ has now the wavelength-pixel-mapping Γ_J, which was calculated with the parameters $d_{j,k}$ following Equations 3.10 and 3.12 and

a cubic spline interpolation on $S_j(i)$. The parameters $d_{j,k}$ are derived by performing a nonlinear fit of the model F to the spectrum J with fixed parameters a_j and c_h. If $p_j = 0$ the spectrum S_j is shifted by $d_{j,0}$ pixels, if $p_j = 1$ the spectrum is additionally linearly squeezed or stretched according to parameter $d_{j,1}$. Higher values of p_j represent a squeeze or stretch of higher order. To achieve the best physical description of the spectra, it is possible to select the degree of the squeeze process p_j for every reference spectrum S_j. It is advantageous to use one set of parameters $d_{j,k}$ for two or more reference spectra if the wavelength calibration is identical for these spectra in order to reduce the number of degrees of freedom. The analysis procedure is a combination of the well-known nonlinear Levenberg-Marquardt-Method [*Levenberg* 1944; *Marquardt* 1963] determining $d_{j,k}$ and a standard linear least-squares fit [*Albritton et al.* 1976; *Bevington* 1969] to derive the a_j and the c_k. Both methods minimize χ^2 between F and J:

$$\chi^2 = \sum_{i=0}^{n} (J(i) - F(i))^2 \tag{3.13}$$

The procedure begins with the calculation of the linear fit with starting values $d_{j,k}$. The results of this fit, the parameters a_j and c_k, are used as input data in the following call of the nonlinear Levenberg-Marquardt fit. Only one step of this nonlinear iterative method is then performed. The resulting parameters $d_{j,k}$ are used in the next call of the linear fit. These results are used in the next call of the nonlinear fit. The procedure invokes the two methods alternatingly, always using the result of the last call of one method as values for the other fit method. This procedure is repeated until one of several stopping conditions for the nonlinear fit is fulfilled. Normally the fit is aborted, when the relative changes of χ^2 in the last step is smaller than a given value (usually 10^{-6}) and thus the fit has converged. The fit also stops if a number of repetitions of the iteration determined by the user is exceeded or if the nonlinear method becomes unstable [*Gomer et al.* 1993; *Stutz and Platt* 1996].

3.1.3 Corrections to the Measured Spectra

1. **Offset**:
   The offset was determined by averaging 10000 scans taken at minimum integration time available (60 ms for Hamamatsu PDA, 3 ms for SONY ILX CCD) at dark conditions. This spectrum contains the the averaged signals of 10000 offsets and a dark current of 600 s (or 30 s in case of the SONY CCD). As can be seen from Table 3.1, the dark current signal in these offset spectra can be neglected. In case of the SONY CCD detector the offset signal was found to strongly increase with decreasing temperature, since the complete USB2000 spectrometer (see section 4.3) including readout electronics is cooled with the detector.

2. **Dark Current**:
   The dark current (DC) was determined by taking one scan with an integration time of 1000 s (PDA) and 60 s (CCD) at dark conditions. Then the corresponding offset signal was subtracted. The dark current is known to slightly decrease with increasing saturation of the PDA [*Stutz* 1991], however, this can be neglected in the evaluation procedure. The dark current signal exponentially decreases with decreasing temperature of the detector. Therefore in Table 3.1 the detector temperature is also given. Several detector pixels exhibit peak dark current signals of more than 10 times the average DC signal. In case of the Hamamatsu PDA detector, about 2-5 pixels show DC peaks, for the SONY ILX detector of the OceanOptics spectrometer, up to 100 pixels are affected. These high DC pixels are probably due to endowment defects of the silicon semiconductor material.

3. **Multichannel Scanning Technique (MCST)**:
   A major problem of the use of array detectors as detectors for LP-DOAS is the high variability of the sensitivity from pixel to pixel. The pixel sensitivity depends on the wavelength of the incoming light and can vary up to some percent between the diodes of one array [*Stutz* 1996]. Since DOAS is intended to observe optical densities down to less than 10^{-3} it is necessary to compensate the different pixel sensitivities correctly. An easy way is the division of each spectrum by a lamp reference spectrum scanned just before or after each spectrum. It was found that this procedure usually leads to additional lamp structures in the spectrum since the Xe emission lines of the lamps used for LP-DOAS measurements differ in both spectra caused by lamp drift and differences of the illumination of the detector using a short cut system for lamp spectra. A common method to eliminate pixel sensitivity structures in multichannel detector spectra, the 'Scanning Multichannel Technique', was introduced by *Knoll et al.* [1990]. The method was adapted for LP-DOAS measurements by *Brauers et al.* [1995]. The basic idea of the 'Multichannel Scanning Technique' (MCST) is the combination of a multi channel detection system (PDA, CCD) with the scanning technique generally used to cover a larger spectral region with a single channel detection system. Every spectrum is separated in several single spectra with slightly shifted wavelength range. These single spectra are recorded subsequently one after another. The spectral shift is performed automatically by the spectrograph system. When adding all single spectra to a sum spectrum the individual pixel sensitivity structure remains at each channel but the spectral information changes depending on the step width of the MCST. The sum spectra can be compared to the application of a low pass filter to the original spectrum as spectral structures are broadened by the shift. Note that the step width must be smaller than any spectral structure like absorption bands otherwise this structure not only

remains in the sum spectra but could also be duplicated near itself. Then every single spectrum is divided by the sum spectrum so that diode resident structures are removed from the single spectra. Finally the single spectra are re-shifted to the correct wavelength calibration (usually done by taking mercury reference spectra for each wavelength range) and added.

Detector type	Hamamatsu PDA @-20°C				OceanOptics	
	Zugspitze (-15°C)	Alert	Crete	Hudson Bay	T = 10°C	T = 0°C
Offset [counts/scan]	213	235	234	230	300	360
Dark current [counts/s]	3.1	1.6	1.6	1.6	1.5	0.6
DC peaks	14	16	4	16	∼120	∼120
Electronic noise [$\frac{counts}{\sqrt{scans}}$]	3.4	3.6	3.5	15	2.8	2.9

Table 3.1: *Characterization of the detector units used for the DOAS measurements*

3.1.4 Error Estimation

A linear least-squares fit will give the best possible result and the correct errors only if several assumptions are valid [*Albritton et al.* 1976]. Some assumptions for the errors of the input data of the fit, i.e. the reference spectra have to be made:

1. The errors of the pixel intensity must have a finite variance [*Albritton et al.* 1976]. Since the error of J(i) is normally dominated by photon noise, the errors are Poisson distributed, therefore this assumption is valid.

2. The normal least-squares fit as discussed in [*Albritton et al.* 1976; *Bevington* 1969] and used in most of the analysis procedures assumes that the intensity errors of the individual pixels are independent. This is not strictly fulfilled because the instrument function usually has a width of 6-8 pixels. Thus neighbor pixels cannot be considered strictly independent.

3. The systematic error of the pixel intensity is zero. This is not always fulfilled, therefore the multi channel scanning technique (MCST) was applied [*Brauers et al.* 1995]. If this is not fulfilled a bias will be introduced in the results. This assumption must be checked for every instrument.

For a more detailed description of the error calculation see [*Stutz and Platt* 1996].

3.1.5 The Effects of Residual Structures

A common problem in the analysis of DOAS spectra is due to the occurrence of structures others than noise in the residuum J-F of the fit. These structures may indicate an unknown absorber or can be caused by the instrument itself and occur randomly in

most of the cases. Stable residual structures cause systematic errors in the analysis which cannot be described by statistical methods. First the question arises how these residuals can be described. In a pure noise spectrum the width of any structure is usually only one pixel, thus indicating the independence of the pixel intensities. In residuals, groups of neighboring pixel intensities appear to change simultaneously in a random way. Therefore it can be suspected that the errors of these pixel intensities are not independent from each other. A way of simulating this would be smoothing, e.g. by a running mean, a pure noise spectrum. In a running mean every pixel intensity is replaced by the average of its neighboring pixel intensities. Therefore the errors of the individual pixel intensities are no longer independent from each other. Smoothed noise spectra look similar to residuals normally found in the analysis of atmospheric spectra. Therefore the assumption of independence of the errors appears to be invalid. This is also the case if measured spectra are smoothed in some way prior to the fitting procedure, as it is common to reduce noise (see [*Stutz and Platt* 1996]). Another approach to quantify the statistical effects of residual structures on the DOAS error was introduced by *Hausmann et al.* based on simple Monte Carlo methods [*Hausmann et al.* 1997; *Hausmann et al.* 1999]. However, in this thesis the method of *Stutz and Platt* [1996] was applied by multiplying the fit errors with the appropriate factor for the respective analysis.

3.1.6 Differential Cross Sections

Here, a brief overview is given over the cross sections used for the spectral retrieval in this thesis. For the spectral analysis literature cross sections were taken and convoluted with the respective instrument function. For the best results the most highly resolved cross sections were used for the spectral retrieval. The cross sections used within this work are listed in Table 3.2. The differential absorption structures for all absorbers studied in this work are shown in Figure 3.3.

3.1.7 Example for a DOAS Evaluation

In Figure 3.4 a sample evaluation is shown for the spectral range between 312 nm and 357 nm as it was used to derive the concentrations of bromine oxide and O_3 for the long path DOAS measurements. The spectrum shown in the upper part (indicated as A) was recorded during the Hudson Bay campaign (see section 5.4). The spectrum was corrected for offset and background and the MCST algorithm applied. In addition to the reference spectra of O_3 (trace B) and BrO (trace C) spectral features of O_4, SO_2, OClO, HCHO and NO_2 need to be corrected in this spectral range. This was done by simultaneously fitting these spectra to the atmospheric spectrum. In the lowermost trace D the residual structure that remained after subtracting all the fitted reference spectra is shown. Note that the y-scale for trace D is expanded by a factor of two as compared to traces A-C.

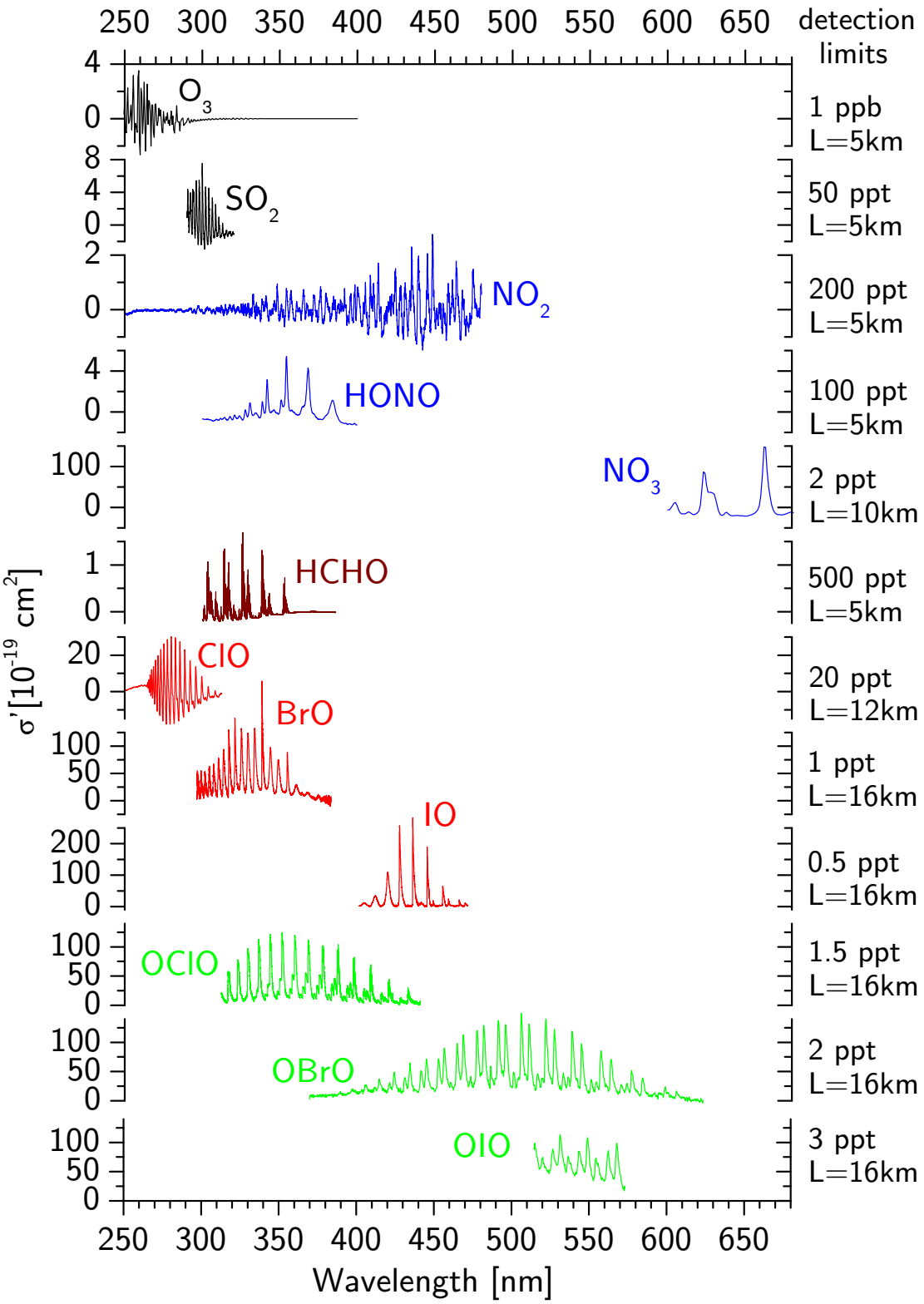

Figure 3.3: *Overview of Differential Absorption Cross Sections. For the calculation of the detection limits for long path DOAS listed on the right side a minimum detectable optical density of 10^{-3} and the indicated lightpath was assumed.*

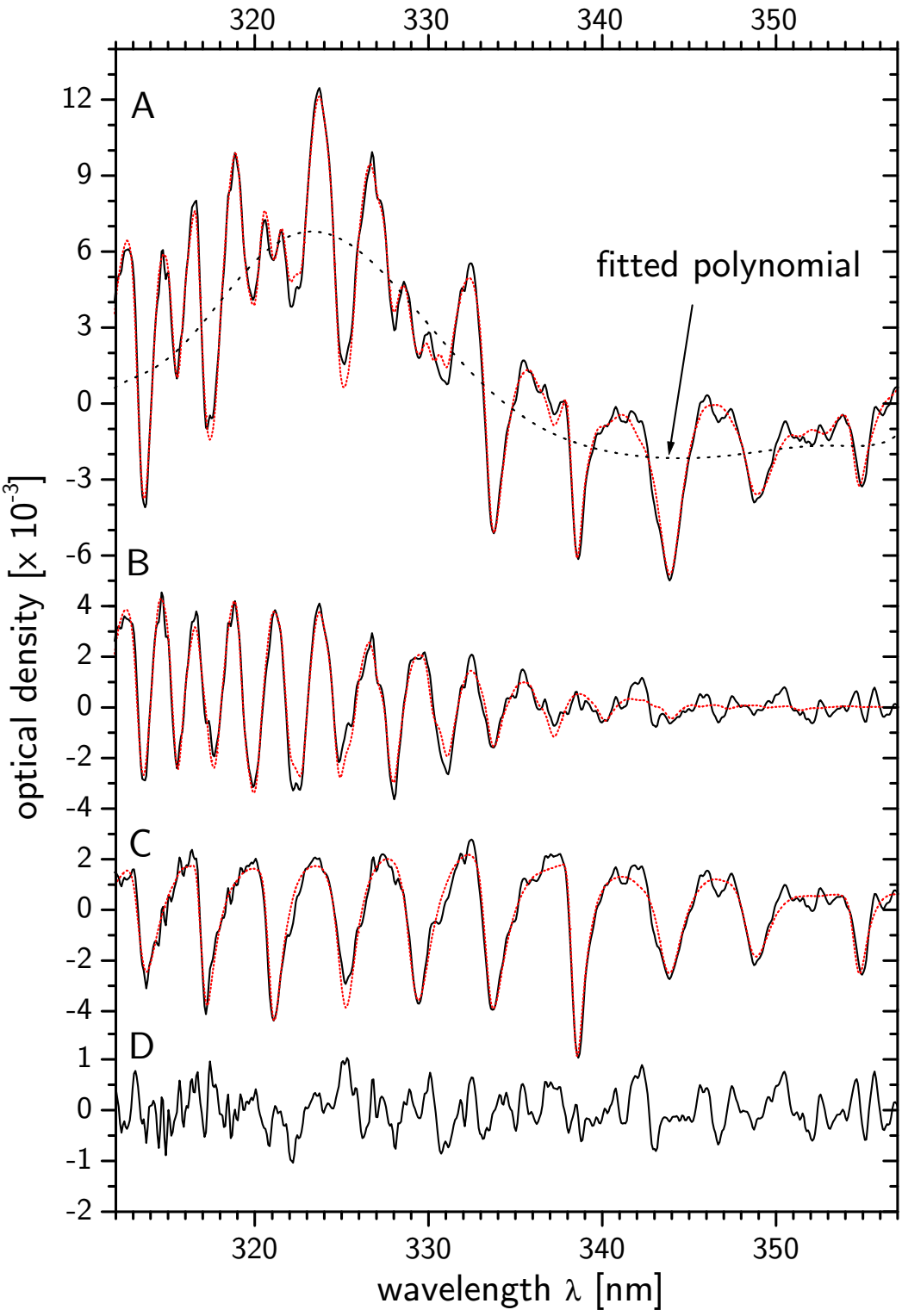

Figure 3.4: *Sample evaluation of a spectrum measured during the Hudson Bay campaign on 16.04.2001 at 18:16 GMT. Trace A: the black line is the measured atmospheric spectrum after MCST applied. Red dotted line: fit result. Black dashed line: fitted polynomial. Trace B: black line: O_3 fit result. Red dotted line: scaled reference spectrum of O_3 ($\approx 6.6 \cdot 10^{11}$ molec·cm^{-3} or ≈ 24 ppb). Trace C black line: BrO fit result. Red dotted line: scaled reference spectrum of BrO ($\approx 3.8 \cdot 10^{8}$ molec ·cm^{-3} or ≈ 13 ppt). Trace D: residual (here: $2.0 \cdot 10^{-3}$ peak to peak, shown on an expanded scale).*

Species	Source	Resolution	Reference
Ozone	FT[a]	5cm^{-1}	[*Voigt et al.* 1999]
NO_2	FT	0.5 - 1cm^{-1}	[*Voigt et al.* 1999]
NO_3	Gr[b]	1nm	[*Sander* 1986]
HONO	Gr	0.1nm	[*Stutz et al.* 1999]
BrO[c]	FT	4cm^{-1}	[*Fleischmann et al.* 2001]
IO	Gr[d]	0.09nm	[*Hönninger* 1999]
OBrO	Gr[e]	0.7	[*Rattigan et al.* 1995]
OIO	Gr	1.13nm	[*Bloss et al.* 2001]
OClO	FT	1cm^{-1}	[*Kromminga et al.* 1999]
O_4	FT	2cm^{-1}	[*Hermans et al.* 1999]
H_2O	HITRAN	0.001nm	[*Rothman et al.* 1998]
H_2O	FT(for 442 nm region)	0.001nm	[*Harder and Brault* 1997]

[a]Fourier transform spectrometer
[b]Grating spectrometer
[c]for the BrO evaluation of spectra from the Zugspitze and Alert, the cross section by *Wahner et al.* [1988] was used after correction
[d]Scaled to the cross section of [*Bloss et al.* 2001]
[e]Scaled to the cross section of [*Knight et al.* 2000]

Table 3.2: *Trace gas cross sections used in this work*

3.2 Active and Passive DOAS

The methods and algorithms described in the previous section are applicable for all variations of the DOAS technique that have been developed to date. There are, however, certain problems and solutions that are specific to the respective DOAS measurements. For example, the MCST technique (see section 3.1.3) was especially adapted for improving certain long path DOAS measurements, however, it might also be useful for other cases where the same problem of variable detector pixel sensitivity is encountered.
In the following specific issues and their solutions will be covered for 'active DOAS', i.e. DOAS systems using an artificial light source, sending and receiving optics to observe trace gas absorptions along a well-defined lightpath, and 'passive DOAS', i.e. the determination of trace gas absorptions in the atmosphere by spectroscopy of scattered, reflected or direct sunlight from the ground, airborne platforms or satellite instruments[1].

3.2.1 The Quartz Fiber Mode Mixer

In modern long path DOAS systems usually a quartz fiber is used to transmit the light from the focal point of the telescope to the entrance slit of the spectrograph. During

[1]Special developments to study the nighttime atmosphere by spectroscopy of direct moonlight or even starlight will not be covered here.

field campaigns the usage of fibers is necessary to ensure a stable illumination of the spectrograph grating and the detector. The quartz fibers used during this work are multi mode step-index fibers with a numerical aperture of 0.12, which fits best the aperture ratio of the employed telescopes. However, when a coaxial arrangement of the sending and receiving telescopes is used (e.g. [*Axelson et al.* 1990]), a ring-shaped parallel light beam is focussed onto the quartz fiber. Most fibers therefore transmit a ring-shaped light cone into the spectrograph. As a result, the grating is not uniformly illuminated. This can lead to strongly structured residuals in the DOAS evaluation, which degrade the performance of the DOAS system and make the detection of weak absorbers impossible [*Stutz and Platt* 1997]. It was found by *Stutz and Platt* [1997] that bending and shaking the quartz fiber in a 'quartz fiber mode mixer' leads to a more uniform distribution of the different modes and thus to a more homogeneous illumination of the grating and the detector. Quartz fiber mode mixers have a much higher light throughput than e.g. diffuser plates. It should be noted that the mode mixing characteristics varied strongly for the employed quartz fibers, some even exhibited very efficient mode mixing without any bending and shaking.
Despite the fact, that quartz fiber mode mixing leads to significant improvement of the instrument performance, residual noise is generally higher compared to laboratory tests of DOAS systems without quartz fibers.

3.2.2 Fraunhofer Structures

All passive DOAS instruments share the sun as their principal light source. Scattered sunlight DOAS measurements from the ground, balloon or satellite as well as direct sunlight measurements have to consider the particular shape of the solar spectrum. The radiation emitted by the sun is determined by the physical and chemical composition of the sun's surface and especially its atmosphere. The solar radiation can as a first approximation be described as the emission of a black body with T $\approx$ 5800 K. This can be explained assuming that most of the solar radiation reaching the planets originates from the so called photosphere, a relatively thin layer (about 1000 km) at the surface of the sun. The spectrum of the photosphere is a continuum (described by the Planck function for T=5800 K) with maximum intensity around 500 nm[2]. This continuum, however, is overlaid by several relatively strong absorption lines called the Fraunhofer lines (first discovered by Josef Fraunhofer, 1787 - 1826). These lines are due to selective absorption and re-emission of radiation by atoms in the solar photosphere. Compared to the absorptions of most absorbers of the terrestrial atmosphere the solar Fraunhofer lines are substantially stronger. In par-

[2]according to Wien's displacement law $\lambda_{max} \cdot T = const. \approx 3 \cdot 10^{-3} K \cdot m$ the maximum intensity of the thermal emission of the earth as seen from space is around $11 \mu m$ corresponding to T=250 K, which is the temperature of the atmospheric layer where most of the thermal radiation seen from space is emitted.

ticular in the UV and visible spectral range (300-600 nm) they are the dominant features in scattered sunlight DOAS spectra (see also upper part of Figure 3.5). The strength and shape of Fraunhofer lines varies over time due to changes in sun spot density and solar cycles (28 day sun rotation, 11 year solar cycle). However, these effects have not been found to play a significant role for the DOAS evaluation in this thesis. Another aspect of Fraunhofer lines is their change when different regions of the solar disc are observed. The so-called *center to limb darkening effect* and its influence on DOAS was studied in detail during the Solar Eclipse in 1999 [*Bösch* 2002; *von Friedeburg et al.* 2001]. The effects on scattered sunlight DOAS are not known to date, however, it can be assumed, that the ensemble of photons received by scattered sunlight spectroscopy largely averages over the solar disc.
In the DOAS analysis procedure Fraunhofer lines have to be carefully removed in order to evaluate the absorption structures of the much weaker trace gas absorptions in the earth's atmosphere (optical densities of 10^{-3} and less compared to Fraunhofer lines with up to 30% absorption). For the DOAS evaluation of scattered sunlight spectra in this thesis a so-called Fraunhofer reference spectrum (FRS) was always included in the fitting process. This spectrum was carefully chosen from the measured spectra in order to minimize the residual structures remaining after the fit. For the MAX-DOAS evaluation usually one fixed FRS taken at small solar zenith angle and zenith observation geometry for minimum trace gas absorption was used (see upper part of Figure 3.5).

3.2.3 The Ring Effect

The *Ring effect* - named after *Grainger and Ring* [1962] - leads to a reduction of the observed optical densities of solar Fraunhofer lines depending on the atmospheric lightpath. Fraunhofer lines observed at large solar zenith angles (SZA) appear weaker ("filled in") than the same lines at small SZA. Precise measurements can only be made if this effect is compensated, otherwise complete removal of Fraunhofer lines by division of spectra taken at small and large SZA, respectively, is impossible. There has been much speculation on the origin of the Ring effect, processes like rotational and vibrational Raman scattering, aerosol fluorescence etc. have been suggested as explanations. Rotational Raman scattering (see section 3.3.2) is thought to be the most probable cause for the Ring effect [*Bussemer* 1993; *Fish and Jones* 1995; *Burrows et al.* 1996]. Although optical density changes due to the Ring effect are only of the order of a few per cent, this significantly affects DOAS measurements of scattered radiation. Thus a very accurate correction is required, since the atmospheric absorptions which are evaluated are sometimes more than an order of magnitude smaller than the filling in of the Fraunhofer lines. Therefore a so called Ring reference spectrum was included in the fitting process when scattered sunlight spectra were evaluated. The scattered sunlight intensity measured by the DOAS detector

can be written as:

$$I_{meas} = I_{rayleigh} + I_{mie} + I_{raman} = I_{elastic} + I_{raman} \tag{3.14}$$

For the DOAS evaluation the logarithm of the measured spectrum is taken (see section 3.1.2).

$$ln(I_{meas}) = ln(I_{elastic} + I_{raman}) = ln(I_{elastic}) + ln(1 + \frac{I_{raman}}{I_{elastic}}) \approx ln(I_{elastic}) + \frac{I_{raman}}{I_{elastic}} \tag{3.15}$$

with

$$I_{Ring} \equiv \frac{I_{raman}}{I_{elastic}} \tag{3.16}$$

This spectrum is usually referred to as Ring spectrum and it is included in the fitting routine to correct the Ring effect. Two different approaches exist to determine a Ring spectrum.

- Measured Ring spectrum:
  This method is based on the fact that different scattering processes in the atmosphere exhibit different polarization properties. While Rayleigh scattering by air molecules is highly polarized for a scattering angle of 90° (see section 3.3.1), light scattered by rotational Raman scattering is only weakly polarized. By taking scattered light spectra from different viewing directions the rotational Raman scattered intensity and therefore a Ring spectrum can be determined [*Solomon et al.* 1987]. Since Mie scattering also enhances the fraction of depolarized light in the scattered solar radiation, the Ring spectrum determined from the polarization measurements also contains structures caused by Mie scattering, which does not contribute to the Ring effect. Also, the atmospheric light paths for different polarization are different and can thus contain different absorptions of atmospheric trace gases. As a result, the measured Ring spectrum may contain an unknown amount of atmospheric absorptions which affects the retrieval of the trace gas absorptions in the DOAS fit. Another problem with measured Ring spectra is that they are valid for specific atmospheric conditions and viewing geometry and for one specific instrument (with specific wavelength calibration). This might therefore be a good approach for some particular cases, however, this method is not applicable for the measurements performed in this work.

- Calculated Ring spectrum:
  From the known energies of the rotational states of the two main constituents of the atmosphere, O_2 and N_2, the cross section for rotational Raman scattering can be calculated. This is done by including Raman scattering into radiative transfer models [*Bussemer* 1993; *Fish and Jones* 1995; *Funk* 2000] or by calculating the pure ratio of

the cross sections for Raman and Rayleigh scattering. For the data analysis in this work the Ring spectra were determined by calculating a rotational Raman spectrum from the measured Fraunhofer spectrum (Y-command of the analysis software MFC [*Gomer et al.* 1993]). This rotational Raman spectrum is divided by the measured Fraunhofer spectrum (corrected for rotational Raman scattering to represent pure elastic scattering). An example for the calculation of a Ring spectrum is shown in Figure 3.5. It was found that the filling in could be properly corrected for by this method.

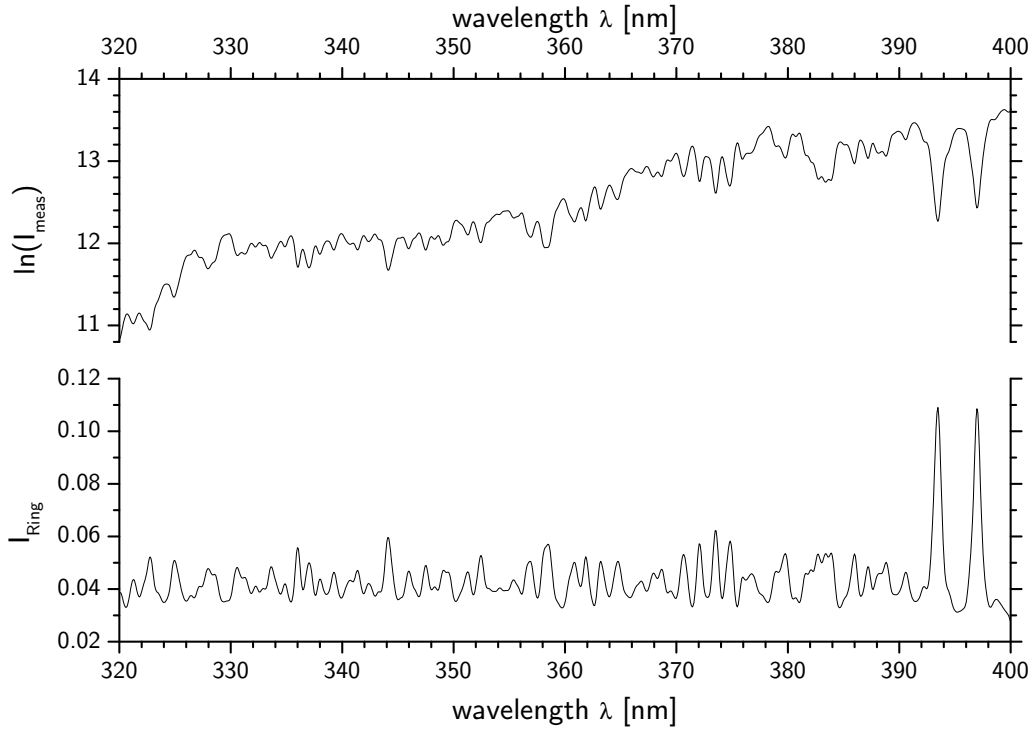

Figure 3.5: *Sample Ring spectrum calculated for the evaluation of UV spectra taken during ALERT2000. Shown is also the logarithm of the Fraunhofer reference spectrum used for the calculation. The spectrum was taken on April 22, 2000 at 15:41 UT at a local solar zenith angle of 70° and zenith observation geometry.*

3.2.4 The Solar I_0 Effect

The high number and optical density of solar Fraunhofer lines leads to strong variations of the intensity of the solar radiation with wavelength. For DOAS, where the resolution of the spectrometers is usually not high enough to resolve narrow absorption lines, this can lead to significant evaluation errors. For example when a strong solar Fraunhofer line and a narrow

absorption line of a trace gas have significant overlap, the atmospheric spectrum measured by a low resolution instrument cannot be correctly described by the standard convolution of the high resolution reference spectrum with the instrument function. Errors due to incorrect calculation of the low resolution absorption band shape result. Because these errors arise from the spectral structures of the I_0 spectrum, it is usually referred to as solar I_0 effect [*Johnston* 1996; *Platt et al.* 1997; *Huppert* 2000; *Van Roozendael et al.* 1999]. While for most of the atmospheric absorbers this leads only to negligible effects, in some cases the I_0 effect has to be corrected for. The solar I_0 effect can be accounted for using so called 'I_0 corrected' reference spectra. These can be calculated in the following manner:
First the absorption spectrum of the chosen trace gas (calculated with a high resolution cross section and solar spectrum) is convoluted with H. The result is then divided by the high resolution solar spectrum $I_0(\lambda)$ convoluted with the instrument slit function H. Applying the logarithm leads to the I_0-corrected reference spectrum:

$$R_{corrected}(\lambda) = \frac{R(\lambda)}{S_o(\lambda)} = \frac{\int_0^\infty H(\lambda', \lambda) \times I_0(\lambda') \mathrm{e}^{-\sigma(\lambda')SCD} d\lambda'}{\int_0^\infty H(\lambda', \lambda) \times I_0(\lambda') d\lambda'} \tag{3.17}$$

Obviously this I_0-corrected reference spectrum can only perfectly match the absorptions in the measured atmospheric spectrum if the same slant column density (SCD, see section 3.4) was assumed for the calculation as was present in the atmosphere. However, it was found that the calculation for a typical SCD could be used for all measured spectra. For the scattered sunlight DOAS evaluations in this thesis, all NO_2 reference spectra were I_0 corrected, for the other trace gases the effect was neglected since they exhibit either no high resolution spectral features or the absorptions are too weak to change significantly due to the I_0 effect.

3.3 Scattering Processes in the Atmosphere

The main scattering processes in the earth's atmosphere are Rayleigh and Raman scattering by air molecules and Mie scattering on aerosol particles and cloud droplets or ice particles. Elastic scattering processes have to be distinguished from inelastic processes. Scattering by molecules can be elastic (Rayleigh scattering) or inelastic (Raman scattering). In the case of Mie scattering it depends on the composition of the aerosol particle and the wavelength, e.g. for liquid water droplets at a wavelength with large liquid water absorption the scattering is highly inelastic, while for wavelengths without absorption the scattering is predominantly elastic.

3.3.1 Rayleigh Scattering

Rayleigh scattering occurs when light interacts with matter of smaller size compared to the wavelength of the incident light. The physical process can be described as electromagnetic

radiation inducing an oscillating dipole in polarizable particles, i.e. air molecules (see e.g. [*Van de Hulst* 1981]). The Rayleigh scattering cross section depends strongly on the wavelength λ ($\propto \lambda^{-4}$) and the polarizability χ ($\propto \chi^2$). An accurate empirical formula is given by *Nicolet* [1984] for λ in units of μm:

$$\sigma_{RS} = 4.02 \times 10^{-28}/\lambda^{4+x} \text{ cm}^2 \tag{3.18}$$

$$\begin{aligned} x = &\quad 0.04 &&\text{for} \quad \lambda > 550 \text{ nm} \\ x = &\quad 0.389\lambda + 0.09426/\lambda - 0.3228 &&\text{for} \quad 200 \text{ nm} < \lambda < 550 \text{ nm} \end{aligned}$$

The Rayleigh scattering phase function for the case of unpolarized incident light is given by

$$\Phi(\cos\theta) = \frac{3}{4}\left(1 + \cos^2\theta\right). \tag{3.19}$$

A polar diagram is shown in Figure 3.6.
If the anisotropy of the polarizability is taken into account (see [*Penndorf* 1957]), Equation 3.19 changes to

$$\Phi(\cos\theta) = 0.7629 \cdot \left(1 + 0.9324 \cdot \cos^2\theta\right). \tag{3.20}$$

3.3.2 Raman Scattering

Inelastic scattering which occurs by air molecules is called Raman Scattering. It can be described as light interacting with an air molecule that changes its excitation state during the scattering process. The photon either transfers part of its energy to the molecule (Stokes lines, $\Delta J = +2$, S-branch) or takes over part of the molecule's excitation energy (Anti-Stokes, $\Delta J = -2$, O-branch). The term rotational Raman scattering (RRS) is used, if only the rotational excitation is affected ($\Delta\nu = 0$), if also the vibrational state changes the term rotational-vibrational Raman scattering (RVRS) is used ($\Delta\nu = \pm 1$). Only discrete amounts of energy given by the difference between the discrete excitation levels can be transferred between the photon and the molecule. For air molecules (oxygen and nitrogen) RRS frequency shifts of up to $\pm$ 200 cm^{-1} occur, in case of RVRS a vibrational shift of $\pm$ 2331 cm^{-1} for nitrogen and $\pm$ 1555 cm^{-1} for oxygen has to be added. The RVRS is one order of magnitude weaker then the RRS, hence only RRS is regarded in the following. Details can be found in the literature [*Burrows et al.* 1996; *Haug* 1996; *Sioris and Evans* 1999]. Rotational Raman scattering is associated with the *Ring effect* (see section 3.2.3). Figure 3.7 shows the transitions for RRS and RVRS on O_2 and N_2 molecules.

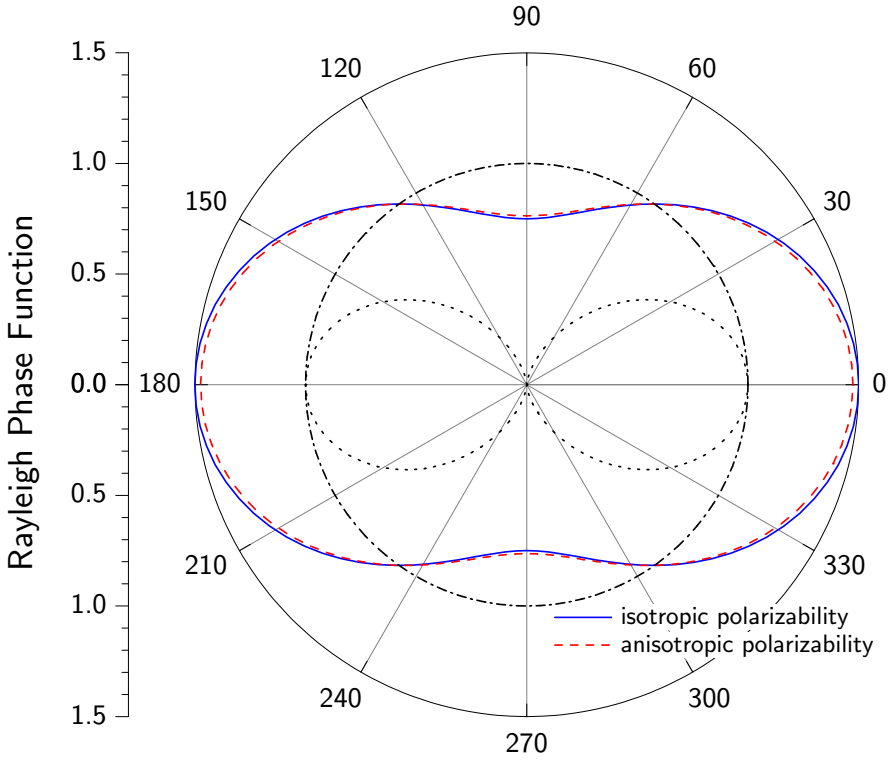

Figure 3.6: *Polar diagram of the Rayleigh scattering phase function* $\Phi(\theta)$ *for unpolarized incident light. The contribution of light polarized parallel to the scattering plane shows the* $\sim \sin^2\theta'$ *dependence of a Hertz dipole (dotted line), with* $\theta' = \pi/2 - \theta$ *being the angle between dipole axis and the Poynting vector, while the contribution of light polarized perpendicular to the scattering plane is independent of* θ *(dash dotted line).*

3.3.3 Mie Scattering

Mie scattering can be described as the interaction of light with matter of dimensions comparable to the wavelength of the incident light. It can be regarded as the radiation resulting from a large number of coherently excited elementary emitters in a particle. Interference effects have to be considered if the linear dimension of the particle is not negligible compared to the wavelength. Therefore the calculation of the differential scattering cross section can be very complicated, depending on the particle shape. However, the Mie theory is well developed and a number of numerical models exist to calculate scattering phase functions and extinction coefficients for given aerosol types and particle size distributions, [*Van de Hulst* 1981; *Wiscombe* 1980]. The most noticeable difference compared to Rayleigh scattering is the weaker wavelength dependence ($\propto \lambda^a, a \approx -1.3$) and a strong dominance of the forward direction in the scattered light. The computational effort is substantially reduced by the introduction of an analytical expression for the scattering phase function, depending only on a few observable parameters. Most common is the *Henyey-Greenstein*

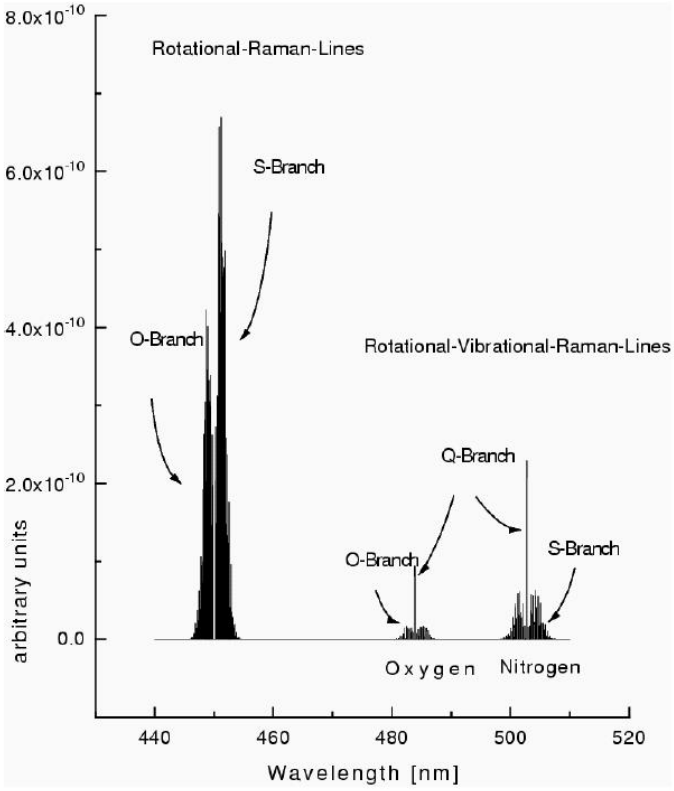

Figure 3.7: *Transitions for rotational and vibrational Raman scattering on O_2 and N_2 molecules. Adapted from Haug [1996]*

parameterization

$$P(\cos\theta) = \frac{1-g^2}{4\pi(1+g^2-2g\cos\theta)^{3/2}}, \tag{3.21}$$

depending only on the asymmetry factor g.

$$g =< \cos\theta >= \frac{1}{2}\int_{-1}^{1} P(\cos\theta)\,\cos\theta\, d\cos\theta \tag{3.22}$$

which is also used in the AMFTRAN model used for the airmass factor calculations in this thesis [*Marquard* 1998].

Tropospheric aerosols are either emitted from the surface (sea salt, mineral dust, biomass burning) or emerge from the gas phase by condensation of chemically formed hygroscopic species (primarily sulfate and nitrate). The aerosol load of the atmosphere, i.e. particle number density and size distribution, depends on the aerosol origin and history. Parameters for typical aerosol scenarios (urban, rural, maritime, background) are assembled in the data base for the radiative transfer model LOWTRAN, [*Isaacs et al.* 1987]. The data base includes the extinction coefficients and the asymmetry factors as well as

their spectral dependence. For the airmass factor calculations performed in this thesis, the LOWTRAN maritime aerosol properties were used as an approximation.
Another important aspect is Mie scattering on cloud particles, however, clouds are very difficult to describe and were therefore neglected in this work. A radiative transfer model including all cloud effects known to date was e.g. developed by *Funk* [2000].

3.4 Radiative Transfer in the Atmosphere

For the analysis and interpretation of DOAS measurements using scattered sunlight it is crucial to correctly describe the radiative transfer in the atmosphere. For trace gases with distinct vertical profiles (O_3, NO_2, BrO, etc.) the apparent absorption measured by a ground based spectrometer depends strongly on the distribution of the light paths taken by the registered photons on their way through the atmosphere. The concept of air mass factors for the interpretation of DOAS measurements using scattered sunlight is introduced in this section. First, a brief summary of the radiative transport theory and the different approaches to model air mass factors and some intrinsic problems concerning the interpretation of results from radiative transport models is described.

3.4.1 The Airmass Factor Concept

The DOAS analysis procedure explained in section 3.1.2 yields the so called *slant column density* (SCD) S, which is defined as the trace gas concentration integrated along the light path:

$$S = \int c(s)\ ds \tag{3.23}$$

It should be noted that for a single SCD measurement the individual photons registered in the detector may have travelled different paths through the atmosphere before being scattered into the DOAS telescope. Therefore equation 3.23 can only account for the most probable path defined by the statistics of the registered photon ensemble. Since the SCD depends on the observation geometry and the current meteorological conditions, it is usually converted to the *vertical column density* (VCD) V, which is defined as the trace gas concentration $c(z)$ integrated along the vertical path through the atmosphere:

$$V = \int c(z)\ dz \tag{3.24}$$

Since V only depends on the trace gas profile, it is independent of the viewing geometry and the trajectories on which the light travelled through the atmosphere before reaching the instrument. The *air mass factor* (AMF) A is defined as the ratio of SCD S and VCD V:

$$A(\lambda, \vartheta, \alpha, \phi) = \frac{S(\lambda, \vartheta, \alpha, \phi)}{V} \tag{3.25}$$

where ϑ denotes the solar zenith angle (SZA), α the telescope elevation angle and φ the relative azimuth angle between the telescope direction and the sun. The observation geometry and the respective angles are shown in Figure 3.8. For simplification the relative azimuth angle φ is set to 180° here. The AMF depends on the radiative transfer in the atmosphere and is therefore determined by factors like the trace gas profile, pressure, temperature, ozone and aerosol profiles as well as clouds, surface albedo etc. To determine the relationship between SCD S and VCD V, the optical density τ of solar radiation passing through a concentration field $c(\vec{x})$ under the assumption that the temperature and pressure dependency of the absorption cross section σ is small:

$$\tau(\lambda) = -\ln\left(\frac{I(\lambda)}{I_0(\lambda)}\right) = \sigma(\lambda) \cdot \int_0^L c(\vec{x})\ ds = \sigma(\lambda) \cdot S(\lambda) \tag{3.26}$$

Here, $I_0(\lambda)$ is the intensity observed in absence of the absorber in the atmosphere. Combining equations (3.25) and (3.26), the air mass factor can also be written as:

$$A(\lambda) = \frac{\tau(\lambda)}{\sigma(\lambda) \cdot V} \tag{3.27}$$

Equation (3.26) is only valid for a well defined light path between the position of the sun and the observer. This is e.g. the case for the observation of direct sunlight (or moonlight) in a plane parallel atmosphere with a stratified trace gas layer. It is also a good approximation for the situation sketched in Figure 3.8 as long as the indicated photon path is representative for the ensemble of photons received in the detector. For the case sketched in Figure 3.8A (e.g. a stratospheric absorption layer), the path integral in equation (3.26) is calculated along a straight line between the sun and the position of the scattering process (if refraction is neglected). Along the path between the scattering process and the detector no additional absorption is encountered. Then the line element for a given solar zenith angle ϑ is $ds = dz/\cos(\vartheta)$ with dz being the vertical line element. Therefore, the slant column density S_{strat} can be calculated as follows:

$$S_{strat}(\vartheta) = \int c(\vec{x})ds = \int c(z)\ \frac{dz}{\cos(\vartheta)} = \frac{V}{\cos(\vartheta)} \tag{3.28}$$

Hence, when neglecting refraction, the air mass factor for this approximation, can be written as:

$$A_{strat}(\vartheta) = \frac{S_{strat}(\vartheta)}{V} = \frac{1}{\cos(\vartheta)} \tag{3.29}$$

Here A_{strat} is only a function of the solar zenith angle ϑ.

The situation changes for a trace gas layer close to the ground as sketched in Figure 3.8B (e.g. an absorber confined to the boundary layer). In this case the scattering process occurs above the absorption layer and therefore the path integral in equation (3.26) is calculated along a straight line between the detector and the position of the scattering process. Now along the path between the scattering process and the sun no absorption is

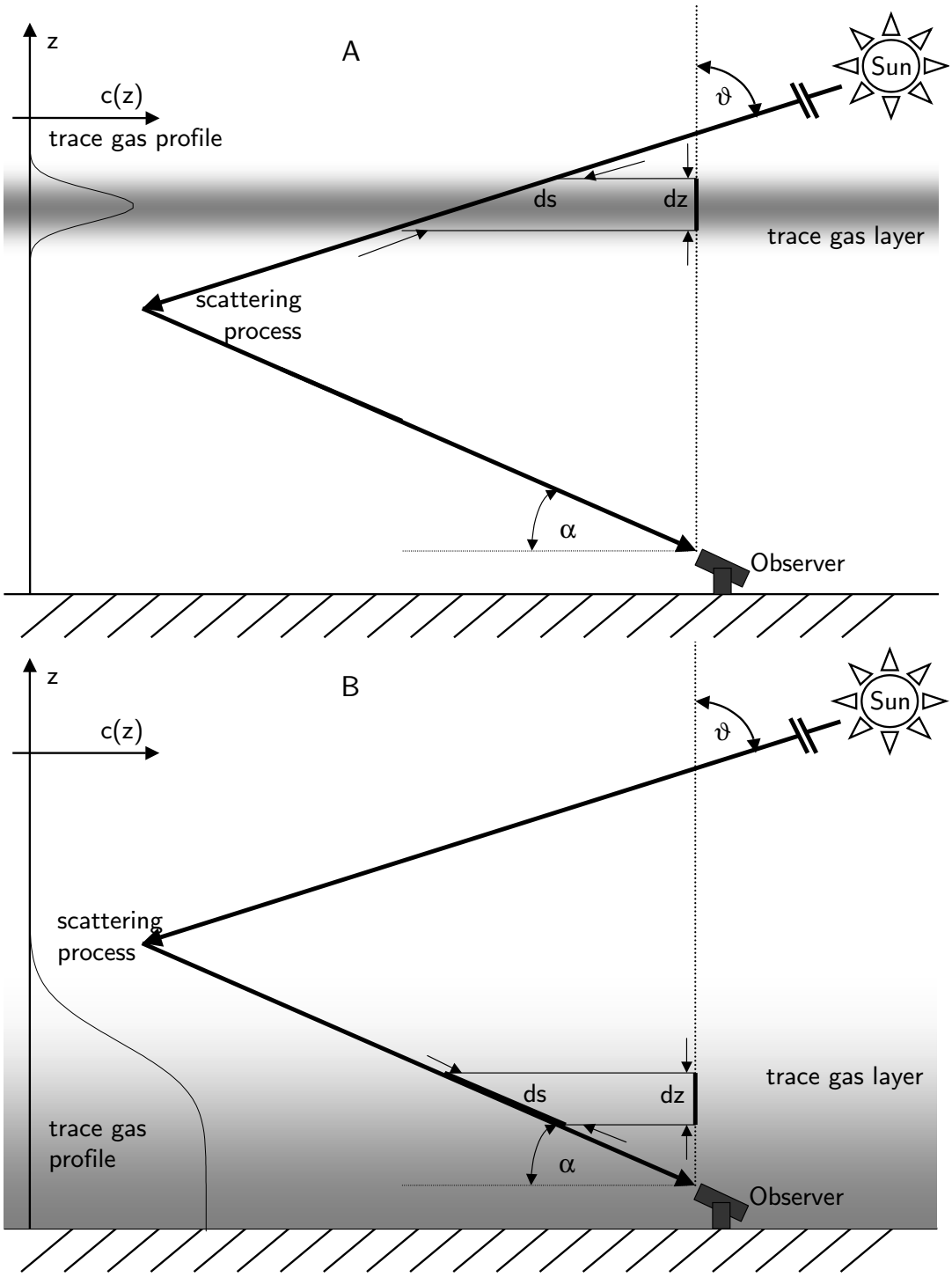

Figure 3.8: *Observation geometry for ground based DOAS using scattered sunlight. Light enters the atmosphere at the solar zenith angle ϑ. For the single scattering approximation light received by the observer was scattered exactly once into the telescope viewing direction defined by the elevation angle α. The observed SCD (integral along ds) is larger than the VCD (integral along dz), with AMF being the conversion factor. Part A represents the situation for a high trace gas layer, part B is representative for a trace gas layer at the surface.*

possible. The line element can now be expressed for a given telescope elevation angle α as $ds = dz/\sin(\alpha)$. The slant column density S_{bl} is calculated as follows:

$$S_{bl}(\alpha) = \int c(\vec{x})ds = \int c(z)\ \frac{dz}{\sin(\alpha)} = \frac{V}{\sin(\alpha)} \tag{3.30}$$

The airmass factor for the surface absorption layer

$$A_{bl}(\alpha) = \frac{S_{bl}(\alpha)}{V} = \frac{1}{\sin(\alpha)} \tag{3.31}$$

is simply a function of the telescope elevation angle. These approximations for A_{strat} and A_{bl} are valid for small solar zenith angles ($\vartheta \lessapprox 70°$) and telescope elevation angles smaller than $\approx 20°$. Equation (3.29) is a good approximation for the air mass factor for zenith scattered sunlight measurements of stratospheric absorbers [*Frank* 1991]. It will be shown in this thesis (see section 3.5.3) that equation (3.31) is a reasonable approximation as long as multiple scattering can be neglected.

For trace gas profiles other than the extreme cases A and B mentioned above, the airmass factor can as a first approximation be written as a superposition of airmass factors for the atmospheric layers, where the trace gas is abundant. For an absorber with both a stratospheric and a boundary layer fraction, the vertical and slant column densities have both stratospheric (V_{strat}, S_{strat}) and boundary layer (V_{bl}, S_{bl}) contributions. In this case the airmass factor A_{tot} can be written as:

$$A_{tot}(\vartheta, \alpha) = A_{strat}(\vartheta) + A_{bl}(\alpha) = \frac{S_{strat}(\vartheta)}{V_{strat}} + \frac{S_{bl}(\alpha)}{V_{bl}} \tag{3.32}$$

Similar relations can be derived for an additional contribution of the free troposphere, etc.

3.4.2 An Improved Airmass Factor Concept

In order to calculate airmass factors more precisely, an improved approach has to be used. For measurements of scattered sunlight, the observed detector signal represents the sum of photons travelling through the atmosphere on many different light paths Γ. This can be described by a parameter a characterizing the probability $p(a, \lambda)$ that a photon of wavelength λ travels through the atmosphere on a given light path $\vec{\Gamma}_a(s)$ from the sun to the observer (detector)[3]. The observed intensity is the integrated intensity over the photons from all possible light paths reaching the instrument, weighted with the respective probability p [*Marquard et al.* 2000] and the observed optical density is:

$$\tau(\lambda) = -\ln\left(\frac{I(\lambda)}{I_0(\lambda)}\right) = -\ln\left(\int p(a,\lambda)\ e^{-\sigma(\lambda)V\ \int \hat{c}(\vec{\Gamma}_a(s))\ ds}\ da\right) \tag{3.33}$$

[3] $p(\lambda)$ can be regarded as the probability density function of an ensemble of possible light paths. It is not evident that p can be parameterized by one ore more parameters a. Therefore the path integrals in the following equations cannot necessarily be solved analytically and should be regarded as a solution formalism only.

As before, σ is assumed to be independent of temperature and pressure and can therefore be regarded as a constant factor for the path integral. The trace gas profile $c(\vec{x})$ is written as the product of the vertical column density and the 'relative' profile shape $\hat{c}(\vec{s}) = c(\vec{s})/V$ which is independent of the trace gas amount. Combining equation (3.27) and (3.33), the air mass factor A for the observation of scattered light is

$$A(\lambda) = -\frac{\ln\left(\int p(a,\lambda)\ e^{-\sigma(\lambda)V\ \int \hat{c}(\vec{\Gamma}_a(s))\ ds}\ da\right)}{\sigma(\lambda)\cdot V} \tag{3.34}$$

Equations (3.33) and (3.34) have several important implications for the interpretation of measurements of scattered radiation:

- Equation (3.33) implies that the observed optical density is not a linear superposition of the optical densities along the individual light paths $\vec{\Gamma}_a$. Therefore the Lambert Beer law is not strictly fulfilled.

- The Lambert Beer law is strictly fulfilled only if there exists a single, well defined light path $\vec{\Gamma}_0(s)$, i.e. when observing direct light. Then the probability density function is a delta distribution, $p(\lambda, a) = \delta(a)$. In this case, equations (3.33) and (3.26) are equivalent.

- The vertical column density is not only a factor in equation (3.34). Hence, the air mass factor for scattered radiation is not only a function of the relative profile shape $\hat{c}$ but also depends on the vertical column density: $A(\lambda) = A(\lambda, V)$. Therefore, the determination of the vertical column density is equivalent to the solution of the implicit relationship (see equation (3.25))

  $$V = \frac{S(\lambda)}{A(\lambda, V)} \tag{3.35}$$

  This equation can in principle be solved using an iterative approach [*Marquard et al.* 2000]. Since the air mass factor needs to be calculated for each iteration step, this method is very time consuming and therefore not applied within this work.

- The air mass factor depends not only on wavelength λ, but also on the product of the absorption cross section $\sigma(\lambda)$ with the slant column density S: $A(\lambda) = A(\lambda, \sigma(\lambda)\cdot S)$. The air mass factor, and therefore also the slant column density, are modulated with the wavelength dependency of the trace gas cross section. This implies that the optical density is not a linear function of the cross section:

  $$\tau(\lambda) = \sigma(\lambda)\cdot S(\lambda) = \sigma(\lambda)\cdot V\cdot A(\lambda, \sigma(\lambda)\cdot S) \tag{3.36}$$

  This has important implications for the spectral retrieval since it is performed over a finite wavelength interval. For strong absorbers, such as ozone in the Huggins

bands, the wavelength dependence of the air mass factors leads to a modulation of the absorption structure which can be compensated for by using $\sigma(\lambda) \cdot A(\lambda)$ instead of $\sigma(\lambda)$ as the trace gas reference spectrum ('modified DOAS') [*Diebel et al.* 1995; *Richter* 1997].

- If a single absorber is present in the atmosphere, the probability density function $p(\lambda, a)$ depends only on Rayleigh and Mie scattering. In this case, $p(\lambda, a)$ is expected to be a broad band function of λ. If more than one species absorbs in the considered wavelength interval, equation (3.26) implies that the probability density $p(\lambda, a)$ is also a function of the cross sections $\sigma_n(\lambda)$ and concentration fields $c_n(\vec{x})$ of all other absorbers:

$$p(\lambda, \sigma_n(\lambda), a) = p_0(\lambda, a) \cdot e^{-\sum_n \sigma_n(\lambda) V_n \int \hat{c_n}(\vec{\Gamma}_a(s)) \, ds} \tag{3.37}$$

  with $p_0(\lambda, a)$ being the probability density function in absence of all absorbers. Therefore, the air mass factor for a trace gas depends also on the abundance of all other species absorbing in the given wavelength range.

- Precise air mass factors can be determined by modelling the intensities $I^M(\lambda)$ and $I_0^M(\lambda)$ in presence and absence of the absorber using a radiative transport model and by applying a spectral retrieval to these modelled spectra. Then the air mass factor is the ratio of the slant column density S^M(derived by the spectral retrieval) and the vertical column density V^M (which is a known input parameter for the radiative transport calculation): $A = S^M/V^M$. This approach is also very time consuming if variable atmospheric conditions need to be taken into account during long term measurements. Therefore this method is not applied within this work.

- Due to photochemistry, the profiles of certain trace gases possibly change with solar zenith angle (chemical enhancement). This fact can be taken into account in the radiative transport model by using a two dimensional concentration field $c(z, \vartheta)$ which depends not only on the altitude z but also on the local solar zenith angle ϑ. The concentration field can be determined by photochemical model calculations. Unfortunately, the AMFTRAN program does not support the modelling of chemical enhancement.

- Due to photochemistry and transport in the boundary layer, the trace gas profiles can also change significantly. In this case reliable modelling of the AMF is only possible in combination with precise 3D chemistry and transport models.

A possible approach to calculate the radiative transport according to equation (3.34) is the single scattering approximation [*Frank* 1991]. In this case, air mass factors are calculated under the assumption that each photon is scattered only once in the atmosphere. It follows that the light is scattered along the line of sight of the instrument (see Figure 3.8). The

individual light paths can be expressed as a well defined function of the scattering position z along the line of sight, i.e. $a \equiv z$, $\vec{\Gamma}_a(s) = \vec{\Gamma}_z(s)$ and $p(z,\lambda)$ is now the probability that a photon is scattered into the viewing direction of the instrument in a distance z relative to the instrument. It follows that:

$$A(\lambda) = -\frac{\int p(z,\lambda) \cdot e^{-\sigma(\lambda)\ V \cdot \int \hat{c}(\vec{\Gamma}_z(s))\ ds}\ dz}{\sigma(\lambda)\ V} \tag{3.38}$$

Single scattering radiative transport models have the advantage to be fast and relatively easy to implement. Reliable air mass factors can be modelled if the probability of multiple scattering is small, i.e. for stratospheric absorbers, small atmospheric aerosol loading, small solar zenith angles and relatively long wavelengths.

Multiple scattering in the atmosphere can be taken into account by using Monte Carlo radiative transport models. In this case, the paths of individual photons are treated as a random process with given probabilities for scattering and absorption events. Equation (3.34) is solved by averaging over many light paths. If all physical processes are implemented correctly in the Monte Carlo model, the precision of the air mass factor only depends on the number of modelled light paths and the accuracy of the atmospheric input parameters.

The AMFTRAN Monte Carlo radiative transfer model [*Marquard* 1998] was used here to calculate air mass factors for the MAX-DOAS measurements. It includes multiple Rayleigh and Mie scattering, refraction and full spherical geometry.

Differential Slant Column Densities and the Langley plot

The primary result of a DOAS retrieval according to section 3.1.2 is the *differential slant column density* (dSCD). The dSCD is the difference between the slant column density in the spectrum I and in the Fraunhofer Reference Spectrum (FRS) I_0 (see section 3.2.2).

$$dSCD(\vartheta,\alpha) = S(\vartheta,\alpha) - S_{FRS} \tag{3.39}$$

For zenith scattered light DOAS measurements of stratospheric absorbers the dependency of the air mass factor on the solar zenith angle ϑ can be used to convert the *differential slant column densities* $dSCD(\vartheta)$ into *absolute slant column densities* $S(\vartheta)$. Combining equations (3.39) and (3.25) leads to

$$dSCD(\vartheta) = A(\vartheta) \cdot V - S_{FRS} \tag{3.40}$$

The differential slant column density is a linear function of the air mass factor, if the vertical column density does not depend on the solar zenith angle. Equation (3.40) implies that the slant column density of the Fraunhofer reference spectrum, S_{FRS}, is given by the intercept of the linear fit when plotting $dSCD(\vartheta)$ versus $A(\vartheta)$ and the slope is the vertical

column density.
The Langley plot method, however, is only applicable when the following criteria are fulfilled:

- constant vertical column density over the measurement time
- the airmass factor in equation 3.35 must be independent of V
- airmass factors must be recalculated in case of changes in any of the model input parameters (especially changes in the vertical profile of the absorber itself are crucial).

For this study none of the mentioned criteria was strictly fulfilled. Especially the high temporal variability of the evaluated absorbers (see section 5.2.3) and their vertical column densities rendered the Langley plot method unusable for the studies presented in this thesis.

3.5 The Multi-Axis-DOAS Technique

In this section the development of the Multi-Axis-DOAS technique is described. The method is based on previous DOAS applications which are combined and modified to result in this new approach. Since it opens a wide field for future applications of the DOAS technique it can be considered a milestone in the DOAS evolution. As already discussed in the DOAS overview (see section 3.1), in the first years of DOAS mainly two different instrumental setups for the measurements of atmospheric trace gases were used:

- Scattered sunlight was used to study stratospheric and tropospheric NO_2 by ground-based absorption spectroscopy [*Noxon* 1975; *Noxon et al.* 1979; *Solomon et al.* 1987; *Solomon et al.* 1987]. These *passive DOAS* measurements yield slant column densities of the respective absorbers. Because the radiative transfer modelling necessary for the determination of vertical column densities is best understood for zenith scattered sunlight, most observations were done using zenith scattered sunlight.

- Artificial light sources were used to study trace gases, especially radical species in the planetary boundary layer by long path DOAS [*Perner et al.* 1976; *Perner and Platt* 1979; *Platt et al.* 1979; *Platt et al.* 1980; *Platt and Perner* 1980]. These *active DOAS* measurements yield trace gas concentrations averaged along the several kilometer long lightpath setup between two ground stations.

In the following years the DOAS technique was subsequently enhanced for various studies of tropospheric and stratospheric trace gases. Measurements using direct sunlight or moonlight, especially from balloon borne instruments were very important for deriving vertical trace gas profiles [*Pommereau and Piquard* 1994; *Harder et al.* 1998; *Fitzenberger et al.* 2000]. In fact, since the beginning of absorption measurements in the atmosphere the vertical distribution of absorbers was of particular interest. Shortly after *Dobson and Harrison* [1926] made the first measurements of atmospheric ozone absorption, *Götz et al.* [1934] developed the so-called 'Umkehr' method, which allowed the retrieval of ozone concentrations in 5 to 8 layers, the first vertical profiles of ozone. In that case the dependance of the atmospheric lightpath on the solar zenith angle ϑ for two different wavelengths was used to derive the profile. Since then many other methods for the retrieval of vertical profiles of atmospheric components have been developed, for more information see e.g. the review by *Rodgers* [1976].

3.5.1 Off Axis DOAS

Off Axis DOAS for Stratospheric Studies

Zenith sky observations had already been performed for many years when the off axis geometry for measurements of scattered sunlight was first introduced by *Sanders et al.* [1993] to observe OClO over Antarctica during twilight. The strategy of their study was to observe OClO in the stratosphere using scattered sunlight as far into the 'polar night' as possible. As the sun rises or sets, the sky is of course substantially brighter towards the horizon in the direction of the sun than it is in the zenith. Thus the light intensity and therefore the signal to noise ratio is improved significantly. Figure 3.9 illustrates the different geometries for zenith and off axis scattered sunlight. The *off axis angle* in this case is defined as the angle between zenith and viewing direction. *Sanders et al.* [1993] also pointed out, that the off axis geometry increases the sensitivity for lower absorption layers. They found out that absorption by tropospheric species (e.g. O_4) is greatly enhanced in the off axis viewing mode, whereas for an absorber in the stratosphere (e.g. NO_2) the absorptions for zenith and off axis geometries are comparable. By the time of the measurements of *Sanders et al.* the existing radiative transfer models did not yet allow the calculation of airmass factors for the off axis viewing mode, so the measurements could only be treated semi-quantitatively.

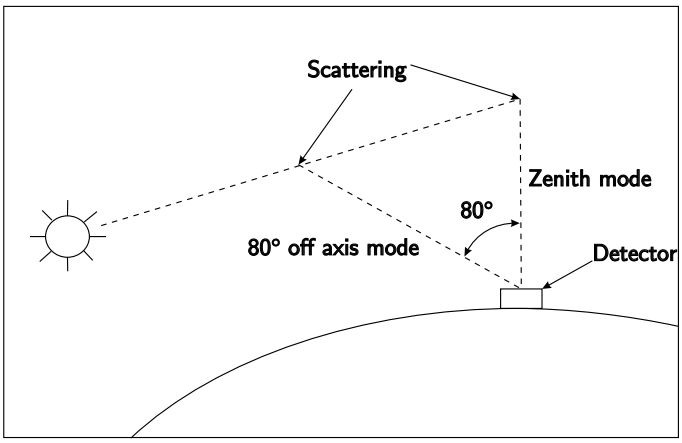

Figure 3.9: *Schematic diagram of the zenith and off axis observing geometries. Adapted from Sanders et al. [1993]*

Off Axis DOAS for Tropospheric Studies

In spring 1995 *Miller et al.* [1997] conducted off axis measurements at Kangerlussuaq, Greenland in order to study tropospheric BrO and OClO related to boundary layer ozone depletion after polar sunrise. They used off axis angles of 87° and 85°, respectively to use

the absorption by the tropospheric BrO fraction more efficiently. However, no comparison was done with zenith sky measurements, so the stratospheric background could not be separated. Instead, they used the behavior of the BrO slant column change with solar zenith angle to identify episodes of tropospheric BrO. The main difference between the slant column change for tropospheric and stratospheric absorbers is that for a stratospheric absorber the absorption increases strongly towards twilight whereas for a tropospheric absorber the signal slightly decreases (see Figure 3.10). *Miller et al.* [1997] reported enhanced

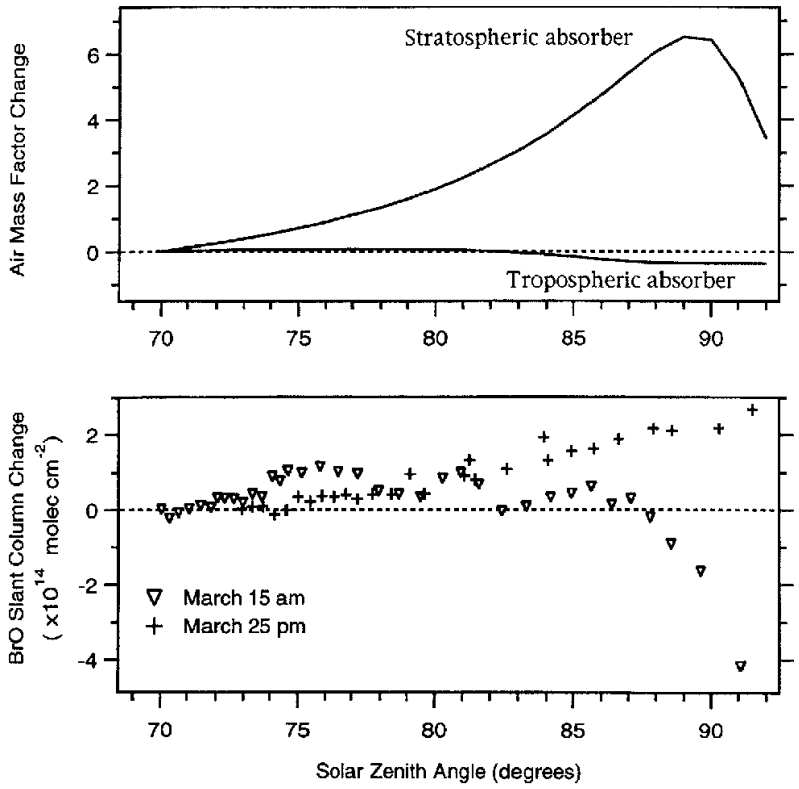

Figure 3.10: *Top: behavior of the airmass factor for a stratospheric and tropospheric absorber. Bottom: observed BrO dSCD during twilight for the case of mainly stratospheric (+) BrO and for low tropospheric BrO (triangles). Adapted from Miller et al. [1997].*

morning and evening twilight BrO slant columns which were correlated with surface ozone depletion events. From the twilight behavior they derive the information that the BrO resides low in the troposphere. Mixing ratios of 13 ppt BrO were calculated based on the assumption that the observed BrO is uniformly distributed in the lowest kilometer. Tropospheric OClO was not reported. Although this study represents the first boundary layer BrO measurements using scattered sunlight in off axis viewing mode, it suffered from several problems:

- the stratospheric column could not be separated properly, especially the diurnal

variation of the stratospheric column masked the changes in tropospheric BrO.

- the use of twilight SCD behavior to identify tropospheric BrO only works when much more BrO resides in the MBL than in the stratosphere.
- phenomena like advection and fast photochemistry which characterize the Arctic boundary layer disturb the diurnal BrO SCD behavior.
- when only the twilight BrO SCD are used, no sudden changes requiring high time resolution can be monitored.

Off Axis DOAS for Profile Retrieval

Off axis DOAS was also used for the measurement of stratospheric profiles and total tropospheric columns of NO_3 by ground based instruments [*Weaver et al.* 1996]. *Smith and Solomon* [1990] had already derived an NO_3 profile covering the stratosphere and reaching down to 3 km by observing direct moonlight as well as scattered sunlight during sunrise in a very similar geometry as for the off axis scattered sunlight measurements. *Smith et al.* [1993] repeated the experiment in the Antarctic region using a Gaussian retrieval to cover the entire troposphere. *von Friedeburg et al.* [2001] further developed the technique to derive vertical profiles for the entire troposphere in urban environments using scattered sunlight during sunrise as the light source. The method utilizes the rapid photolysis of NO_3 combined with the special illumination situation during sunrise. Before local sunrise, only elevated layers of the atmosphere are directly illuminated by sunlight. When the sun rises, the solar terminator decreases in height, which exposes subsequently lower layers to direct solar light (see Figure 3.11). In the directly illuminated part of the atmosphere (line A-B and above) the nitrate radical concentration is rapidly depleted. Information on the vertical distribution is obtained from a series of measurements of the slant column density (SCD) which is the integrated concentration along the line B-C as derived from recorded spectra using DOAS. The DOAS system employed by *von Friedeburg et al.* [2001] was also the first prototype of a MAX-DOAS (see below) instrument, the PROTO-MAX-DOAS [*von Friedeburg* 1999]. However, the application for the sunrise NO_3 profile measurements did not require the Multi-Axis capability, which was later applied to monitor NO_2 emissions and variability next to a highway in spring 2001 [Chr. von Friedeburg, personal communication, 2001].

3.5.2 Multi-Axis-DOAS Observations from the Ground

In the framework of this thesis the first MAX-DOAS measurements were performed from the ground. The MAX-DOAS setup used for the ground-based observation of boundary layer BrO during the ALERT2000 field campaign (see section 5.2) is shown in Figure 3.12. The ground-based instrument receives scattered sunlight using a single telescope.

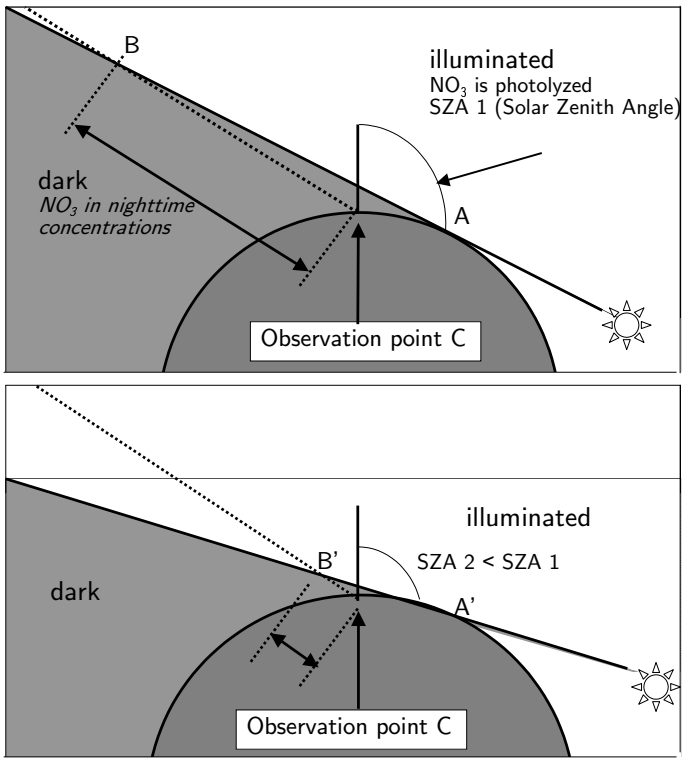

Figure 3.11: *Viewing geometry of off-axis-spectroscopy for NO_3 measurements. The technique utilizes the light scattered into the detector when the sun is still below the horizon. Shown as dotted line is the instrument's line of sight, which crosses the solar terminator (straight line). Top: At SZA 1 the scattered light traverses the distance between B and C in the dark airmass. Bottom: At the smaller SZA 2, the direct sunlight zone extends further down, and the light path B' - C through the dark layers is shorter, leading to a smaller SCD of NO_3 [von Friedeburg et al. 2001].*

By changing the telescope pointing light can be received from different directions, thus allowing to derive spatial information on the absorbers. For observation of zenith scattered sunlight the photons received in the telescope have travelled a relatively long path in the stratosphere and a comparatively short path in the troposphere (a more quantitative description is given in section 3.5.3). The low telescope elevation angles, however, emphasize the absorption path in the lowermost atmospheric layers. In particular the sensitivity for absorbers in the boundary layer is strongly enhanced. Figure 3.12 illustrates the situation for the setup at Alert, where elevation angles of 5°, 10° and 20° were combined with zenith observations. Radiative transfer model (RTM) calculations (see section 3.4 and 3.5.3) show, that for zenith observation the scattering processes at 355 nm are most likely in the lower stratosphere and upper troposphere, for decreasing elevation angles the most probable scattering altitude shifts towards the ground. For the employed elevation angles most of the light received by the telescope was scattered into the telescope above the trace

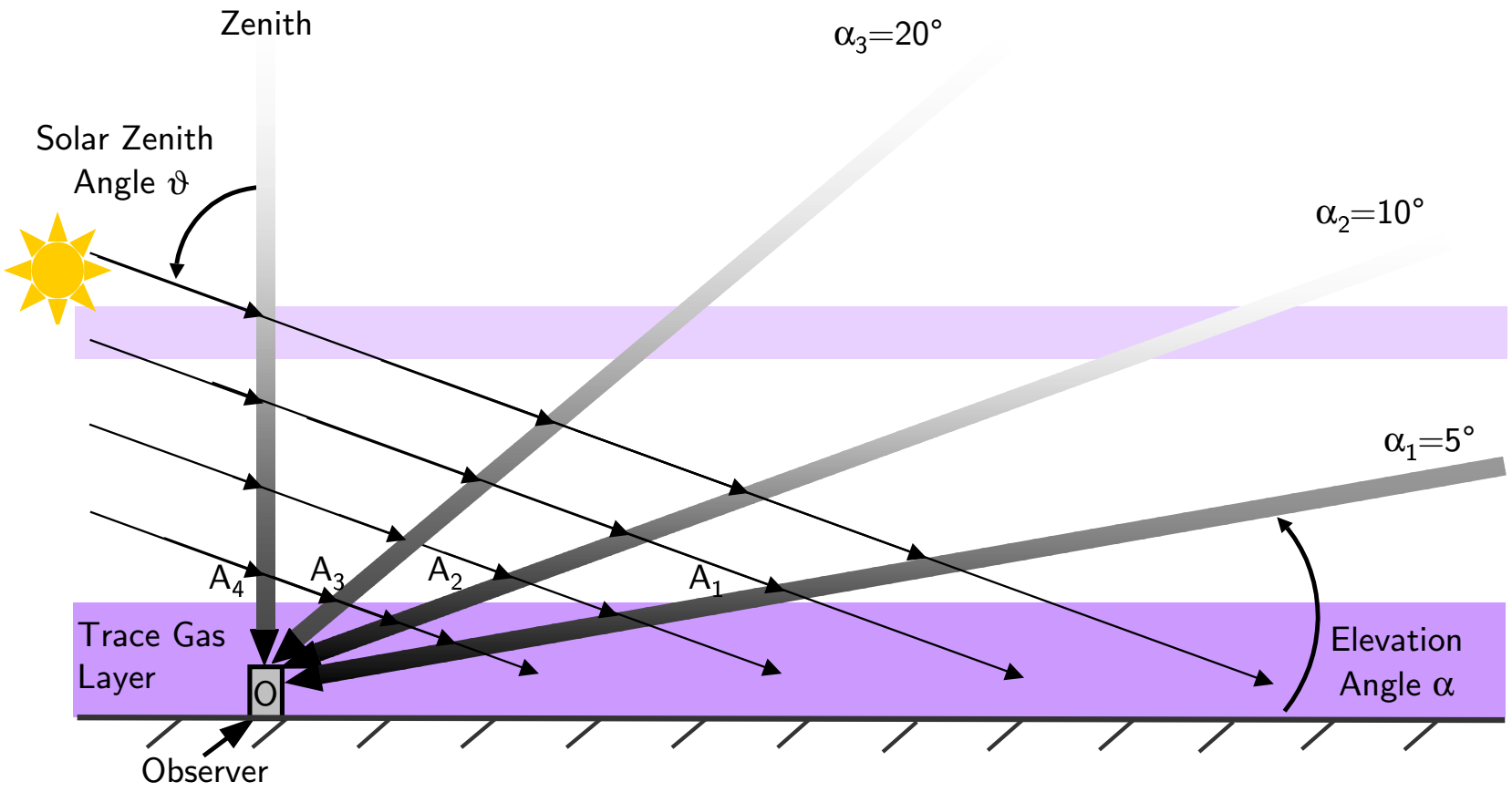

Figure 3.12: *Ground-based MAX-DOAS setup for boundary layer studies: spectra are recorded from 5°, 10° and 20° above the horizon as well as from zenith direction. The arrows indicate photon paths through the atmosphere and into the telescope (O). A_1 to A_4 mark the intersections of the main photon paths (wide arrows) for the 4 elevation angles and the upper limit of a sample trace gas layer near the surface. The absorption path in the trace gas layer ($\overline{OA_1}$, $\overline{OA_2}$, $\overline{OA_3}$ and $\overline{OA_4}$, respectively) decreases approximately according to 1/sin(α). Thus the sensitivity for absorbers in the boundary layer increases strongly for the low elevation angles (Figure not to scale). Adapted from Hönninger and Platt [2002].*

gas layer at the surface. Hence the effective absorption path can be approximated as the distances $\overline{OA_i}$ (i=1, 2, 3, 4), which increase according to $1/\sin(\alpha)$ for decreasing telescope elevation angle α.

The Telescope Elevation Angle

In Figure 3.12 the definition of the important angles in the MAX-DOAS approach is the following:

- *Solar Zenith Angle* (SZA) ϑ:=the angle between **zenith** and the direction of the sun
- *Telescope Elevation Angle* or short 'elevation angle' α:=angle between the **horizontal** direction and the viewing direction of the telescope

The definition of the solar zenith angle is exactly the standard definition found in the literature and used for decades now when studies of direct or scattered sunlight are described. The definition of the telescope elevation angle, however, is new, so a justification will be given here why such a definition was chosen. At first, the definition seems to disagree with previously published approaches (see section 3.5.1). Since the first studies using off axis geometries were done for the purpose of stratospheric measurements the strong dependence of the sensitivity for low atmospheric layers on the viewing direction was not further considered. In analogy to the definition of the solar zenith angle the off axis angle was defined as the *observation zenith angle* measured between viewing direction and zenith [*Sanders et al.* 1993]. Radiative transfer model calculations performed in this thesis (see section 3.4 and 3.5.3) show that the MAX-DOAS method is especially useful for probing the atmospheric layer where the instrument is located: for ground-based MAX-DOAS this refers to the boundary layer, for AMAX-DOAS this corresponds to the layer around flight altitude. Viewing directions into this layer yield the highest absorption signals, so most likely viewing directions towards the horizon are used. According to equation 3.31 the airmass factor for an absorption layer below the most probable scattering altitude[4] is approximately given by $1/\sin(\alpha)$. For an absorber in the boundary layer (see also AMF dependence on the trace gas profile below) the absorption path (described by the slant column density S) in the boundary layer is inversely proportional to the telescope elevation angle α, so S can be simply expressed as:

$$S \propto \frac{1}{\alpha} \tag{3.41}$$

For example, doubling of the elevation angle will lead to approximately half the absorption signal if an absorber in the boundary layer is observed by ground-based MAX-DOAS. If

[4]the approximation is also valid for an absorption layer at flight altitude in case of AMAX-DOAS, see [*Wagner et al.* 2001]

observation zenith angles were used (ranging between 80° and 90° for most cases), the corresponding relation would not be as simple and plausible. This fact should motivate the chosen definition since it facilitates the argumentation significantly. Moreover, this work represents the first application of the MAX-DOAS approach for boundary layer studies, where the chosen definition proved very useful. Therefore this new definition is considered legitimate.

3.5.3 MAX-DOAS Airmass Factors

As already introduced in section 3.4.1 from slant column densities S, which depend on the solar zenith angle and the viewing geometry of the receiving telescope, vertical column densities V can be calculated using the formula:

$$S = V \times A \tag{3.42}$$

where A denotes the air mass factor. As shown in section 3.4.1 for a rough approximation, the geometric approach using the formula A≈1/cos(ϑ) (for scattering below the trace gas layer), where ϑ is the solar zenith angle, or A≈1/sin(α) (for scattering above the trace gas layer) can be used, where α is the telescope elevation angle. Air mass factors for this study were calculated using the Monte Carlo RTM AMFTRAN [*Marquard* 1998] which includes single and multiple Rayleigh and Mie scattering, refraction and full spherical geometry. It relies on input data like pressure, temperature and ozone profiles of the atmosphere as well as a priori profiles of the respective absorbers. The numerical limit of the RTM did not allow the calculation of airmass factors for elevation angles smaller than 8°[5]. The situation for an absorber (here BrO is considered as an example) which has a stratospheric as well as a tropospheric component is illustrated in Figure 3.13. For the absorber (BrO) being present only in the stratosphere (Panel A), the AMF depends strongly on the solar zenith angle ϑ. The highest AMFs are calculated for large solar zenith angles. The dependence on the telescope elevation angle is relatively weak as can be seen from the small differences between the symbols. Only for high ϑ a remarkable difference exists. For BrO being present only in the boundary layer up to 1 km at a mixing ratio of 20 ppt the situation changes completely (Panel B). The dependence of the AMF on ϑ is very weak. However, the AMF depends strongly on the telescope elevation angle α. The AMF increases with approximately a 1/sin(α) dependence as expected from the geometric approximation. The dependence on the solar azimuth angle is also very small in this case. Therefore it is obvious that for an absorber in the boundary layer the observed slant column densities and the corresponding AMFs vary accordingly with α. Because the differences in the AMF for the used observation geometries are quite large, the method is

[5]this limit for low viewing angles can in principle be overcome using a very narrow vertical grid, however, since the number of atmospheric layers is restricted this approach is limited, too.

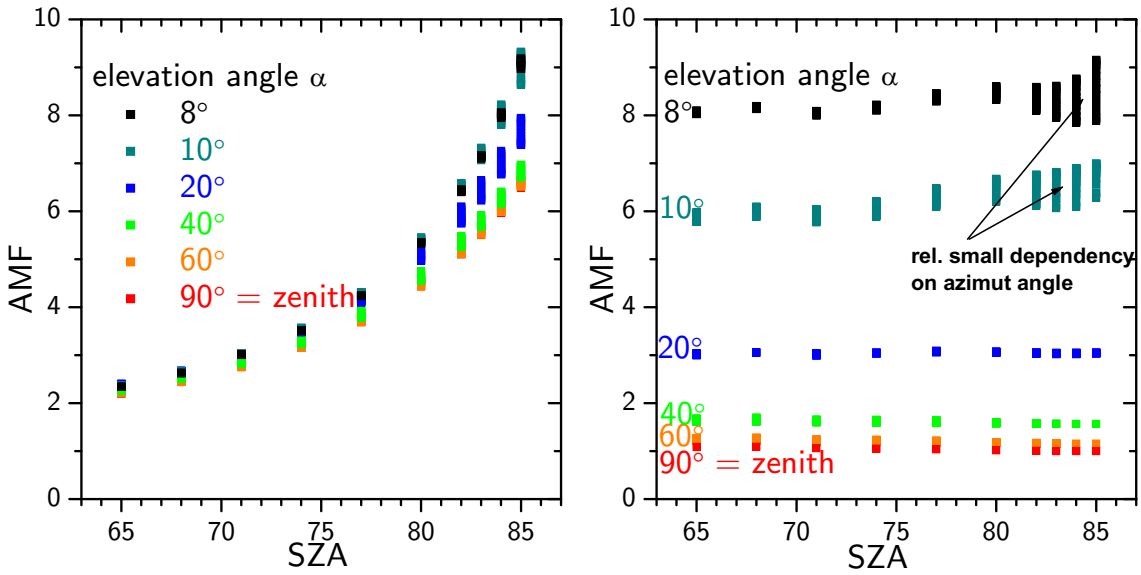

Figure 3.13: *Max-DOAS airmass factors for a stratospheric absorber (left) and for an absorber in the boundary layer (right). SZA: solar zenith angle ϑ.*

very sensitive for absorbers near the surface. If the successive measurements at the different elevation angles α are taken within a short period of time (typically 5-15 minutes) there is essentially no change in ϑ (particularly not in polar regions) and thus in the stratospheric part of the AMF during a series of measurements. Thus the stratospheric BrO column can be regarded as an essentially constant offset to the observed $S(\alpha, \vartheta) \approx S_{trop}(\alpha) + S_{strat}$.

AMF dependence on the relative azimuth angle

In contrast to zenith sky measurements, all off axis geometries are characterized by two degrees of freedom. Besides the telescope elevation angle, the relative azimuth angle (i.e. the angle between the sun and the line of sight of the telescope) has to be known. The *relative azimuth angle* φ is here defined as

$$\varphi \equiv 0 \quad \text{for looking in the direction of the sun.}$$

For different φ the radiative transfer may vary significantly, therefore radiative transfer calculations have been performed to quantify the differences. The dependence of the AMF for an absorber (here BrO is taken as an example) in the stratosphere and the comparison with an absorber confined to the boundary layer has already been shown in Figure 3.13. Both, for the stratospheric as well as for the boundary layer case the dependence on the solar azimuth angle, which is represented in Figure 3.13 as vertically extended dots, is very small. Only for high solar zenith angles a dependence becomes significant. Figure 3.14 shows the airmass factors for the boundary layer case as a function of ϑ and φ for

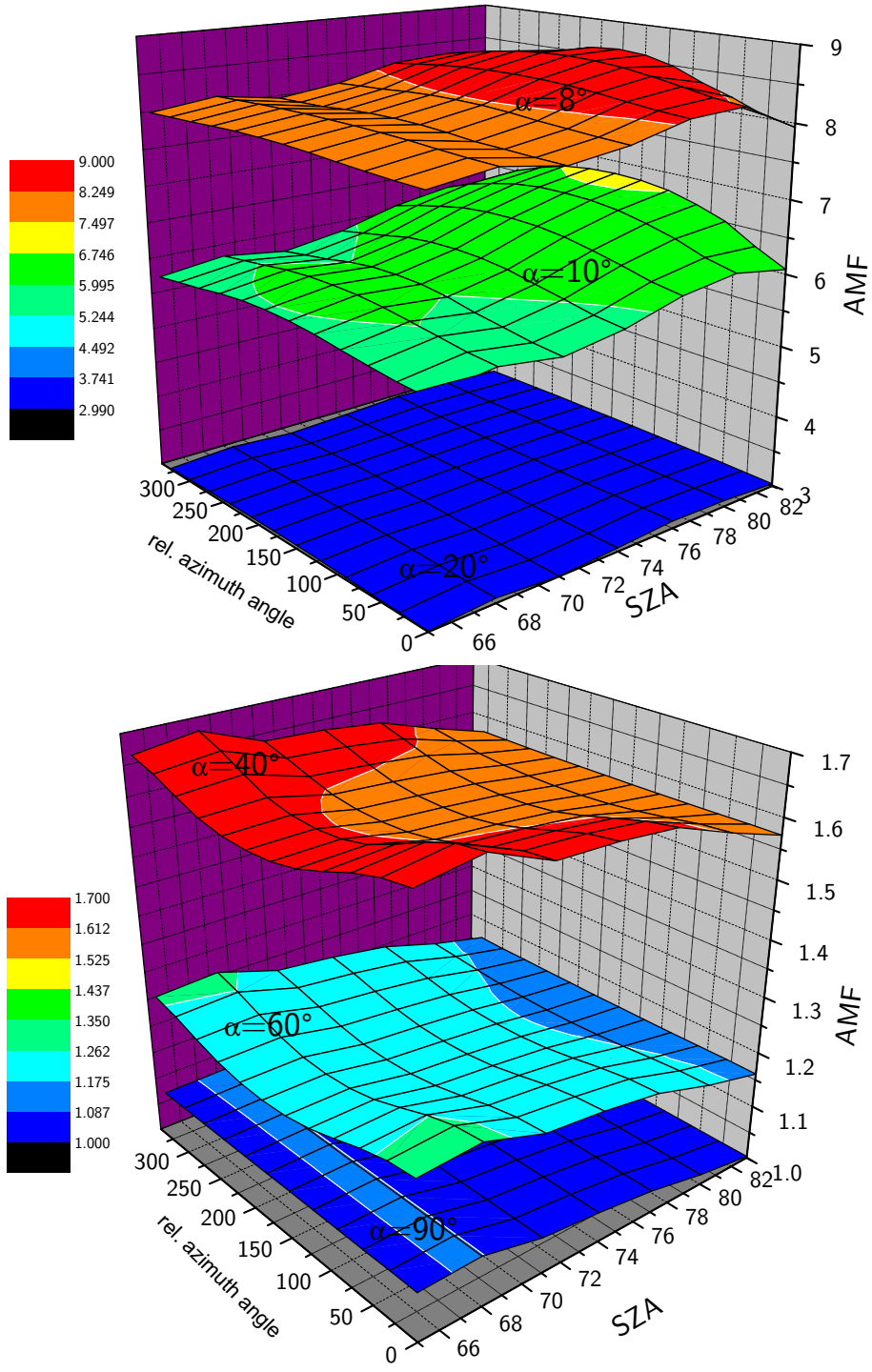

Figure 3.14: *Max-DOAS airmass factors for an absorber in the boundary layer as a function of solar zenith angle and relative azimuth angle between the sun and the viewing direction. Each plane represents airmass factors for the indicated elevation angle. Top: 8°, 10° and 20° elevation angle. Bottom: 40°, 60° and 90° elevation angle. Note the different scales on the AMF axis.*

the elevation angles used in this work. The range of ϑ is restricted to 65°-82°, which is representative for the conditions during ALERT2000 (see section 5.2). For the elevation angles smaller than the sun's elevation (8° and 10°) the airmass factor shows maximum variations of ∼10% with φ, with generally lower AMF for φ near zero. In this case the high fraction of forward scattered light from aerosols near the ground can lead to the shorter absorption path (smaller AMF). For the high elevation angles (40° and 60°) the pattern reverses, but the dependence on φ is very weak.
In summary it can be assumed that the variation of the relative azimuth angle over its complete range (0° to 360°) has only a minor effect (maximum 10%) on the airmass factor of an absorber in the boundary layer.

Dependence on the trace gas profile

It has already been shown above (see Figure 3.13), that the MAX-DOAS airmass factors strongly depend on the trace gas profile. A purely stratospheric absorber and an absorber well-mixed in the lowest 1 km are only extreme cases of the various trace gas profiles found in the atmosphere. Here the sensitivity of the MAX-DOAS airmass factor is studied for various box profiles of an absorber in the lower troposphere. In order to understand the results of the airmass factor calculations, the concept of the scattering height (see Figure 3.8) has to be kept in mind. The scattering process most likely occurs at an altitude given by the elevation angle α and the mean free path l of photons at the respective wavelength. The scattering height in the wavelength region used in this work ($\lambda \approx$355 nm) is as low as 1.29 km for the lowest elevation angle (α=5°, l =14.8 km[6]). Therefore, only for absorbers in the boundary layer the $1/\sin(\alpha)$ dependence of the airmass factor can be expected. Figure 3.15 shows the airmass factor dependence on the elevation angle for different vertical extents of the boundary layer (500 m, 1 km and 2 km) and for three elevated layers (1 km vertical extent, starting at 1 km, 2 km and 3 km). The airmass factors for the boundary layer cases show a strong dependence on the elevation angle, the AMF for the elevated layers is nearly independent of α. This can be explained by the concept of the scattering altitude. For the boundary layer cases the scattering process most likely occurs above the absorption layer (partly inside already for the 2 km case). This results in a strong AMF dependence on the elevation angle (see section 3.4.1 and Figure 3.8). For the elevated absorption layers the largest fraction of the photons is scattered in or even below the absorption layer, particularly for the low elevation angles. Therefore the AMF is only weakly dependent on α, and a behavior rather similar to that of a stratospheric absorber (strong SZA dependence) is expected. In Figure 3.15 (right panel) the bottom x-axis is scaled linearly in $1/\sin(\alpha)$. This shows that for the 8° elevation (indicated on the top x-axis) the geometric approach (AMF$\approx 1/\sin\alpha$) is a good approximation only for the

[6]The increase of l with height due to the pressure decrease was taken into account.

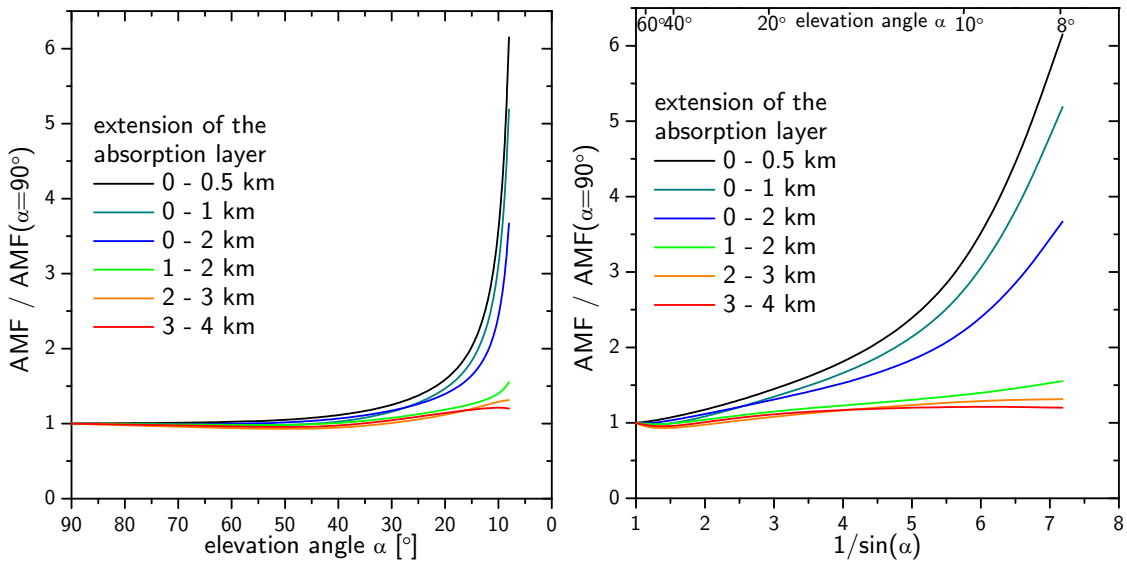

Figure 3.15: *Max-DOAS airmass factors calculated for different vertical profiles in the low troposphere as a function the elevation angle for a fixed SZA of 75°. Left: Dependence of the normalized AMF on the elevation angle for the absorption layers indicated in different colors. Right: Normalized AMF as a function of 1/sin(α). All airmass factors are normalized with respect to AMF(α=90°).*

500 m and 1 km boundary layer case. For the higher elevation angles and if the absorber is present at higher levels this approach strongly overestimates the AMF. For the boundary layer cases the formula

$$AMF \approx \frac{1}{\alpha} \tag{3.43}$$

is a good approximation because the absorption path in the lowest kilometer is roughly halved when the elevation angle is doubled.
In summary the AMF is strongly dependent (Equation 3.43) on the elevation angle only for trace gas profiles where the bulk of the absorber is present below 1 km in the boundary layer. For trace gas profiles with maxima at higher altitudes, the airmass factor becomes independent of the elevation angle, similar to a stratospheric absorber.

Influence of multiple scattering

All airmass factor calculations shown above were based upon single Rayleigh and Mie scattering only. Especially for low elevation angles a significant contribution of multiple scattering may alter the airmass factors calculated when only single scattering is considered. Figure 3.16 shows both, airmass factors calculated for single scattering only (left panel) and taking multiple scattering into account (right panel), for a ground albedo of 0.9. For the scenario considered here, including multiple scattering into the radiative transfer

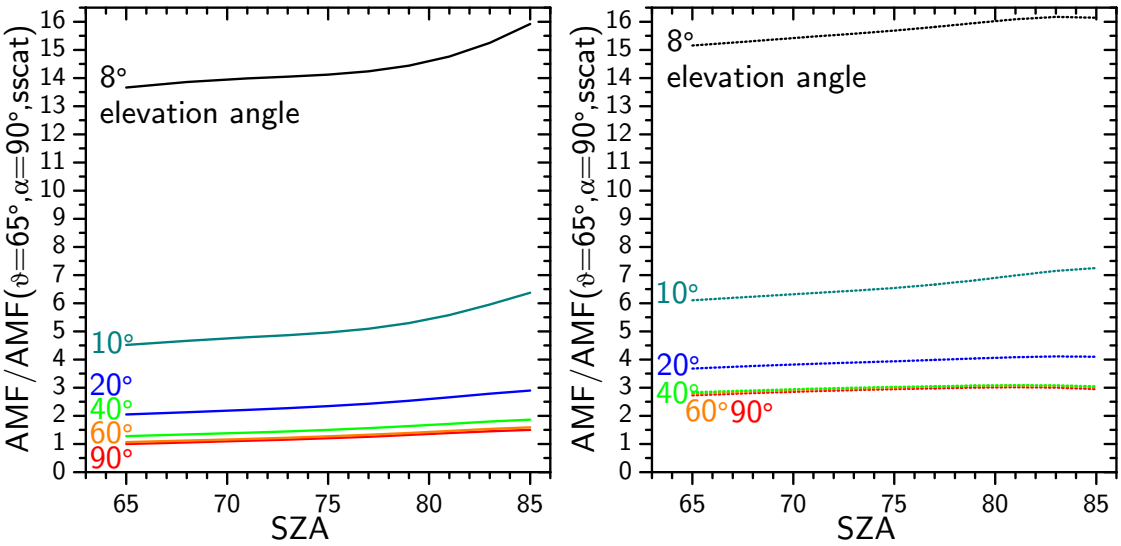

Figure 3.16: *Max-DOAS airmass factors calculated for an absorber in the boundary layer (0-500 m) as a function of SZA for single scattering only (left) and including multiple scattering (right). The relative azimuth angle was fixed to 180°. All AMFs are normalized with respect to the AMF for $\vartheta = 65°$, $\alpha = 90°$, calculated for single scattering.*

model yields generally higher airmass factors compared to the single scattering approximation. However, relative changes are much higher for the high elevation angles (40°, 60° and 90°) than for the low elevation angles. An important finding for the application to ground-based MAX-DOAS is the fact, that the ratios

$$\frac{AMF(\alpha = 5°) - AMF(\alpha = 90°)}{AMF(\alpha = 10°) - AMF(\alpha = 90°)}$$

remain almost unchanged for both, multiple and single scattering airmass factors. Therefore, if all differential slant column densities (dSCD) for the different elevation angles are differential with respect to a zenith (α=90°) Fraunhofer reference, the results of the MAX-DOAS evaluation - based on the change of the dSCD with elevation angle - will not change significantly.

Influence of the ground albedo

The high albedo of snow covered surfaces (up to 0.9 for fresh snow, see section 6.21), in particular in the polar regions, but also in mid-latitudes during winter, has a strong influence on the radiative transfer. The influence on MAX-DOAS measurements of an absorber in the boundary layer is shown in Figure 3.17. The influence of a change in albedo from 0.5 to 0.9 only leads to a constant offset to the calculated airmass factors of ~0.2. For the high airmass factors derived for MAX-DOAS measurements of an absorber in the boundary layer this small change does not significantly affect the large changes of

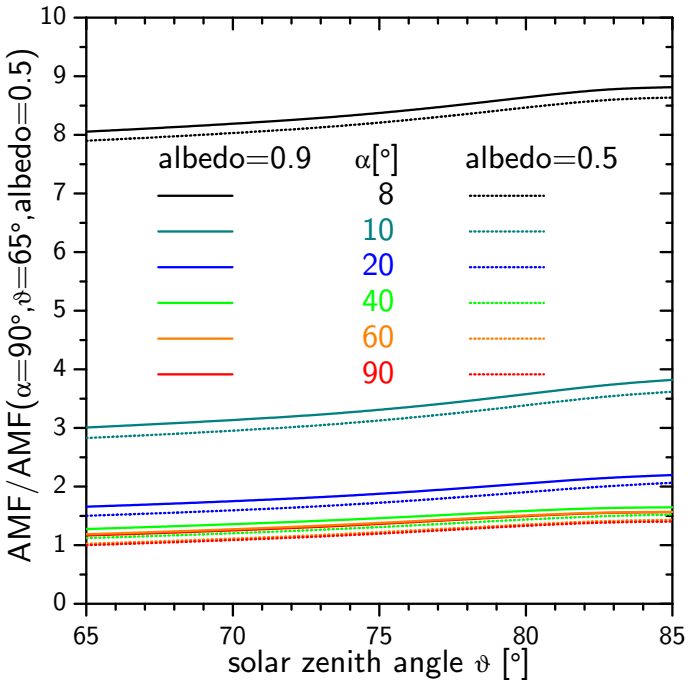

Figure 3.17: *Max-DOAS airmass factors for an absorber in the boundary layer (0-500 m), calculated for a ground albedo of 0.9 (solid lines) and for a ground albedo of 0.5 (dashed lines) for different elevation angles. All AMFs are normalized with respect to the AMF for* $\vartheta = 65°$, $\alpha = 90°$, *calculated for an albedo of 0.5.*

the dSCD for different low elevation angles shown above.

3.5.4 Airborne MAX-DOAS (AMAX-DOAS)

For the validation of the SCIAMACHY satellite instrument on ENVISAT (to be launched in 2002) an airborne MAX-DOAS instrument, the so called AMAX-DOAS will be applied. *Wagner et al.* [2001] summarized the capability and main purposes of the instrument. The principle is illustrated in Figure 3.18. The AMAX-DOAS is a MAX-DOAS system specially adapted and optimized for airborne measurements. In particular the multi-axis viewing geometry comprises measurements in several directions above and below the aircraft (see Figure 3.18). To derive information on the vertical profiles of the measured species trace gas absorptions will be compared from the different directions below and above the aircraft. The comprehensive set of (typically 10) different atmospheric absorption paths allows the vertical column densities above and below the aircraft to be separated, e.g. for a flight altitude around the tropopause the different absorption signals allow the separation of the stratospheric and tropospheric columns. Further vertical profile information can be derived by comparing the slant column densities observed from the low elevation angles combined with the knowledge of the flight altitude. These vertically resolved trace gas measurements

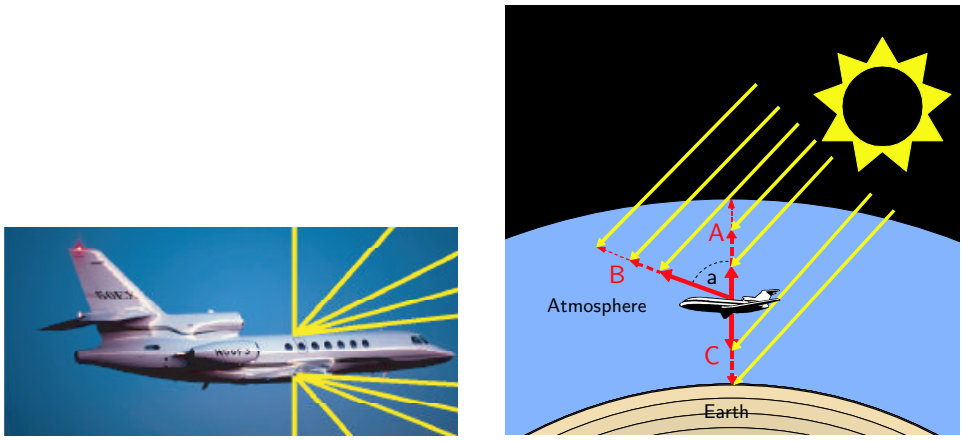

Figure 3.18: *Left: viewing geometries of the AMAX-DOAS instruments on board the DLR Falcon aircraft. In addition to zenith and nadir view several telescopes observe light from smaller elevation angles. Right: The different viewing geometries are sensitive to different atmospheric regions. The zenith mode (***A***) is only sensitive to the layers above the aircraft; the signal from nadir view (***C***) contains contributions from both the atmosphere above and below the aircraft. The additional telescopes observing low elevation angles (***B***) are very sensitive to the atmospheric layers close to flight altitude. Adapted from Wagner et al. [2001]*

contribute to the validation of the SCIAMACHY instrument because SCIAMACHY will also yield vertical profile information on trace gases derived from limb observations.
A short observation time is very critical in this application due to the fast motion of the aircraft leading to a rapid change of several parameters (altitude, ground albedo, clouds, etc.). Therefore simultaneous MAX-DOAS (using CCD detectors, see below) is much more preferable for airborne MAX-DOAS.

3.5.5 Multi-Axis-DOAS Instruments

MAX-DOAS using Imaging Spectroscopy for Simultaneous Observations

The recent development of large CCD detectors (chip sizes up to 30 mm×15 mm) and high quality imaging spectrographs with a flat field of comparable size now allows the simultaneous recording of several spectra from different viewing geometries (multi axis approach). *Hönninger et al.* [2000] presented this new technique for various studies of trace gases in the troposphere. Figure 3.19 shows the basic principle of the spectra acquisition. A set of telescopes[7] receiving light from different directions (e.g. elevation angles) is coupled to the imaging spectrometer using a quartz fiber bundle which transmits the light from

[7]telescopes here could be e.g. telescopes for receiving scattered sunlight, direct sunlight or moonlight or LP-DOAS telescopes aiming at different retro reflectors. However, for simplification purposes only the application for scattered sunlight is described.

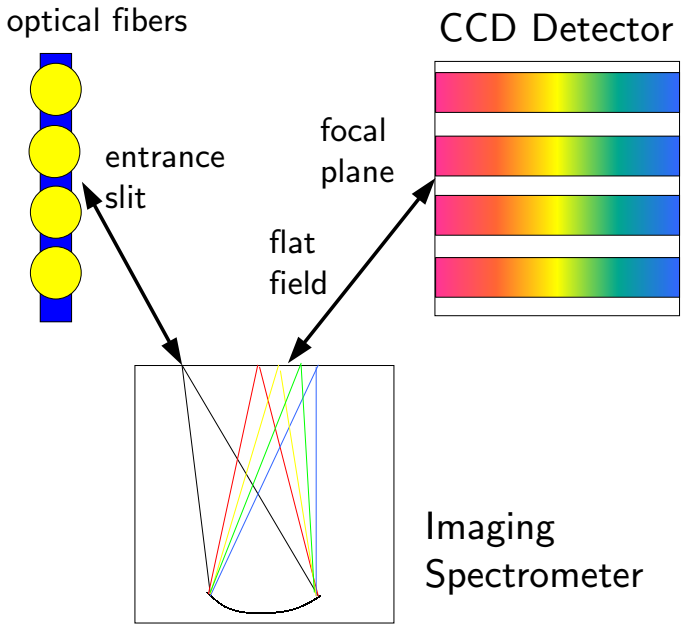

Figure 3.19: *Principle of spectra acquisition using a MAX-DOAS spectrometer: Light is received from 4 (in practice up to 10) different viewing directions. The light is transmitted into the entrance slit using quartz fibers. An imaging spectrometer disperses the light and focusses the spectra onto the CCD detector without vertical overlap. See also [von Friedeburg 1999]*

each telescope to a certain vertical position of the spectrometer's entrance slit. The light is then dispersed by the diffraction grating and focussed onto the detector. As shown in Figure 3.19 the imaging spectrograph produces a set of vertically separated spectra, each corresponding to the respective quartz fiber at the entrance slit (and the respective telescope coupled to it). Care has to be taken in order to exclude vertical overlap of the spectra on the detector. Tests in our laboratory have shown that at least 10 individual spectra can be properly separated using a commercial imaging spectrograph (e.g. Acton SpectraPro® 300i). A problem that has to be addressed is the change of the instrumental line shape for the individual spectra including a possible change in resolution (instrument function) and wavelength to pixel mapping. While it is always possible to compare the individually measured slant columns from the various geometries, for special applications it is desirable to directly compare e.g. spectra taken from zenith direction with simultaneously measured spectra from a low elevation angle. When spectra taken with different instrument function are to be compared directly they have to be cross convoluted[8] and interpolated onto a common wavelength scale first. Since this is a possible source of error, especially in the presence of undersampling, it is desirable to optimize the imaging quality

[8]cross convolution of spectra I_1 and I_2 means convoluting I_1 with the instrument function H_2 of the second spectrum and vice versa.

of the spectrograph. Another approach to account for the changing instrument functions by fitting difference spectra between the CCD regions was applied by *von Friedeburg*.

Sequential Scanning MAX-DOAS

Another possibility to apply MAX-DOAS is to scan several different observation geometries sequentially taking a series of corresponding spectra with a conventional DOAS spectrograph and 1D detector. This second approach has several advantages:

- for a stabilized spectrograph the instrument function and wavelength to pixel mapping remains constant over time, so a direct comparison of spectra from different geometries is possible (see e.g. evaluation of IO spectra at Alert, section 5.2.4).
- if the same detector area (and efficiency) is regarded, the integration time per observing geometry (e.g. elevation angle) is significantly shorter ($\approx \frac{1}{n}$, where n is the number of different geometries.)
- the integration time can be optimized for each spectrum individually which is restricted when a CCD is used.
- usually only one telescope and quartz fiber is required since it can receive light from different viewing geometries when mounted to a tracking system.

However, there are obviously also drawbacks:

- the measurements are not simultaneous anymore, so unless the series of spectra is taken within a short time interval compared to the timescale on which trace gas concentrations or radiative transfer conditions (e.g. cloud conditions) change, the different geometries cannot be compared directly.
- the active tracking system requires additional mechanical parts and electronics that reduce the reliability and may need extra power and regular service.

For each application different arguments may be relevant since the individual requirements differ from measurement to measurement. For the measurements performed during this study the second approach was applied since an existing scattered sunlight DOAS system could be easily adapted. The requirement of mechanical and electronic parts (stepper motor) was no major concern because the instrument was only operated during 3 to 4 week intensive field studies and could be checked several times a day. The time difference for a set of spectra taken from different geometries was also short enough to trace sudden changes of the trace gas concentrations due to chemical changes or changing air masses (see also section 6.3).

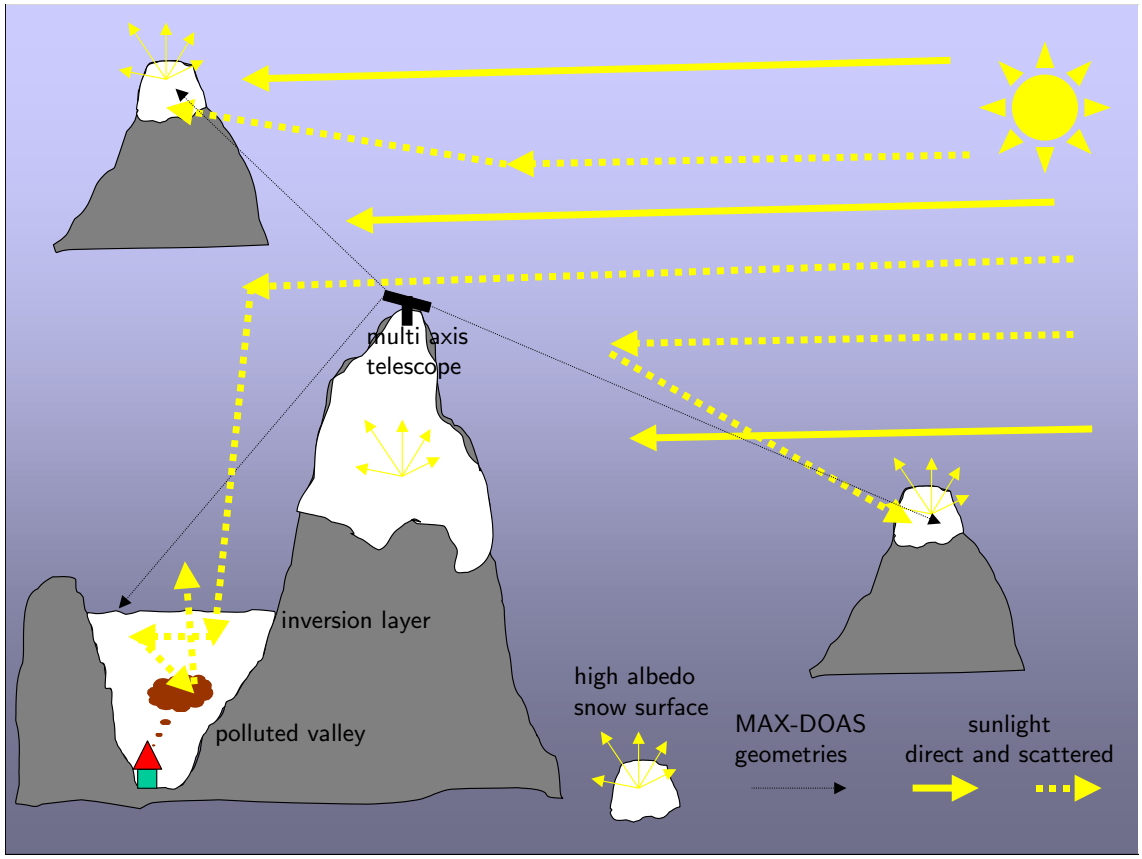

Figure 3.20: *Sketch of a MAX-DOAS setup in an alpine environment. Free tropospheric studies are possible using absorption paths defined by mountain tops. Pollution measurements use light scattered back from the top of an inversion layer, which frequently isolates valleys from the rest of the atmosphere.*

3.5.6 Other Possible MAX-DOAS Applications

Alpine MAX-DOAS

One possible application of the MAX-DOAS approach is to make use of the high albedo of e.g. snow surfaces (also water glint or salt, see below) to study

- vertical profiles of trace gases on a local scale
- free tropospheric background conditions and pollution episodes in the alpine environment
- winter smog episodes in valleys which are isolated from the free troposphere due to temperature inversions

The setup of the respective MAX-DOAS geometries are sketched in Figure 3.20. Due to the relatively long mean free path of photons at higher altitudes (>21 km for 360 nm at

3000 m altitude) the assumption of a straight well-defined lightpath between the observed high albedo snow surface and the MAX-DOAS instrument is valid for most cases. The background signal from the higher layers and the stratosphere can be eliminated by simultaneously observing a snow surface in a very short distance or correction with zenith sky absorption measurements. Vertical profiles can be measured by pointing the light receiving telescopes at snow surfaces in different altitudes.
Winter smog episodes can be monitored from mountains above the polluted valley by observing light scattered back from the usually cloudy top of the inversion layer which isolates the valley. Multiple scattering in the valley leads to large absorption paths and signals in the observed backscattered light. Besides simple qualitative results, this method can also be used to calculate approximate concentrations by correction with simultaneously measured O_4 absorption, which gives an indication of the total lightpath.

Salt Lake MAX-DOAS

The property of many salt lakes to be covered with a perfectly white salt surface allows to use the high albedo of the salt lake for MAX-DOAS measurements. Observing the diffuse light reflected by the salt surface at different positions and angles from an elevated location (e.g. nearby hill) allows to characterize local inhomogeneities as well as vertical profiles. This information can improve the knowledge of reactive halogen release processes, known to occur on salt surfaces [*Hebestreit et al.* 1999; *Platt* 2000]. By MAX-DOAS observations possible local inhomogeneities including vertical profiles can be studied. A possible MAX-DOAS experiment to study halogen release processes associated with the surface of a salt lake is shown in Figure 3.21. In the sketched case background absorption can be easily determined and corrected for to yield slant columns densities in the layer between the MAX-DOAS altitude and the salt lake surface. The spherically averaged absorption signal for the atmosphere above the MAX-DOAS site can be determined by analyzing scattered and direct sunlight collected by a 2π integrating sphere (e.g. known from measurements of downwelling actinic fluxes by filter and spectroradiometers). The light collected by this sphere is representative for the light which is then diffusely reflected by the high albedo salt surface. Measuring only the direct sunlight is not appropriate since in the blue and UV spectral ranges a significant fraction of the downwelling solar radiation is scattered sunlight, even under clear sky conditions ($\sim$80% at 300 nm, $\sim$40% at 420 nm [*Lefer et al.* 2001]). Thus one MAX-DOAS geometry should measure this signal, which can then be used to correct slant column densities derived from the various geometries observing different locations of the bright salt surface below the instrument. Depending on the scale of inhomogeneities spatially resolved trace gas concentrations can be derived by applying analytical or numerical inversion techniques.

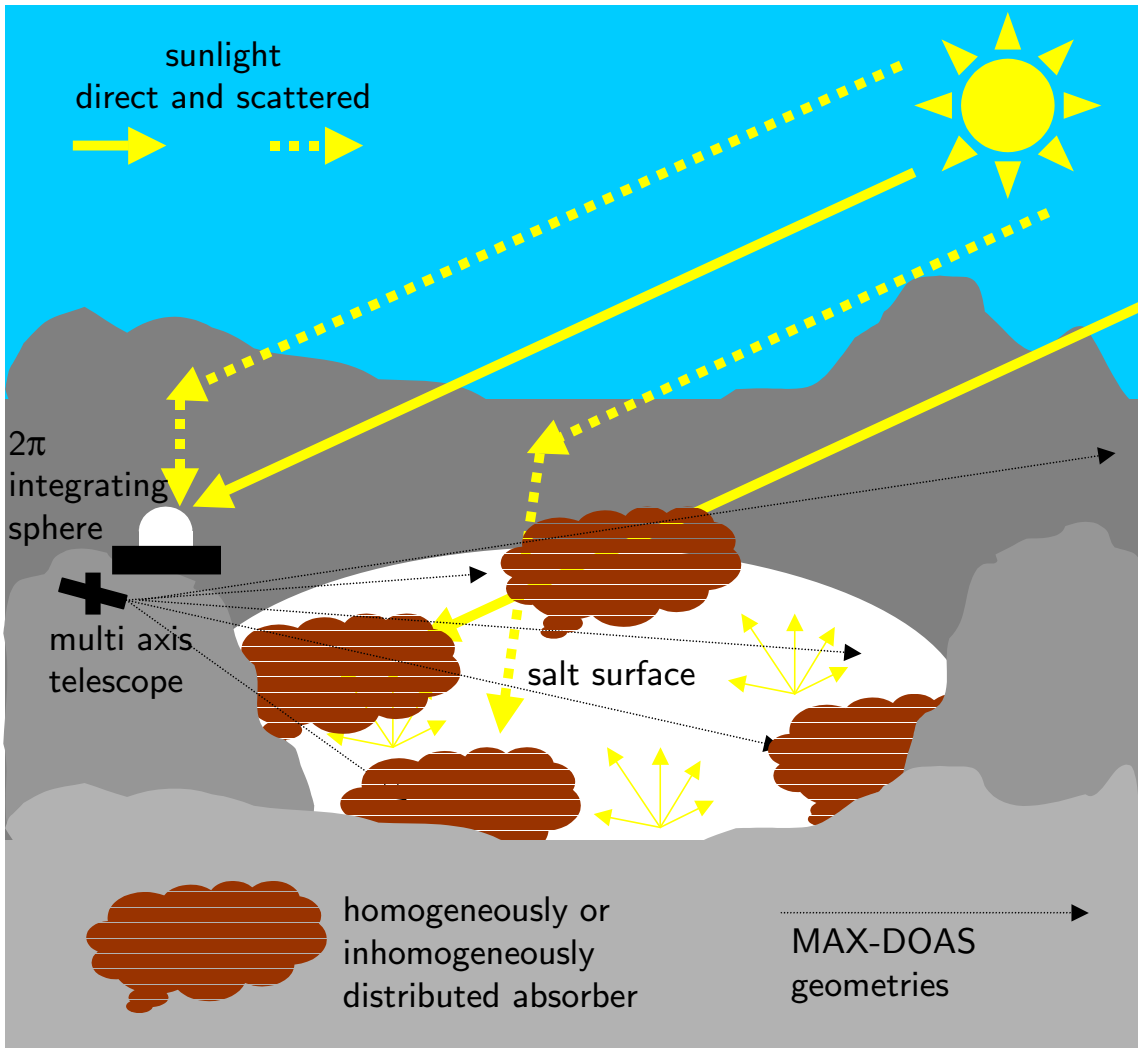

Figure 3.21: *MAX-DOAS setup for measurements of halogen emissions from a salt lake surface.*

Urban Air Pollution Monitoring by MAX-DOAS

Routine monitoring of trace gases involved in urban air pollution is also a possible application for the MAX-DOAS technique. While the method does not yield localized concentration data like point measurements from in situ monitors, it is very sensitive to major pollutants (e.g. NO_2, SO_2, etc.) and average concentrations in the boundary layer can be derived. MAX-DOAS measurements of NO_2 near a Highway have been reported by *Xie et al.* [2001]. To characterize pollution levels in cities and urban areas, average concentrations often prove to be much more useful than highly variable in situ measurements which have to be averaged over time to allow statements on the effects of pollution on human beings and the environment. Sensitivity studies in section 3.5.2 and actual mea-

surements performed in this work (see section 6.3) show, that MAX-DOAS measurements alone provide enough information to derive the approximate height of the mixing layer and calculate average mixing ratios. Especially in highly polluted environments where variable visibility is a major problem for other optical monitoring techniques (e.g. long path DOAS) MAX-DOAS measurements are better suited because the method also works at low visibility and yields qualitatively correct values (see also section 6.5.4). When airmass factor concepts and in particular simultaneous measurements of photon path distributions by O_4 and O_2 absorption measurements are further improved (e.g. [*Funk* 2000]), also quantitative measurements during cloudy and low visibility periods will be possible. Besides scattered sunlight, in urban areas also the high albedo of certain points or even guided mirrors to observe reflected sunlight are possible MAX-DOAS observation geometries. However, this requires instruments with moving parts which makes the measurements more complicated.

'Modern COSPEC' MAX-DOAS

The COSPEC instrument (Barringer Research Inc., Canada), developed in the late 1960s [*Millán et al.* 1969; *Davies* 1970] has been applied over more than three decades for measurements of total emissions of SO_2 and NO_2 from various sources, e.g. industrial emissions [*Hoff and Millán* 1981] and volcanic plumes [*Stoiber and Jepsen* 1973; *Hoff* 1992]. This very successful, but outdated measurement technique could in the near future be replaced by MAX-DOAS instruments for studying the emissions of volcanoes, power plants, industrial regions, etc. The instrumental setup of MAX-DOAS for the study of volcanic or other emission plumes is sketched in Figure 3.22. The MAX-DOAS systems (A and B in Figure 3.22) can be applied in static mode by sequentially scanning spectra from different geometries or simultaneous measurements using an imaging spectrometer with 2D-CCD detector coupled to several telescopes. The combination of different elevation angles and two instruments at different locations allows to derive the plume density and height by triangulation. Another approach is mobile monitoring of the trace gas columns (especially that of SO_2) inside a volcanic plume along different transects by taking a series of measurements from different locations. The height of the plume as well as the 2D distribution of the trace gas columns in the plume can be obtained by operating the instrument on a mobile platform (e.g. positions 1, 2 and 3 in Figure 3.22 of a car, ship or airplane). The advantage of MAX-DOAS over the traditional techniques is the much higher time resolution and the reduced effect of fluctuations inside the plume on the measurement results. Recent instrument developments allow the use of rugged, lightweight MAX-DOAS instruments with relatively low power consumption (see also section 4.3.1).

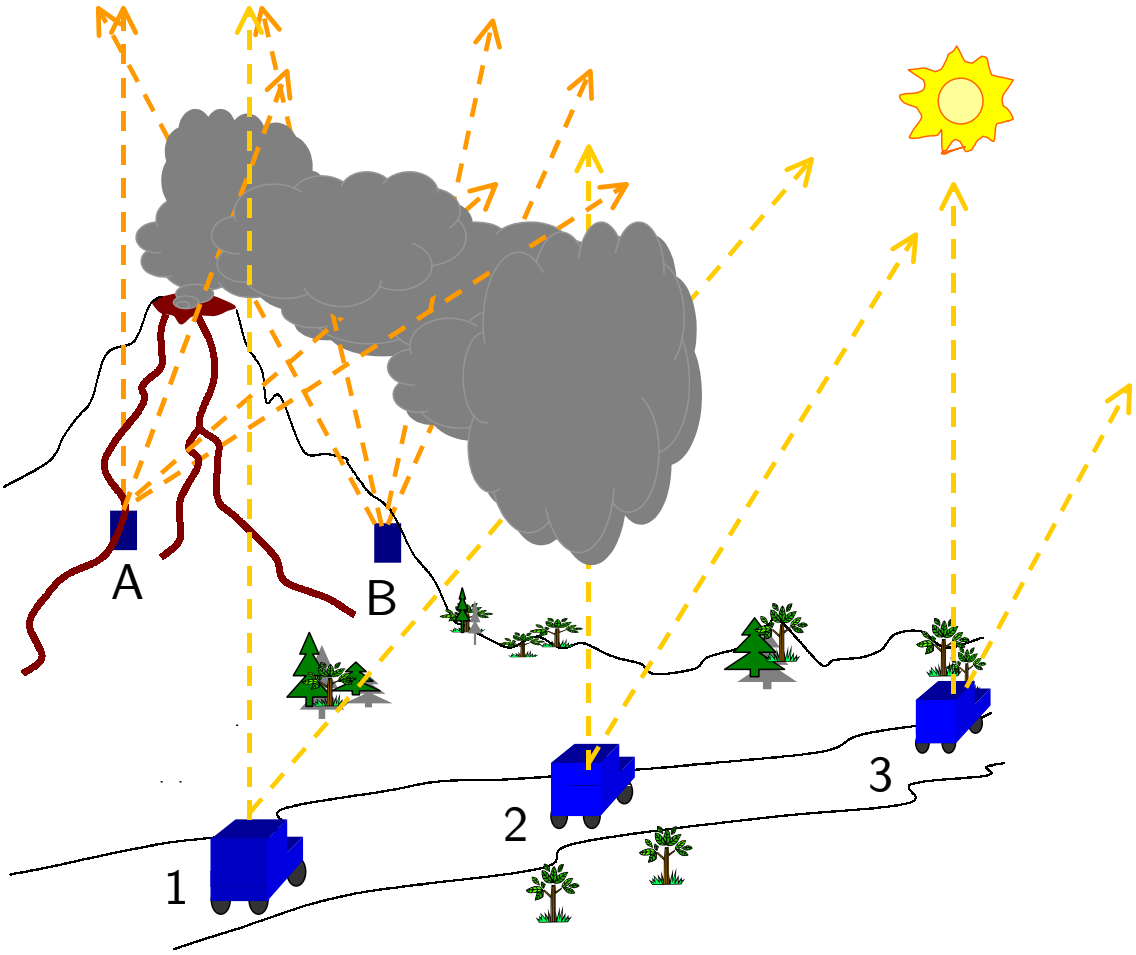

Figure 3.22: *'COSPEC' type MAX-DOAS application for monitoring of volcanic or industrial plumes. Combination of different geometries yields plume height and density and allows to calculate emission fluxes and distributions.*

Chapter 4

Instrumental Setups

The measurements presented in this thesis were performed using both commercial and custom built instruments. Commercial systems were also adapted to the special needs required for atmospheric measurements in the course of this work.
In this chapter the applied DOAS systems (MAX-DOAS, LP-DOAS, Mini-MAX and Portable LP-DOAS) will be explained and their characteristics will be presented and compared.

4.1 The MAX-DOAS Instrument

The instrumental setup discussed in this section was first assembled and tested for the measurements on the Zugspitze mountain from October 1999 until mid-March 2000 (see section 5.1.1). During this long-term experiment the system was thoroughly characterized and improved over the period of 6 months. The system was then used for the measurement campaigns in Alert, Canada (see section 5.2), onboard the German research vessel FS Polarstern during a transect from Bremerhaven, Germany to Cape Town, South Africa in October 2000 by *Leser* [2001] and with a slight modification during the Hudson Bay campaign in April/May 2001 (see section 5.4).
Figure 4.1 shows how the different components are arranged in the MAX-DOAS setup. Only the key components are characterized here.

4.1.1 Entrance Optics

The entrance optics were adapted from the system used by *Kreher* [1991] and *Senne* [1996]. It consisted of a quartz lens (focal length f = 100 mm, diameter d = 30 mm) and a round bundle of 25 individual quartz fibers (core diameter 100 μm, diameter of the circular arrangement $d_{entrance} = 0.8$ mm). This quartz fiber bundle (length l = 8 m) transmits the light from the focal point of the quartz lens to the entrance slit of the spectrometer for spectral analysis. At the entrance slit the fiber exits form a column of 2.5 mm height.

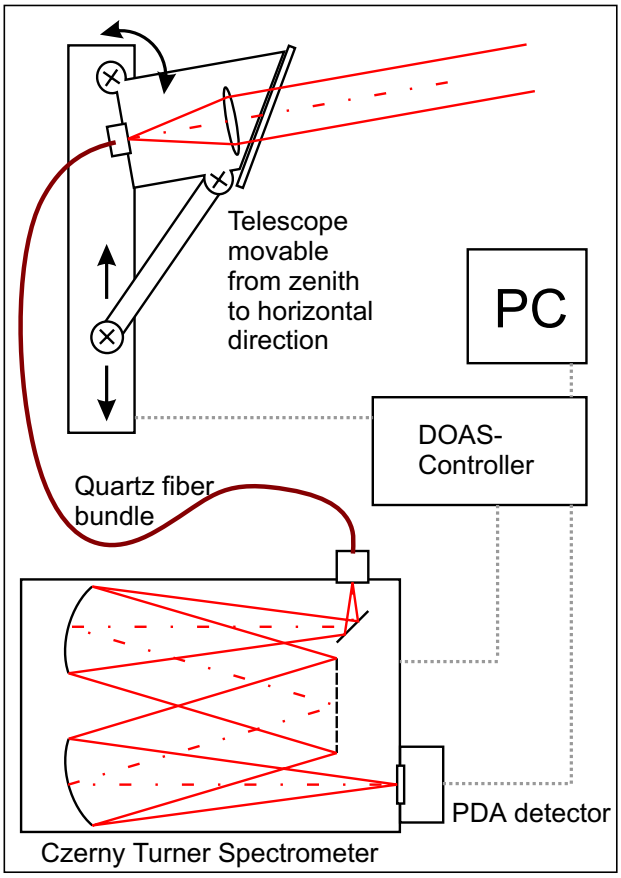

Figure 4.1: *Simplified sketch of the MAX-DOAS setup*

The aperture of the telescope can be calculated from f and $d_{entrance}$ to be less than 1°. The telescope arrangement was assembled in a dry atmosphere and sealed to prevent contamination and condensation of water on the interior optics. The stainless steel telescope housing was sealed with a UV-transmitting quartz window mounted at 45° angle which also prevented snow from accumulating in front of the telescope.
The telescope housing was equipped with a joint system to transform the movement of a linear stepper motor drive into a change in elevation angle of the telescope. By mounting the stepper motor arrangement perpendicular to the surface telescope elevation angles of 20° to 90° (Zugspitze) and 5° to 90° (Alert, Polarstern, Hudson Bay) could be realized.

4.1.2 Spectrograph and Detector Unit

For the measurement of the atmospheric absorption spectra a Czerny-Turner spectrograph was used. This device is based on a setup originally developed by *Czerny and Turner* [1930]. The quartz fiber which transmits the light from the telescope to the spectrograph is mounted in the focal point (entrance slit) of the first convex mir-

ror (collimating mirror). The parallel light from this mirror is then dispersed by a plane diffraction grating. A second convex spherical mirror unit (focussing mirror) then focusses the dispersed light onto the detector. The wavelength region observed by the detector can be changed automatically by a computer controlled stepper motor drive (tolerance 0.5 steps). In order to minimize thermal instability the whole spectrograph unit is insulated and temperature stabilized to a few K above maximum room temperature (usually 30 $\pm 0.2\,^{\circ}$C). The mainly used ACTON Spectra Pro 500 with a focal length of 500 mm was equipped with a plane diffraction grating (aperture ratio f/6.9, entrance slit (fiber exit) width 100 μm for the MAX-DOAS fiber bundle and 200 μm for LP-DOAS, grating 600 grooves/nm, dispersion: 3.08 nm/mm (or 0.077 nm/pixel), spectral resolution: 0.54 nm). Only for the MAX-DOAS measurements at the Hudson Bay a smaller spectrograph (ACTON Spectra Pro 275) with a focal length of 275 mm (collimating mirror) and 310 mm (focussing mirror), respectively, was used (aperture ratio f/3.8, grating 1200 grooves/mm, dispersion: 2.46 nm/mm (or 0.062 nm/pixel) For recording the spectra, a 1024 pixel photodiode array detector (PDA) was mounted in the focal plane of the spectrograph. A detailed discussion of the usage of photo diode arrays as DOAS detectors is given by [*Stutz* 1991; *Stutz and Platt* 1992].The principal component of the unit is a photo diode array from Hamamatsu (Type S3904-1024) with 1024 Si photo diodes (CMOS) of 25 μm width and a height of 2.5 mm. The PDA is placed in a housing that can be evacuated and filled with 1.2 bar Argon 5.0. Every photo diode consists of a n-p semiconductor junction. During operation an inverse voltage of 2.06 V is applied to the diode inducing a depletion layer which is almost as large as the whole diode area. Incoming light excites a number of electrons proportional to the light intensity into the conducting layer of the semiconductor. The capacity of a diode is 10 pF, the full well depth corresponds to 1.286×10^8 photo electrons. These photo electrons reduce the applied inverse voltage. However this is also possible by thermally excited electrons. This effect is called dark current and must be considered and corrected for in the evaluation procedure at low light intensities. In order to reduce dark current the PDA was cooled down to temperatures between -15 and -30 °C by a Peltier cascade. Thereby the dark current decreases exponentially regarding Boltzmann statistics. After the integration time the PDA is read out by re-charging the photodiodes. The charge needed is amplified electronically. To prevent negative signals (which cannot be converted by the used ADC) an offset signal is added to every PDA signal. The offset is proportional to the number of scans added and must be corrected for during the evaluation process. The signals are digitized by a 16 bit analog - digital converter (full saturation corresponds to $2^{16} = 65536$ counts) and then transferred to the computer. Due to the cooling of the detector unit water vapor could freeze on the PDA surface and possibly cause etalon structures due to interference effects. Therefore the detector is evacuated and filled with dry argon as inert gas. Another effect of PDAs is the so called memory effect. That means that structures of a former spectrum can be seen in the following spectra. This effect was

discussed e.g. in [*Stutz* 1996; *Leser* 2001], however its origin is unclear up to date. Usually the memory effect can be significantly reduced by multiple scans without light or just waiting for a short time.

4.2 The Active Long Path-DOAS System

The active long path-DOAS systems employed during the field studies on Crete (see section 5.3) and at the Hudson Bay (see section 5.4) during this work have already been described elsewhere [*Ackermann* 2000; *Geyer* 2000; *Alicke* 2000; *Hebestreit* 2001]. Therefore only an overview of the different components will be given here. Figure 4.2 shows the different components needed for the LP-DOAS setup. Only the telescope and the light source are described here. The spectrometer and detector system is identical to the one already characterized in section 4.1.2.

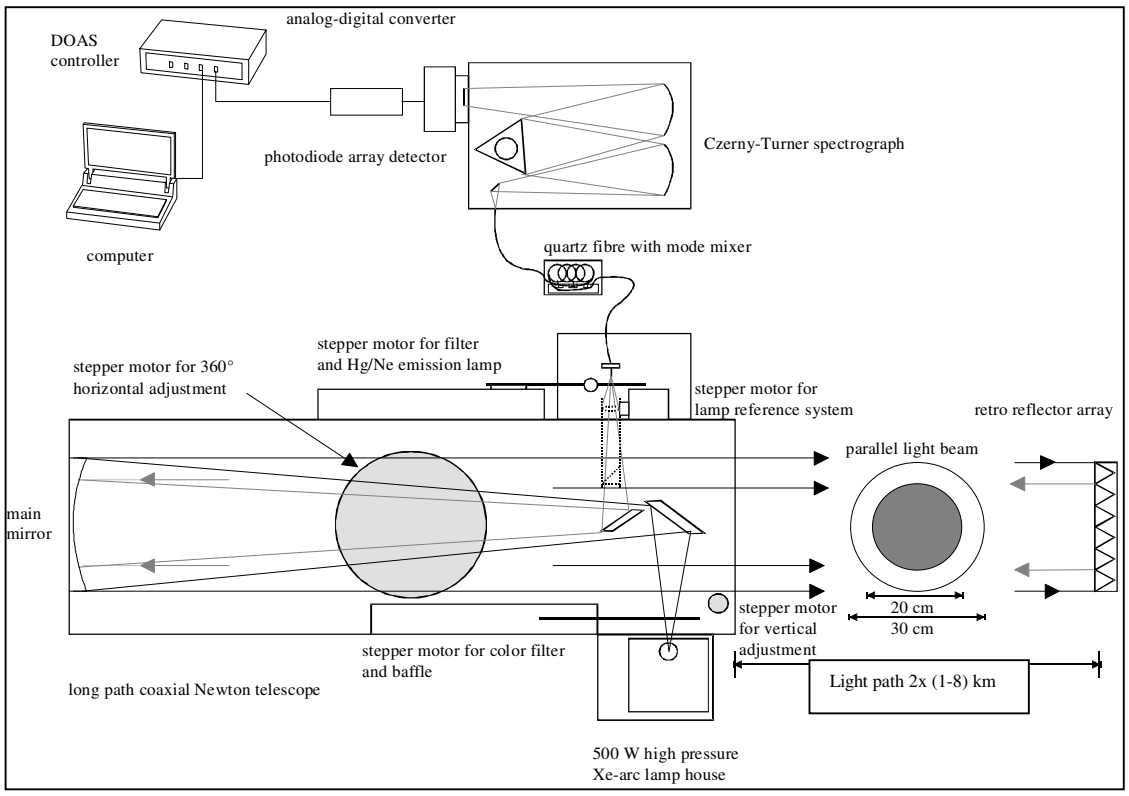

Figure 4.2: *The main components of the LP-DOAS system*

4.2.1 The LP-DOAS Telescope

The telescope of the long path system consists of two coaxial Newtonian telescopes with transmitting and receiving optics combined in one device. In the optical axis of the tele-

scope two elliptical plane mirrors are mounted to reflect the light of both outgoing and incoming beams by 90 degrees. The main component is a parabolic mirror of 30 cm diameter and a focal length of 150 cm. The light source is placed in the focal point of the main mirror. Thus the outgoing light beam is parallel. A retro reflector array in a distance of several kilometers is used to reflect the parallel light beam exactly back into the telescope, where it is focussed onto a quartz fiber. The quartz fiber transmits the light into the spectrograph. The optical image, however, is not perfect. Since the light source is not a point the light beam slightly diverges along its path through the atmosphere resulting in a loss of light depending on the distance to the retro reflectors. Because of the two plane mirrors in the optical axis of the telescope only a ring can be sent into the atmosphere leading to a light loss of 50 % compared to a fully illuminated mirror without the shade of the plane mirrors. Altogether five stepper motors control the telescope and its parts:

- Two motors are used to align the telescope on the retro reflector array (and possibly at others) in horizontal and vertical direction.
- One stepper motor carries a filter wheel equipped with various filters, e.g. UG5 from Schott, Germany (in order to remove light at wavelengths above 400 nm to reduce stray light in the spectrograph) and a baffle to record background spectra.
- At one motor a mercury emission lamp is mounted which can be positioned in front of the quartz fiber to determine spectral resolution and wavelength calibration at several times during the measurements.
- The fifth motor carries the lamp reference system, which can be moved into the outgoing light beam. The reference system consists of an elliptical plane mirror, which reflects a part of the light of the outgoing light beam onto a quartz lens from which it is focussed onto the quartz fiber.

4.2.2 The Light Source

The light sources of all LP-DOAS measurements in this work were Xenon high pressure short arc lamps. A light arc of less than 1 mm diameter between anode and cathode is produced from a high voltage ignition discharge producing a dense plasma in the Xenon gas bulb. The spectrum of a Xenon arc lamp is the superposition of the thermal emission according to the Planck function and single Xenon emission lines, which are pressure broadened due to the high operating pressure of Xenon arc lamps. The distance of the electrodes is generally small resulting in a short arc length (thus reducing the divergence of the light beam emitted from the telescope) and high local light intensity. The pressure inside the lamp is very high (up to 10^7Pa under operating conditions) yielding a high density plasma. The color temperature of the used Xenon lamps of $\sim$ 6000 K is similar

lamp	PLI HSA-X5002	Hamamatsu SQ 150W
power [W]	500	150
voltage [V]	18	18
current [A]	28	8.5
lifetime [h]	200	3000
size of brightest spot [mm×mm]	0.3×0.3	1.0×2.0

Table 4.1: *Comparison of the employed Xenon arc lamps*

to that of the sun with maximum spectral intensity around 500 nm. The bulb of a Xenon lamp consists of quartz glass, which is extremely resistant to the pressure and temperature. The electrode material is tungsten with endowments depending on the lamp type. The cathode has an edged peak to enhance the electron emission. In contrast to that the anode is made out of massive material to absorb the kinetic energy of the incoming electrons. In this Ph.D. thesis mainly one type of Xenon arc lamps (HSA-X5002 supplied by PLI Inc., NJ, lamp design adapted from Hanovia lamps) was used, only for the test of the portable LP-DOAS system a smaller lamp was used (Hamamatsu SQ 150 W). For a comparison see Table 4.1. The variability of the emission features of Xenon short arc lamps caused by flaring lamp plasma was studied by *Hermes* [1999]. Xenon emission lines were found at several wavelengths including the red spectral region. The emission strength and pressure broadening of the Xenon lines was found to change over time and therefore the lamp structures are difficult to remove from a spectrum. It was found that lamp structures are easier removed from a spectrum in the case of the PLI lamp as its Xenon emission bands are broader and therefore can be better reduced by high pass filter routines.

4.3 New Miniature DOAS Instruments

This section introduces new DOAS instrument developments that were part of this thesis. A major drawback of the current DOAS systems is their size and the relatively large effort in adapting and maintaining the individual parts to fit the needs of the respective experiments. Since the instruments assembled for particular experiments within this thesis can be considered as prototypes for future systems, a short description of the major parts will be given only.

4.3.1 The Mini-MAX-DOAS System

The logistical requirements for the measurement campaign in the Indian Ocean during December 2000 allowed only the use of a very small setup. This section describes the instrumental setup that was assembled and tested for these measurements aboard the French research vessel R/V Marion Dufresne during the cruise from Réunion Island via

the Crozet islands, Kerguelen island, St. Paul and Amsterdam island back to La Réunion (see section 5.1.2). During these 3 weeks the first set of measurements using the new USB2000 spectrometer by OceanOptics were performed.
Figure 4.3 shows how the different components are arranged in the Mini-MAX-DOAS setup. The components are very similar to the ones of the MAX-DOAS system described in the previous section 4.1. Therefore only the differences to that system will be discussed here.

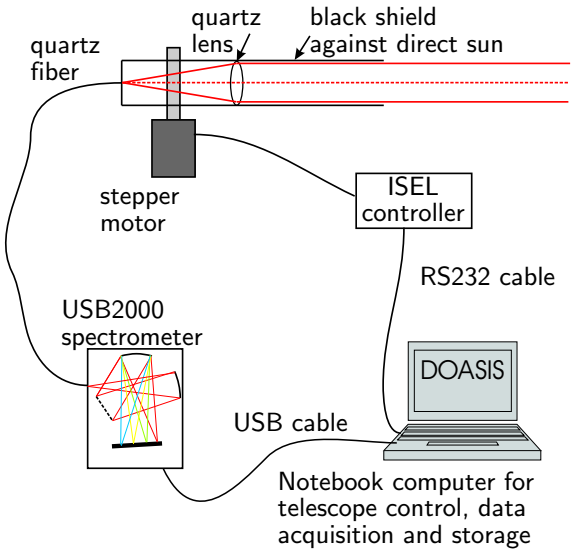

Figure 4.3: *Simplified sketch of the Mini-MAX-DOAS setup*

Mini-MAX Telescope

The light receiving optics were assembled from standard optical bench parts. The 200μm single quartz fiber was fixed in the focal point of a quartz lens (ø = 20 mm, f = 50 mm). The arrangement was wrapped with black cardboard and sealed against rain and weather using aluminum foil. To prevent direct sunlight from being scattered into the fiber by dust and sea spray particles on the quartz lens a removable black sun shield was attached to the telescope. The field of view of the telescope was $\approx 0.3°$. The elevation angle of the telescope could be adjusted using a computer controlled stepper motor drive.

The USB2000 Spectrograph

For the spectral analysis of the received skylight the USB2000 spectrometer by OceanOptics was used. The main components of the device are sketched in Figure 4.4. The spectrograph type is a crossed Czerny-Turner, which reduces the required optical bench size. The quartz fiber transmits the light received by the telescope to the entrance slit (width

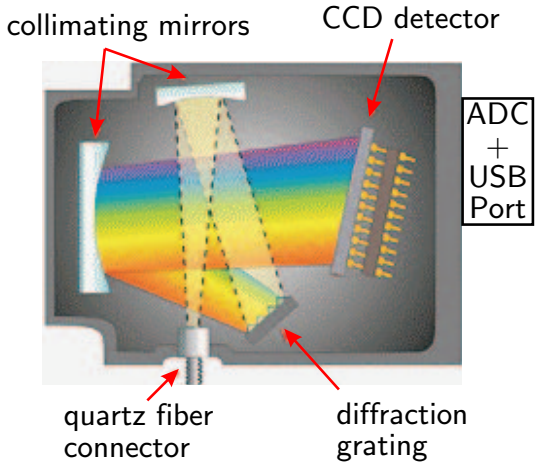

Figure 4.4: *Main components of the OceanOptics USB2000 spectrometer*

= 50μm), which guarantees the minimum required spectral resolution. The entrance slit is mounted in the focal point of the collimating mirror (f = 42 mm). The parallel light from this mirror is then dispersed by a plane diffraction grating (OceanOptics Grating #11, 1800 l/mm, holographic, efficiency curve see Figure 4.5). With the focussing mirror

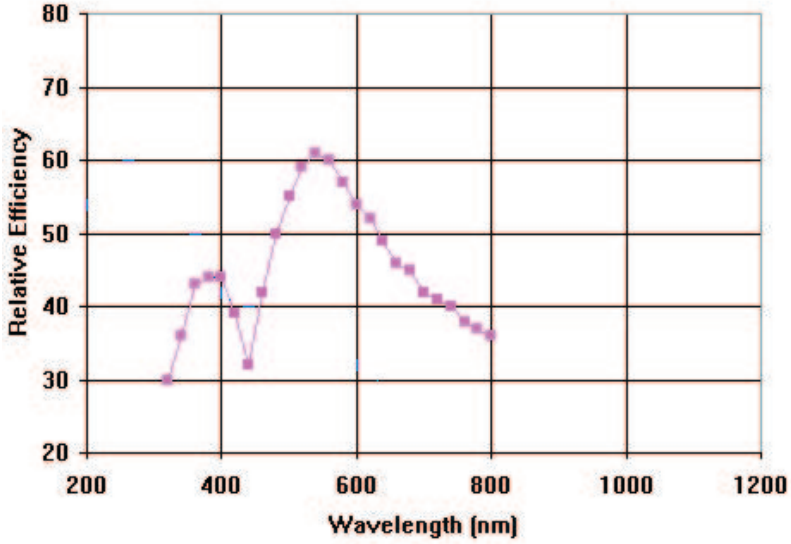

Figure 4.5: *Grating efficiency curve of the used 1800 l/mm holographic grating*

(f = 68 mm) the dispersed light is then imaged onto the detector. The wavelength region observed by the detector was set to 330 nm - 530 nm by adjusting the grating position. The spectra are recorded by a 2048 pixel CCD detector (SONY ILX511). The wavelength to pixel mapping was determined by taking a spectrum of a mercury emission lamp (typical line width is 1 pm). Figure 4.6 shows the wavelength as a function of detector pixel num-

ber. Shown is also the linear and 2^{nd} order fit result and the FWHM[1] of the individual mercury lines. Each of the 2048 pixels is 14μm×200μm in size and represents a potential

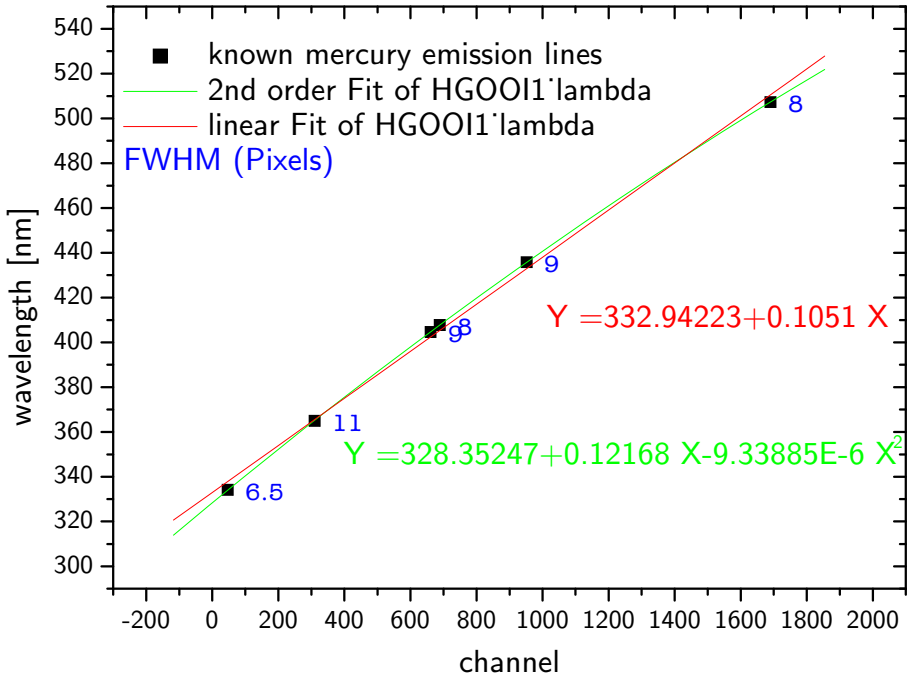

Figure 4.6: *Wavelength to pixel mapping and optical resolution of the USB2000 spectrometer.*

well which accumulates the energy dissipated on light exposure as electrical charge which is proportional to the light intensity. The full well depth corresponds to 160000 photo electrons. However, thermally activated electrons also produce a signal which is called dark current signal. The typical dark current spectrum of the used OceanOptics spectrometer is shown in Figure 4.7. It has to be considered and accounted for during the DOAS evaluation procedure. In order to reduce the dark current of the CCD and stabilize the optical bench the whole USB2000 device was cooled to temperatures around 0°C using Peltier elements controlled by a temperature control unit. Thereby the dark current decreases exponentially regarding Boltzmann statistics.

During the readout process the charges are shifted to a buffer and after addition of an electronic offset the signal is being transferred to the ADC (12 bit, operating at 1 MHz) and digitally transferred to the computer via a USB cable. The offset signal at 0°C is shown in Figure 4.8. It was found that the offset signal depends on temperature, since also the readout electronics are cooled by the Peltier cooler. In order to prevent moisture condensation and freezing onto optical and electronic parts the whole unit was dried in a vacuum exsiccator and then placed in a sealed aluminum box surrounded by silica gel.

[1]full width at half maximum

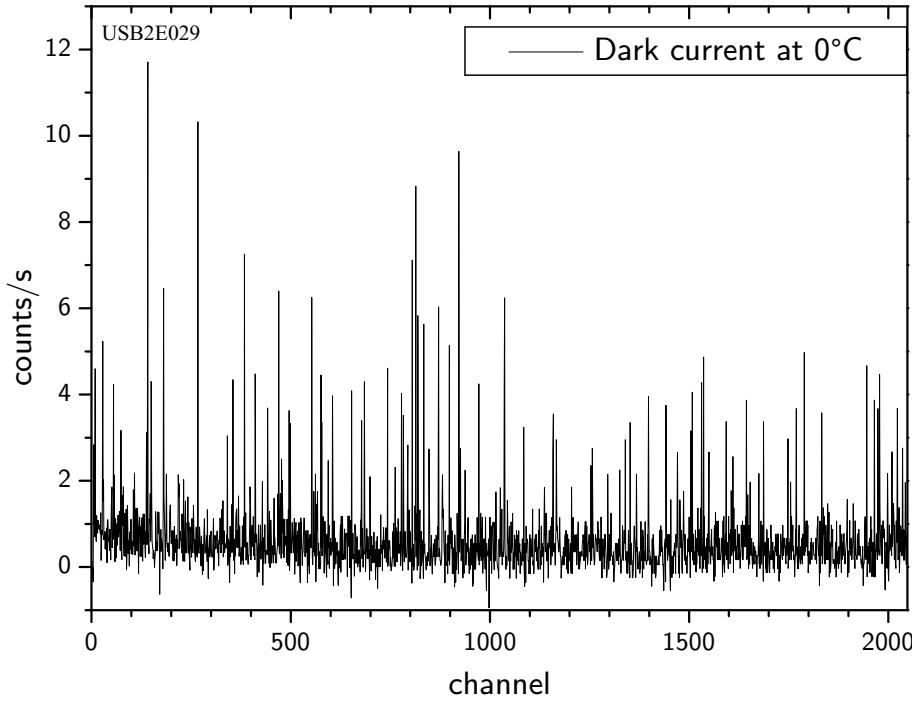

Figure 4.7: *Dark current spectrum recorded at a detector temperature of 0° C.*

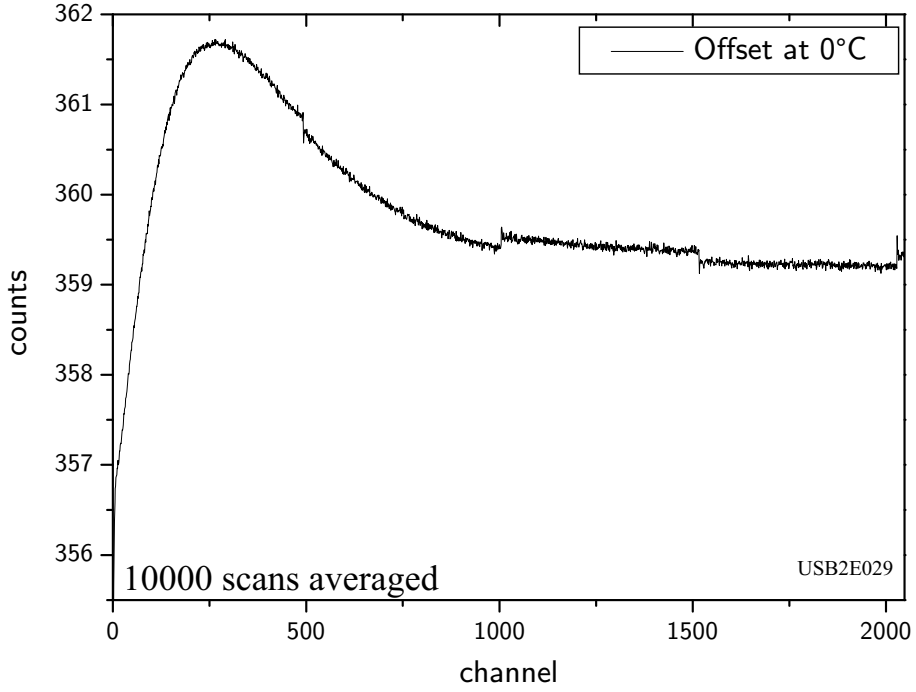

Figure 4.8: *Offset spectrum recorded at a detector temperature of 0° C.*

4.3.2 The Portable Active LP-DOAS System

The portable long path-DOAS system was specially built for and employed during the field measurements on Kerguelen island in the Indian Ocean in December 2000 (see section 5.1.2). Figure 4.9 shows an overview of the arrangement of components in the portable LP-DOAS system. The OceanOptics USB2000 spectrometer is identical to the one described in section 4.3.1. Therefore only the portable telescope will be characterized here.

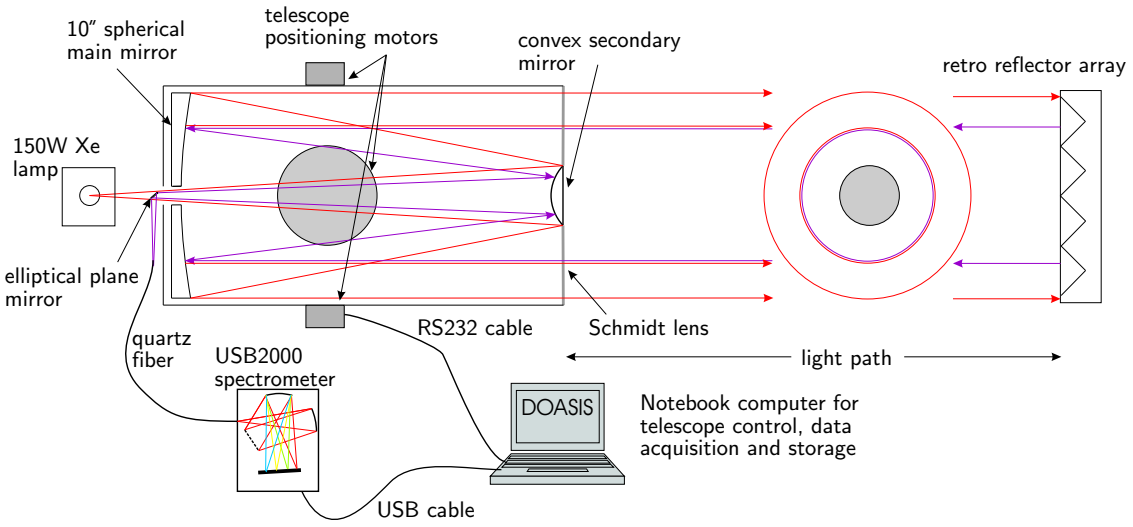

Figure 4.9: *The main components of the portable active LP-DOAS system*

The Meade LX200 Telescope

The Meade LX200 is a commercially available astronomers telescope. Its optical setup is a Schmidt-Cassegrain arrangement, which combines the following main advantages:

- small size because of folded lightpath (Schmidt-Cassegrain System)
- cheapness of optical components (spherical instead of parabolic primary mirror)
- simple alignment because main mirror can be moved along the optical axis

Figure 4.10 explains the optical components of the Meade LX200 telescope. Light enters from the right, passes through a thin lens (Schmidt correcting lens) with 2-sided aspheric correction, proceeds to the spherical primary mirror, and then to a convex aspheric secondary mirror. The convex secondary mirror multiplies the effective focal length of the primary mirror and results in a focus at the focal plane, with light passing through a central perforation in the primary mirror. As indicated by rays 1 and 2 in Figure 4.10 the oversized primary mirror results in a wider field of view. However, this feature is of no use for the application of the telescope for LP-DOAS measurements. The assembly used for

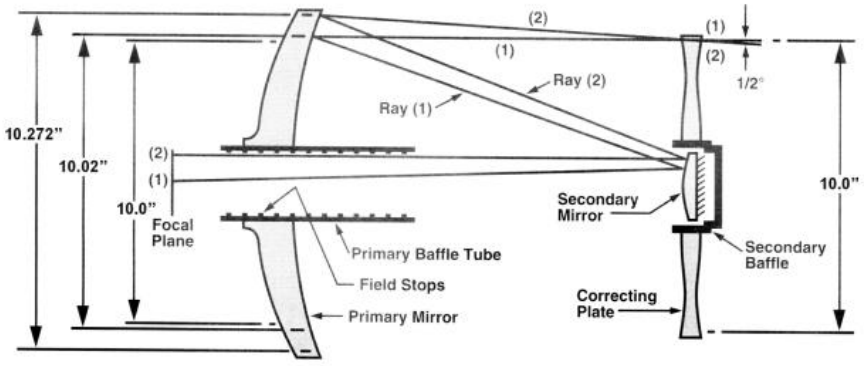

Figure 4.10: *The Meade Schmidt-Cassegrain optical system*

the measurements consisted of a 254 mm primary mirror, the overall focal length of the system was 1600 mm (aperture ratio f/6.3).
In order to adapt the telescope for DOAS measurements a Xenon short arc lamp (Hamamatsu SQ 150W, see section 4.2.2) was placed in the focal point of the telescope. Thus a parallel light beam of 254 mm diameter is emitted. Note that both the convex secondary mirror and the elliptical plane mirror shade the center part of the light beam, so only a ring-shaped beam remains. The 4" secondary mirror shades 16% of the total area. The plane elliptical mirror was mounted so that the inner 7.5" of the primary mirror were shaded. The telescope tube can be moved both horizontally and vertically by 2 computer controlled DC servo motor drives with 0.3 arc-sec resolution encoders. This allows a precise alignment on the retro reflector array in a distance of several kilometers. The retro reflectors reflect the light beam exactly back with a precision better than 3 arc seconds. The parallel light is then received by the same telescope. Again about 16% of the light is lost due to the obstruction by the secondary mirror. A ring-shaped beam of 7.5" outer and 4" inner diameter is seen by the receiving telescope and reflected onto a 200 μm core diameter quartz fiber by the elliptical plane mirror placed in the optical axis outside the telescope tube (see Figure 4.9). The main disadvantage of the Schmidt-Cassegrain telescope design for DOAS measurements is the need for the Schmidt correction lens which is currently not available in UV grade fused silica or any quartz glass version. For DOAS applications in the UV a Cassegrain-type telescope with an aspheric main mirror has to be used. These telescopes do not need any correction lens and can therefore be used for a wide wavelength range.

Chapter 5

Field Measurements

In this chapter the five field studies carried out during this work will be described. The general objective of the field work was to study the tropospheric chemistry of halogen oxides using Differential Optical Absorption Spectroscopy (see chapter 3). Both, traditional active long path DOAS and Multi-Axis-DOAS (see section 3.5) were applied in the field. First, a brief description of two preparatory field campaigns will be given. One main part of this thesis was the ALERT2000 Polar Sunrise Experiment in the Canadian high Arctic, which will be presented in section 5.2. The following sections will show halogen oxide measurements from the first two field campaigns of the EU project ELCID[1] in the Mediterranean (section 5.3) and the Hudson Bay region (section 5.4). The field study at the Hudson Bay represents the first ground-based DOAS measurements in this most interesting low Arctic region (see also section 2.3).

5.1 Preparatory Field Studies

5.1.1 First MAX-DOAS Measurements on the Zugspitze Mountain

The first MAX-DOAS experiments were carried out in winter 1999/2000 on the Zugspitze Mountain in the German Alps. The main objective of this study was to test the MAX-DOAS instrument and to find a possible BrO background in the free troposphere (see also section 2.3). After the description of the measurement site and a brief overview of the meteorological conditions the MAX-DOAS measurements and evaluation will be presented.

Measurement Site

The Environmental Research Station Schneefernerhaus (**U**mwelt **F**orschungsstation **S**chneefernerhaus, UFS) is located just below the summit of Germany's highest mountain

[1] **E**va**L**uation of the **C**limatic **I**mpact of **D**imethylsulfide

Zugspitze (10°59'E, 47°25'N, altitude 2650 m above sea level). The UFS was established in 1998 to promote atmospheric research, it also participates in the United Nation's Global Atmosphere Watch program (GAW). Due to its location high above all sources of pollution the station is representative for the background continental free troposphere most of the time. Local sources of pollution are very sparse, mainly pollution from the nearby ski area can be expected during winter.

Meteorological Parameters

An overview of the meteorological parameters observed at the Zugspitze summit weather station for the period of the DOAS measurements is shown in Figure 5.1. The ambient temperature at the Zugspitze summit ranged between +6°C and -24°C with a mean value of -9°C. At the UFS temperatures are on average 2 degrees warmer compared to the summit assuming a typical adiabatic lapse rate of 0.7 K/100 m. The pressure at the UFS is about 30 hPa higher at the UFS than at the summit, where a mean value of 700 hPa was recorded. As expected for northern mid-latitudes the prevailing wind direction is from the west. The visibility and opacity data can serve as indicators for understanding the radiative transport which is crucial for DOAS measurements using scattered sunlight.

MAX-DOAS Measurements

From October 6, 1999 to March 13, 2000 MAX-DOAS measurements were performed at the UFS station[2]. The instrument employed for these measurements is described and characterized in section 4.1. The telescope/stepper motor assembly was mounted at the facade of the fifth floor (observation deck) of the Schneefernerhaus station. The telescope could be moved from zenith observation mode to elevation angles down to 20° by means of the computer controlled stepper motor drive. The telescope azimuth orientation was exactly south. Figure 5.2 shows the light receiving telescope in zenith position. The viewing direction of the telescope is shown as an image of the Webcam mounted close to the DOAS telescope. The automated measurement routine was continuously recording spectra of scattered sunlight in the wavelength region from 320 nm to 400 nm at a spectral resolution of 0.35 nm during daytime (solar zenith angle $\vartheta \leq 97°$). After five spectra in the zenith viewing mode, one spectrum at 20° elevation angle was taken. During nighttime routine offset and dark current measurements were performed.
During local noontime (around 11h UT) the relative solar azimuth angle, i.e. the azimuth angle between the sun and the telescope viewing direction was very small in the 20° elevation angle measurements. This causes particular changes in the radiative transfer, the related problems are discussed below. On November 26, 1999 the combination of a

[2]The data acquisition was interrupted between the morning of November 26 and December 15, 1999 due to repair of the quartz fiber assembly.

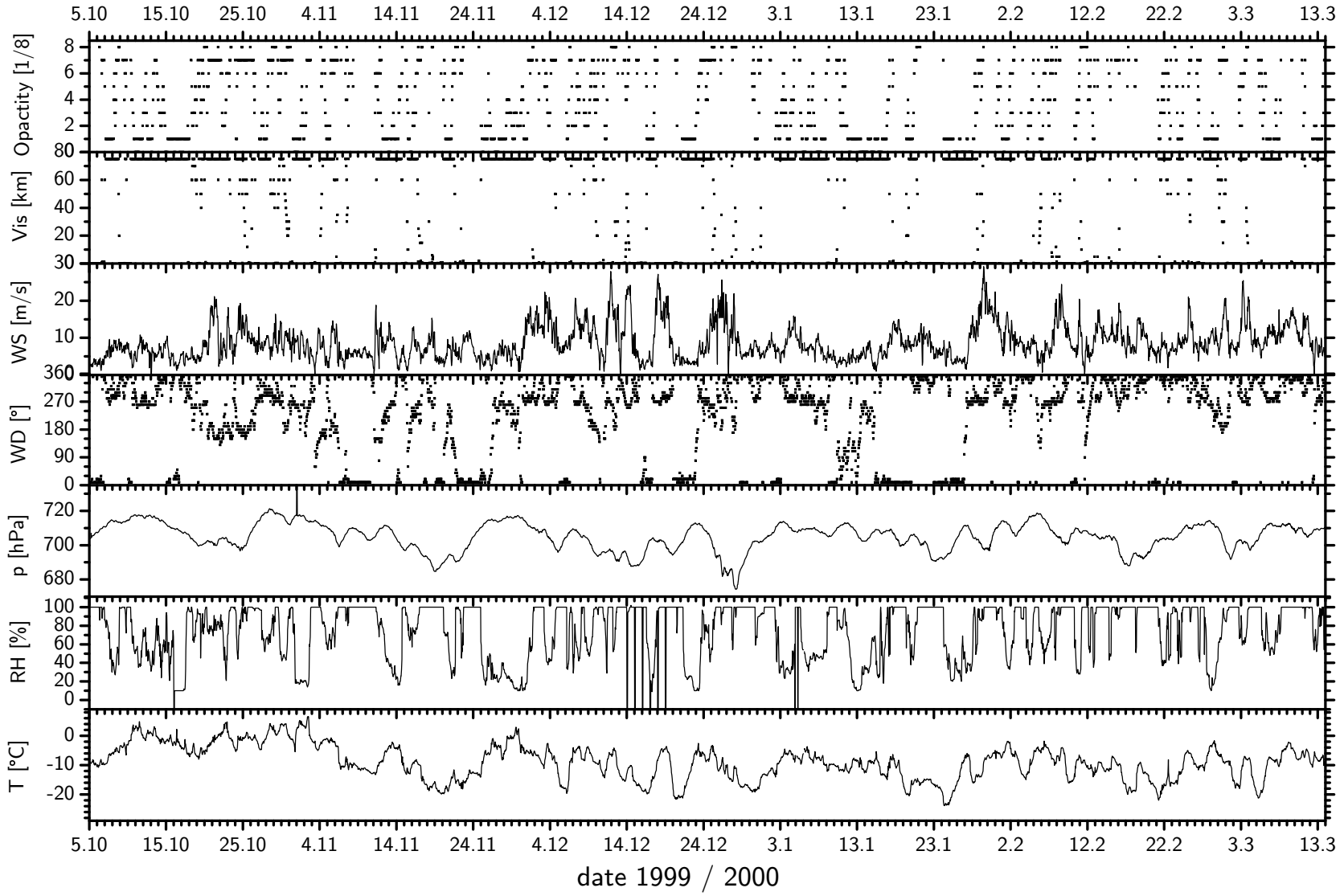

Figure 5.1: *Overview of the meteorological parameters temperature, relative humidity, pressure, wind direction, wind speed, visibility and opacity for the period of the DOAS measurements in October 1999 to March 2000.*

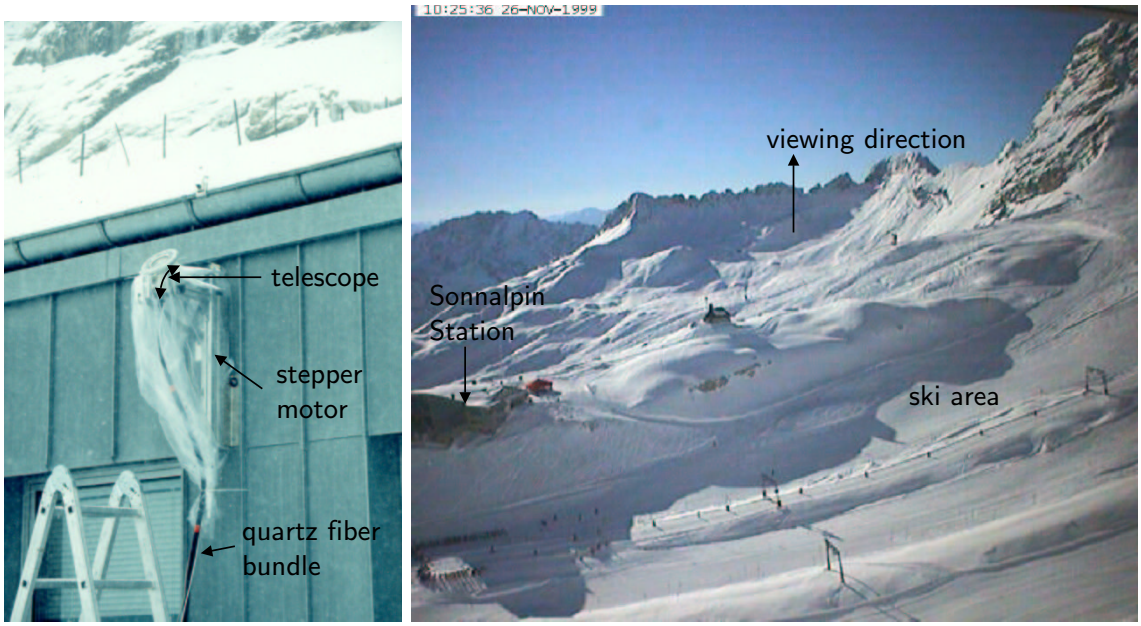

Figure 5.2: *Left: DOAS telescope and stepper motor assembly at the Schneefernerhaus. The telescope is in zenith mode, the 45° angle of the telescope front window (see section 4.1.1 prevents snow from accumulating and obscuring the field of view. Right: View from the Schneefernerhaus towards the south. The Sonnalpin station and the ski area are the only possible local sources of pollution.*

small relative azimuth angle and a noontime solar elevation of ≈20° led to a damage of the quartz fiber bundle due to the heat related to the focus of direct sunlight inside the telescope housing. After the repair the measurements continued on December 15, 1999. Integration times for the spectra ranged from 5 min during daytime to 10 min during twilight.

MAX-DOAS Evaluation

All scattered sunlight spectra recorded during the Zugspitze measurements were evaluated by the same DOAS analysis procedure (see section 3.1.2). After subtraction of the electronic offset and dark current signal the logarithm was applied. For the DOAS fit the wavelength range between 346 nm and 359 nm was used, since this wavelength range provides the optimum results (minimum residual structure) for the BrO retrieval. As reference spectra the following spectra were included in the fitting process:

- Fraunhofer reference spectrum (FRS, see section 3.2.2) from October 7, 1999 at 11:00 UT (SZA=53°) taken at 90° elevation angle (zenith mode).
- Ring spectrum as described in section 3.2.3. The Ring spectrum was calculated from the FRS using the 'Y' command of the software MFC [*Gomer et al.* 1993] to derive

the rotational raman spectrum.

- reference spectra of BrO at 228 K [*Wahner et al.* 1988], NO_2 at 230 K, O_3 at 221 K and 241 K and O_4 were convoluted with the 334.15 nm mercury line to match the instrumental line shape.

All reference spectra were simultaneously fitted to the atmospheric spectra using the linear-nonlinear fit procedure of the analysis software MFC. A polynomial of 2^{nd} order is also included to remove broadband absorption structures due to Rayleigh and Mie scattering. An example of the fit results of the BrO evaluation is shown in Figure 5.3. The complete data set obtained during the Zugspitze measurements is included in the appendix (see pages 218 to 222). The DOAS evaluation yielded differential slant columns for the absorbers included in the fitting process. For ozone and NO_2 most of the time the well known diurnal behavior of dSCDs for stratospheric absorbers was found. Figure 5.4 shows typical examples for the stratospheric background of these species. For the NO_2 dSCD time series shown in Figure 5.4 the red data points representing the 20° elevation are on average slightly higher than the corresponding zenith values, which is an indication for the presence of local NO_2 pollution which enhances the absorption in the low elevation angle (see section 3.5.3). Some events of relatively high local pollution were also observed, in general correlated with high tourist season in the Zugspitze ski area (Christmas holidays, 26.12.1999 to 29.12.1999 and the weekends 21.-22.01.2000, 19.-20.02.2000, which were all cloudy days leading to large tropospheric lightpath enhancement, see also enhanced O_4 absorption signal).
To assess the abundance of free tropospheric BrO two typical time periods are regarded. From January 11 to January 14, 2000 typical clear sky conditions prevailed at the measurement site and over the Alps. The MAX-DOAS results for this period are shown in Figure 5.5. During noontime significant changes in the BrO dSCD are found, generally the zenith values drop during this time. For O_4, which is a strong absorber in the lower atmosphere, the differences are not as strong. These observations point to one major problem encountered during the Zugspitze measurements: since the telescope pointed to the south during noontime the direct sun was very close to the line of sight of the MAX-DOAS instrument for the 20° elevation geometry (very small relative azimuth angles). This might have led to a significant amount of direct sunlight received by the telescope. Even though the telescope's field of view was less than 1°, illumination of dust particles on the quartz lens has possibly led to a significant fraction of direct sunlight scattered into the quartz fiber[3]. Alternatively the origin could also be a change in the radiative transfer in the atmosphere when the angle between the sun and the viewing direction is small. In this case

[3]The layout of the receiving telescope is such, that the part of the quartz lens seen by the fibers can be illuminated by direct sunlight when the angle between viewing direction and sun is less than 25°. This is consistent with the azimuth interval exhibiting the sudden changes.

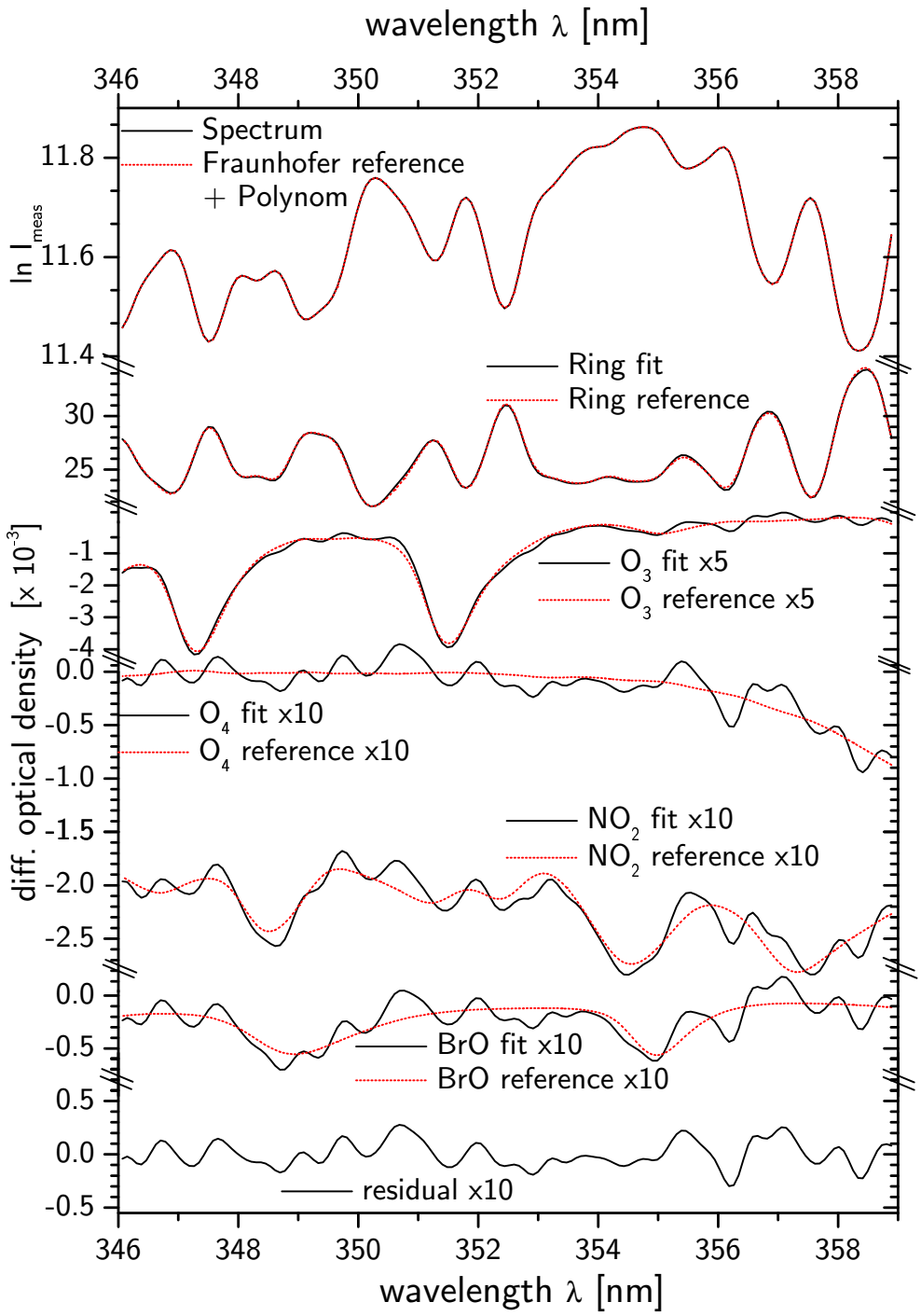

Figure 5.3: *Example of the DOAS BrO evaluation for the Zugspitze spectra. The atmospheric spectrum was taken on 26.02.2000 at 7:30UT and a local SZA of 77°. Note that the Fraunhofer lines have typical optical densities of 0.3-0.5. All other optical densities are given in units of 10^{-3}. For better comparison the y-scale for the different absorbers is expanded by a factor of 5(O_3) and 10 (O_4, NO_2, BrO), respectively. The BrO absorption found corresponds to $(6.2\pm0.7)\times10^{13}$molec/cm^2. Typical residual structures during the Zugspitze measurements were less than 10^{-3}.*

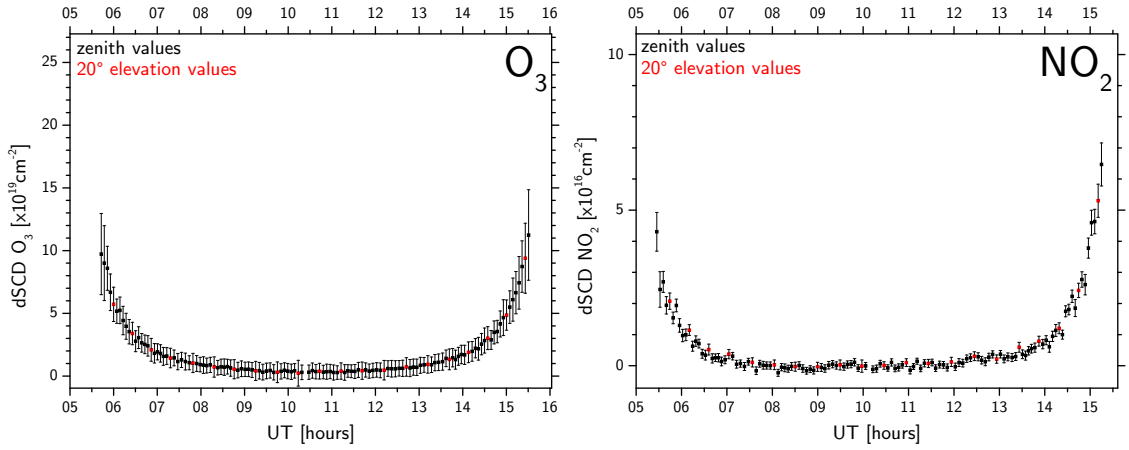

Figure 5.4: *Sample dSCDs of O_3 and NO_2 for October 30, 1999. Left: typical diurnal pattern of the ozone dSCD. Only stratospheric O_3 can be identified, no difference is visible between the different viewing directions. Right: the shape of the NO_2 dSCD series is characteristic for a stratospheric NO_2 profile. However, slightly elevated dSCDs for the 20° elevation (red data points) indicate a fraction of NO_2 in the lower atmosphere, possibly from local pollution.*

dramatic changes of the radiative transfer, which determines the light paths of photons received by the telescope, could originate from a significant amount of quasi-direct sunlight, which is forward scattered by Rayleigh and Mie scattering very close to the direct solar rays. However, the observations are most likely due to direct light scattered in the telescope because the anomalies are found in the spectra taken in zenith mode, not in the low elevation ones. For the telescope pointing in zenith direction the sun could illuminate dust on the quartz lens because the front window is tilted by 45° (see also Figure 4.1 for a sketch of the telescope).

To show the difference for observations during overcast or cloudy periods, as an example the period from March 1 to March 4, 2000 is plotted in Figure 5.6. Since one objective of the Zugspitze measurements was to study BrO in the free troposphere, another effect should be mentioned here. As mentioned above stratospheric absorbers show a U-shaped diurnal variation of the slant column densities. Measurements by D. Perner (private communication, 1999) at Sondrestrøm Fjord, Greenland and at the Jungfraujoch in the Swiss Alps showed an anomalous behavior of 'W-shaped' diurnal variations of the BrO SCD. It was speculated whether these anomalies could be explained by free tropospheric BrO. Since the events were correlated with the occurrence of clouds and tropospheric fog, *Pfeilsticker et al.* [1998] proposed that 'cloud effects' lead to optical path modifications and enhanced absorption due to interstitial BrO. During the measurements on the Zugspitze, several similar diurnal variations were observed, Figure 5.7 shows an example of March 4-5, 2000. Also plotted is the visibility recorded by the weather station, which was less

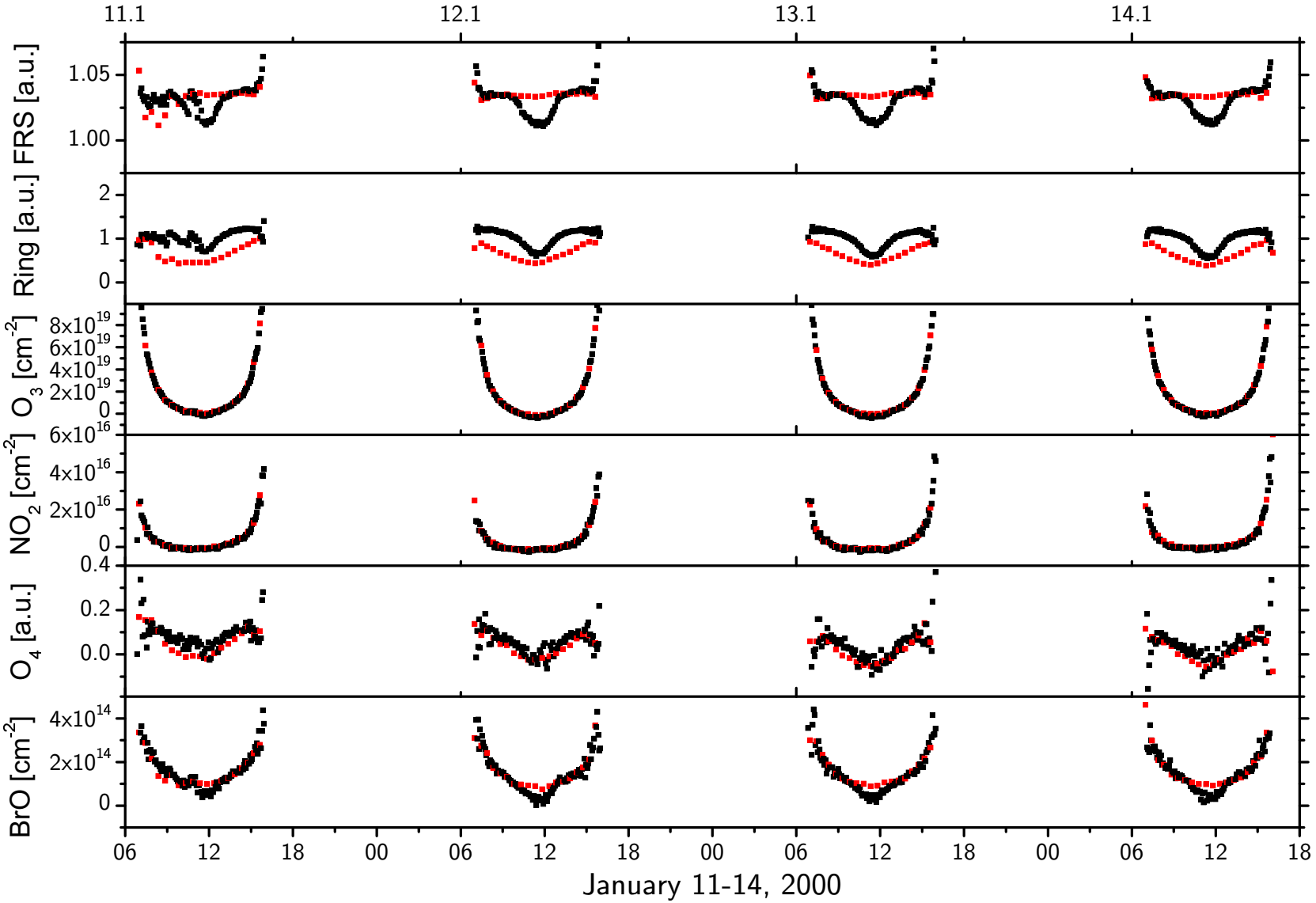

Figure 5.5: *MAX-DOAS results (black points: zenith, red points: 20° elevation) for the typical clear sky period from January 11 to January 14, 2000. Strong differences for the 2 elevation angles are found around noontime. Correlated strong changes in the Fraunhofer and Ring fit coefficients point to sudden changes in the radiative transfer.*

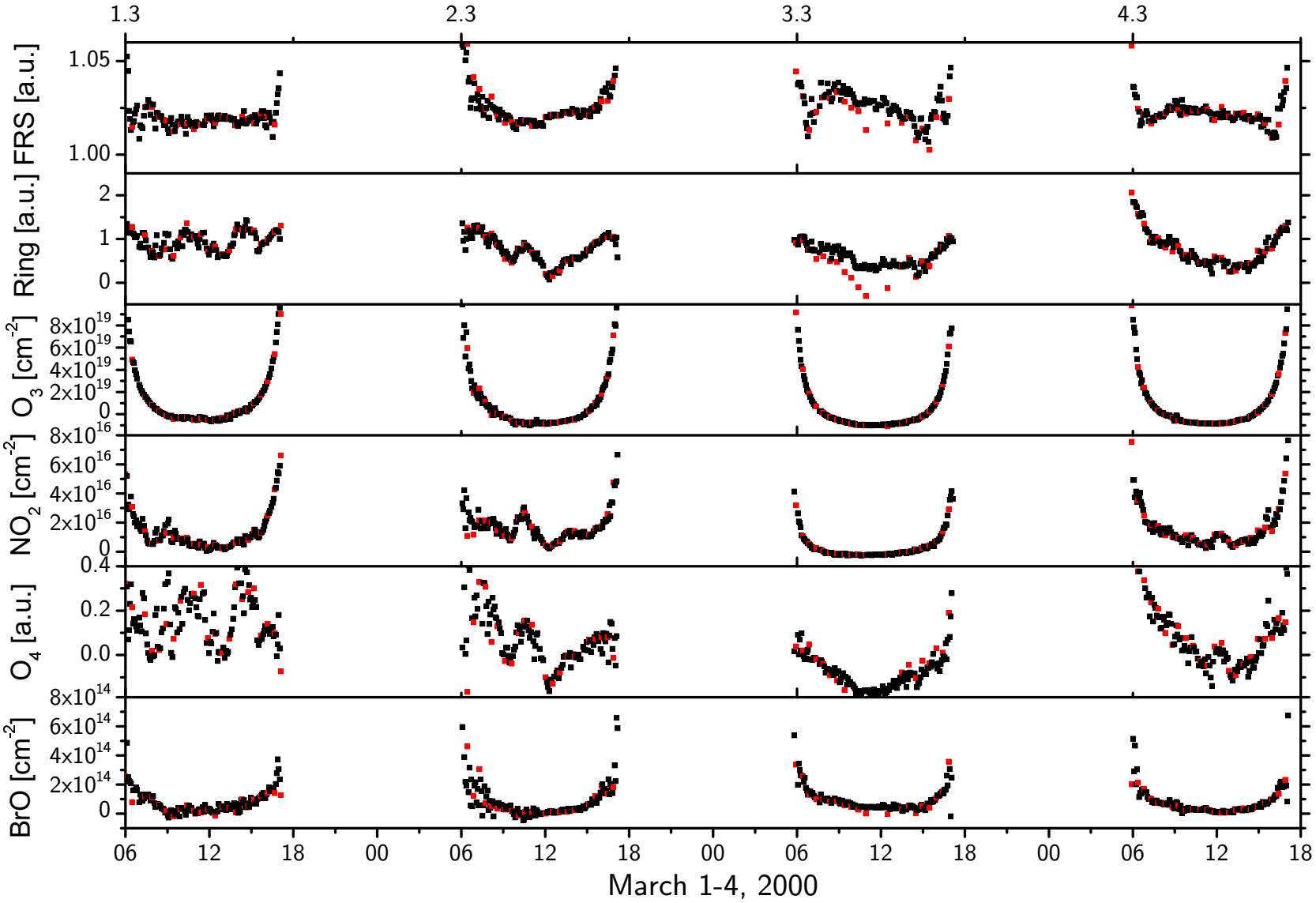

Figure 5.6: *MAX-DOAS results (black points: zenith, red points: 20° elevation) for a typical cloudy sky period from March 1 to 4, 2000. No significant differences for the 2 elevation angles can be identified for BrO and O_4. Fraunhofer and Ring fit coefficients show the expected behavior, the correlation of Ring and O_4 fit coefficients can be explained by enhanced rotational Raman scattering for longer light paths.*

than 50 m due to dense fog until the late afternoon of March 5, 2000. A study suggesting a free tropospheric background of 1-3 ppt of BrO based on multi-platform observations of BrO has been recently presented by [*van Roozendael et al.* 2000].

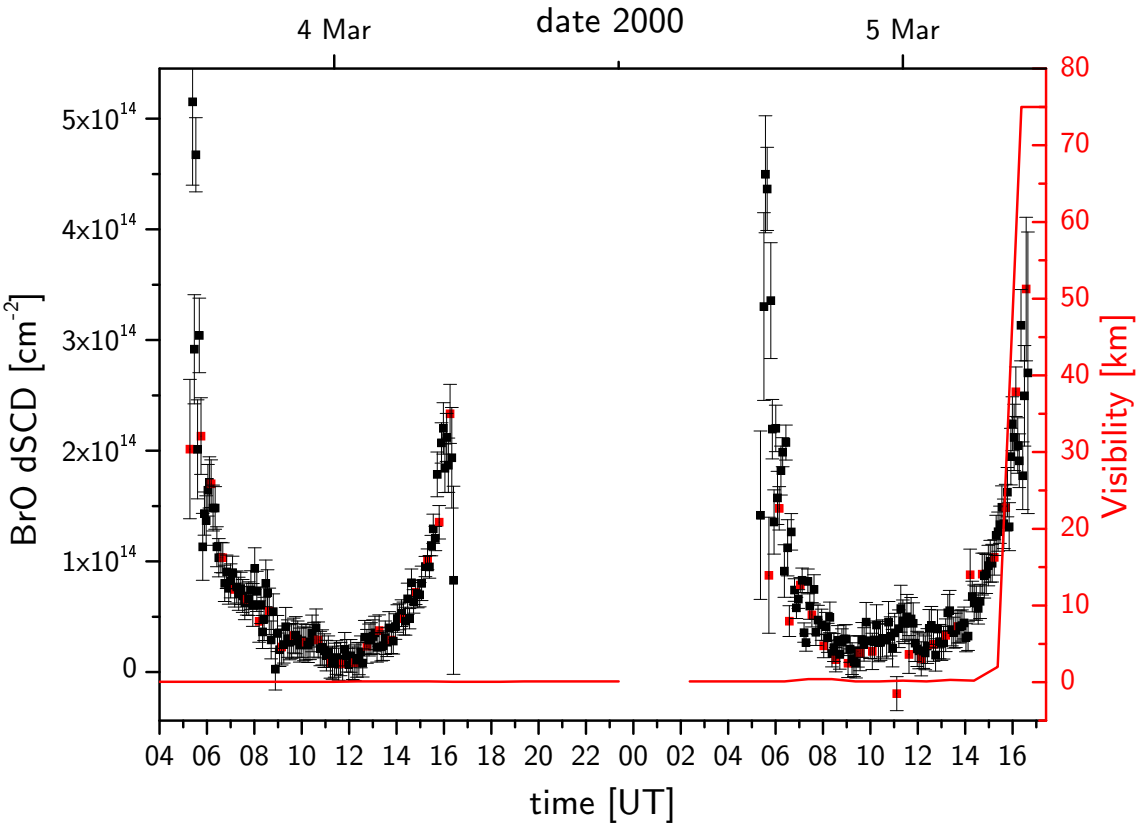

Figure 5.7: *BrO dSCDs measured during a fog period on March 4 and 5, 2000. Especially the March 5 diurnal variation shows a clear deviation from the U-shape expected for a purely stratospheric absorber.*

5.1.2 Preparatory Field Campaign in the Southern Indian Ocean

Overview of the Campaign

In December 2000 measurements in the southern Indian Ocean were carried out as preparative study for an intensive field campaign within the ELCID[4] project planned for austral summer January to March 2002 in the French TAAF[5] overseas district. Due to their remoteness - the French islands are situated approximately in the middle between South

[4] **E**valuation of the **C**limatic **I**mpact of **D**imethylsulfide
[5] **T**erres **A**ustrales et **A**ntarctiques **F**rançaises

Africa and Australia, with South Africa being the closest upwind source of anthropogenic pollution at a distance of about 4000 km - the TAAF islands are ideal for studying the background marine boundary layer chemistry. The islands are inhabited by 20 to 100 scientists per station, so local pollution is minimal. Two types of experiments were performed:

- shipborne MAX-DOAS measurements (on board the research vessel Marion Dufresne) on the route from Réunion Island via Crozet, Kerguelen and Amsterdam Island back to Réunion.

- Active Long-Path DOAS measurements were carried out for $1\frac{1}{2}$ days during the 2 day stopover at Port-aux-Français on Kerguelen Island.

The ship track and the location of the French islands in the southern Indian Ocean are shown in Figure 5.8.

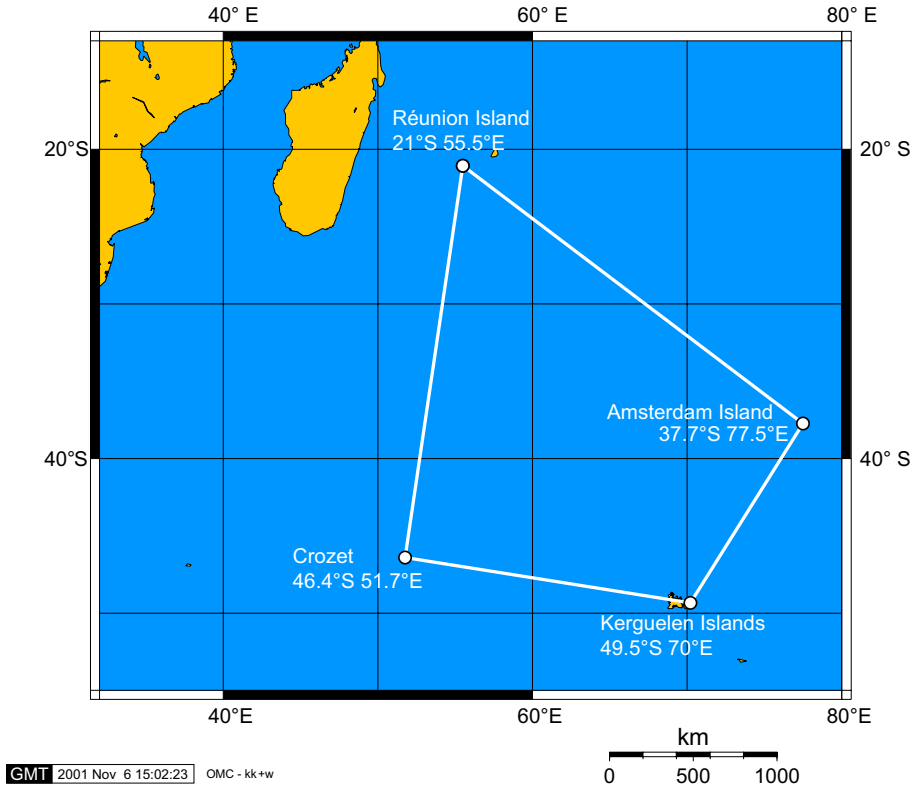

Figure 5.8: *Map of the Indian Ocean Measurement Region: The shipborne measurements started on the French Island Réunion 700 km east of Madagascar, the indicated track was followed in a counterclockwise direction. Active Long-Path DOAS measurements were performed during the stopover at Kerguelen Island.*

Measurements aboard Marion Dufresne

The French islands in the Indian Ocean are - except for Réunion Island - only accessible by sea. The research vessel Marion Dufresne serves the islands Crozet, Kerguelen and Amsterdam as means of transportation and for atmospheric and oceanographic research. In December 2000 a newly developed MAX-DOAS instrument (see section 4.3.1) was tested on board of Marion Dufresne. The measurements were carried out from December 10 until December 18, 2000 from the tropical island Réunion via Crozet to the subpolar Kerguelen Islands. After the stop at Kerguelen, scattered sunlight DOAS measurements were continued from December 21 to December 28 on the way back to Réunion via Amsterdam Island, which is located at mid-latitudes.
The MAX-DOAS telescope was mounted on the top level deck just behind the bridge. Because of a failure of the stepper motor controller the telescope could only be adjusted manually to receive light from different elevation angles. In standard mode the telescope observed off axis scattered sunlight from a 5° elevation angle[6]. Once daily multi-axis measurements were done by manually turning the telescope to elevation angles of 10°, 20°, 40°, 60° and 90° (zenith). The integration time per spectrum was 200 ms, during the spectra acquisition 1000 scans were co-added. The spectra were evaluated using the DOAS evaluation software WINDOAS (kindly provided by C. Fayt, IASB). An example of the DOAS analysis in the spectral range 346 nm-359 nm for the evaluation of BrO is shown in Figure 5.9. The atmospheric spectrum was taken on December 10, 2000 at 10:45:43 UT (Start time 10:42:18, End time 10:49:08). The average number of counts in the evaluation range is 4×10^5 counts (corresponding to 3.2×10^6 photoelectrons). As minimum theoretical residual noise the photon noise of 5.6×10^{-4} RMS can be calculated. The residual noise after simultaneous fitting of all known reference spectra in this wavelength range yields 7.5×10^{-4} RMS, which is nearly the expected theoretical noise level. In order to further decrease the noise more spectra had to be co-added. However, in this evaluation co-adding did not improve the results but rather degraded the quality of the fit. This was probably due to the variability of several critical parameters, e.g. instrumental (spectrograph and detector temperatures), atmospheric (SZA, clouds, etc.) and other effects. Due to the higher noise level the DOAS fit errors and also the errors of the derived dSCDs are on average a factor of 3 to 4 higher compared to the other measurements shown in this thesis. The results of the evaluation for ozone and NO_2 dSCDs do not show any deviation from the behavior expected for stratospheric absorbers and are therefore only included in the appendix on page 224 together with latitude, longitude and SZA.
Since one main objective of the study was to assess the abundance of BrO in the southern Indian Ocean marine boundary layer, in Figure 5.10 four example days of the BrO evaluation are shown. The O_4 MAX-DOAS series of December 10 shows the expected increase

[6]the roll of the ship (usually less than 3°) was not compensated

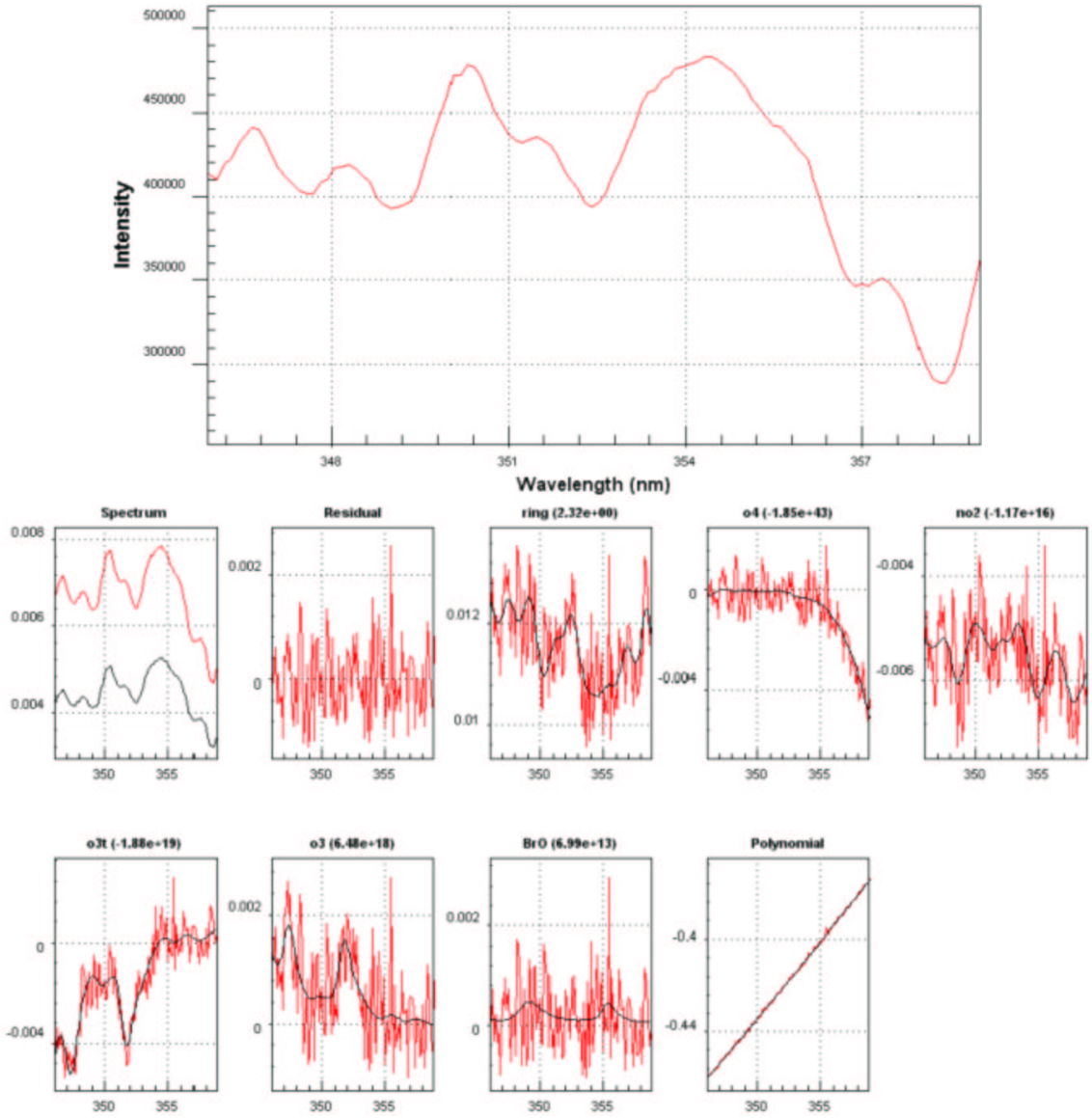

Figure 5.9: *Top: atmospheric spectrum in the range 346 nm to 359 nm taken on December 10, 2000 at 10:45:43UT. Bottom: typical DOAS fit results in the BrO fit range. Peak-to-Peak residual structures are in the range (2-4)*$\times 10^{-3}$.

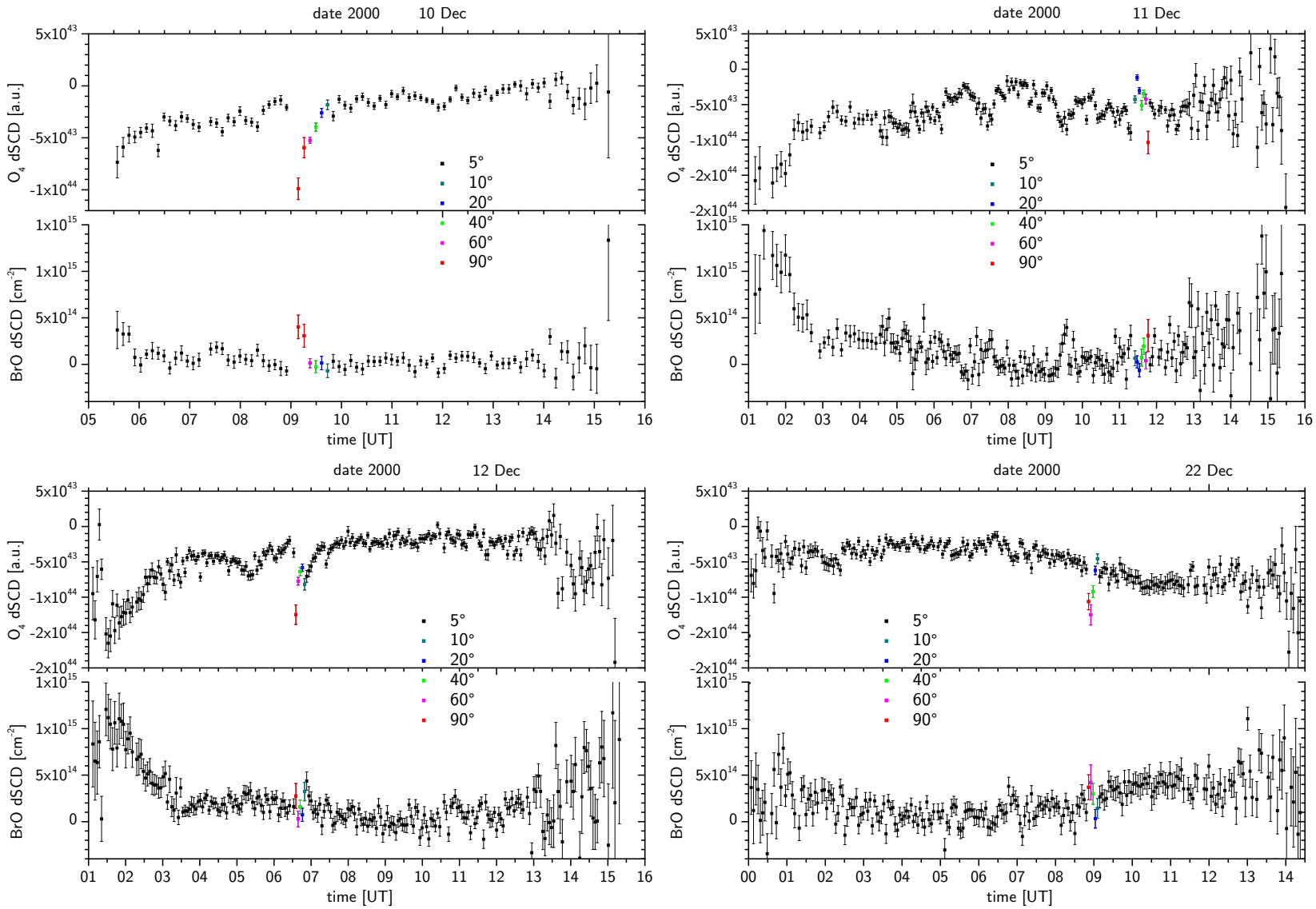

Figure 5.10: *Four days of the BrO MAX-DOAS evaluation results are shown. The dSCDs measured at different elevation angles are indicated in different colors. O_4 dSCDs show the expected increase in dSCD with decreasing elevation angle, while for BrO no significant systematic behavior can be found.*

in dSCD, whereas for BrO the low elevation angles show no increased values. The 60° and zenith value even show higher dSCD than the neighbor points, which cannot be explained so far. The three other days show the same behavior for the O_4 series. For BrO no significant differences between the geometries exist. Also, no anomalies like on December 10 were observed. It can also be seen from Figure 5.10 that the noise level for that day is lower than for the rest of the days. This is due to a change in integration time per spectrum from 400 s to 200 s on December 11 because of detector saturation problems in the visible spectral range.
From the measurements carried out on Marion Dufresne therefore only upper limits of BrO in the marine boundary layer of the southern Indian Ocean can be derived. Assuming a boundary layer height of 1 km, on December 10, 2000 an enhancement of 1×10^{14}molec/cm^2 could have been identified if present. This corresponds to a mixing ratio of $\leq$4 ppt if averaged along a 10 km lightpath in the boundary layer (geometric approximation for α=5°). For the other days this upper limit is higher due to the shorter integration time per spectrum. The problems associated with co-adding of spectra after the measurements were already mentioned above.

Active LP-DOAS Measurements at Kerguelen

During the 2 day stopover at Kerguelen from December 19 to December 21, 2000, a feasibility study was carried out as preparation for the intensive long path DOAS measurements planned in the framework of the ELCID project for austral summer 2001/2002. The French research station Port-aux-Français is located at 49.5°S, 70°E at the north coast of Golfe Morbihan, a large bay of ≈300 km^2 and 30 m average depth, which is connected to the circumpolar ocean to the southeast (see Figure 5.11). The Kerguelen islands are geologically classified as continental shelf and the waters around the islands are a biologically very productive region. A large fraction of the waters is populated with different kinds of macroalgae. Therefore precursor species of reactive iodine and bromine should be abundant. The main objective of the measurements presented here was to prepare an intensive long path DOAS field campaign at Port-aux-Français for austral summer 2001/2002 and also to take test measurements to determine if iodine oxides can be identified in the marine boundary layer at Kerguelen. Figure 5.11 shows the surroundings of the French research station where a long path instrument was operated for two days. The specially built small footprint LP-DOAS instrument described in section 4.3.2 was used for the first time at Kerguelen. After the arrival of R/V Marion Dufresne in the morning of December 19, 2000 the retro reflectors were set up in a distance of 5.35 km along the shoreline. LP-DOAS measurements were started in the afternoon at 10UT (15h local time). Atmospheric spectra were recorded in the range from 390 nm[7] to 536 nm. The absorbers of interest in this

[7]below 390 nm light was absorbed by the Schmidt lens of the telescope, which is opaque in the UV

Figure 5.11: *Map of the measurement site on Kerguelen Island. The French station Port-aux-Français is located in a Bay which is protected from the open ocean. The site is characterized by large fields of macroalgae covering the waters around the island. The DOAS lightpath between the station and the retro reflectors in a distance of 5.35 km is indicated as black arrow.*

range are iodine oxide (IO) and NO_2, which could be emitted locally. The time series of both species for the measurements at Kerguelen is shown in Figure 5.12. During December 19, some local pollution from Port-aux-Françcais was observed with NO_2 mixing ratios up to 3 ppb. Also a few data points of IO mixing ratios above the detection limit could be measured during the afternoon. An example of the IO evaluation using the WINDOAS software (C. Fayt, IASB) is shown in Figure 5.13, yielding an IO mixing ratio of (9.8 ± 3.9) ppt. The residuals of the fit (and therefore the fit errors) are generally about a factor of 3 larger compared to the ship borne scattered sunlight measurements using the same spectrograph and detector. The two main problems encountered for the evaluation of the long-path measurements were the temporal variability of the lamp structures and possible structures caused by the quartz fiber, since only simple mode mixing was performed (only shaking of the fiber, no squeezing; for details on quartz fiber mode mixing and its importance for LP-DOAS see section 3.2.1). The variable lamp structures (pressure broadened Xenon emission lines) had to be excluded from the fit, because no lamp reference spectrum included in the performed test fits could eliminate the strong structures.

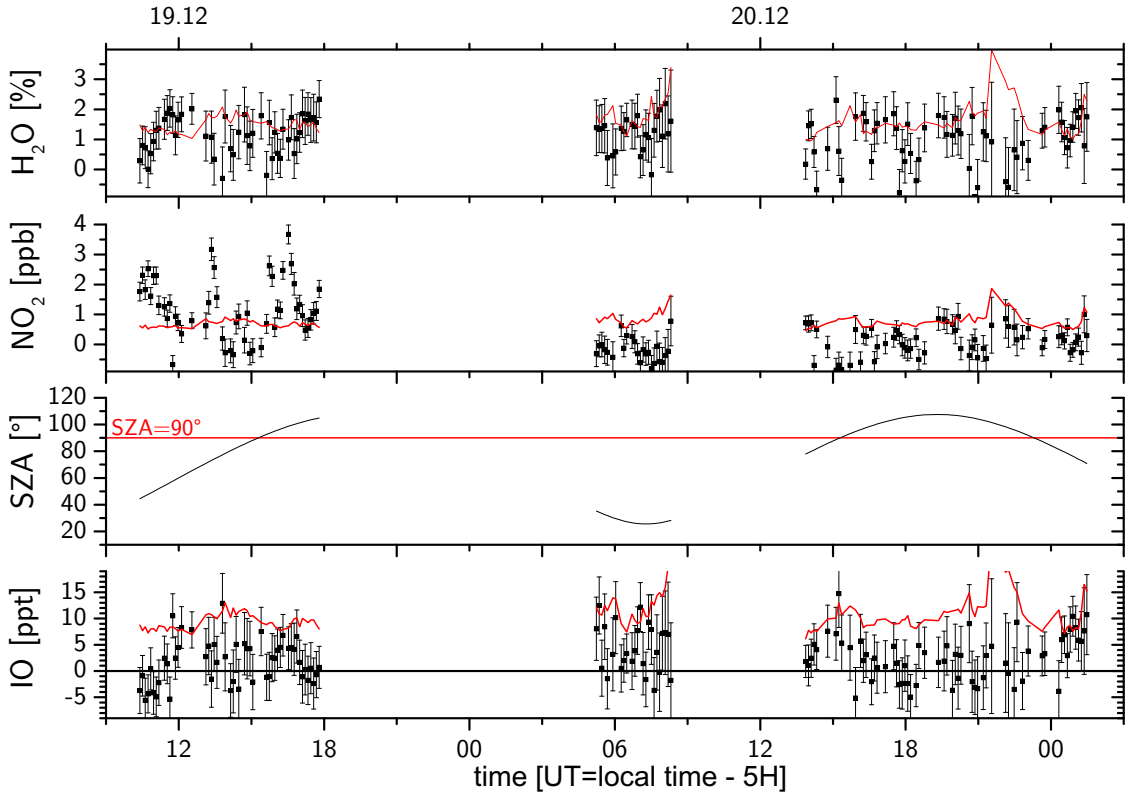

Figure 5.12: *Overview of the LP-DOAS results from the measurements at Kerguelen Island. The evaluated absorbers are shown with their errors (2× fit error) and the 2σ detection limit (red line). Wind speeds of 150 km/h and more did not allow measurements during the first night.*

Unfortunately the lamp emission lines overlap largely with the IO absorptions, so only 1 and a half absorption bands could be fitted. Nevertheless several data points showing IO mixing ratios above the detection limit could be found. Most part of the first night no measurements were possible due to extremely high wind speeds of 150 km/h and more. After the retro reflectors were cleaned the next morning the measurements continued until the morning of December 21, when R/V Marion Dufresne left for the return trip to Réunion via Amsterdam Island.

5.2 MAX-DOAS Measurements during the ALERT2000 Polar Sunrise Experiment

From February to mid-May 2000 the Polar Sunrise Experiment ALERT2000 took place in the Canadian Arctic. ALERT2000 was a follow up experiment of several previous studies. During the last 15 years these Polar Sunrise Experiments have first discovered and sub-

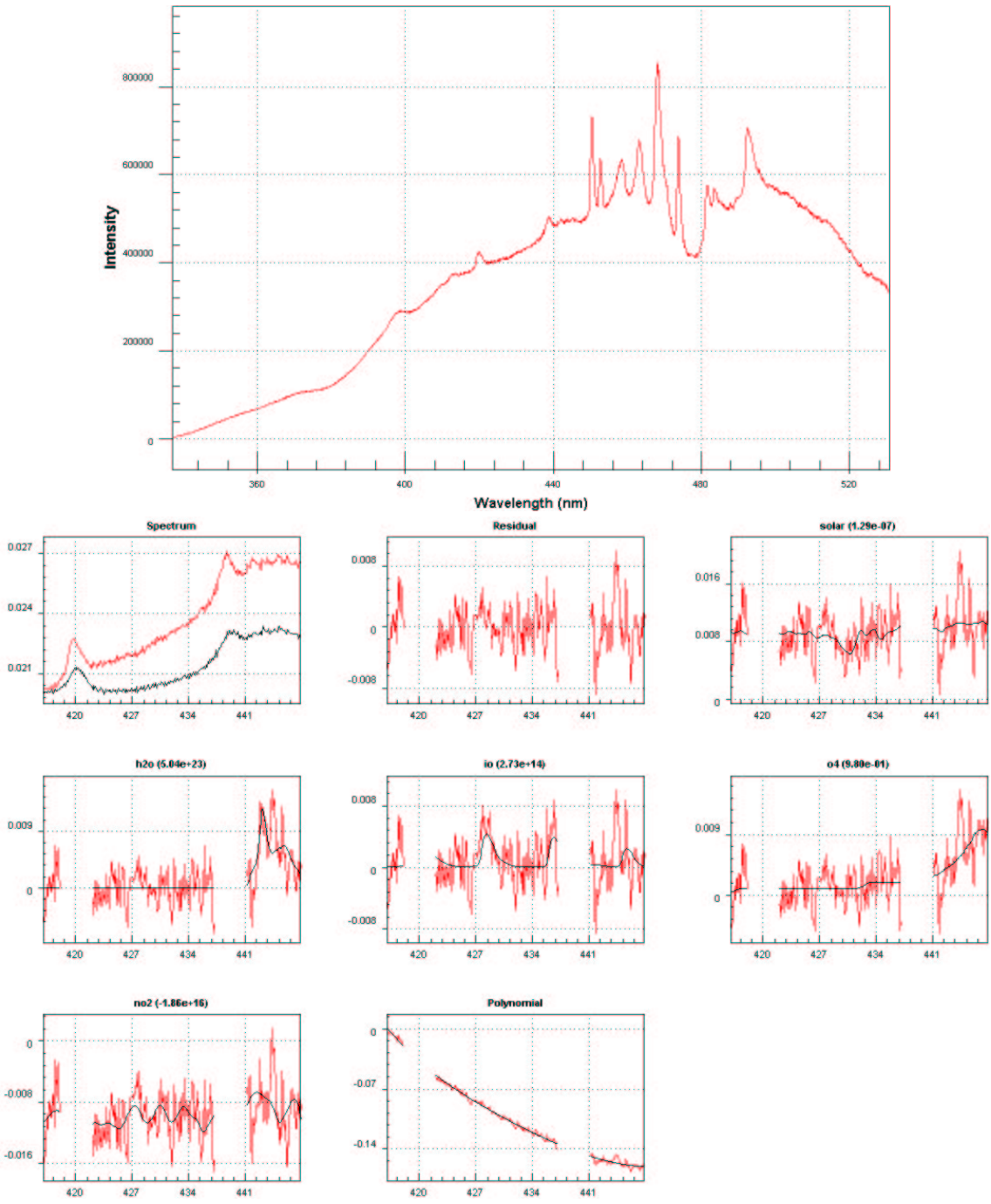

Figure 5.13: *Top: Measured atmospheric spectrum at 11:45UT on December 19, 2000 during the LP-DOAS measurements at Port-aux-Français, Kerguelen. The Xenon emission lines visible in the spectrum originate from the used high pressure Xe arc lamp. Bottom: DOAS fit result for the IO evaluation region. Two Xe emission lines had to be excluded from the fit due to fluctuations of the lamp spectrum. The IO column density calculated by the fit corresponds to a mixing ratio of (9.8±3.9)ppt.*

sequently elucidated the phenomenon of sudden surface ozone loss and related processes after polar sunrise (see Section 2.3). Between February 1 and May 10, 2000 (for the dates of polar sunrise see Figure 5.14) more than 30 scientists from North America, Europe, and Japan conducted a diverse set of experiments at the Canadian Forces Station (CFS) Alert, Nunavut, Canada, which will be described in this section. Details can also be found on the ALERT2000 web page (http://www.msc-smc.ec.gc.ca/alert2000/).

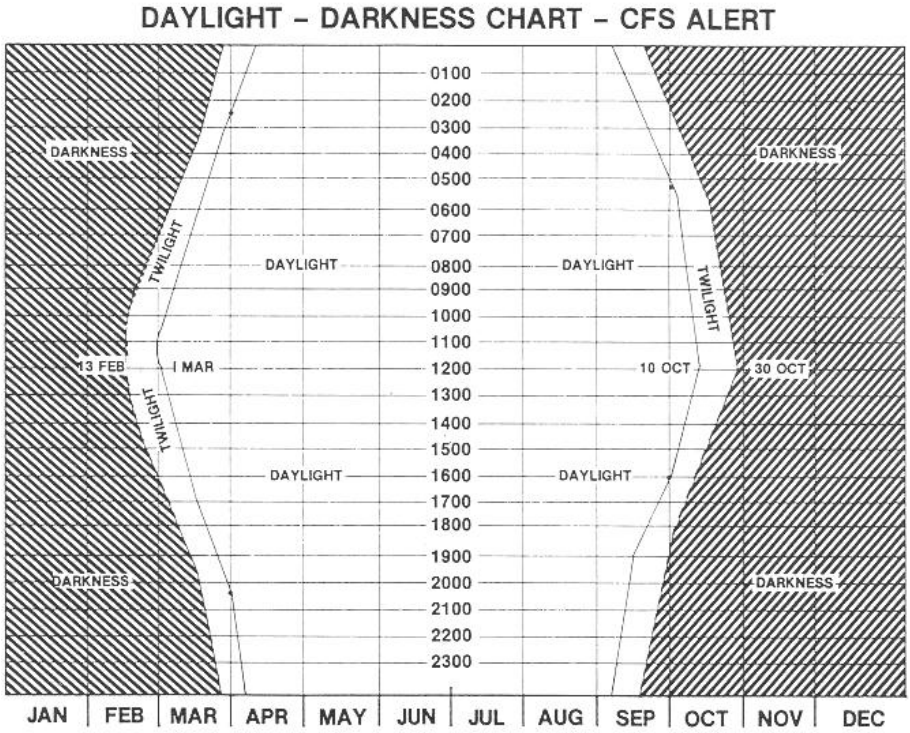

Figure 5.14: *Daylight/Darkness Chart for Alert*

5.2.1 Measurement Sites

Alert, Nunavut, Canada is a Canadian Forces military base and the world's northernmost climate and weather station. It is located at the northern end of Ellesmere Island in the Canadian Arctic at 82.5°N, 62.3°W. Figure 5.15 shows the North Pole region and the location of Alert. The surroundings of the measurement site are shown in Figure 5.16. MAX-DOAS measurements were performed at the Ice Camp (82°32'N, 62°43'W) on the Arctic Ocean sea ice surface just west of Williams Island in Black Cliffs Bay. The site was located in 7 km distance from the Alert base and about 9 km north of the GAW (Global Atmospheric Watch), SST (Special Studies Trailer) and FTX (Far Transmitter building) sites, where other experiments were located. MAX-DOAS measurements were performed using the instrument described in section 4.1. The viewing direction of the MAX-DOAS

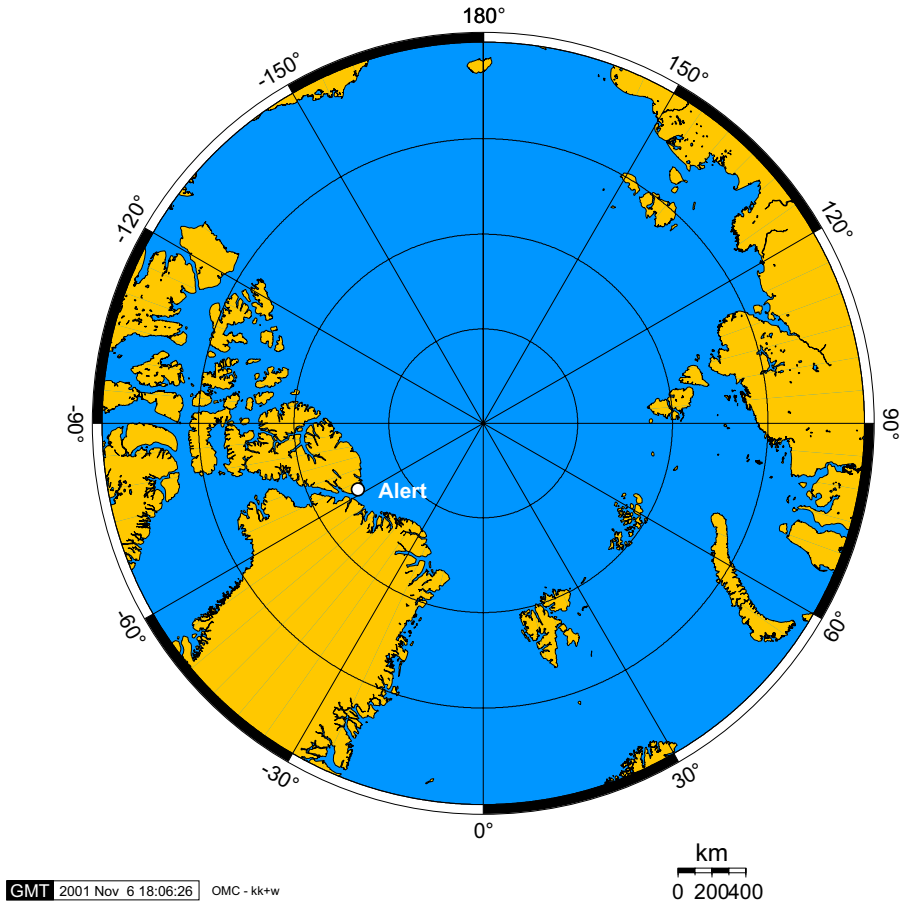

Figure 5.15: *Map of Alert and the North Polar Region: Alert is situated at the northern tip of Ellesmere Island at 82.5°N, in about 800 km distance from the North Pole.*

telescope was true north and the closest land shore was in a distance of 3 km perpendicular to the viewing direction (see Figure 5.16). The view towards the horizon was unobstructed due to the generally flat sea ice surface. The MAX-DOAS system operated at Alert received scattered (by Rayleigh and Mie scattering) and reflected sunlight from different elevation angles. It combined zenith measurements (elevation angle $\alpha = 90°$) with measurements at $\alpha = 60°$, 40°, 20°, 10° and 5° above the horizon. The MAX-DOAS receiving telescope could be automatically moved to point in these directions using a stepper motor drive. The setup of the MAX-DOAS telescope and stepper motor arrangement at the ice camp is shown in Figure 5.17.

5.2.2 Meteorological Parameters

An overview of the meteorological parameters (T, Wind, p) observed at the Global Atmospheric Watch (GAW) station and the climate station (cloud fraction and visibility) at

Figure 5.16: *Overview of the locations of the measurement sites during the ALERT2000 measurement campaign.*

Alert for the period of the DOAS measurements is shown in Figure 5.18. At the beginning of the study ambient temperatures ranged between -30°C and -20°C during a period of high pressure, low wind speeds and clear sky. On April 26, the weather changed suddenly when the wind changed to northerly direction at wind speeds of up to 10 m/s. Temperatures rose to values between -20°C and -13°C, the visibility decreased significantly and low clouds/blowing snow prevailed during the next 10 days associated with a low pressure system. The visibility and opacity data provide important information on associated changes

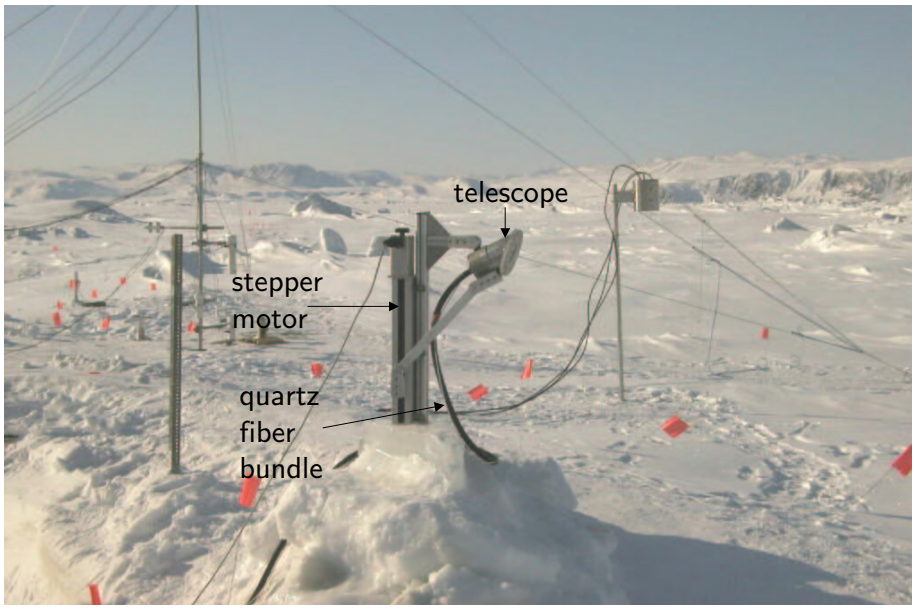

Figure 5.17: *Photograph of the MAX-DOAS setup at the Ice Camp near Alert. The small telescope could be turned to different elevation angles by a stepper motor. The light was transmitted to the spectrograph by the quartz fiber bundle.*

in the radiative transport which can strongly influence the MAX-DOAS measurements.

5.2.3 MAX-DOAS BrO Measurements

Continuous measurements of scattered sunlight were performed after polar sunrise from April 20 to May 9, 2000. In an automated measurement loop after each series of 10 spectra taken at 5° elevation one MAX-DOAS series including elevation angles of 10°, 20° and 90° was completed. Around midnight (SZA ϑ around 85°, relative azimuth angle <20°) a different loop taking MAX-DOAS series at 90°, 60° and 40° elevation was executed. During daytime this measurement program led to a time resolution of 5 minutes for the 5° geometry and 1 hour for the higher elevation angles, respectively. Besides BrO, ozone, NO_2 and O_4 absorptions were measured simultaneously in the same wavelength region. The spectra recorded in the wavelength range from 320 nm to 400 nm were analyzed for atmospheric trace gases by the DOAS fit (see section 3.1). As FRS (Fraunhofer reference spectrum, see section 3.2.2) a noontime atmospheric spectrum (from April 22, 2000, 15:44 UT, SZA=70°, SAA[8]=173°) taken at elevation angle $\alpha = 90°$ was used, where only minimum background trace gas absorption was present. In order to detect the BrO absorptions, reference spectra of NO_2, O_3 (221 K and 241 K), O_4, a Ring spectrum (see section 3.2.3), the FRS and the BrO reference spectrum were simultaneously fitted to the atmospheric

[8]**S**olar **A**zimuth **A**ngle, for the Alert measurements SAA and relative azimuth angle are identical because the telescope direction was true north

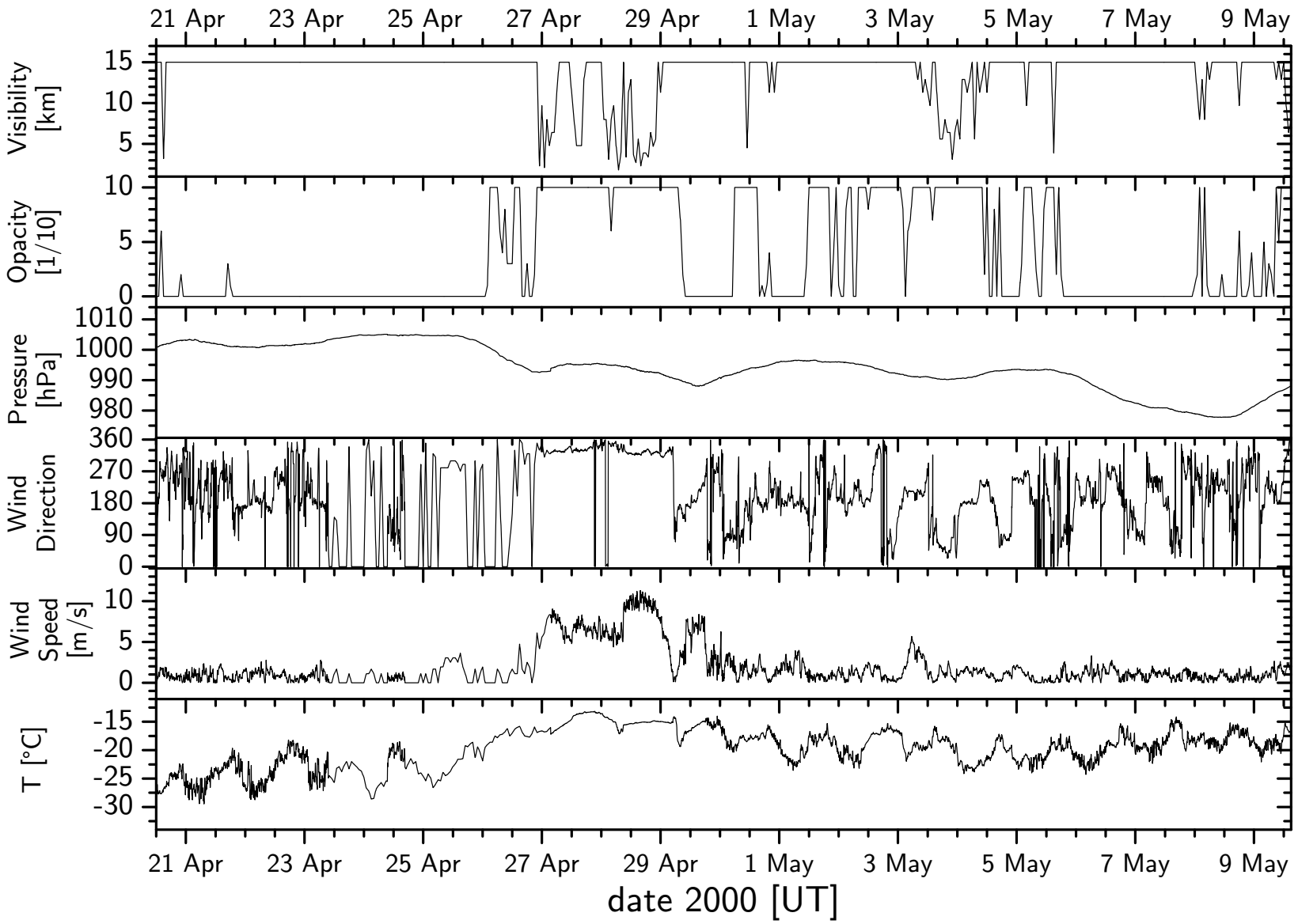

Figure 5.18: *Overview of the meteorological parameters temperature, wind speed, wind direction, pressure, opacity and visibility for the period of the DOAS measurements at Alert in April/May 2000.*

spectrum. A polynomial of 2^{nd} order was also included to remove broadband absorption structures and the effects of Rayleigh and Mie scattering. An example of the fit result for the spectral range from 346 nm to 359 nm as used for the BrO evaluation is shown in Figure 5.19.

The fit procedure yields differential slant column densities (dSCD) for the atmospheric absorbers (differential with respect to the FRS). The results for the fit coefficient of the Ring spectrum, the O_3 and NO_2 dSCDs and O_4 fit coefficients from this analysis are shown in Figure 5.20. For the mainly stratospheric absorbers O_3 and NO_2 the dSCD strongly resembles the behavior of the solar zenith angle ϑ (cf. upper part of Figure 5.21). The dSCD for these species depends on ϑ only, no significant difference for different elevation angles α can be found. Only a few single data points from the 5° elevation NO_2 series are significantly larger than the stratospheric background, indicating that local pollution was observed (possibly from the Alert base or the diesel power generator near the Ice Camp). In contrast, the absorption by O_4, which is abundant in the lower atmosphere[9], is almost independent of the solar zenith angle. Instead, large absorption is found for the lowest elevation angles, very small absorption for zenith observations. This proves the excellent sensitivity of MAX-DOAS for measurements in the low troposphere. Enhanced O_4 absorption is also found for high elevation angles between April 27 and April 29, 2000. During this period high wind speeds led to snowdrift in the surface layer at Alert and at the measurement site at the Ice Camp. In this low cloud/snowdrift layer near the ground of approximately 100 m vertical extent enhanced lightpaths due to multiple scattering and reflection resulted in generally higher O_4 absorption for all elevation angles. Additionally multiple scattering averaged (to a certain extent) the photon path distributions for the different elevation angles. However, the method still yields qualitatively correct results. The lightpath enhancement seen in the O_4 absorption is also visible for the fit coefficient of the Ring spectrum, which is proportional to the intensity of rotational Raman scattering. Since the rotational Raman scattered light is proportional to the slant column density of air molecules, it is also sensitive to light path enhancement. The low elevation angle measurements generally exhibit higher Raman scattered intensities than the zenith data. The 40° and 60° measurements were possibly influenced by direct sunlight received by the telescope (see below).

The complete time series of BrO dSCDs for all elevation angles is shown in Figure 5.21. On the first day of measurements (April 20) very small differences between the different geometries can be seen, the following two days show no difference between the data from different elevation angles, typical for BrO at higher altitudes. From April 24 small and after April 26 very large BrO values are found. For the small elevation angles, the highest BrO absorption is found. This is the typical behavior of an absorber in the boundary layer as seen above for O_4 and explained in section 3.5.2. On April 27, 2000 BrO slant column

[9]The O_2 dimers O_4 decrease vertically with a scale height of ≈4 km

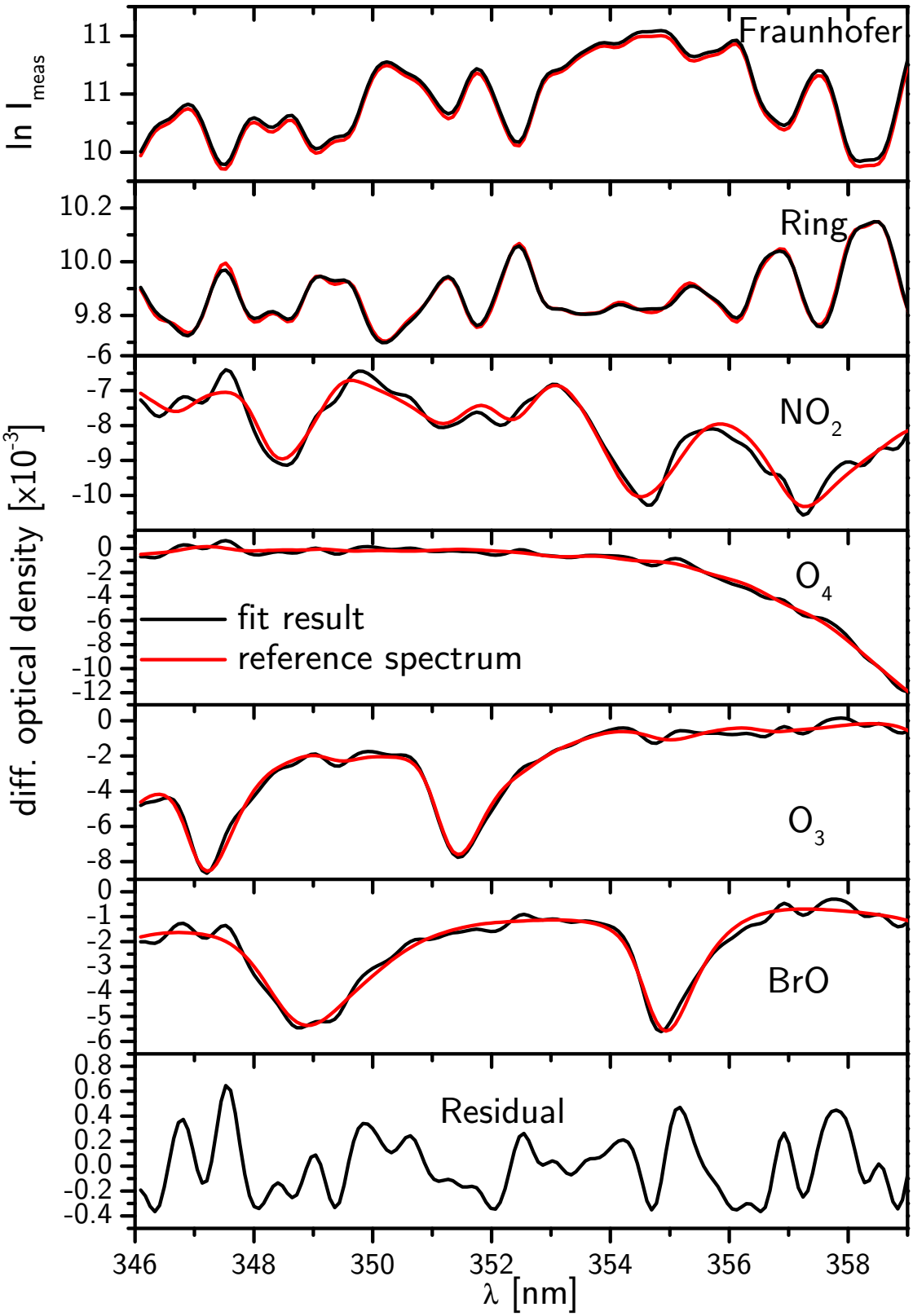

Figure 5.19: *Example of the BrO DOAS analysis applied to the UV spectra measured during ALERT2000. The black lines indicate the respective fit results after subtracting all other absorbers, the overlaid red lines are the scaled reference spectra. Typical residual structures left after subtracting all known absorptions were of the order of (0.5-2)×10^{-3}.*

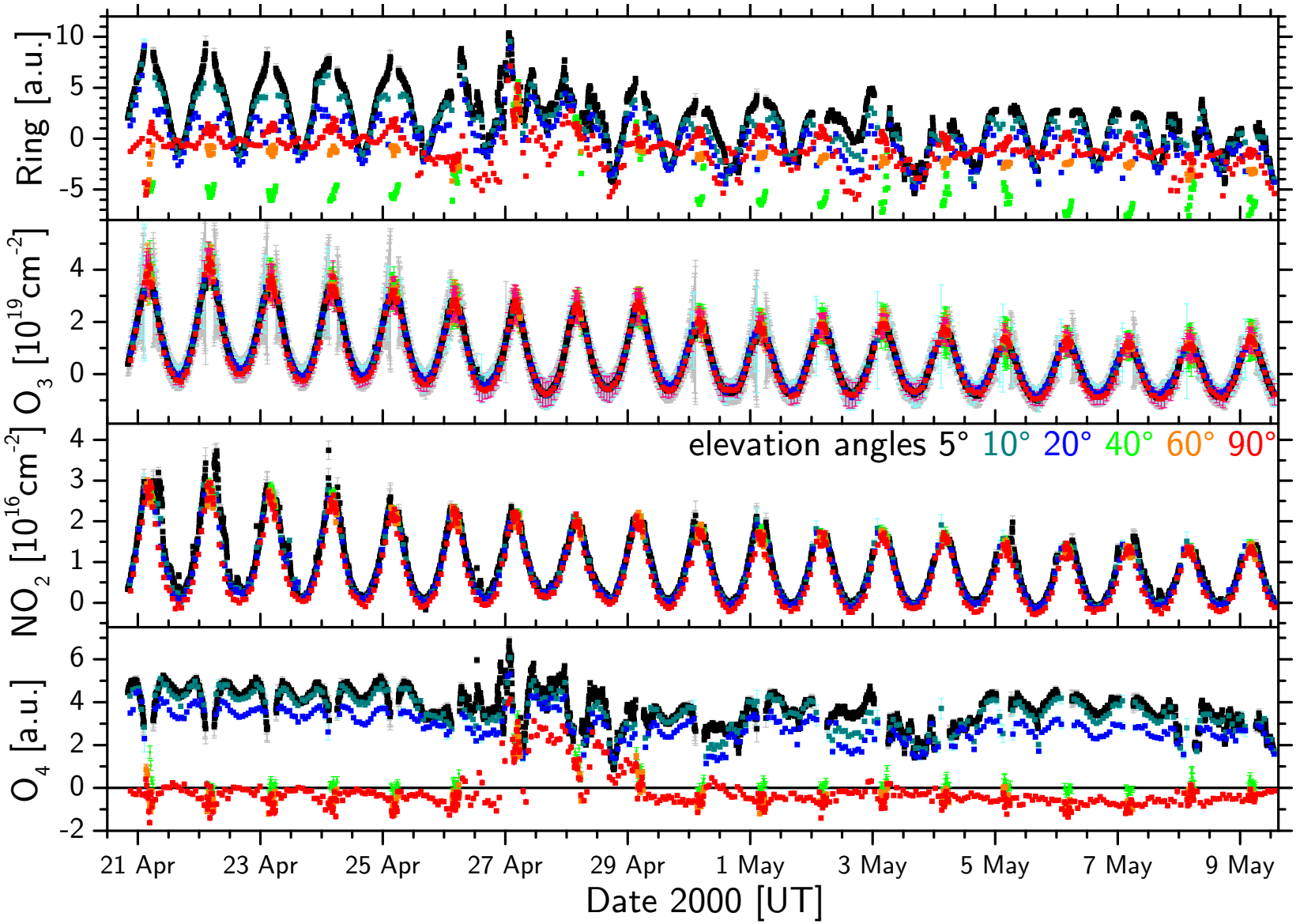

Figure 5.20: *DOAS fit results from the ALERT2000 BrO measurements. Shown are Ring fit coefficients as well as dSCDs of O_3 and NO_2 and the O_4 fit coefficients. Data from different elevation angles α are plotted in different colors.*

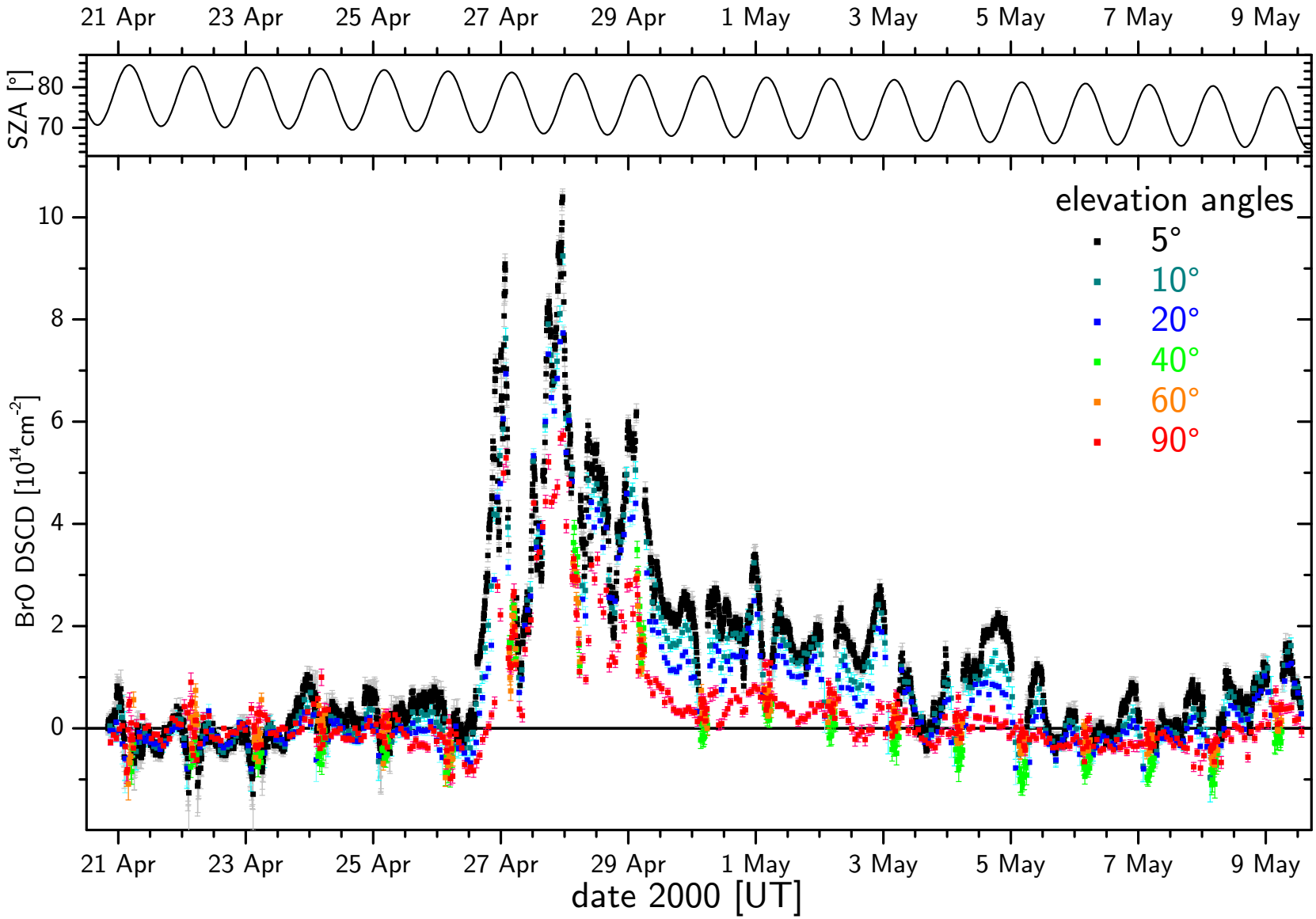

Figure 5.21: *DOAS analysis results from the ALERT2000 BrO measurements. Values corresponding to different elevation angles are plotted in different colors. Values generally increase for decreasing elevation angles. During the ozone depletion period after April 26 very high BrO dSCDs were observed.*

densities of more than 10^{15}molec/cm^2 were observed. Until the end of the campaign BrO SCDs remained elevated, only on May 3 and from May 6 to 7 BrO absorption approached the baseline for all geometries.
As already mentioned above for the Ring effect, the 40° and 60° elevation angle measurements around midnight were probably again influenced by a significant amount of direct or quasi-direct sunlight (see also section 5.1.1) received by the MAX-DOAS telescope. Here, the zenith measurements were not affected because of the high solar zenith angle of ≈85° around midnight. Therefore the 40° and 60° data will not be included in further analysis.

5.2.4 MAX-DOAS IO Measurements

From the afternoon of May 1 until the end of the measurements on May 9, 2000, spectra were also recorded in the wavelength range from 359 nm to 439 nm. After each MAX-DOAS series in the UV spectral range (see section 5.2.3), spectra were taken in the blue wavelength region at α=90° and 5°. In the wavelength range from 400 nm to 439 nm absorption by iodine oxide radicals (IO) could be analyzed. Besides IO only NO_2, Fraunhofer and Ring reference spectra and a 3^{rd} order polynomial were fitted to the atmospheric spectra. In order to identify IO in the arctic boundary layer, the 5° elevation spectra were always evaluated using the previous 90° spectrum as reference spectrum. Thus ΔSCD values with

$$\Delta\text{SCD} = \text{SCD}_{\alpha=5^\circ} - \text{SCD}_{\alpha=90^\circ}$$

could be derived. The IO ΔSCD time series is shown in Figure 5.22. Most IO data points range below the detection limit defined by twice the measurement error and indicated as red line in Figure 5.22. However, there are many values near and several also above the detection limit. To show how IO absorption structures were identified in the atmospheric spectra, a sample evaluation for May 6, 2000 21:06UT at ϑ=71° is given in Figure 5.23. The IO column density found in this case was $(1.9\pm0.6)\cdot10^{13}$molec/cm^2. Assuming the IO to be homogeneously distributed in a 1 km surface layer, this slant column corresponds to a mixing ratio of (0.73±0.23) ppt.

5.2.5 Ozone Measurements during ALERT2000

Since the main objective of the Polar Sunrise Experiments at Alert is to study the physical and chemical processes involved in Arctic boundary layer ozone depletion, a comprehensive set of ozone measurements was collected during the ALERT2000 field study. The surface ozone reference data set from the Global Atmospheric Watch (GAW) station, Alert is shown in Figure 5.24 together with the DOAS BrO data measured at the Ice Camp. Both species are clearly anti-correlated which was expected from previous measurements (see section 2.2). Detailed results will be presented in section 6.3. The vertical profile of ozone was also studied in detail during ALERT2000. Twice daily ozone sonde measurements were

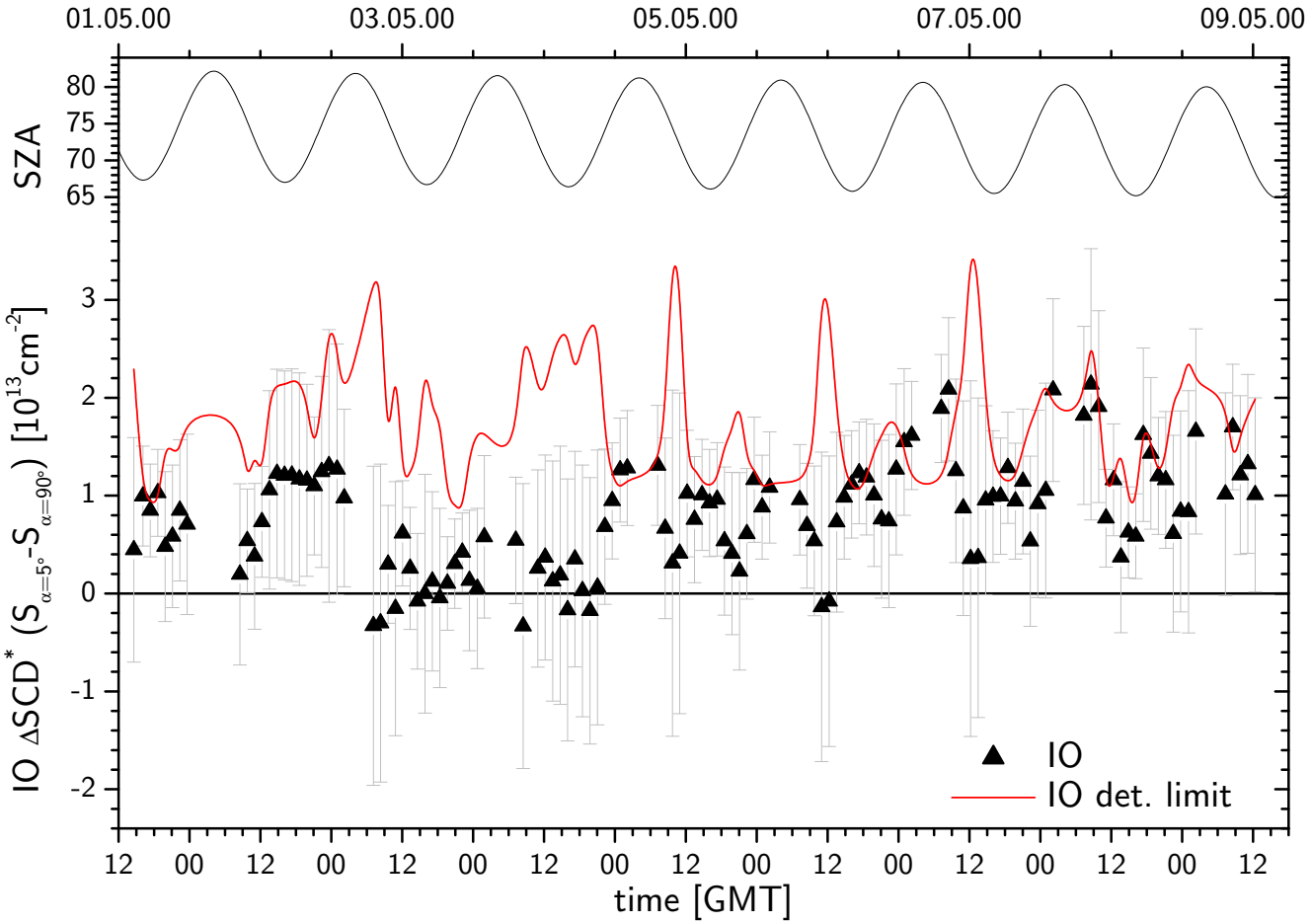

Figure 5.22: *Time series of the IO ΔSCD during Alert2000. The red line indicates the detection limit defined by twice the 1σ error.*

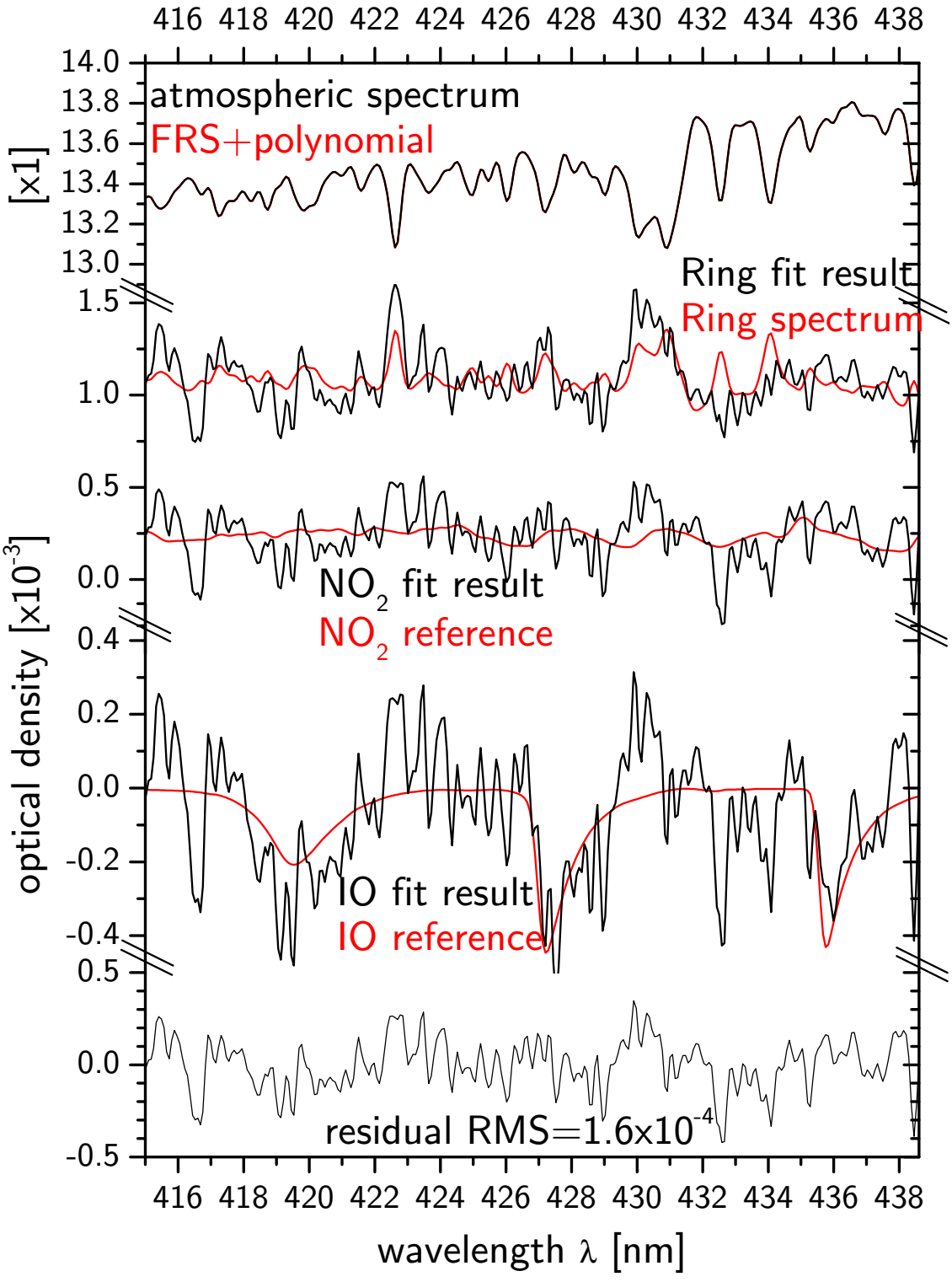

Figure 5.23: *Sample evaluation of Iodine Oxide for May 6, 2000 at 21:06UT and a local SZA of 71°. Note, that the IO scale is expanded by a factor of 2 compared to the other optical densities. The Peak-to-Peak residual structure (bottom trace) is* $8{\cdot}10^{-4}$.

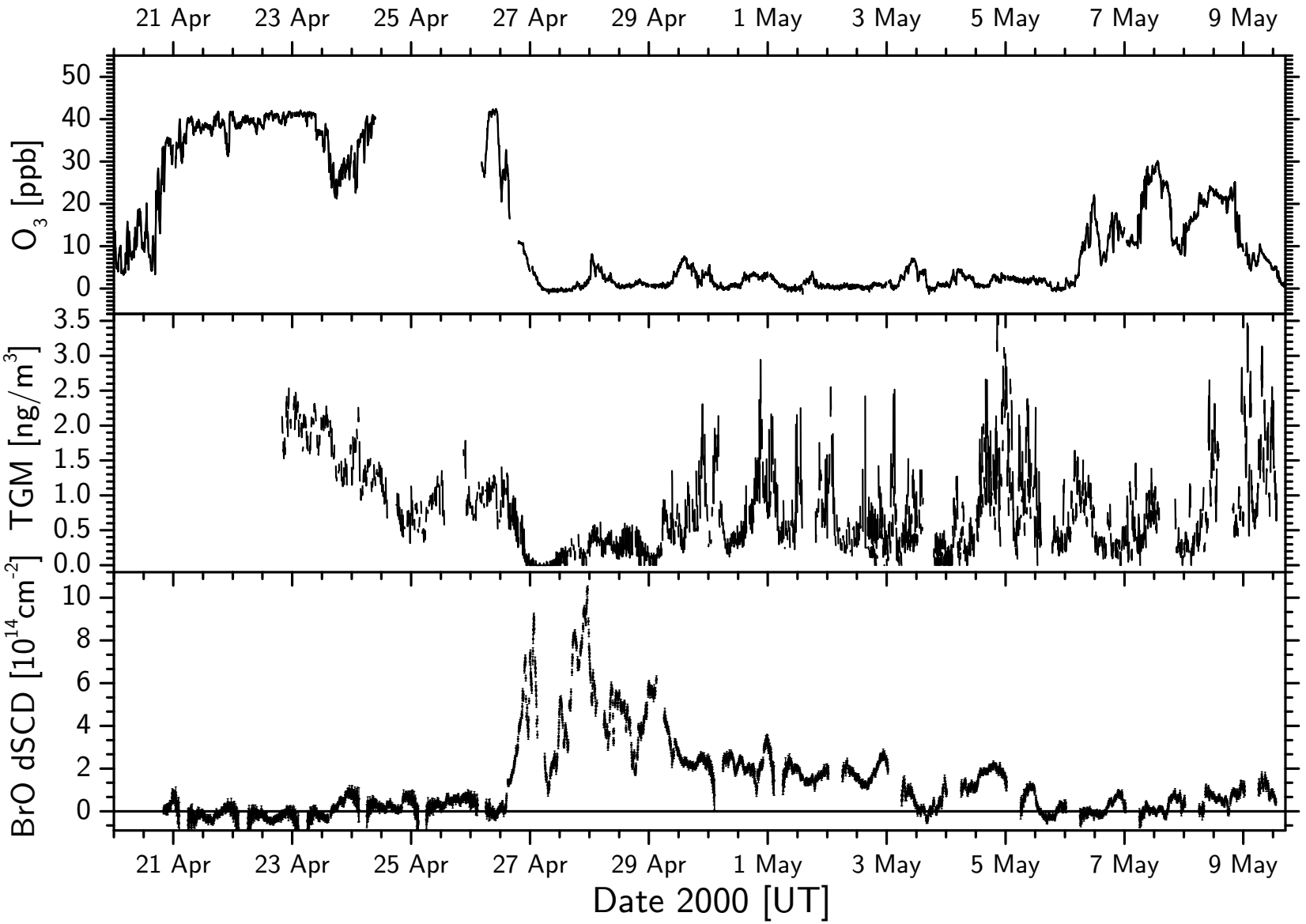

Figure 5.24: *Top: Time series of the surface ozone mixing ratios during ALERT2000. The measurements were taken at the Global Atmospheric Watch (GAW) station. Middle: Time series of TGM (total gaseous mercury) during ALERT2000. The measurements were taken at the Ice Camp. Mercury data kindly provided by Steffen et al. [2002] Alert. Bottom: DOAS BrO data, only the 5° elevation measurements are shown.*

performed by *Bottenheim et al.* [2002]. In Figure 5.25 a contour plot of the vertical profile of tropospheric ozone during ALERT2000 as a function of time is shown. Additionally, several height profiles for the lowest 1000 m were recorded at the Ice Camp using a tethered balloon [*Bottenheim et al.* 2001]. The blue regions indicating ozone depletion are always

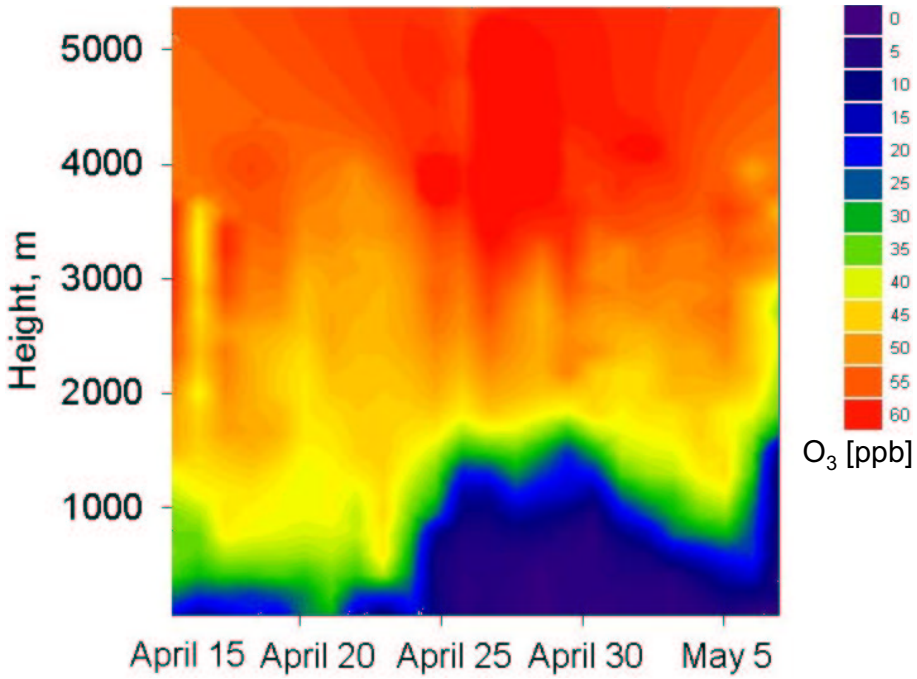

Figure 5.25: *Vertical distribution of the ozone mixing ratio during ALERT2000. Contour plot produced by J.W. Bottenheim, MSC, Environment Canada.*

at the ground, extending to heights between 500 m and 1.5 km.

5.2.6 Mercury Measurements during ALERT2000

To monitor the mercury depletion episodes during polar spring (see section 2.5), atmospheric mercury concentrations were measured at 3 different sites using commercial Tekran® mercury analyzers for total gaseous mercury (TGM) and different filter packs to collect total particulate mercury (TPM). The time series of TGM measured by *Steffen et al.* [2002] at the Ice Camp is shown in Figure 5.24. The behavior of gas phase mercury for the beginning of the ozone depletion strongly resembles the one of ozone. However, later during the complete ozone loss period Hg shows a correlation with solar radiation, which might be due to re-emission of Hg^0 from the snow or aerosol to the gas phase (see also section 6.3). The mass concentrations given for Hg (in ng/m^3) can be converted to volume mixing ratios (in ppt) by multiplication with the factor $0.115\,ppt{\cdot}m^3/ng$ for the temperature and pressure levels at Alert. Maximum Hg mixing ratios therefore range between 0.2 and 0.3 ppt.

5.3 LP-DOAS Measurements during the Crete2000 Field Campaign at Finokalia

In July and August 2000, a 4 week intensive field study was carried out within the ELCID project (see also section 5.1.2 and 5.4) to study the oxidants of dimethylsulfide (DMS) in the moderately polluted Mediterranean atmosphere. As pointed out in section 2.3.3 halogen oxides (especially BrO) can be an important sink for DMS.

5.3.1 Measurement Site

Finokalia (35°19'N, 25°40'E, altitude ~130 m above sea level) is a coastal remote site 70 km eastward of Heraklion on the Greek island Crete in the Mediterranean Sea. It is located at the top of a hilly elevation facing the sea within the sector of 270° to 90°. Depending on the weather conditions the air masses reaching the station originate from Europe or Africa.

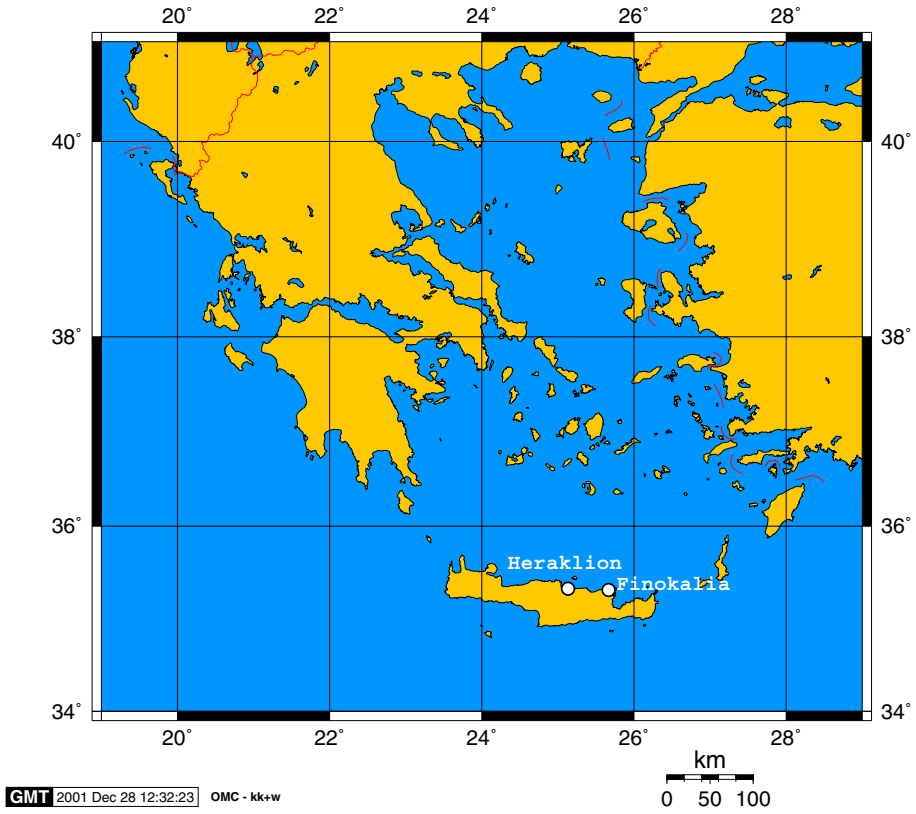

Figure 5.26: *Finokalia is located 70 km east of Heraklion at the northern coast of the Greek island Crete in the eastern Mediterranean Sea.*

5.3.2 Meteorological Parameters

The meteorological parameters obtained during the Crete2000 field campaign at the Finokalia measurement site are shown in Figure 5.27. Typical temperatures at Crete ranged

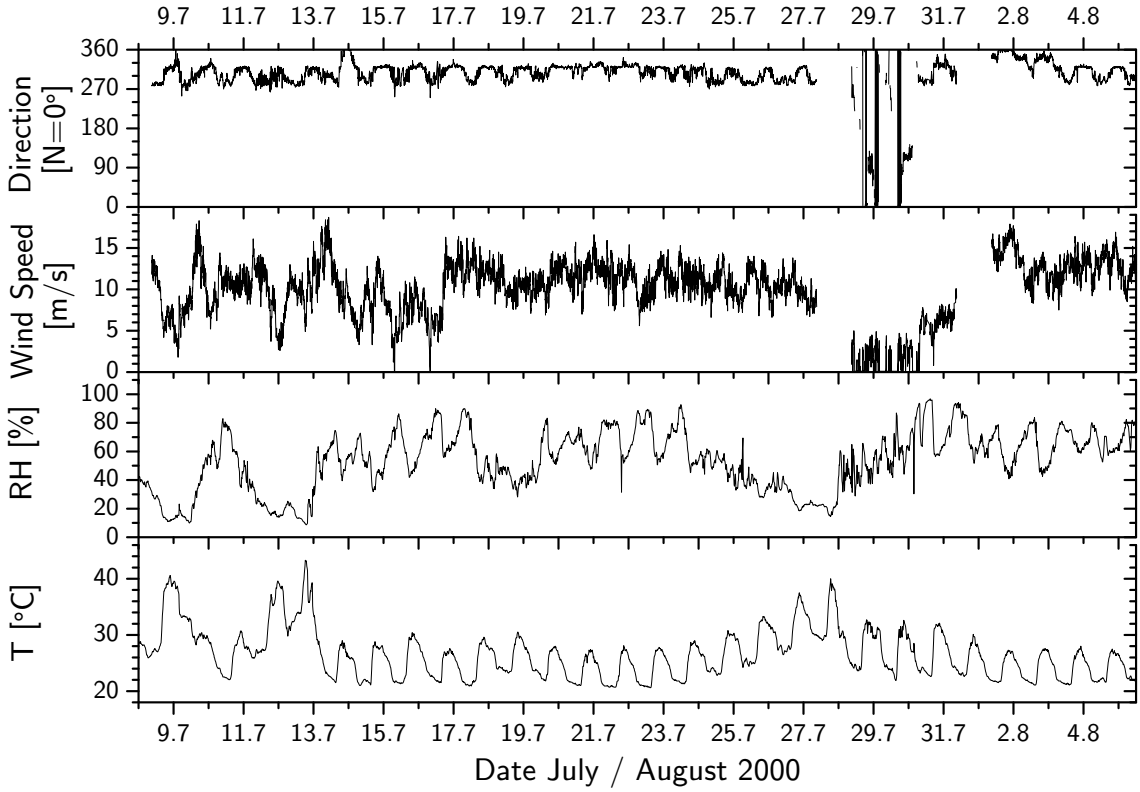

Figure 5.27: *Temperature, relative humidity, wind speed and wind direction time series for the period of the DOAS measurements at Finokalia, Crete.*

between 20°C at night and 30°C during noontime, with occasional peaks up to 40°C. During the dry summer months on Crete the relative humidity was as low as 10%, reaching 90% only during a few nights. Winds were from the northwest during almost the complete period of the measurements, light winds from southeasterly directions were observed only on 2 days. The frequency distribution of the wind direction is illustrated in Figure 5.28.

5.3.3 Active LP-DOAS BrO, IO, OIO Measurements

From July 8 to August 7, 2000 active long path DOAS measurements were performed at Finokalia. The used LP-DOAS instrument is described in section 4.2. Two light paths were set up, with one retro reflector array in a distance of 8.16 km and one for hazy conditions in a distance of 5.18 km. The reflectors were set up at 10-20 m above sea level, therefore the measurements yielded concentrations vertically averaged for the lower 150 m

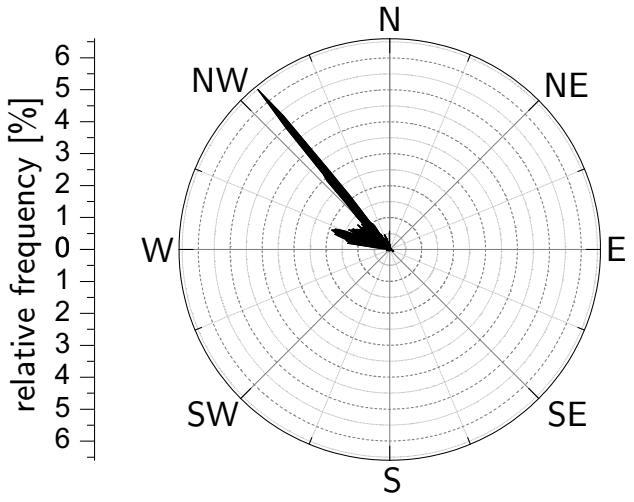

Figure 5.28: *Relative frequency distribution of the wind direction during the DOAS measurements at Finokalia, Crete, in intervals of 1°.*

of the marine boundary layer at the north coast of Crete. Figure 5.29 shows the view from the DOAS instrument at the Finokalia site in the direction of the lightpaths along the coastline. In the continuous measurement loop for the DOAS instrument at Finokalia,

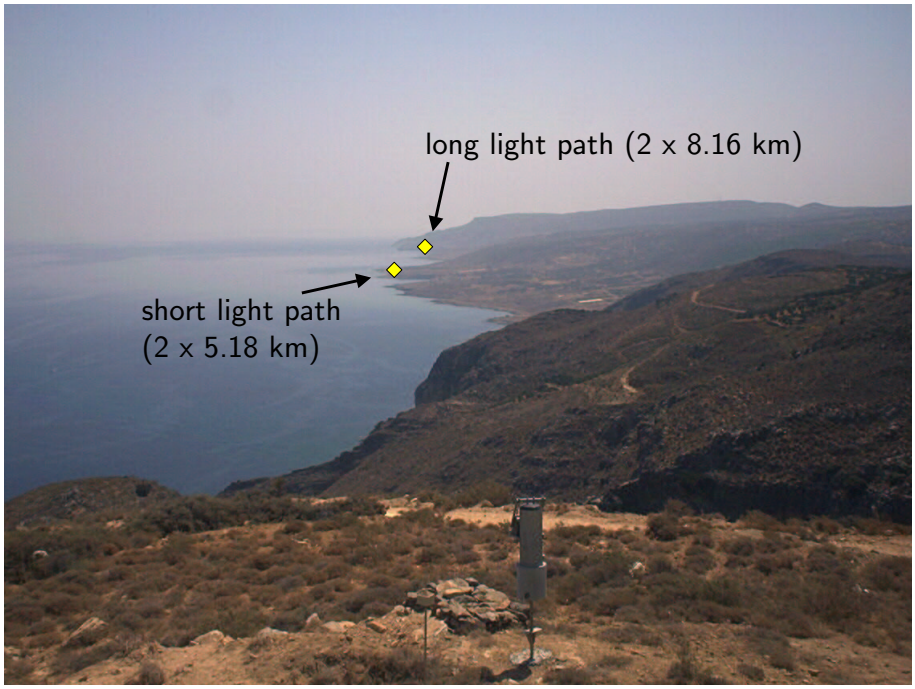

Figure 5.29: *View from the DOAS instruments at the Finokalia measurement site in the direction of the DOAS lightpaths along the coast.*

atmospheric absorption spectra were taken in the UV (295 nm - 375 nm), blue (390 nm - 470 nm) and green (510 nm - 590 nm) spectral ranges, where the halogen oxides BrO, IO and OIO exhibit high differential absorption cross sections. The analysis for the halogen

oxides was carried out according to the procedure described in section 3.1.2. The data obtained for the halogen oxides is shown in Figure 5.30 together with the simultaneously measured ozone mixing ratios. During the complete 1 month measurement period the halogen oxides remained below their respective detection limits given in Table 5.1.

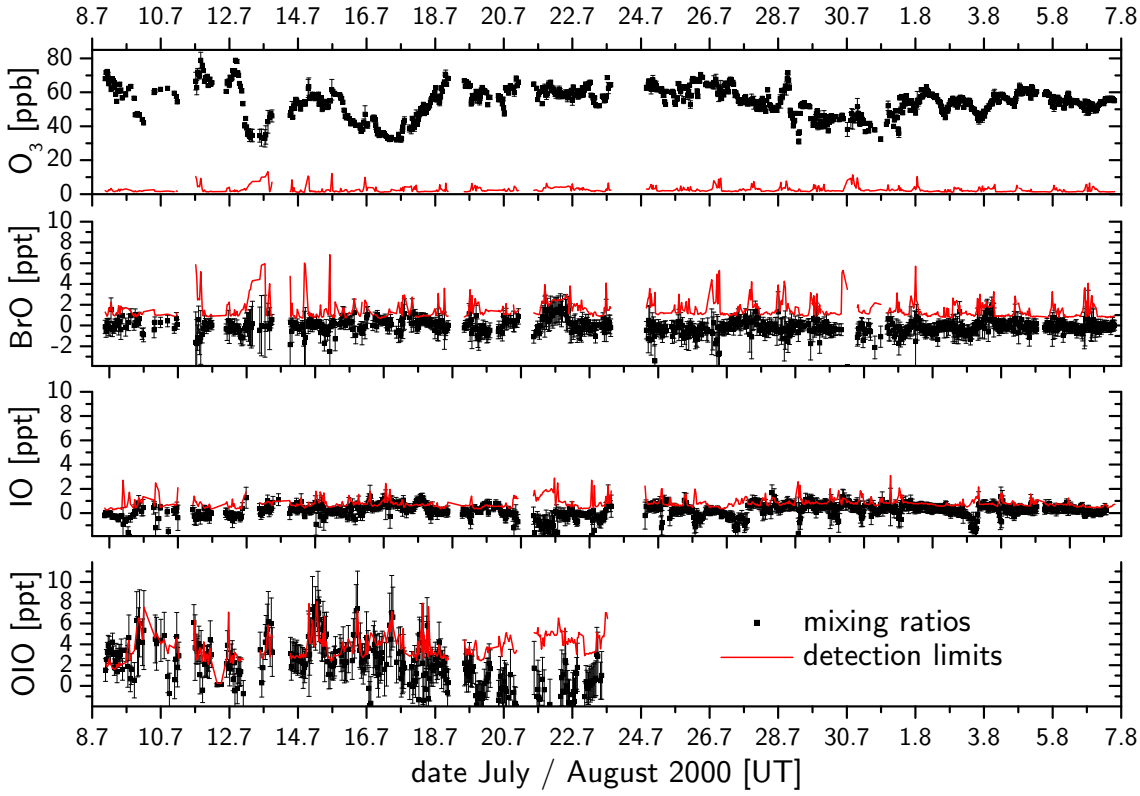

Figure 5.30: *Results of the measurements of O_3, BrO, IO and OIO. While ozone mixing ratios ranged between 40 ppb and 80 ppb, the halogen oxides always remained below their respective detection limits (red lines).*

Species	average detection limit [ppt]	minimum detection limit [ppt]
BrO	1.5	0.7
IO	0.8	0.25
OIO[a]	4	1.6

[a] for OIO the cross section reported by *Bloss et al.* [2001] was used. However, other data by *Ingham et al.* [2000] suggest a value 2.5 times higher. This would result in all OIO mixing ratios to be divided by 2.5

Table 5.1: *Detection limits of the investigated halogen oxides at Finokalia on Crete during July/August 2000. Since no halogen oxides were found above the detection limit, these values can be considered as upper limits of the atmospheric mixing ratios.*

5.3.4 Nitrogen Compounds at Finokalia

Because of their influence on the halogen chemistry in the marine boundary layer, DOAS data of nitrogen species will also be shown here. In the UV spectral range absorption by NO_2 and nitrous acid (HONO) were evaluated. NO_2 was also measured in the blue and green wavelength range. Measurements in the spectral range from 605 nm to 680 nm, where the nitrate radical (NO_3) has its strongest absorption bands, were taken daily from the late afternoon overnight until the morning and around noon for additional daytime reference spectra. An overview of all the nitrogen species measured with the LP-DOAS system is given in Figure 5.31. Ozone mixing ratios are also shown for comparison. From

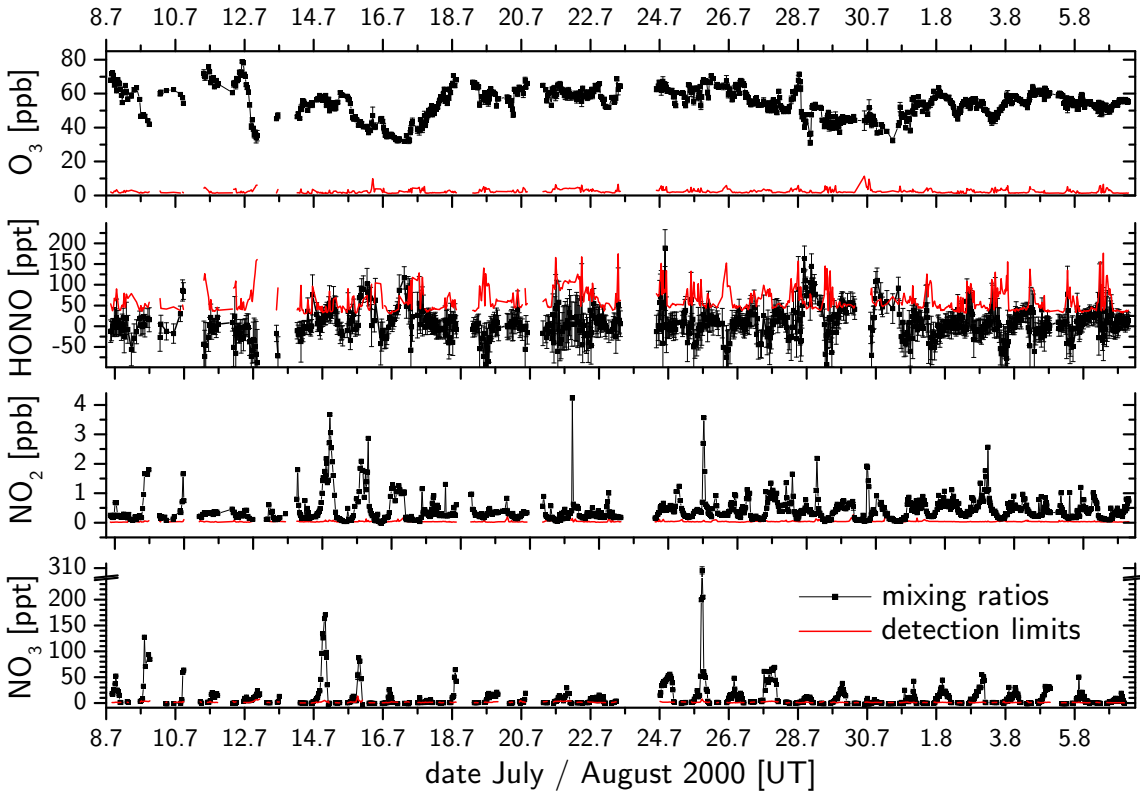

Figure 5.31: *Overview of all nitrogen compounds measured by the LP-DOAS system. Nitrous acid (HONO), nitrogen dioxide (NO_2) and nitrate radicals (NO_3) mixing ratios (data points) and their respective detection limits (red lines) are shown. Also included is the ozone time series (top).*

the NO_2 time series it can be seen that Finokalia is a moderately polluted marine site, in some nights NO_2 values reached 3-4 ppb. The mean value was 0.5 ppb over the complete measurement period, minimum values scattered around ≈100 ppt. Nitrous acid (HONO), an important nighttime compound in the urban atmosphere (see e.g. [*Alicke* 2000]) was below the detection limit of 60 ppt on average. During several nights when the flow was

from the west (air masses influenced from Heraklion, which is located 70 km to the west), HONO rose above the detection limit to values up to 100-150 ppt. Nitrate radical mixing ratios increased to values between 10 and 20 ppt during most nights, at sunrise NO_3 was quickly photolyzed due to its short photolytic lifetime of ~1 s during daytime. In several nights very high NO_3 of more than 100 ppt and in one night up to 310 ppt of NO_3 were observed. The corresponding atmospheric spectrum and the NO_3 DOAS fit results are shown in Figure 5.32.

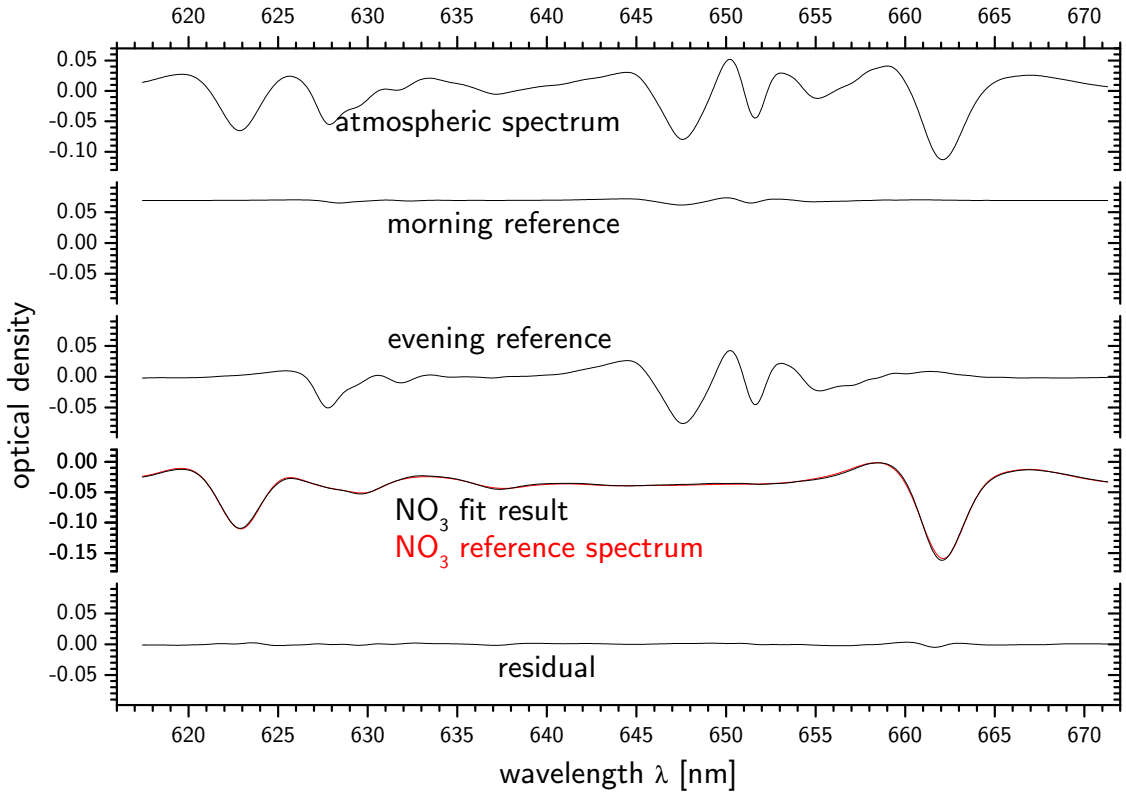

Figure 5.32: *Atmospheric spectrum in the red spectral region taken at Finokalia on July 25, 2000 at 23:27UT. Two daytime reference spectra, where no NO_3 absorption is present were included in the analysis and subtracted from the atmospheric spectrum. The 4^{th} trace shows the atmospheric spectrum after subtracting the daytime spectra, thus eliminating the strong water absorption between 623 nm and 660 nm. The result is perfectly described by an NO_3 reference spectrum scaled to show absorption of 310 ppt NO_3. The residual after the fit (lowest trace) results in an error of ±4 ppt for NO_3 in this case.*

5.4 LP-DOAS and MAX-DOAS Measurements at Kuujjuarapik, Hudson Bay, Canada

During April/May 2001, a 3 1/2 week intensive field campaign was carried out in the framework of the ELCID project (see also section 5.1.2 and 5.3) to investigate the role of bromine oxide as oxidant of DMS in the lower Arctic. The measurement location at the east coast of Hudson Bay was chosen also to prove the high tropospheric bromine oxide levels observed by the GOME satellite instrument (see section 2.3 [*Richter et al.* 1998; *Wagner et al.* 2001]).

5.4.1 Measurement Site

Kuujjuarapik, Nunavik, Quebec, Canada is located at the south east coast of Hudson Bay at 55.31°N, 77.75°W. Besides its official Inuit name the small village can also be found as Poste-de-la-Baleine (French), Great Whale River (English) or Whapmagoostui (Cree Indian) on different maps. For an overview map of the Hudson Bay region and the surrounding Canadian low Arctic see Figure 5.33. Kuujjuarapik is a small settlement of 1200 inhabitants, there is no local industry but some pollution from the local community power plant is possible. The airport is frequented by two small aircraft per day. The DOAS instruments were set up in a container about 2 km north of the village on a hillock to allow an unobstructed view towards the Bill of Portland Islands just off the coast where the main retro reflector array was set up. The long lightpath used for the LP-DOAS was 2×7.6 km across the ice-covered Hudson Bay at an average height of 30 m above the sea ice surface. In case of low visibility due to snowdrift, haze or rain the short lightpath to a retro reflector array in 1.95 km distance along the shore (2×1.95 km=3.9 km total lightpath) was used instead. For the first parallel measurements of LP-DOAS and MAX-DOAS simultaneous measurements with a ground-based MAX-DOAS were performed. The MAX-DOAS telescope received light from direction north at different elevation angles above the horizon as well as from zenith direction in a sequential mode. A detailed comparison of both measurement techniques and results will be given in section 6.5.4.

5.4.2 Meteorological Parameters

An overview of the meteorological parameters (T, Wind, p, RH, visibility) observed at the Centre d'études nordiques (CEN) weather station (T, Wind, RH) and the local climate station (p, visibility) at Kuujjuarapik covering the time period of the DOAS measurements is shown in Figure 5.35. The measurements during the field study were strongly influenced by the local and synoptic scale weather conditions, that can be seen in Figure 5.35. At the beginning of the study associated with generally high pressure ambient temperatures ranged between -20°C and near 0°C, prevailing winds were from the north and northwest,

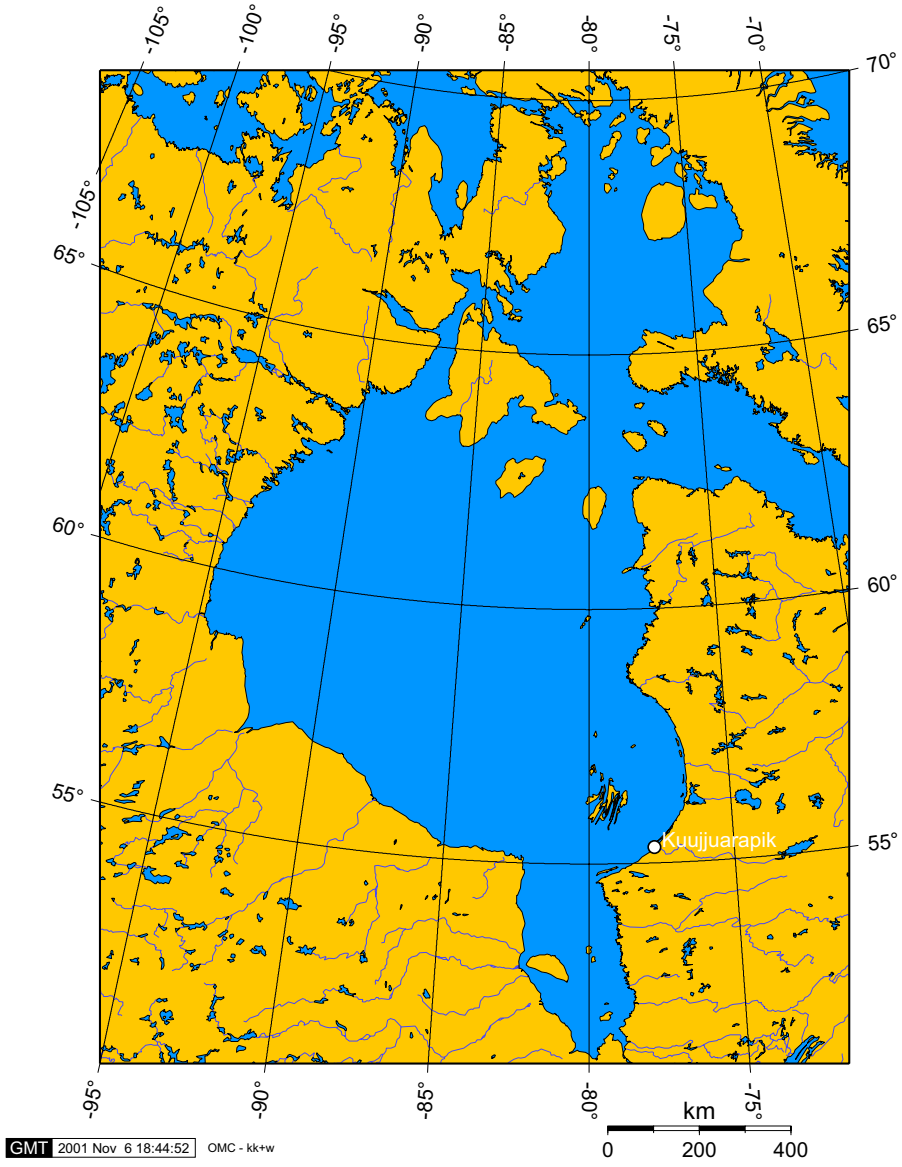

Figure 5.33: *Map of the Hudson Bay Region: Kuujjuarapik (55.31°N, 77.75°W) is situated at the south east coast of Hudson Bay.*

so arctic air masses reaching the site have travelled a long way over Hudson Bay. During the middle and the end of the measurement period low pressure systems usually associated with southerly and easterly winds led to warmer temperatures up to 20°C and continental air masses reaching the site. The frequency distribution of the local wind direction at Kuujjuarapik during the measurement period is shown as polar diagram in Figure 5.36. The visibility data in Figure 5.35 provides important information on several snowdrift episodes encountered during the measurements.

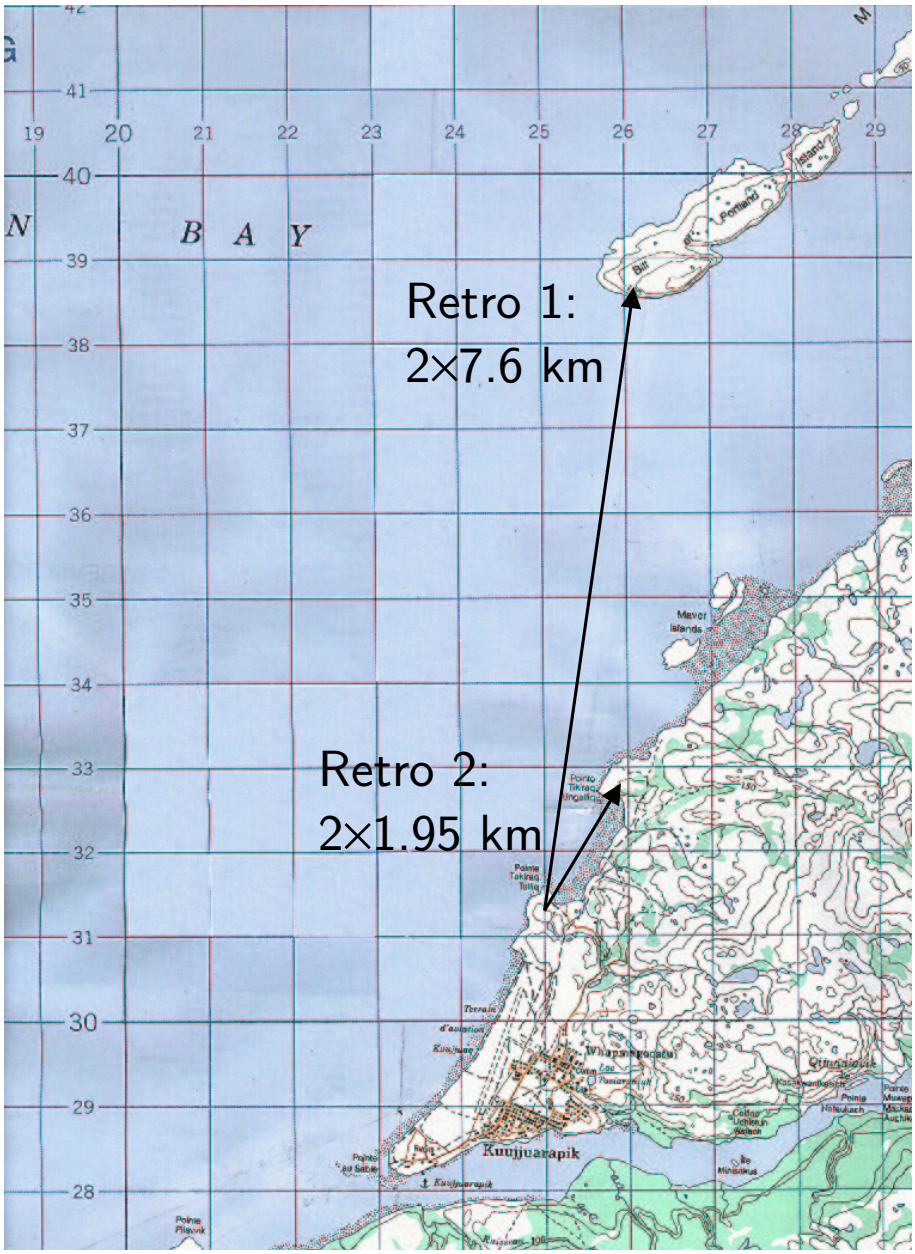

Figure 5.34: *Topography and Lightpaths at Kuujjuarapik, Hudson Bay*

5.4.3 First LP-DOAS Measurements at the Hudson Bay

Active long path DOAS measurements were performed between April 15 and May 8, 2001 from the DOAS container located ≈ 2 km north of Kuujjuarapik. The employed LP-DOAS instrument is described in section 4.2. The continuous measurement loop for the LP-DOAS instrument recorded atmospheric absorption spectra in the UV (295 nm - 375 nm), blue (390 nm - 470 nm) and green (510 nm - 590 nm) spectral ranges. These are the spectral

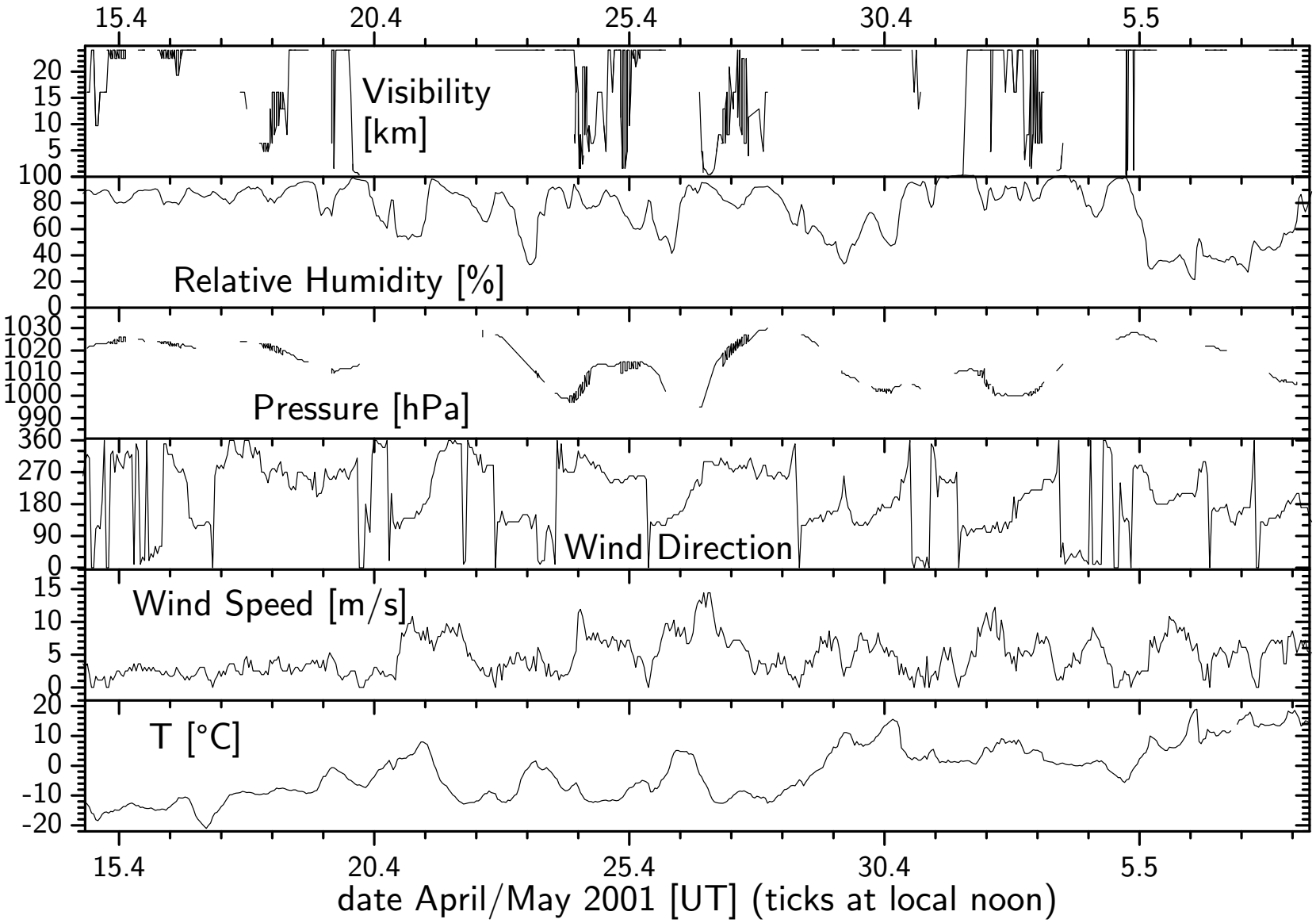

Figure 5.35: *Overview of the meteorological parameters temperature, wind speed, wind direction, pressure, relative humidity and visibility for the period of the DOAS measurements at Kuujjuarapik, Hudson Bay, in April/May 2001.*

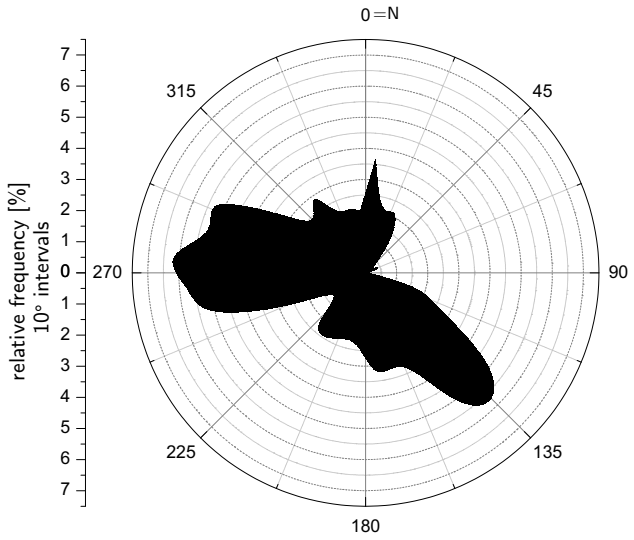

Figure 5.36: *Relative frequency distribution of the wind direction during the DOAS measurements at Kuujjuarapik, Hudson Bay in 10° intervals.*

intervals, where the halogen oxides BrO, OClO, OBrO, IO and OIO have their highest differential absorption cross sections. For solar zenith angles larger than 80° also spectra in the red spectral region (605 nm - 680 nm) were taken to measure NO_3 radicals. Spectra were taken from the long light path, only during periods of low visibility the short light path was used instead. Since the probed atmospheric column was smaller by a factor of ∼4, the measurement errors and detection limits were ∼4 times higher for the short light path compared to the long one. The DOAS fit for the halogen oxides and other trace gases was performed according to the analysis procedure described in section 3.1.2.

Bromine Oxide and Ozone Data

Atmospheric spectra in the UV spectral range were analyzed for O_3 and BrO absorption in the wavelength interval between 312 nm and 357 nm. This interval contains the 10 strongest absorption bands (4-0 to 13-0) of the $A^2\Pi_{3/2} \leftarrow X^2\Pi_{3/2}$ transition of the BrO radical. An example showing the fit results of the LP-DOAS evaluation for O_3 and BrO is shown in Figure 3.4 in section 3.1.7. The time series of BrO and ozone during the Hudson Bay measurements is shown in Figure 5.37. Until the end of April several events of high BrO mixing ratios reaching 30 ppt were observed, correlated to sudden drops in the ozone mixing ratio from background levels between 40 and 50 ppb to 30 ppb and in several cases to less than 20 ppb. Strong winds and snowdrift frequently prohibited LP-DOAS measurements in the beginning of the campaign, especially during several BrO events. Sometimes very low visibility of less than 100 m did not even allow measurements on the short lightpath. In the night from April 26 to April 27, 2001 ozone was almost completely depleted. During this night the visibility was less than 1 km (see visibility data in Figure 5.35 for 27.04.01 00:00-12:00UT) and wind speeds of 15 m/s led to drifting snow. DOAS measurements were possible only until a solar zenith angle of 98.5 °, when BrO had reached

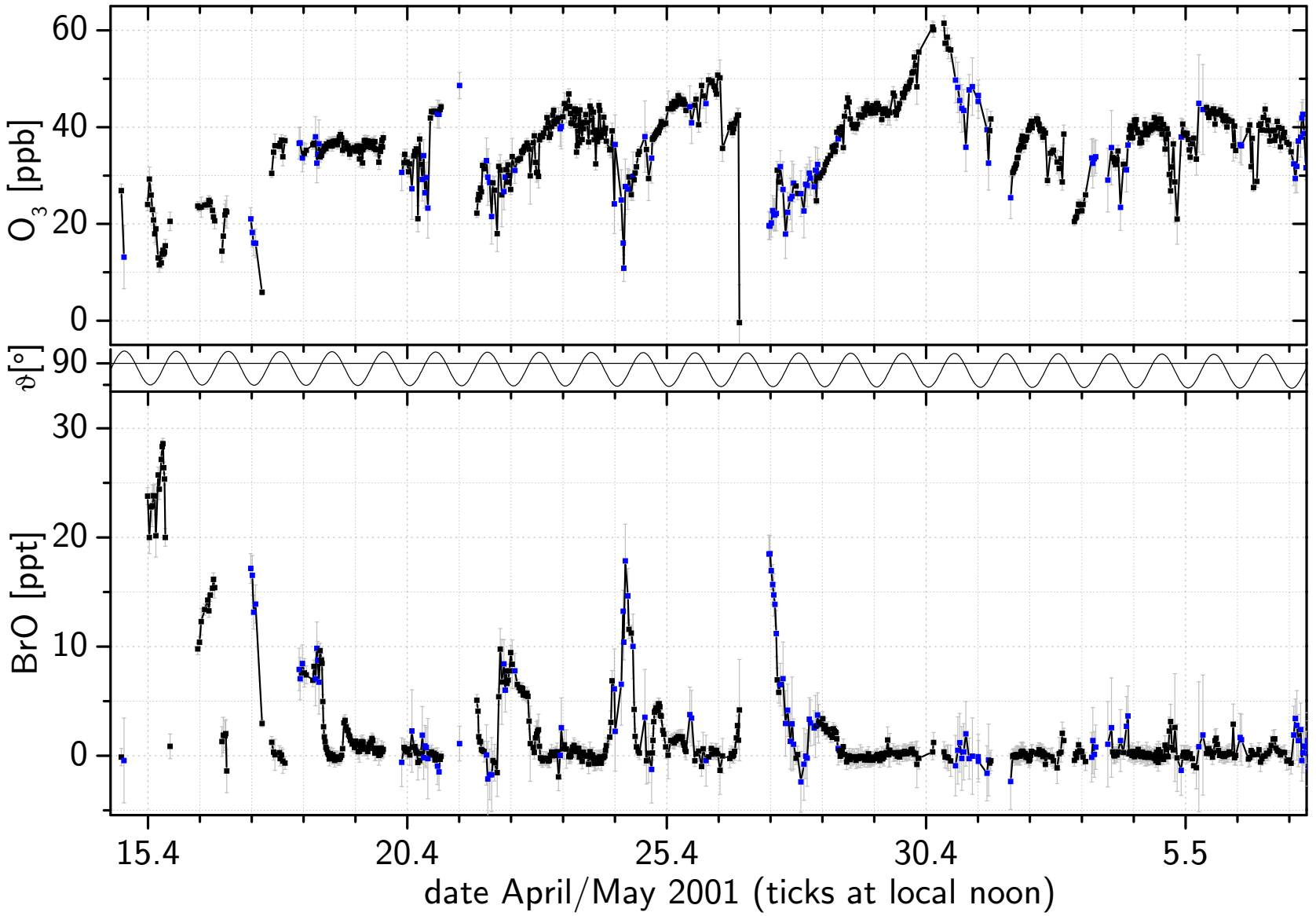

Figure 5.37: *Time series of the first LP-DOAS Measurements of Bromine Oxide radicals at Kuujjuarapik, Hudson Bay. Besides BrO mixing ratios the DOAS data for ozone and the solar zenith angle ϑ are shown. Measurements during low visibility conditions taken on the short lightpath are indicated as blue data points.*

4 ppt.
From the beginning of May on BrO mixing ratios always remained below 5 ppt. However, still small events of halogen activation with BrO mixing ratios of 2-3 ppt and small ozone losses were observed before sunrise on May 3 and May 5, 2001. These measurements represent the first ground-based DOAS measurements of bromine oxide at Hudson Bay. The observation of nighttime BrO (SZA=97°) is also reported for the first time here.

Other Halogen Oxides

In the UV spectral range, besides BrO also OClO has strong absorption features. Therefore OClO was also included in the DOAS fit for BrO. However, including OClO in the BrO fit did not yield any significant absorptions attributed to OClO. Therefore, the evaluation of OClO was optimized by narrowing down the fit interval to the range 331.5 nm to 354 nm, which contains only the three strongest UV absorption bands of the OClO molecule for the best signal to noise ratio. The mean detection limit of OClO in this analysis was 1.7 ppt (2σ) on average.
Iodine oxide (IO) was evaluated in the blue spectral range from 423-447 nm comprising the three strongest IO absorption bands (2-0, 3-0 and 4-0) of the $A^2\Pi_{3/2} \leftarrow X^2\Pi_{3/2}$ transition of the IO radical. Besides IO, reference spectra of water vapor, NO_2, O_4, OBrO, OClO and a Xenon lamp spectrum were included in the DOAS fit. The limiting factor for optimizing the IO analysis was the correct removal of the Xenon lamp emission lines (e.g. at 438 nm and for $\lambda \geq 446\,nm$). The best results, i.e. the lowest residual structures, were obtained when a lamp reference spectrum averaged over the complete measurement period was used, resulting in a mean detection limit of 1.3 ppt for IO.
The strongest absorption bands of the halogen dioxides OBrO and OIO are in the green spectral range between 500 nm (OBrO) and 550 nm (OIO). Therefore an optimized DOAS evaluation for these species was performed between 541 nm and 565 nm, where both molecules exhibit four strong absorption bands. Besides the two halogen dioxides OIO and OBrO, reference spectra of water vapor, NO_2, O_4 and a lamp reference spectrum were simultaneously fitted to the measured atmospheric spectra. Variable Xenon lamp structures were again the limiting factor when analyzing the absorption spectra in this spectral range. Frequently residual structures of up to 5×10^{-3} (peak-to-peak value) due to changes of the shape of the Xenon emission lines could not be adequately described by the reference spectra included in the analysis. The resulting average detection limits were 5.5 ppt for OBrO and 6.6 ppt for OIO, respectively.
The complete data set obtained for the halogen oxides OClO, IO, OBrO and OIO is shown in Figure 5.38. During the measurement period none of the halogen oxides besides BrO was identified in the measured absorption spectra. The respective detection limits for all halogen oxide species investigated at Kuujjuarapik are given in Table 5.2.

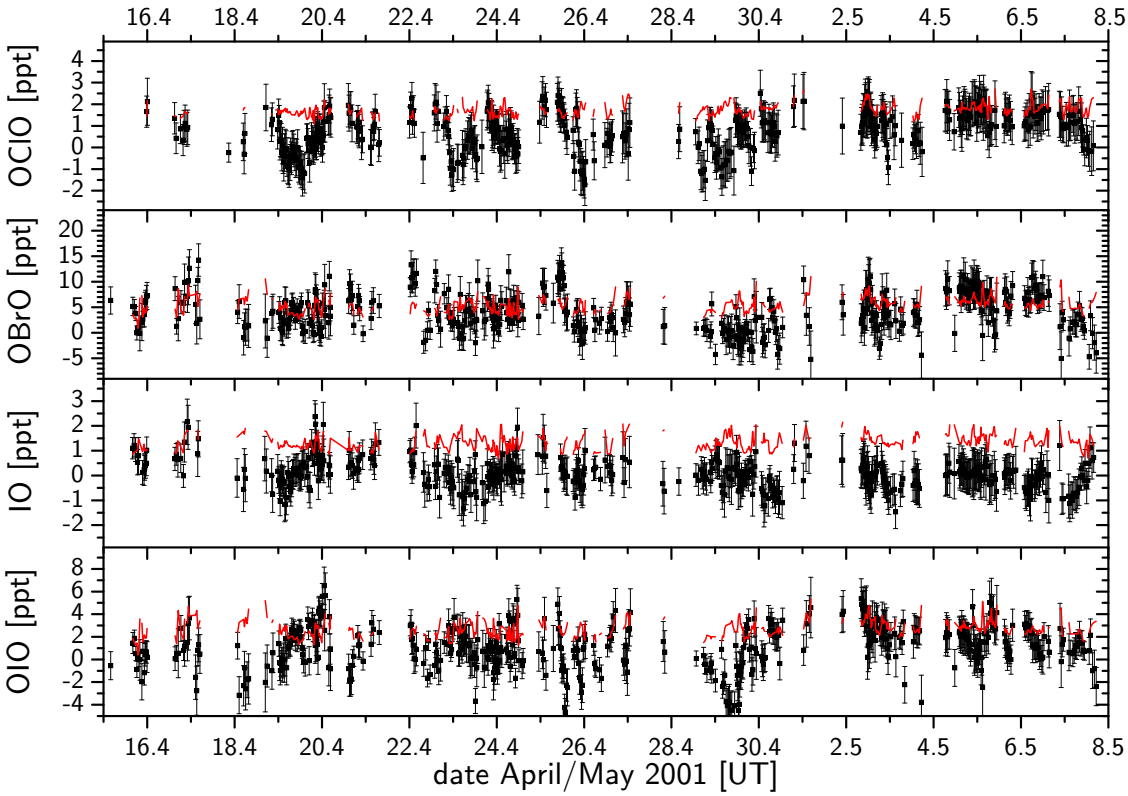

Figure 5.38: *Time series of the evaluated halogen oxides OClO, OBrO, IO and OIO during the Hudson Bay measurements. Only data from the long lightpath is shown. The red lines indicate the respective detection limits.*

5.4.4 Etalon Structures

During the measurements at the Hudson Bay at several occasions strong, but so far unknown structures were observed in the atmospheric spectra besides the known features

Species	average detection limit [ppt]	minimum detection limit [ppt]
BrO	1.5	0.6
OClO[a]	1.7	0.9
OBrO[a]	5.4	0.9
IO[a]	1.3	0.7
OIO[a,b]	6.6	1.0

[a] not detected

[b] taking the cross section by [*Bloss et al.* 2001]

Table 5.2: *Detection limits of the investigated halogen oxides during the Hudson Bay campaign in April/May 2001. The values can be considered as upper limits of the atmospheric mixing ratios.*

like structures from the diffraction grating of the spectrometer and Xenon lamp structures (see lower part of Figure 5.40. The features were strongest in the green spectral range, but at the same time, the spectra taken in the blue and UV exhibited similar features. Since the spectral width of the structures was $\sim 1 - 1.5\,\mathrm{nm}$ and did not vary over time, while the intensity of the structures did vary from day to day, a so far unknown absorber was proposed first to explain the observations. A reference spectrum for the respective fit interval was derived by manually removing all known absorptions from a measured spectrum clearly exhibiting the unknown features (typically in the range of 1-2% optical density). Further investigations showed, that when the so-derived reference spectrum was included in the fit, residual structures decreased significantly for spectra taken on the short lightpath. Furthermore, the occurrence of the phenomenon was strictly correlated with measurements on the short lightpath. Figure 5.39 shows the time series of the fit coefficient for the additional reference spectrum included e.g. in the BrO fit procedure. The

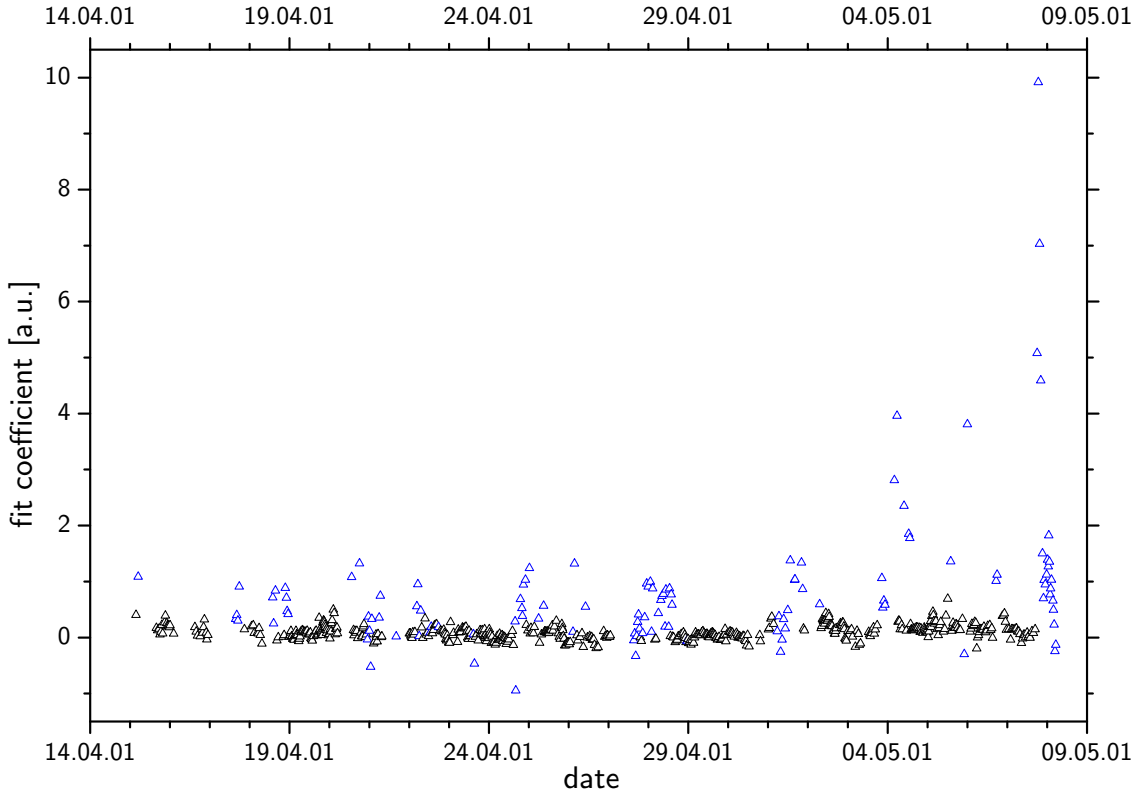

Figure 5.39: *Time series of the fit coefficient for a reference spectrum prepared to contain only the etalon structures. Blue data points indicate spectra taken on the short lightpath, black triangles are spectra taken from the long lightpath.*

blue triangles indicate all measurements taken on the short lightpath, which exclusively show fit coefficients significantly different from zero. The main difference between the two

light paths besides the total length was the fact, that the short path was very close to surface (vegetation and ice) and oriented parallel to the coastline, where the melting of the ice set in first at temperatures above freezing. However, the unknown structures were found both at sub-zero temperatures and above zero.
Another approach to explain the structures is the so-called Etalon effect (see Appendix on page 215). It is an instrumental effect caused by multiple reflections between reflecting parallel surfaces in the optical path. These multiple reflections lead to interference effects which are visible in the spectrum as wave-form modulations of the light intensity. The Etalon effect and its influence on DOAS measurements has been studied by *Stutz* [1991], who reported relatively broadband modulations (∼10-30 nm) caused by multiple reflections between the detector material and a possible coating or thin layer of water or ice. *Hönninger* [1999] found high frequency modulations (0.03 nm) originating from quartz windows with a thin reflective layer in the optical path. Those modulations could be correctly modelled by a function describing multiple reflections between two parallel plates with reflective surfaces. Measurements at Kuujjuarapik were taken using different color filters to reduce stray light (e.g. UG5 filter to remove the visible spectrum above 400 nm for the UV measurements). However, no combination of color or grey filters was strictly correlated with the structures observed in spectra from the short lightpath. In particular, several spectra taken without any filters still exhibited the features. The only further difference between long and short lightpath, however, are the different retro reflector arrays applied. Retro reflectors themselves behave the same way as a back surface mirror in a distance from the reflector front surface, which is determined by twice the distance between the cube corner and the front surface. This depends on the particular geometry of the respective retro reflector. For all retro reflectors used on the short lightpath this geometric distance was 96 mm. The retro reflectors therefore act as a parallel plate of 96 mm thickness with a reflectivity of 100% at the back surface as long as the angle of the incident light is small. Multiple reflections causing Etalon effects are strongly enhanced when an additional reflecting layer (e.g. a film of water or ice) is present on the front surface of the retro reflector. Thin ice and water layers were indeed noticed and removed during the campaign when the retro reflector arrays were routinely cleaned. To assess this possibility, a model function for multiple reflection between two layers (equation A.5 in the appendix on page 216) was fitted to the observed structures in the blue and green wavelength regions. The result is shown in Figure 5.40 (top) as red lines. The model function can reasonably explain the wavelength modulation in both spectral intervals. For the parameters of the model fit the dimension of one reflecting layer was held constant[10]. The fit predicts an additional reflecting layer of ≈200 μm optical thickness on the surface of the retro reflectors. It is assumed that thin ice layers and particularly thin water films were

[10]the optical path in the retro reflector is 96 mm×n_{quartz}, with n_{quartz} ≈1.54, resulting in an input parameter of 14.784 cm=1.4784E8 nm

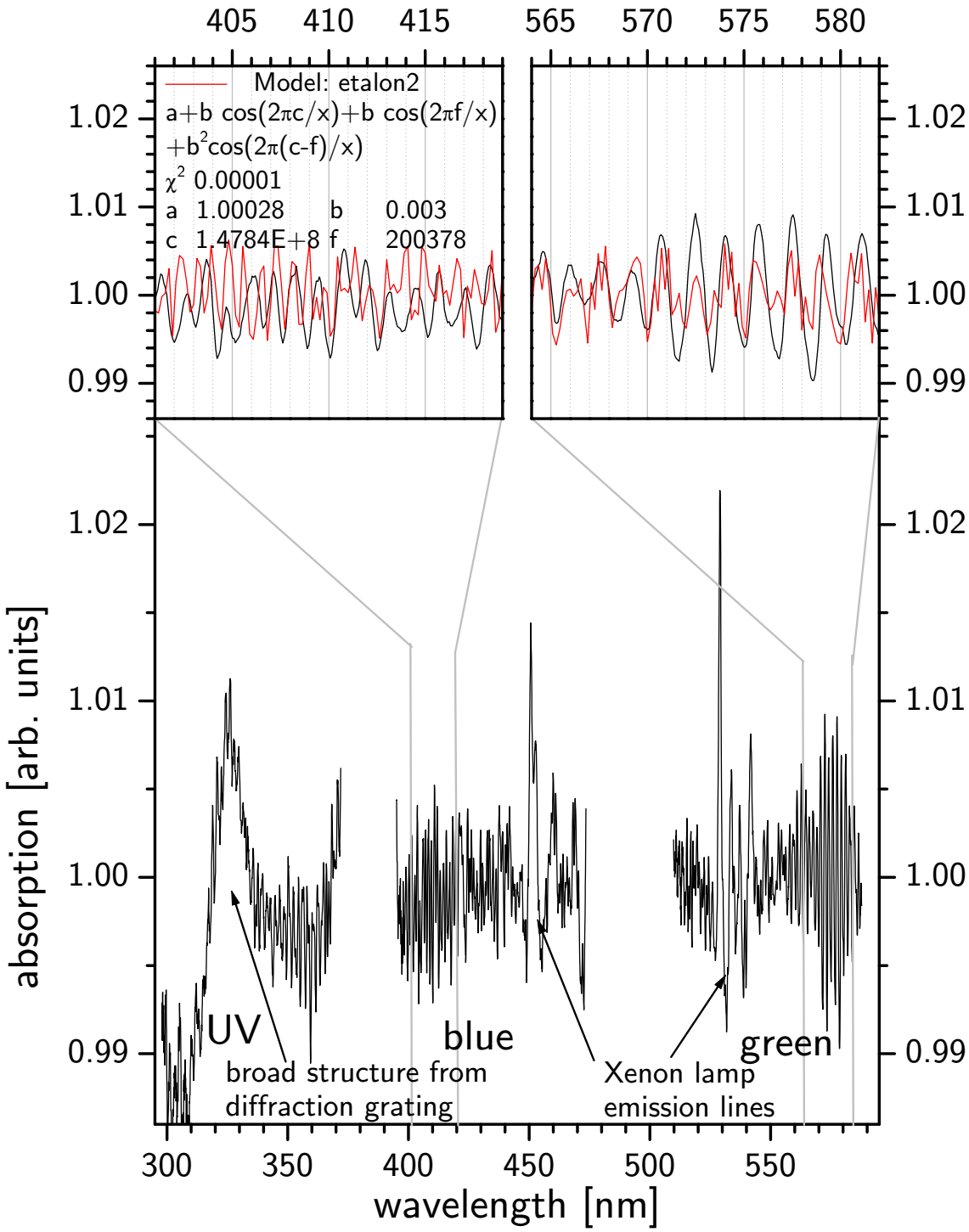

Figure 5.40: *Bottom: High pass filtered atmospheric spectra exhibiting etalon structures are shown for the UV, blue and green spectral regions. Besides the known structures from the grating and the Xe emission lines very strong high frequency structures are visible. Top: Etalon structures on an expanded scale. Shown is also the fitted etalon model function.*

responsible for the observed strong structures in the measured spectra. This assumption is supported by the fact that the intensity of the structures or the amplitude of the etalon effect (corresponding to the fit coefficient in Figure 5.39) increased strongly towards the end of the measurements, when the Hudson Bay sea ice surface was melting and a lot of moisture was present at the site where the retro reflectors were located. In contrast to the retro reflector array for the long lightpath which was set up at ≈30 m above the ice, the small array for the short lightpath was set up on a rock ≈10 m from the Hudson Bay ice (water) surface at ≈1 m above sea level. The 'reference spectra' of the described Etalon effect were included like an additional absorber in all DOAS evaluations for the short lightpath in order to remove the structures and allow to evaluate all other investigated species.

5.4.5 Local Pollution

Besides halogen oxides local pollution was monitored at Kuujjuarapik by simultaneous measurements of SO_2 (in the UV range) and NO_2 (best in the blue range), which can be regarded as tracers for anthropogenic pollution. During background conditions both species ranged below their respective detection limits of 0.16 ppb (min 0.02 ppb) for SO_2 and 0.08 ppb (min 0.04 ppb) for NO_2. However, several spikes are visible in the time series of both species in Figure 5.41. These spikes indicate local pollution very close to the measurement site. Sharp NO_2 peak values of up to 8 ppb were correlated with wind directions from the southeast where the village of Kuujjuarapik is located. Additionally the DOAS lightpath is almost parallel to this wind direction leading to high concentrations over the full length of the lightpath (see bottom part of Figure 5.41). Even more important than pollution from Kuujjuarapik is probably the plume of the power generator next to the DOAS container where the instruments were set up. For southeasterly winds the plume of the generator was very likely affecting the DOAS measurements. Also, in some cases the exhausts of aircraft landing at Kuujjuarapik and passing over the DOAS measurement site could have contributed to the observed pollution levels. SO_2 is not correlated to the NO_2 peaks, most elevated values are during the last two days of the measurements when fire was set on the local dump site at Kuujjuarapik and the plume was blown towards the DOAS measurement site. SO_2 emissions from the power generator are very unlikely since it was operated with unleaded gasoline which has a very low sulfur content.
In general the NO_2 and SO_2 levels measured by DOAS are representative for clean background air, especially during BrO events which were always associated with north-westerly wind and arctic air masses reaching Kuujjuarapik. The effects of the observed pollution spikes on the BrO measurements is therefore negligible.

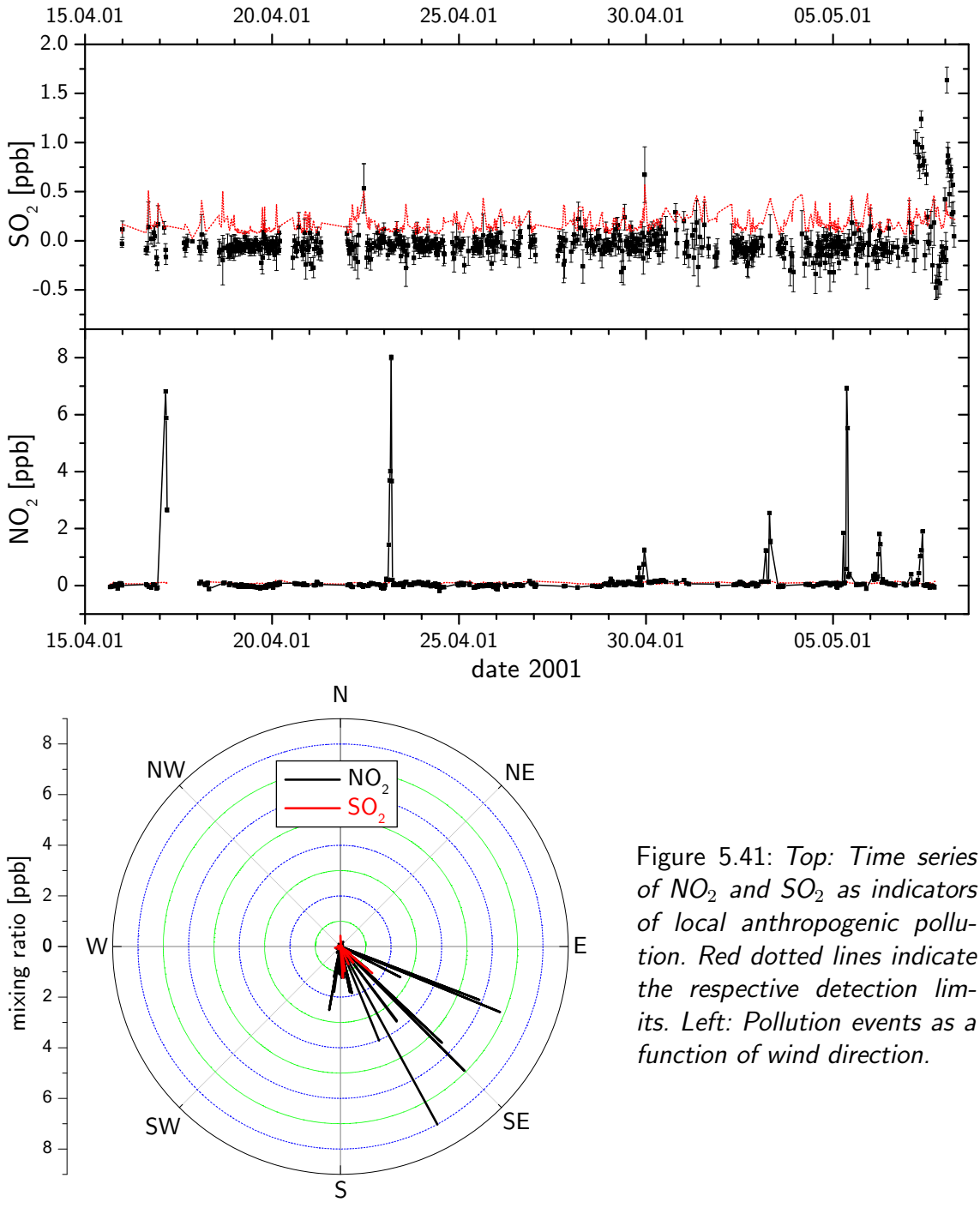

Figure 5.41: *Top: Time series of NO_2 and SO_2 as indicators of local anthropogenic pollution. Red dotted lines indicate the respective detection limits. Left: Pollution events as a function of wind direction.*

5.4.6 MAX-DOAS BrO Measurements

For the first time during the Hudson Bay field campaign MAX-DOAS measurements were performed simultaneously with LP-DOAS measurements. A sequential MAX-DOAS instrument (for an instrument description see section 4.1) was operated at the DOAS

Figure 5.42: *Setup of the MAX-DOAS telescope/stepper motor arrangement at the DOAS site near Kuujjuarapik.*

measurement site from April 19 until May 8, 2001. The viewing direction of the MAX-DOAS telescope was true north, passing approximately 1 km west of the LP-DOAS retro reflectors located at the southern tip of Bill of Portland Island. Therefore towards the horizon the line of sight of the telescope was above the Hudson Bay sea ice surface. The MAX-DOAS system was operated in a sequential mode receiving scattered sunlight from elevation angles of 5°, 10° and 20° as well as from zenith direction. The MAX-DOAS receiving telescope was mounted to a stepper motor drive/joint system allowing to move the telescope in these directions by computer control. The setup of the MAX-DOAS telescope and stepper motor arrangement at the DOAS container is shown in Figure 5.42. Continuous measurements of scattered sunlight were performed in an automated measurement loop for solar zenith angles smaller than 93°. After 2 spectra taken at 5° elevation a MAX-DOAS sequence at elevation angles of 90°, 20° and 10° was recorded. During daytime the integration time was ∼5 minutes, so one complete MAX-DOAS series was usually measured within 30 minutes. Only at dawn and dusk integration times reached 10 min. The spectra recorded in the wavelength range from 319 nm to 381 nm were analyzed for atmospheric absorbers by the DOAS analysis procedure (see section 3.1.2). In order to evaluate the bromine oxide absorption reference spectra of BrO, ozone, NO_2 and O_4 as well as a FRS (Fraunhofer reference spectrum, see section 3.2.2) taken on April 30, 2001

at 16:25UT (SZA=41°, SAA=164°, α=90°) and a calculated Ring spectrum (see section 3.2.3) were simultaneously fitted. Additionally, a polynomial of 2^{nd} order was included in the fit process to remove broadband absorption structures and the effects of Rayleigh and Mie scattering. For the fitting process the spectral range between 346 nm to 359 nm was used (see also section 5.2.3 and example in Figure 5.19). The time series of BrO dSCDs resulting from the DOAS fit is shown in Figure 5.43. Until April 29, 2001, the MAX-DOAS dSCDs show clear differences between the measurements at low elevation angles and in zenith mode. Like during the measurements at Alert (see section 5.2.3) this indicates, that a large fraction of the observed BrO is present in the boundary layer. In the evening of April 24 and in the early morning of April 27, the 5° elevation dSCDs reached maximum values of 10^{15}molec/cm^2, which is the same range as for the Alert measurements. From April 30 until the end of the measurements the BrO dSCDs are almost entirely characterized by the absorption of stratospheric BrO, which manifests itself in the typical U-shape of the diurnal dSCD cycle. However, between May 3 and 5 small differences between the 90° data and values at the lower elevation angles are visible.

5.4.7 Ozone Measurements at Kuujjuarapik

Ozone measurements at Kuujjuarapik were performed both by DOAS (as a side product of the BrO measurements, see sample evaluation on page 59) and using a commercial in situ ozone analyzer. The commercial ozone instrument was operated at the Centre d'études nordiques (CEN) in Kuujjuarapik, about 2 km south of the DOAS measurement container (O_3 data kindly provided by L. Poissant, Meteorological Service of Canada, [*Poissant* 2001]). The ambient ozone data measured at the CEN is shown in Figure 5.44 together with the LP-DOAS ozone data measured between the DOAS container and Bill of Portland Island. In order to correlate both measurements the in situ ozone data with a time resolution of 5 min was averaged over the respective DOAS integration time of 30 min on average. However, sampling of different air masses, which is possible since the instruments were located on opposite sides of the village, could not be corrected for. The correlation plot for both ozone data sets is shown in Figure 5.45. Both data sets are clearly correlated, but some deviations are visible. However, there are no systematic differences in the data sets, but rather single data points which show high deviations. This could be explained by sampling of different air masses by both instruments, e.g. when CEN in situ data was influenced by local NO_x emissions from the village which did not affect the DOAS measurements for northerly flows. In general it can be assumed that both data sets correctly quantify the ozone levels at Kuujjuarapik.

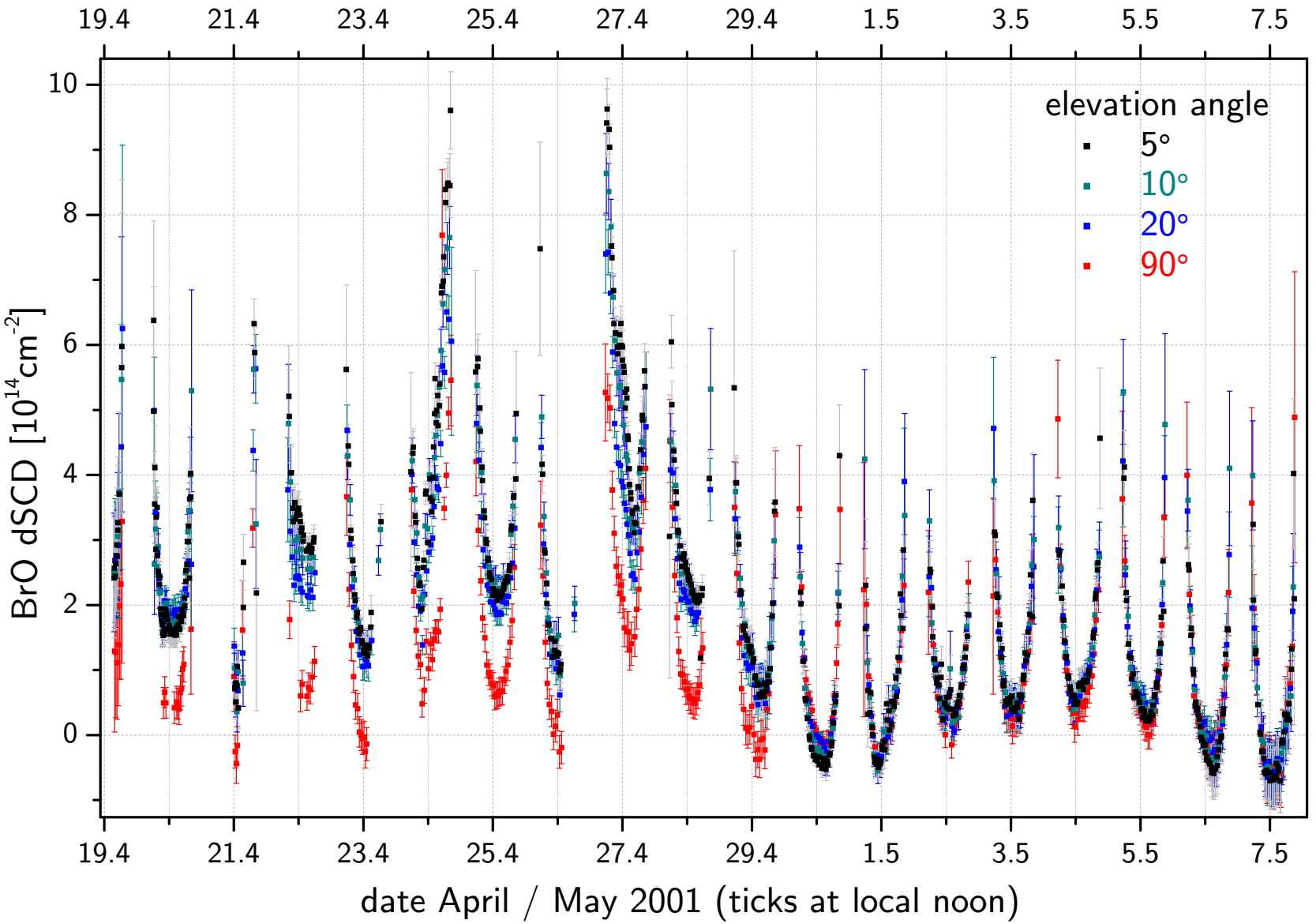

Figure 5.43: *MAX-DOAS BrO dSCDs measured at Kuujjuarapik, Hudson Bay. Measurements taken at different elevation angles α are shown in different colors.*

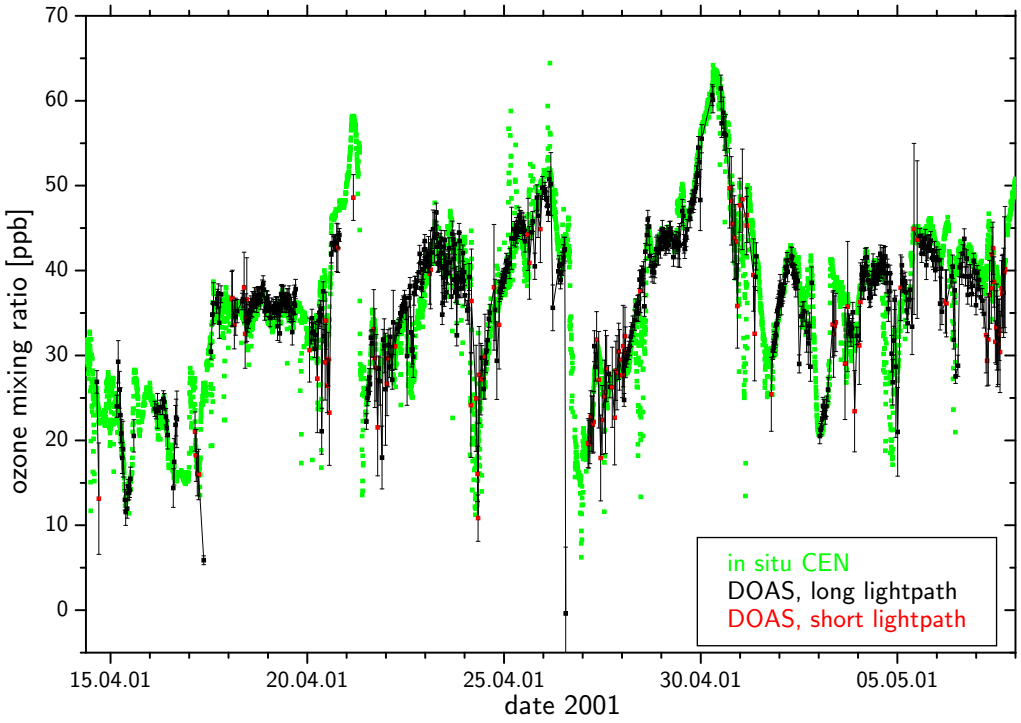

Figure 5.44: *LP-DOAS ozone data overlaid on the time series of the in situ ozone measurements at the Centre d'études nordiques, Kuujjuarapik. In situ O_3 data provided by L. Poissant, MSC [Poissant 2001]*

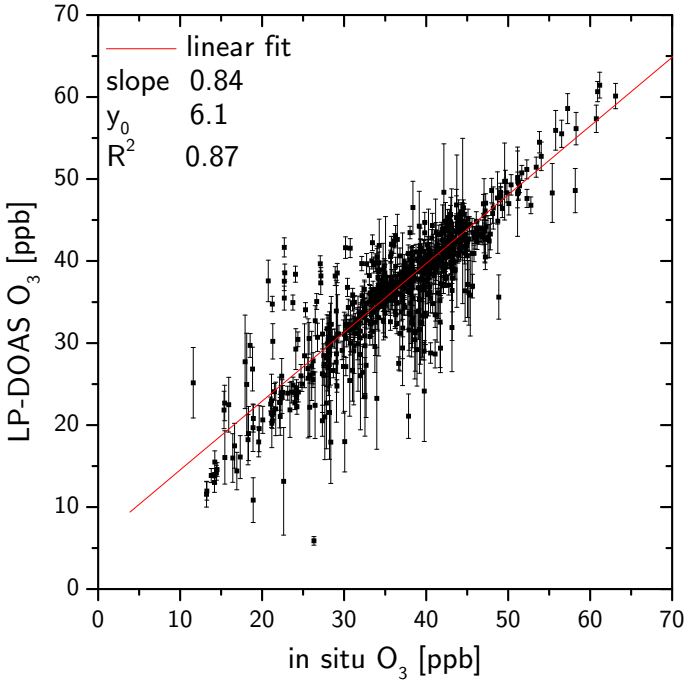

Figure 5.45: *LP-DOAS ozone mixing ratios versus in situ O_3 data measured at the CEN [Poissant 2001]. In situ O_3 was averaged over the respective LP-DOAS integration time.*

5.4.8 Mercury Measurements at Kuujjuarapik

For measurements of total gaseous mercury (see section 2.5) at Kuujjuarapik during spring 2001, a commercial Tekran® mercury analyzer was installed at the Centre d'études nordiques in Kuujjuarapik [*Poissant* 2001]. The time series of TGM measured by *Poissant* [2001] at the CEN is shown in Figure 5.24. The behavior of gas phase mercury is

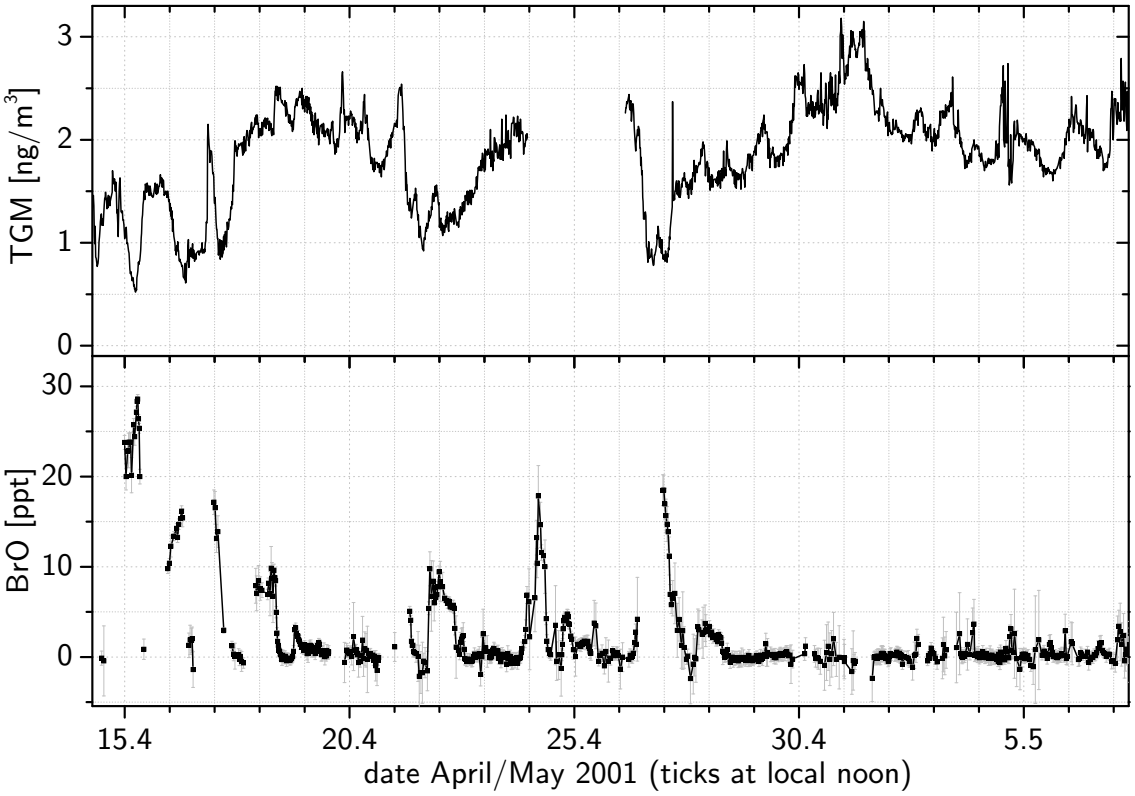

Figure 5.46: *Top: Total gaseous mercury time series measured at the CEN by Poissant [2001] (1 ng/m^{-3} ≈0.1 ppt). Bottom: BrO mixing ratios measured by LP-DOAS.*

anti-correlated to that of BrO like it was the case for Alert (see section 5.2.6). However, at Kuujjuarapik no complete Hg depletion was found, but rather small episodic events of several hours duration. During these mercury depletion events (MDE) TGM dropped from background levels of ∼2 ng/m^3 to below 1 ng/m^3 within a few hours (3-5). The behavior of gaseous mercury at Kuujjuarapik is further discussed in section 6.6.

Chapter 6

Results

6.1 BrO in the Free Troposphere

As already mentioned in section 5.1.1 the BrO measurements at the Zugspitze show some further indications for a background of free tropospheric BrO, at least during certain periods. Anomalous W-shapes of the BrO dSCD diurnal variation, especially during cloudy periods could be explained by additional BrO absorption due to tropospheric interstitial BrO. This observation supports the findings of other authors (see section 2.3) who derive a free tropospheric background of BrO in the range 1-2 ppt. This background could either be due to efficient upward mixing of BrO from the planetary boundary layer, which probably contributes significantly to free tropospheric BrO in polar regions during springtime. In mid-latitudes and in the tropics, however, organic bromine precursors like methyl bromide and bromoform (see section 2.3.1) could play the major role. Due to its high efficiency in destroying ozone, a free tropospheric background of reactive bromine would significantly affect the chemistry of the troposphere (especially ozone, HO_x and NO_x cycles, see section 2.2.1).

6.2 Halogen Oxides in the Southern Indian Ocean

The ship borne measurements performed in the Indian Ocean did not yield any BrO above the detection limit, however, if more than 4 ppt of BrO had been present, a signal would have been observed by the MAX-DOAS measurements. Nevertheless bromine chemistry could still play a role in the Indian Ocean marine boundary layer, because model simulations by [*Vogt et al.* 1996] for the remote marine boundary layer indicate that even at BrO levels below 1 ppt reactive halogen chemistry can account for 5-40% of the total ozone loss, depending on aerosol surface and speciation.
The first LP-DOAS measurements in the southern Indian Ocean at Port-aux-Français, Kerguelen Island showed that IO is likely present in the marine boundary layer at Kerguelen

Island at maximum levels of approximately 10 ppt. This agrees well with previous findings at Mace Head, Ireland [*Alicke et al.* 1999; *Hebestreit* 2001], the Canary Islands and Cape Grim, Tasmania [*Allan et al.* 2000; *Allan et al.* 2001] as well as with the observations of *Frieß et al.* [2001] at Neumayer Station, Antarctica. Although these measurements still represent only a limited data set, it can be concluded that iodine oxide mixing ratios in the range 0 - 10 ppt are always present in the boundary layer of remote coastal regions. As was shown by *Stutz et al.* [1999] these levels of reactive iodine can destroy up to ∼0.45 ppb ozone per hour. Additionally, IO at these levels strongly influences the boundary layer photochemistry, namely the ratios of OH/HO_2 and the Leighton ratio NO/NO_2 (cf. section 2.1.2). This significant perturbation of standard boundary layer chemistry is likely to alter the results of currently used chemistry and transport models.

6.3 Results from ALERT2000

6.3.1 Time Series of BrO during ALERT2000

Measurements of BrO were performed on 20 days from April 20 to May 9, 2000. During 12 days BrO SCDs clearly exceeded the stratospheric background levels. The smallest detectable deviation from the stratospheric background column was 1×10^{13} molec/cm^2. The time series of BrO ΔSCDs during the campaign are shown in Figure 6.1. ΔSCDs are defined as

$$\Delta SCD(t) \equiv dSCD(\alpha, t) - dSCD(\alpha = 90^\circ, t) \tag{6.1}$$

where both dSCDs are differential with respect to the slant column density of the same Fraunhofer reference spectrum (FRS) SCD_{ref}. In this case there is no difference if differential SCDs or total SCDs are subtracted, since a possible contribution of SCD_{ref} is cancelled out. ΔSCDs are a good measure for boundary layer concentrations, since the stratospheric and possible upper tropospheric fraction of the absorber has nearly identical airmass factor contributions for all elevation angles, whereas the boundary layer SCD is highly enhanced for the low elevation angles. Subtracting the dSCD(α=90°) therefore eliminates the stratospheric and possible upper tropospheric part of the total SCD. The small amount of the boundary layer SCD contained in the slant column of the zenith measurement, which is also subtracted, has to be considered and corrected for, when the ΔSCDs are converted to trace gas concentrations.
Two possibilities were investigated to calculate ΔSCD for the BrO time series:

1. The data shown in the upper part of Figure 6.1 (ΔSCD*) were derived by analyzing all DOAS spectra at low elevation angles with the immediately previous zenith spectrum as the Fraunhofer reference spectrum. This method yields very small DOAS fit errors since both spectra are taken at very similar atmospheric and instrumental conditions except for the different elevation angle.

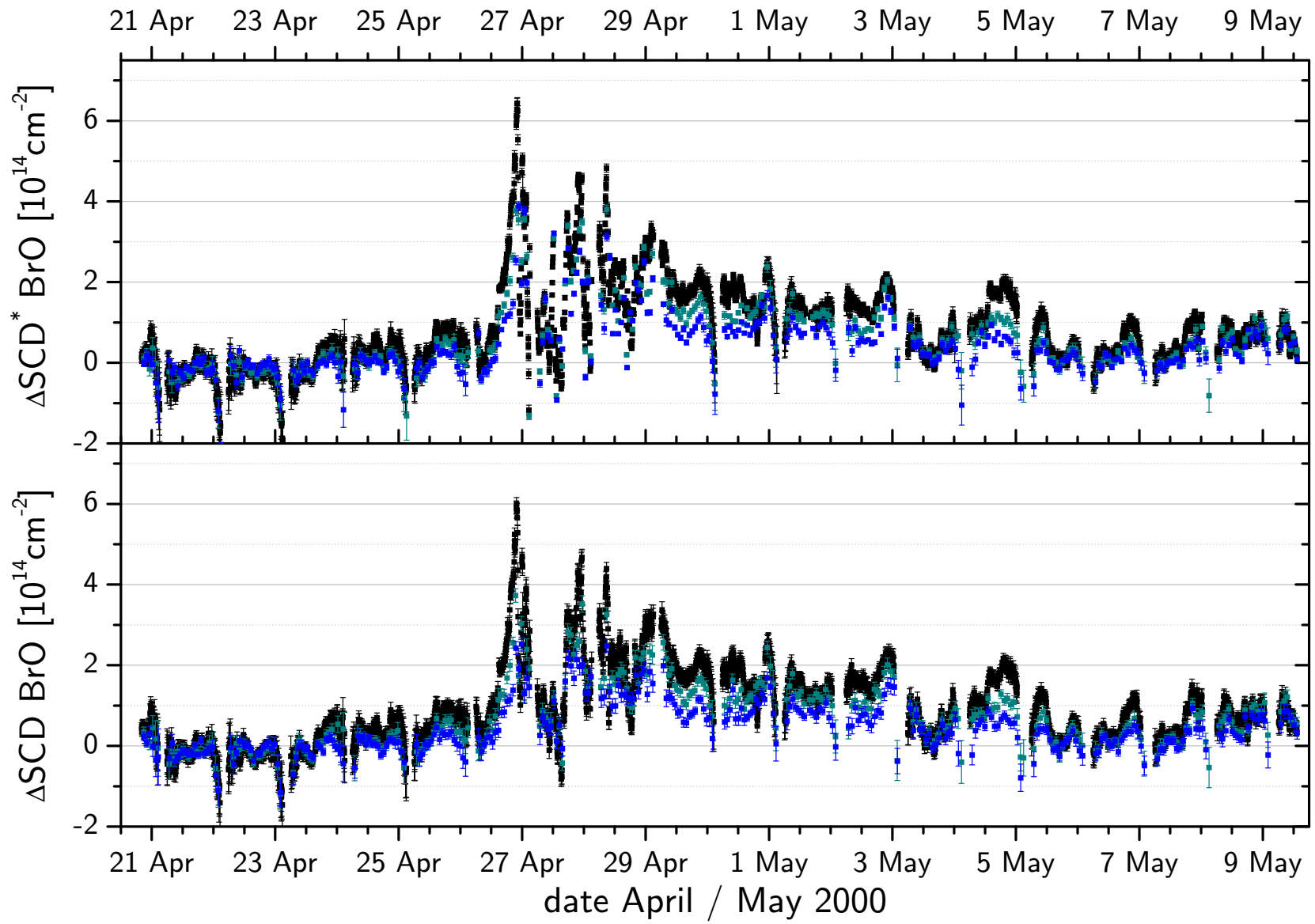

Figure 6.1: *MAX-DOAS time series of BrO ΔSCD for the elevation angles 5°, 10° and 20°. Two possible approaches to determine the ΔSCD are shown. Top: ΔSCD derived by the DOAS fit when the immediately previous zenith spectrum is taken as FRS. Bottom: ΔSCD derived by subtracting the zenith dSCDs from the dSCDs at the low α's, all evaluated using the same FRS as shown in section 5.2.3*

2. The time series in the bottom part of Figure 6.1 (ΔSCD) was derived from the complete BrO data set (shown in Figure 5.21), which was entirely evaluated with only one single Fraunhofer reference spectrum for all spectra (cf. section 5.2.3). From all dSCDs at the low elevation angles (α=5°, 10° and 20°) then the dSCD linearly interpolated between the previous and the following zenith measurements were subtracted. This method leads to generally slightly higher DOAS fit errors, because of spectral shifts and squeezes allowed during the nonlinear fit to account for possible instrumental differences between the overall Fraunhofer reference and the respective spectrum to be analyzed. However, the advantage is that interpolation between the zenith measurements before and after the MAX-DOAS series (typically one hour apart) yields more reliable results when the changes in the BrO column are not negligible over the one hour MAX-DOAS measurement interval.

Obviously, a combination of both methods could further improve the analysis. However, since the slightly higher DOAS fit error was not the limiting factor for most conclusions derived from the measurements, the second approach was generally found to be sufficient. In Figure 6.1 both time series show identical ΔSCDs within the respective measurement errors for almost the complete measurement time. Only between April 26 and April 28, 2000, when the highest BrO values and the fastest changes were observed, the methods yield different results.

6.3.2 The Vertical Extent of the BrO Layer

Using the dependence of the BrO ΔSCDs on the elevation angle α, the height of the BrO layer can be derived. In Figure 6.2 the ΔSCDs of May 4, 2000 for the low elevation angles are plotted in different colors. As a general pattern the ΔSCD is highest for the 5° elevation angle, on average the ΔSCD nearly doubles when comparing the 20° with the 10° and the 10° with the 5° elevation measurements. As a case for deriving the BrO layer height the data from this particular day was taken as an example, because BrO was elevated during the ozone depletion period and the cloud-free conditions of May 4 allow reliable modelling of the AMFs. The high sensitivity of the airmass factor differences for different assumed BrO profiles in the lowest part of the troposphere can be seen in Figure 6.3, where the measured data from May 4, 2000 and predicted ΔSCDs for various BrO profiles are shown. The four different lines show the expected behavior for a vertical extent of the BrO layer of 0.5 km, 1 km and 2 km, respectively, and for an elevated layer between 1 km and 2 km. A BrO layer height of 1 km at the ground is best compatible with the measurements, whereas BrO layers of 0.5 km and 2 km can be considered as lower and upper limits. A BrO layer starting e.g. at 1 km altitude and extending to 2 km cannot explain the observed SCDs. There are cases, however, where the observed SCDs show a different pattern which could be explained by an elevated BrO layer. An example for a

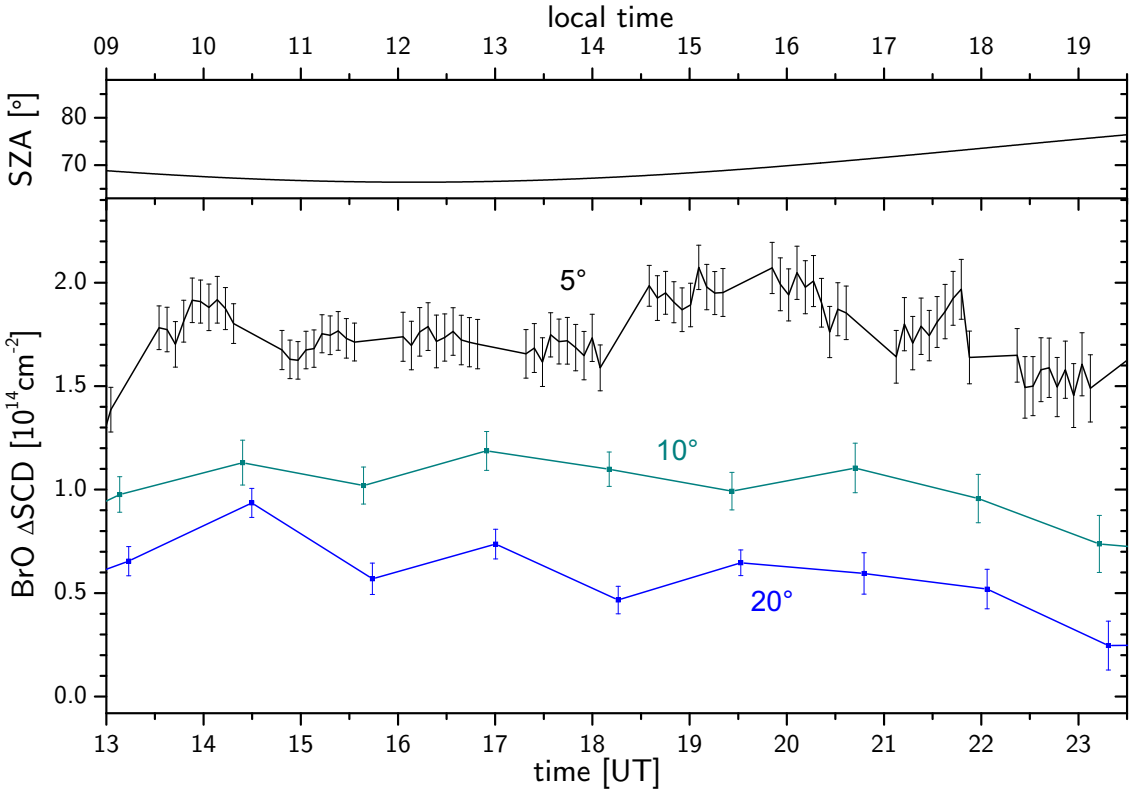

Figure 6.2: *BrO ΔSCDs measured at Alert on May 4, 2000. This day was characterized by a nearly constant vertical BrO column in the boundary layer (for SZA<75°) and clear-sky conditions.*

day which is in agreement with an elevated BrO layer is shown in Figure 6.4. The small differences between the ΔSCDs for the low elevation angles, especially the fact that the ΔSCD for α=5° and 10° are almost equal agrees well with the assumption that BrO was present in an elevated layer on April 30, 2000. The behavior of the ΔSCDs can be explained by the green line in Figure 6.3, which represents an elevated layer between 1 km and 2 km. In the majority of cases, however, the comparison of modelled and measured ΔSCDs shows that the observed BrO can be attributed to the boundary layer of approximately 1 km thickness at the surface. This agrees very well with the height of the ozone depletion layer determined by *Bottenheim et al.* [2002] (see contour plot in Figure 5.25).

6.3.3 BrO during Ozone Depletion

The time series of the BrO ΔSCDs from the 5° measurements can be converted to mixing ratios, when a boundary layer of 1 km is assumed. In Figure 6.5 the high resolution BrO time series is shown together with the ozone data set from the GAW station, located approximately 9 km south of the ice camp. BrO concentrations $[BrO]_{bl}$ and mixing ratios

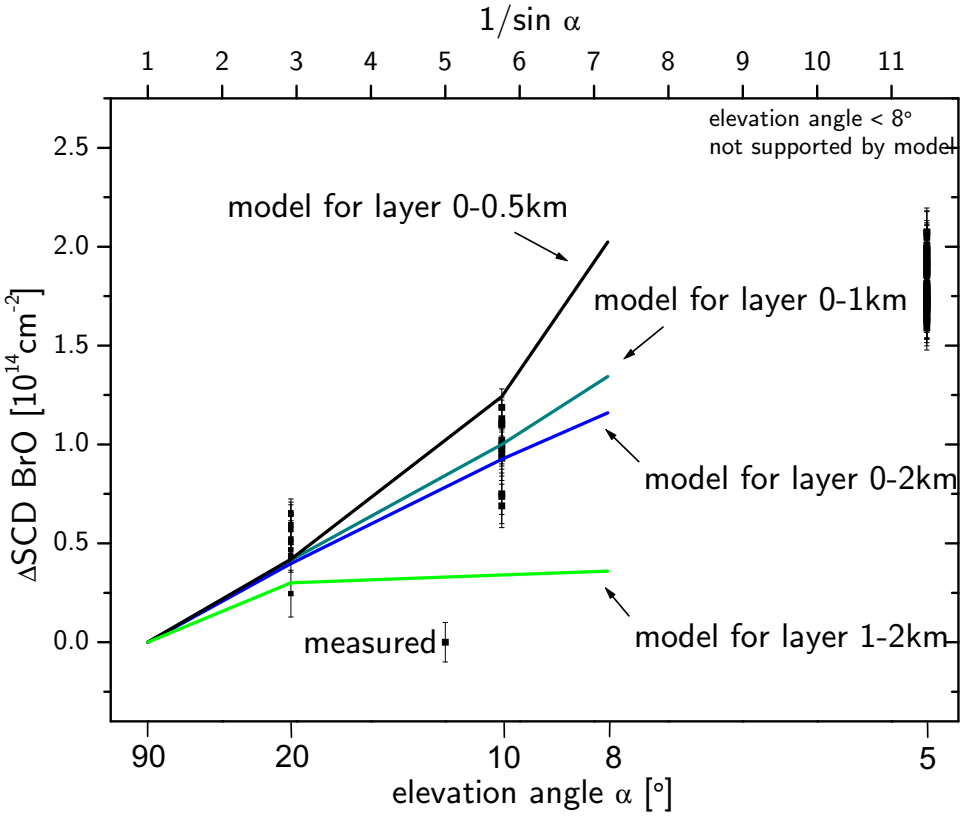

Figure 6.3: *Comparison of measured and modelled BrO profile: Measured data points are from May 4, 2000, when a nearly constant vertical BrO column of 2×10^{13} molec/cm^2 was present in the boundary layer. Solid lines represent the predicted behavior of the ΔSCD for different elevation angles. The different colors indicate models for the different indicated BrO box profiles in the low troposphere.*

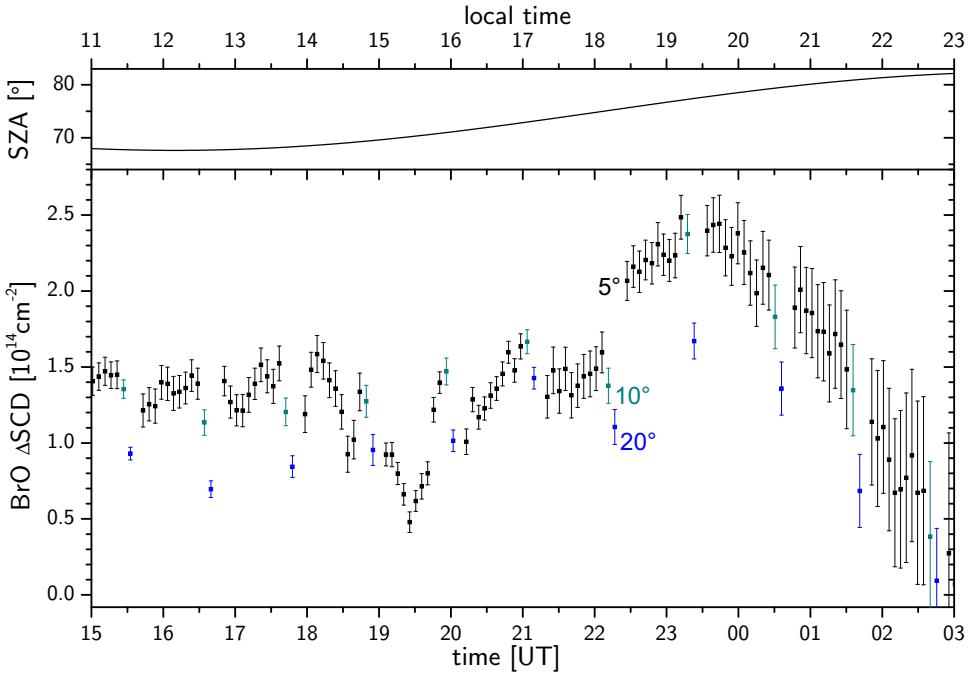

Figure 6.4: *BrO ΔSCDs measured at Alert on April 30, 2000. On this cloud free day the ΔSCDs indicate an elevated BrO layer.*

in the boundary layer were calculated assuming a homogeneous BrO layer of 1 km thickness according to:

$$\begin{aligned}[\mathrm{BrO}] &= \frac{\mathrm{VCD_{bl}}}{1\,\mathrm{km}} \\ &= \frac{1}{1\,\mathrm{km}} \cdot \frac{\Delta\mathrm{SCD}}{\mathrm{AMF_{bl,\alpha=5^\circ}} - \mathrm{AMF_{bl,\alpha=90^\circ}}} \end{aligned} \tag{6.2}$$

The anti-correlation of ozone and BrO is clearly visible over the complete measurement period. Cloudy periods are hashed to indicate that the radiative transfer could have been strongly influenced by cloud layers due to multiple reflection and by blowing and drifting snow at the surface due to multiple scattering. This fact could have led to enhanced absorption paths in the lowest atmospheric layer and thus to an overestimation of the calculated BrO mixing ratio. However, taking into account the fact that multiple scattering also significantly enhances the absorption for dSCD_{zenith}, which is subtracted, and the uncertainty of the mixing layer height (∼50 %), BrO levels could also have been underestimated in these cases. The lack of information on the exact shape of the BrO profile constitutes another possible source of uncertainty. The first week of measurements was a period of low boundary layer BrO. The diurnal cycle of BrO shows variations of less than 5 ppt[1] and only few cases with significant difference for the different elevation angles can be found in Figure 6.1. Only two small tropospheric BrO events with mixing ratios up to 5 ppt occurred (April 23-24 and April 25-26). Ambient ozone dropped somewhat but did not reach zero during that time. Probably the depletion was just starting or occurring in a layer not extending all the way down to the surface (near surface layers of zero - ozone air were e.g. observed in Antarctica [*Wessel et al.* 1998; *Frieß* 2001]). Starting April 26 in the late morning hours BrO rose to very high values of more than 25 ppt. During that time there was strong wind from the North causing drifting snow. Ozone levels dropped from 40 ppb at 10:00 UT on April 26 to less than 1 ppb by 7:30 UT on April 27. This corresponds to an average ozone destruction rate of

$$\frac{\mathrm{d[O_3]}}{\mathrm{dt}} \approx 2\,\mathrm{ppb/h}$$

This very fast O_3 loss can only partially be explained by catalytic destruction by 25 ppt of BrO, which can destroy ∼0.5 ppb/h. Taking into account 0.7 ppt of IO (see also section 6.3.5) and 1 ppt of HO_2 leads to O_3 loss rates of 0.6-0.7 ppb/h. The very fast drop in the ozone mixing ratio can, however, be explained by a combination of fresh catalytic bromine chemistry and advection of an airmass which has already been affected by O_3 depletion for several days. Indeed, 5 day back trajectories ending at Alert on April 25 and 26, respectively, show that air masses reaching Alert changed from subpolar air, which has passed

[1] for very low sun (SZA>83°) equation 6.1 is not a good approximation anymore and can yield negative ΔSCDs and therefore negative [BrO].

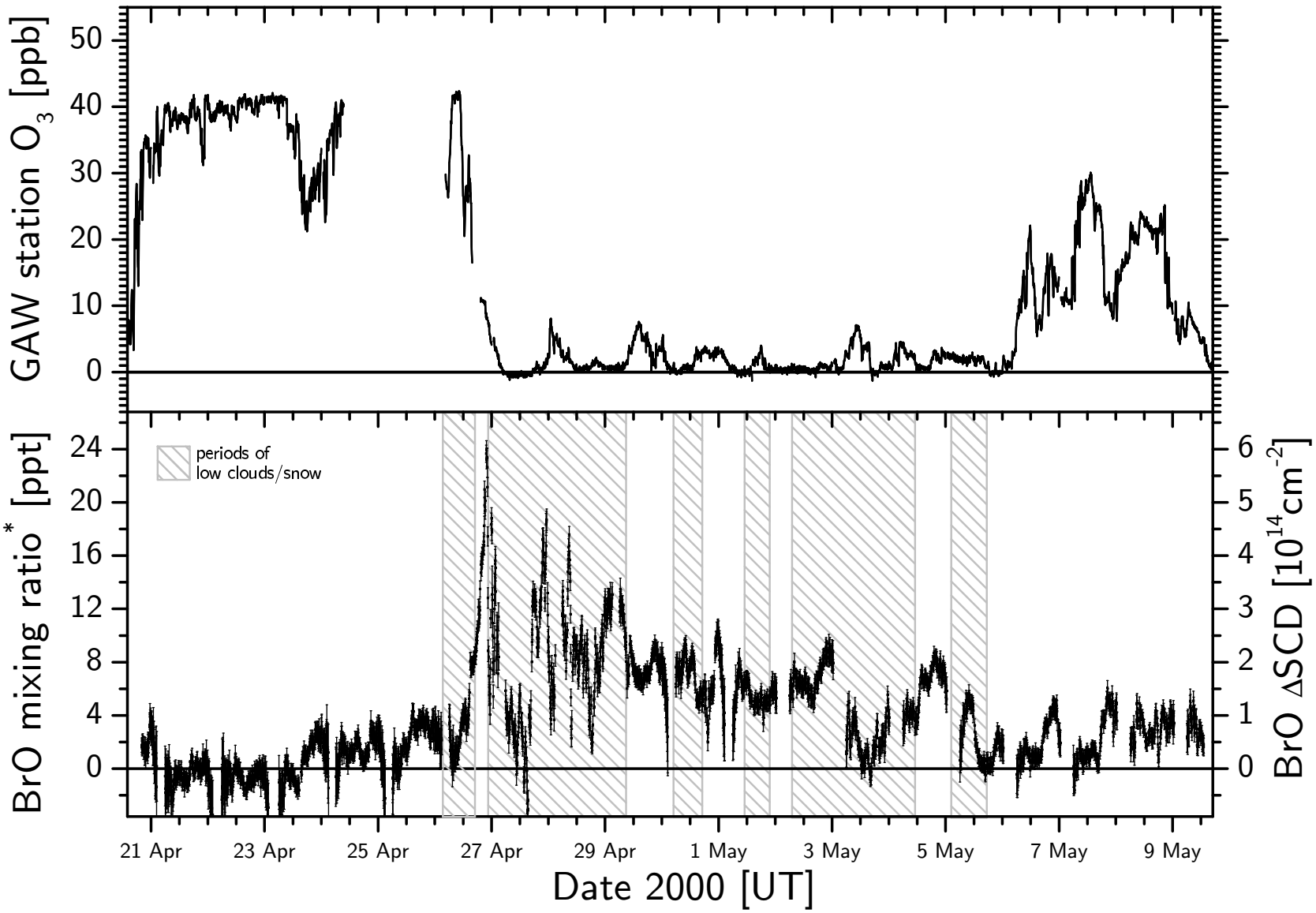

Figure 6.5: *Ozone and BrO Mixing Ratios during ALERT2000. BrO mixing ratios were calculated from the concentrations derived using equation 6.2 for a 1 km BrO layer.*

mostly over land, on April 25 to air from the north pole, which was in contact with sea ice for several days, on April 26 (see Figure 6.6). When ozone at the surface was completely

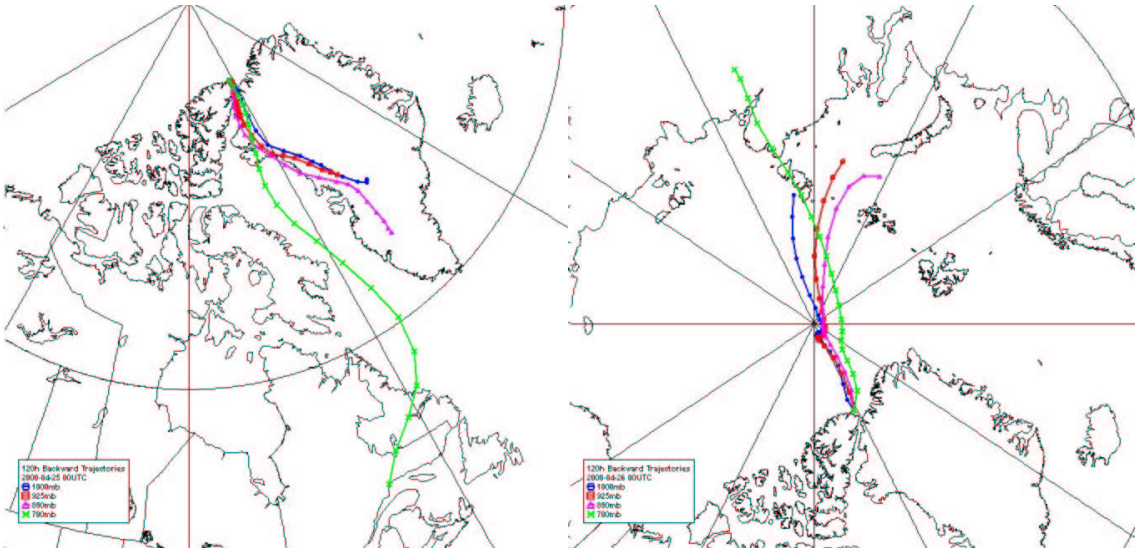

Figure 6.6: *5 day back trajectories ending at Alert just before (left) and after (right) surface ozone destruction was observed.*

lost, BrO also decreased to values near zero around 10:00 UT on April 27. The period of ozone depletion is shown in Figure 6.7 on an extended scale. The next day (April 27) BrO reached again a maximum of almost 20 ppt. Over a period of 10 days elevated BrO levels were present, during the same time surface ozone levels were below the detection limit most of the time (see Figure 6.7). Enhanced BrO could still be found when ozone was already depleted at the surface, probably due to ozone advection from aloft. Especially after ozone was completely depleted at the surface, BrO is likely present in an elevated layer. Small recoveries of surface ozone, probably due to ozone rich air mixed in from the free troposphere, were usually correlated with disturbances of the BrO layer which can be seen in Figure 6.7. For example on May 3, BrO is near zero and the low elevation angles show no difference in BrO ΔSCD, indicating that the BrO layer was elevated. This is supported by the fact that ozone was present above 500 m altitude as measured by an ozone instrument operated on a tethered balloon at the ice camp (see Figure 6.8). Ozone remained low until May 6, when BrO had also decreased to stratospheric background levels. At the ice camp ozone had already recovered down to $\approx$200 m above the surface as shown by the tethersonde profile in Figure 6.9. In the following ozone at the surface was recovering to 20-30 ppb, however, there were still dips in the ambient ozone time series coinciding with elevated BrO levels, indicating that reactive bromine chemistry is taking place. An analysis of back trajectories for the complete O_3 depletion period (see appendix on page 226) shows, that O_3 depletion always coincides with air masses having travelled

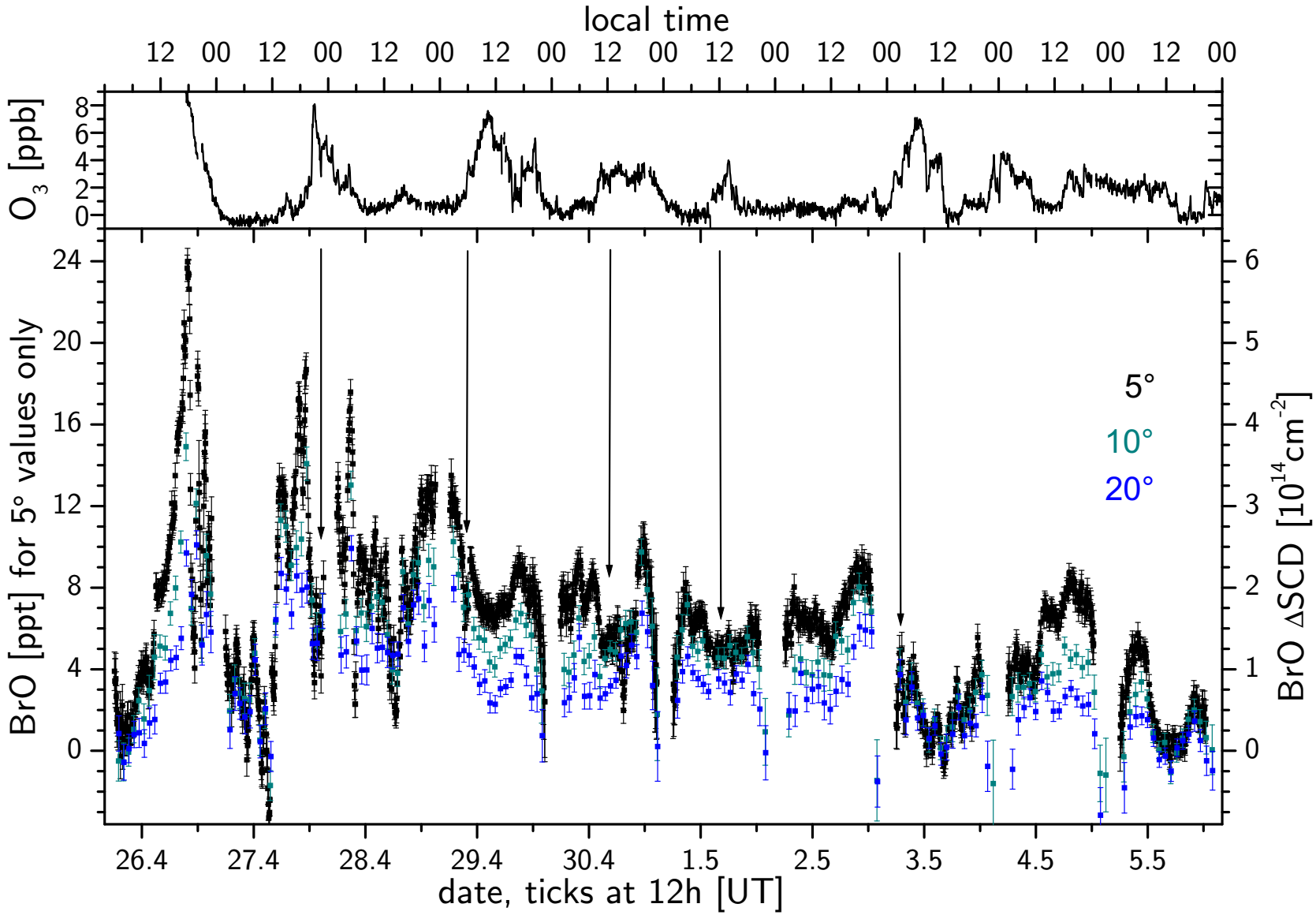

Figure 6.7: *Behavior of O_3 and MAX-DOAS BrO during the period of ozone depletion. The scale for the BrO mixing ratio only applies to the 5° values (black points). Arrows indicate ozone recovery events.*

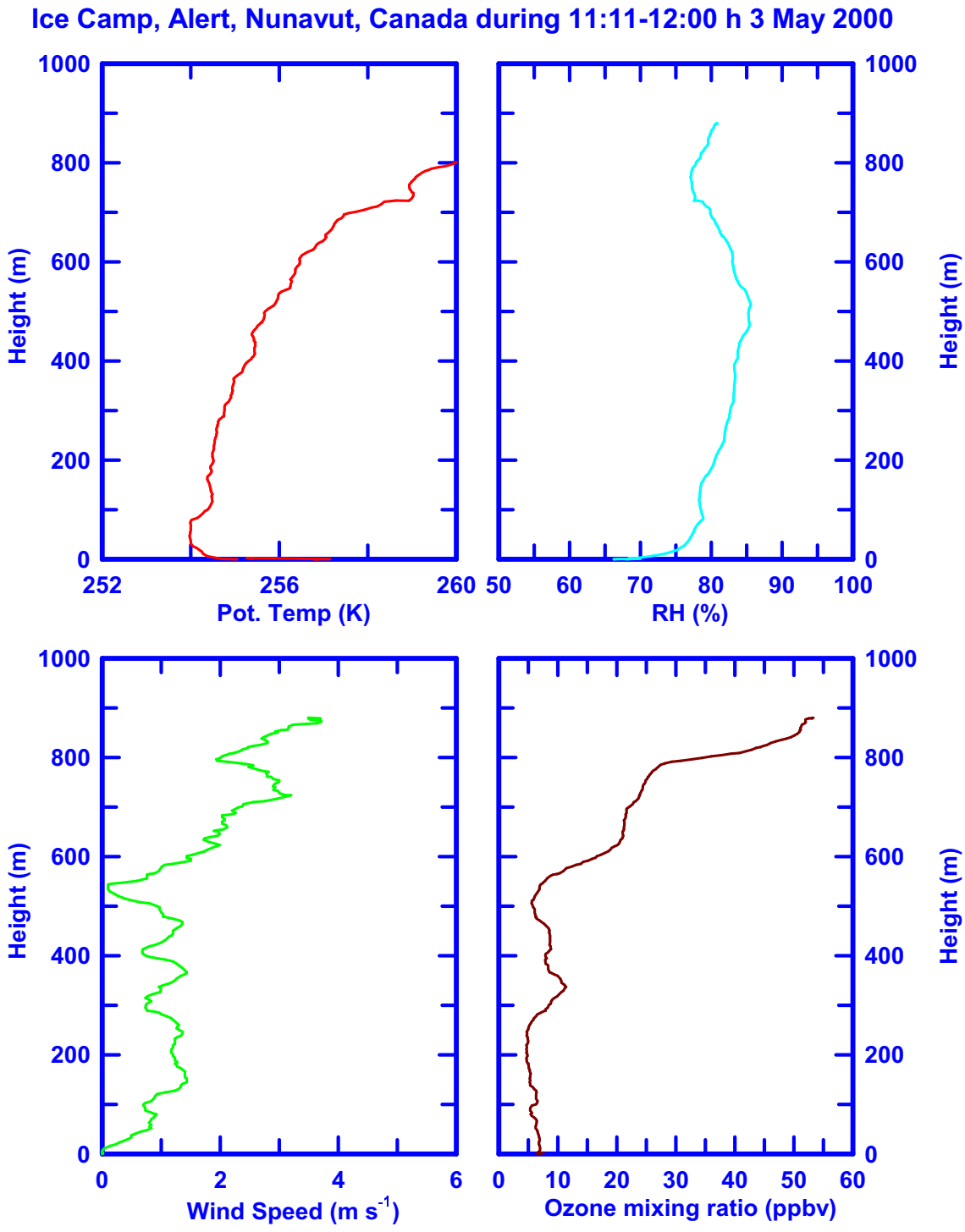

Figure 6.8: *Profiles of potential temperature, relative humidity, wind speed and ozone mixing ratios (not calibrated) measured at the Ice Camp on May 3, 2000 around noon, local time. Data provided by J. Bottenheim, J. Fuentes and J. Arnold (priv. comm. 2001).*

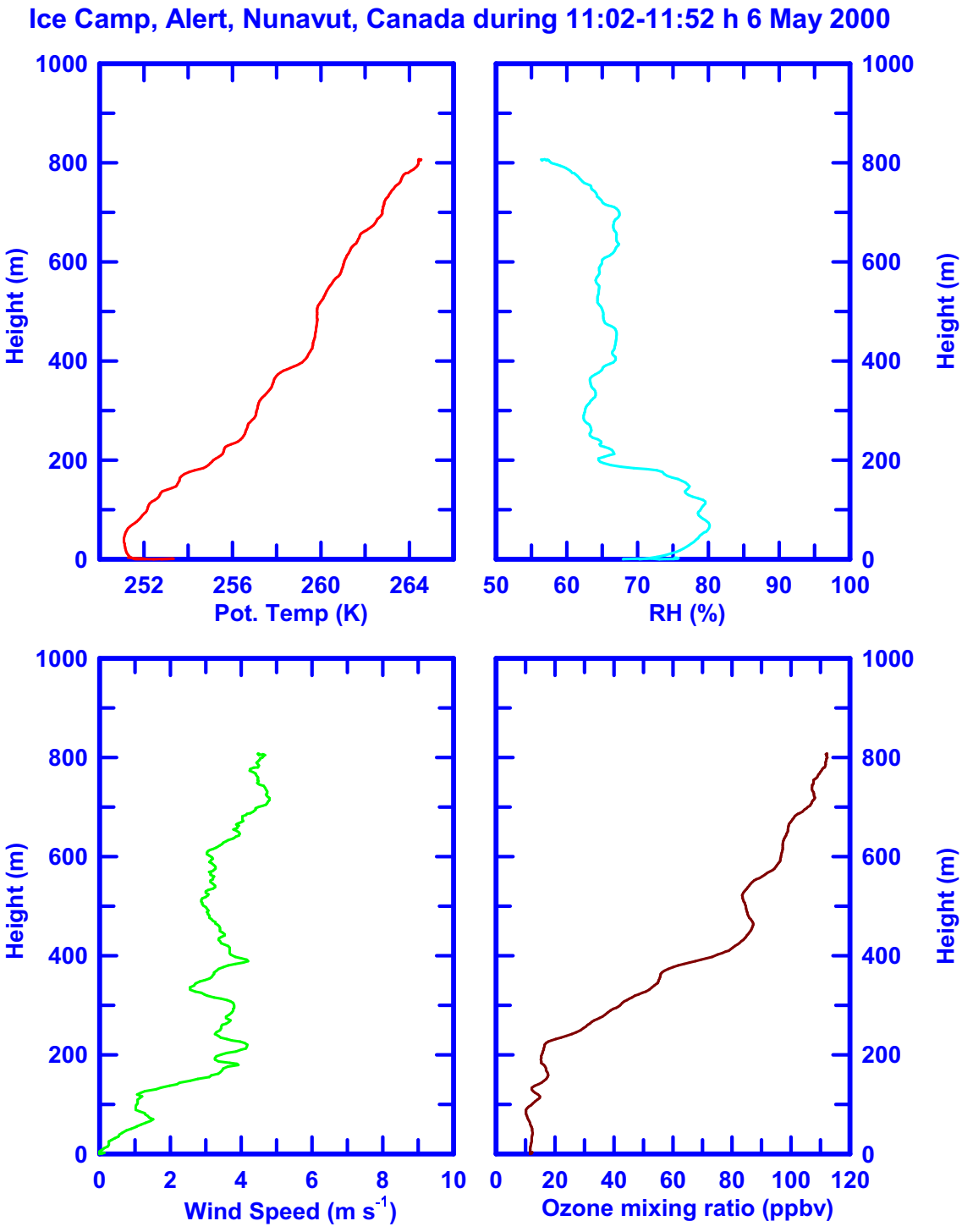

Figure 6.9: *Profiles of potential temperature, relative humidity, wind speed and ozone mixing ratios (not calibrated) measured at the Ice Camp on May 6, 2000 around noon, local time. Data provided by J. Bottenheim, J. Fuentes and J. Arnold (priv. comm. 2001).*

over the Arctic Ocean sea ice surface before reaching Alert. The fact, that sometimes enhanced BrO levels were still observed when ozone was already completely depleted at the surface can be explained by Br/BrO reactions taking place not at the surface but rather in parts of the boundary layer where ozone is still present. BrO is produced by reaction 2.26a destroying ozone that is mixed in from the free troposphere.
In Figure 6.10 DOAS BrO mixing ratios are plotted versus ozone mixing ratios. The

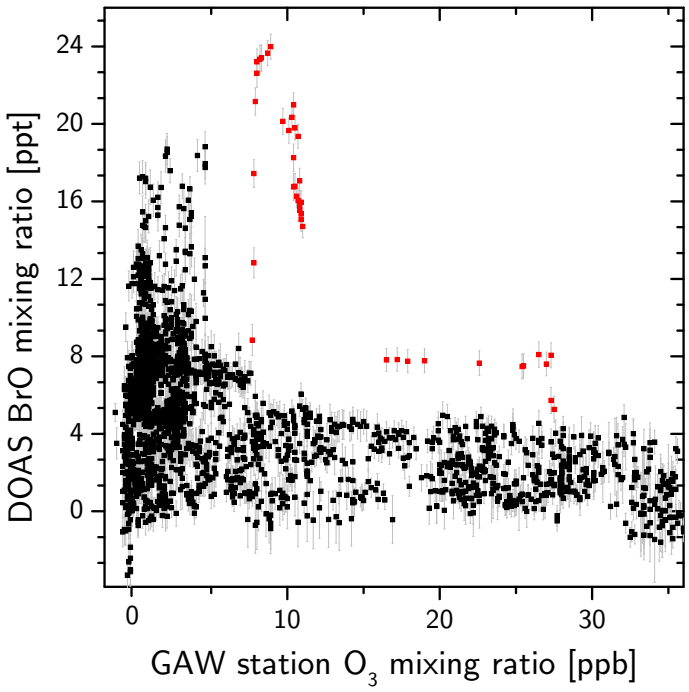

Figure 6.10: *BrO mixing ratios measured at the Ice Camp versus O_3 measured at the GAW station. The red data points indicated periods of fresh ozone depletion.*

anti-correlation of both species is obvious and agrees very well with previous studies [*Hausmann and Platt* 1994; *Tuckermann et al.* 1997; *Martinez et al.* 1999; *Lehrer* 1999]. All data points are shown for ozone levels below 36 ppb, which was taken as threshold indicating bromine chemistry. In general high levels of BrO (up to 24 ppt) coincide with ozone depletion at the surface whereas during periods of background ozone levels no BrO is detectable in the boundary layer. This behavior is typical for 'old' air masses, where catalytic ozone destruction by Br/BrO was already taking place for some days. The red data points in Figure 6.10 indicate the very beginning (April 26) of the long ozone depletion period when the catalytic ozone destruction was just starting and both species, BrO and ozone, could be observed at high mixing ratios. These results show again the importance of BrO for the understanding of Arctic ozone chemistry and stress the importance of vertical profile measurements of all involved species. The results of these measurements in the Arctic also contribute to the understanding of bromine chemistry in the marine boundary layer on a global scale.

6.3.4 Comparison with GOME Vertical Column Densities

Spectra taken from the GOME satellite instrument can be evaluated to yield vertical column densities for various trace gases, e.g. for BrO [*Wagner* 1999]. For regions polewards of 75° GOME provides a daily coverage, which can be compared to ground based measurements. For BrO GOME measurements do not provide vertical profiles. However, in many cases, particularly in polar regions, it is possible to distinguish between stratospheric background levels and BrO in the boundary layer [*Wagner and Platt* 1998; *Richter et al.* 1998; *Hegels et al.* 1998]. High BrO levels in the boundary layer usually appear as large 'clouds' on the GOME BrO maps, frequently covering several million square kilometers [*Wagner et al.* 2001]. In Figure 6.11 BrO maps for the period of the ground-based MAX-DOAS measurements are shown for the north pole region (BrO maps provided by J. Hollwedel, IUP). The GOME data shows large areas covered by BrO 'clouds', which are indicated in Figure 6.11 as red regions ($VCD_{BrO} \gtrapprox$6-7$\times10^{13}$molec/cm^2). On April 20, 2000 Alert is located at the eastern end of a large BrO cloud, so some boundary layer BrO could be derived from GOME data. It should be noted, that GOME measurements are averaged over a ground pixel size of 320$\times$40 km^2. Therefore no perfect agreement between satellite data and ground-based measurements can be expected. Nevertheless, if no large horizontal gradients are present, the comparison yields generally good agreement. From April 21 to April 26, 2000, the GOME maps show BrO VCDs for Alert of (4-5)$\times10^{13}$molec/cm^2. This is also the background VCD_{bg} for regions, where no boundary layer BrO clouds are present. The ground-based MAX-DOAS observations show maximum BrO levels of 4 ppt during this time. Assuming that 4 ppt BrO are well mixed in the lowest 1 km, a vertical column density of VCD_{bl}=1$\times10^{13}$molec/cm^2 results, which is within the variability of the satellite data. High GOME BrO VCDs are found for April 27 and for the period from April 29 to May 5, 2000 as well as on May 9, 2000. The values range between 6$\times10^{13}$molec/cm^2 and 8$\times10^{13}$molec/cm^2. The MAX-DOAS shows up to 25 ppt BrO in the boundary layer. This translates to a VCD_{bl} of 6$\times10^{13}$molec/cm^2. Adding a VCD_{bg} of 4-5$\times10^{13}$molec/cm^2 yields total VCDs of about (1-1.1)$\times10^{14}$molec/cm^2, which is higher than measured by GOME. There are several possible explanations for these deviations:

- snowdrift during high BrO events leads to lightpath enhancement in the boundary layer to which the ground-based instrument is highly sensitive, whereas the satellite likely underestimates BrO in the boundary layer because light received by the satellite might not have penetrated all the way down to the earth's surface.

- the temporal coincidence between both measurements is not guaranteed for the GOME maps and the ground-based MAX-DOAS. When the ground-based MAX-DOAS BrO data are averaged over a day, mixing ratios of 10-12 ppt result, which are in agreement with the satellite data. The BrO satellite maps are interpolated, which leads to temporal and spatial averaging. Thus smaller values for the GOME

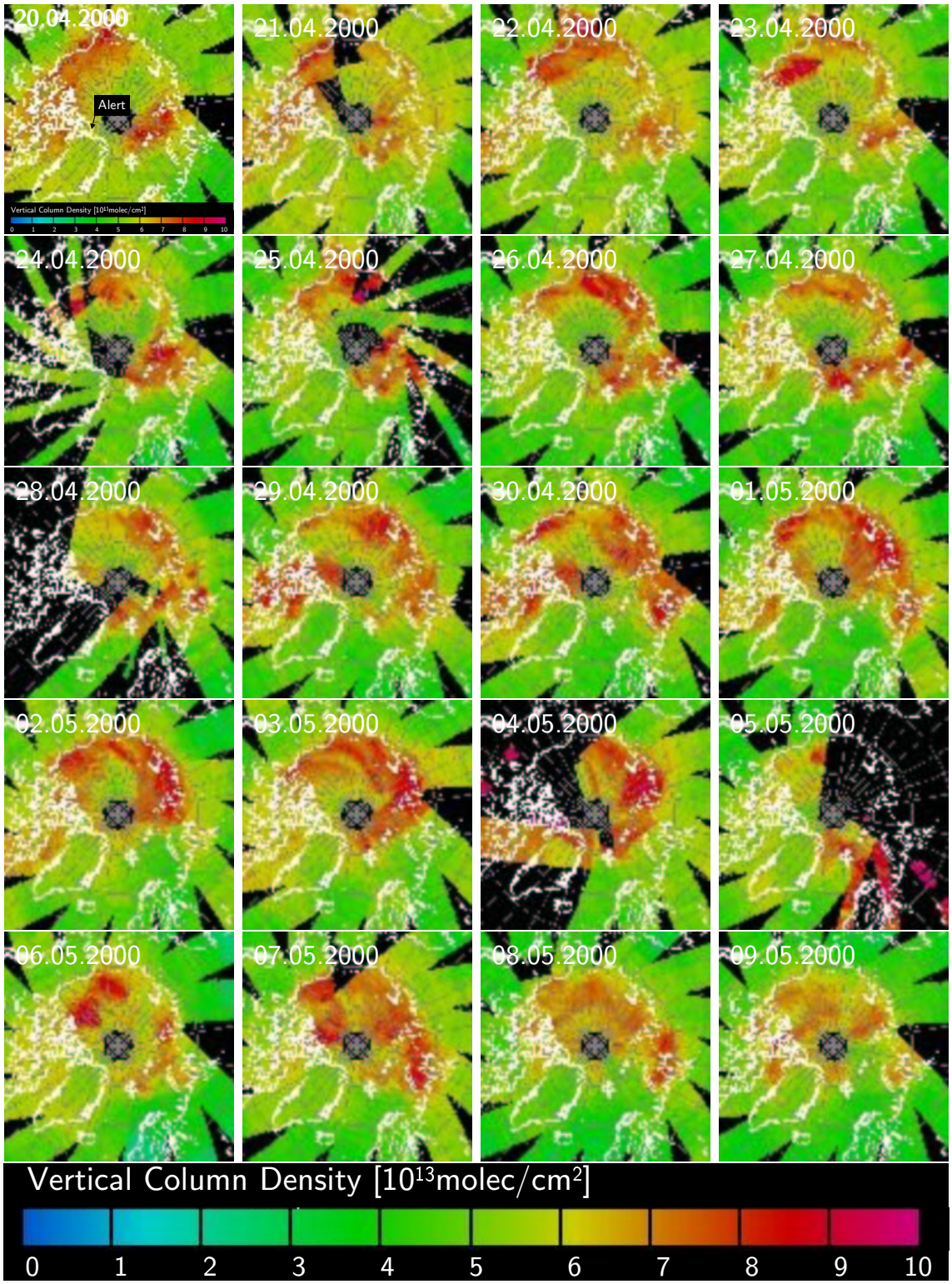

Figure 6.11: *GOME Satellite BrO Maps during ALERT2000. Vertical column densities range between 5×10^{13}molec/cm^2 and 8×10^{13}molec/cm^2 at Alert, which is indicated on the Map for April 20, 2000. GOME BrO maps were kindly provided by J. Hollwedel, IUP.*

maps result.

- BrO located higher in the free troposphere is cancelled out in the MAX-DOAS data, when ΔSCDs are calculated, since this fraction is present both in the zenith dSCDs and for the low elevation angles. Cases, when the satellite maps show higher values than calculated from precise boundary layer data and a stratospheric background VCD could point to BrO in the free troposphere. However, both deriving the stratospheric background from satellite measurements and from ground-based measurements have large uncertainties, which mask small amounts of free tropospheric BrO.

As a result it can be summarized, that the GOME BrO VCDs and the ground-based MAX-DOAS agree quite well, however, the differences between the measurements listed in Table 6.1 should be kept in mind.

	GOME	ground-based MAX-DOAS
Horizontal Resolution	320×40 km^2	10-15 km
Vertical Resolution	2 points[a]	0.5-1 km near the ground[b]
Time Resolution	<1-3 days	5 min - 1 hour
Data Product	global maps of VCD_{BrO}	$[BrO]_{boundarylayer}$, layer height

[a]boundary layer can be separated from total VCD using a regional background
[b]above 3 km altitude the method is insensitive to the vertical profile

Table 6.1: *Comparison of GOME with ground-based MAX-DOAS measurements*

6.3.5 Iodine Chemistry in the Arctic Boundary Layer

During the ALERT2000 field campaign the first MAX-DOAS measurements of the IO radical in the Arctic boundary layer were performed. While the majority of measurements yielded values below the detection limit of 1.7×10^{13}molec/cm^2 on average (minimum detection limit: 8×10^{12}molec/cm^2) there were also several cases when IO boundary layer ΔSCDs rose above the detection limit and the absorption structures of 3 IO absorption bands of the $A^2\Pi_{3/2} \leftarrow X^2\Pi_{3/2}$ transition (3-0, 4-0, 5-0) could be clearly identified in the boundary layer absorption spectra (see Figure 5.23). No IO precursors have been measured during ALERT2000. It can be assumed, however, that iodocarbons are present at low ppt levels from emissions by sea ice algae and released from the ocean which is exposed to the atmosphere at open leads (cf. Figure 2.8) in the pack ice [*Legendre et al.* 1992]. The derived IO mixing ratios of up to 0.8 ppt (corresponding to $\Delta SCD_{bl}=2\times10^{13}$molec/cm^2) are too low to cause significant destruction of O_3 themselves. However, the interaction of up to 1 ppt of IO with the observed levels of BrO can dramatically increase the ozone loss rate due to combined BrO/IO catalytic O_3 destruction cycles described in section 2.2.1.

The O_3 loss rate calculated according to equation 2.29 in ppb/h as a function of the BrO and IO mixing ratios in the range observed at Alert is shown in Figure 6.12. The fast self

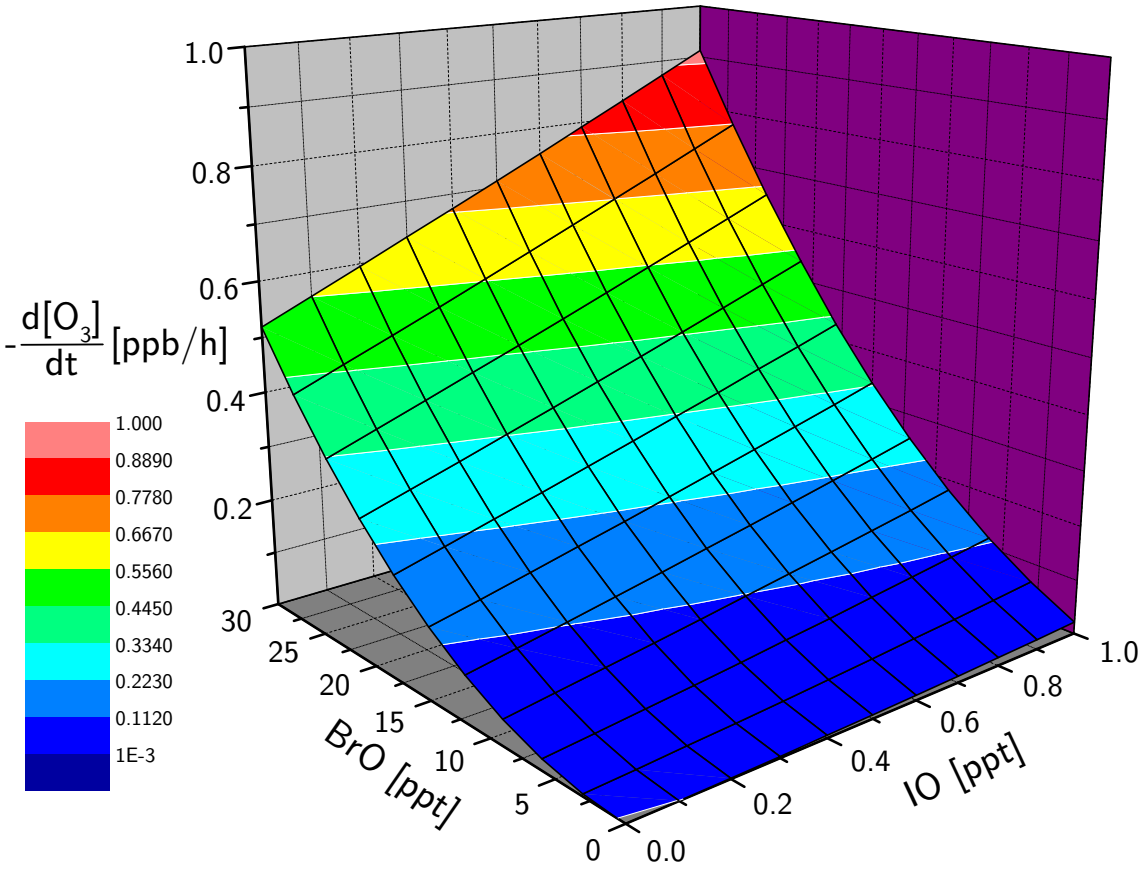

Figure 6.12: *O_3 Loss Rate as Function of [BrO] and [IO] for the levels observed at Alert. For HO_2 a mixing ratio of 1 ppt is assumed.*

and cross reactions involving IO can strongly accelerate the ozone destruction chemistry. Compared to an ozone loss of 0.5 ppb/h at 30 ppt BrO, taking into account additional 0.8 ppt IO yields O_3 destruction rates of ∼0.85 ppb/h. Therefore reactive iodine chemistry can - even at the sub-ppt concentrations measured at Alert - significantly enhance boundary layer ozone destruction during Arctic spring.

6.4 Results from Crete2000

6.4.1 Upper Limits of Halogen Oxides in the Mediterranean Region

During the Crete2000 field study the measured halogen oxides BrO, IO and OIO always ranged below the respective detection limits of the LP-DOAS instrument. Besides halogen

Species	Average	Maximum	average Detection Limit (Minimum)
BrO	n.d.[a]	-	1.5 ppt (0.7)
IO	n.d.	-	0.8 ppt (0.25)
OIO	n.d.	-	4 ppt (1.6)[b]
NO_2	0.46 ppb	4.24 ppb	0.04 ppb (0.012)
NO_3	SZA>75° 17 ppt	308 ppt	1.6 ppt (0.24)
	SZA<30° 0.29 ppt	3.8 ppt	1.6 ppt (0.45)
HONO	SZA>75° 13.8 ppt	188 ppt	53 ppt (30)
O_3	54.5 ppb	79 ppb	2.5 ppb (1.1)
SO_2	0.6 ppb	5.0 ppb	0.06 ppt (0.022)
HCHO	1.18 ppb	3.17 ppb	0.31 ppb (0.14)

[a] not detected
[b] assuming the cross section by *Bloss et al.* [2001]

Table 6.2: *Average and maximum trace gas mixing ratios of the species investigated by LP-DOAS on Crete. Also shown is the mean and minimum detection limit for the respective trace gas.*

oxides, also nitrogen compounds were a major focus of the measurements on Crete. The average levels and detection limits of all species measured by DOAS during the 4 weeks of measurements are listed in Table 6.2. The results for the measurements at Finokalia, Crete, show that the region is influenced by moderate anthropogenic pollution levels. Therefore a chemical model was used to verify, if the observed trace gas levels agree with the present understanding of the chemistry of the moderately polluted marine boundary layer.

6.4.2 Results from MOCCA Model Simulation

The chemical box model MOCCA (**M**odel **O**f **C**hemistry **C**onsidering **A**erosols) [*Sander and Crutzen* 1996; *Vogt et al.* 1996] was run in order to compare the model results with DOAS observations on Crete. MOCCA was written by *Sander and Crutzen* in FACSIMILE [*Curtis and Sweetenham* 1987], a numerical integration package for stiff differential equations. It includes the basic chemistry of HO_x, NO_x, halogen (Cl, Br, I) and limited VOC chemistry[2] both in the gas phase and in sea salt and sulphate aerosols. Details can be found in the MOCCA User's manual[3]. To model the gas phase chemistry for Crete2000, the initial gas phase mixing ratios and emission rates listed in Table 6.3 were used for the model run. The initial values were set to the average measured values where available (ozone, NO_2). For the other species and emission rates values were assumed such, that equilibrium conditions were reached after several days. Besides the initial mixing ratios and emission rates the model was adapted to the Crete2000 case by adjusting the

[2] volatile organic compounds
[3] accessible at http://www.mpch-mainz.mpg.de/~sander/mocca/

Species	Initial Mixing Ratio	Emission[a]
O_3	60 ppb	5×10^{10}molec/(cm^{2}s)
NO_2	1 ppb	
NO		5×10^{10}molec/(cm^{2}s)
CH_3I	2 ppt	6×10^{6}molec/(cm^{2}s)
C_3H_7I	1 ppt	1×10^{6}molec/(cm^{2}s)
CH_2ClI		2×10^{6}molec/(cm^{2}s)
CH_2I_2		3×10^{6}molec/(cm^{2}s)
CH_2BrI		2×10^{6}molec/(cm^{2}s)

[a]Emissions are treated as fluxes from the surface, mixed over a boundary layer of 1 km height.

Table 6.3: *Initial mixing ratios and emission rates for the MOCCA run to simulate the situation for Crete2000.*

photolysis rates to 35°N latitude during July, the temperature was set to 300 K. MOCCA was run for a period of 8 days, gas phase concentrations were output every hour. The complete model results for all gas phase species are included in the appendix on pages 228 to 235. The model results for ozone, NO_2, NO_3 and HO_x for the first 2 days of the run are shown in Figure 6.13. The model results for the species shown in Figure 6.13 com-

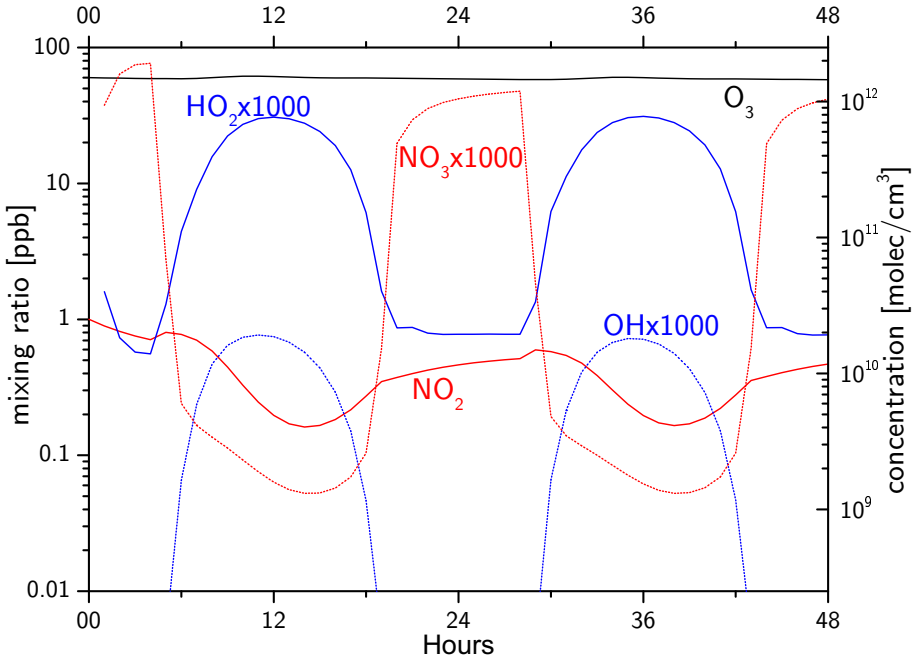

Figure 6.13: *Ozone, NO_x and HO_x results for Crete2000 MOCCA run for the first 48 hours. Note that all radical species are multiplied by 1000.*

pare very well to the average values measured at Finokalia (see Table 6.2). It is therefore assumed that the basic NO_x chemistry is correctly described by the model.

The model predictions for the bromine and iodine species $BrNO_3$, BrO, Br, Br_2, HBr, HOBr, IBr, INO_3, IO, OIO, I, HOI and HI are shown in Figure 6.14 for the first 2 days. Note that for iodine emissions of organic precursors (see Table 6.3) were included, while bromine can also be produced by heterogenous reactions on sea salt aerosol (besides the emission of CH_2BrI). Immediately after the start of the simulation (at midnight) nearly

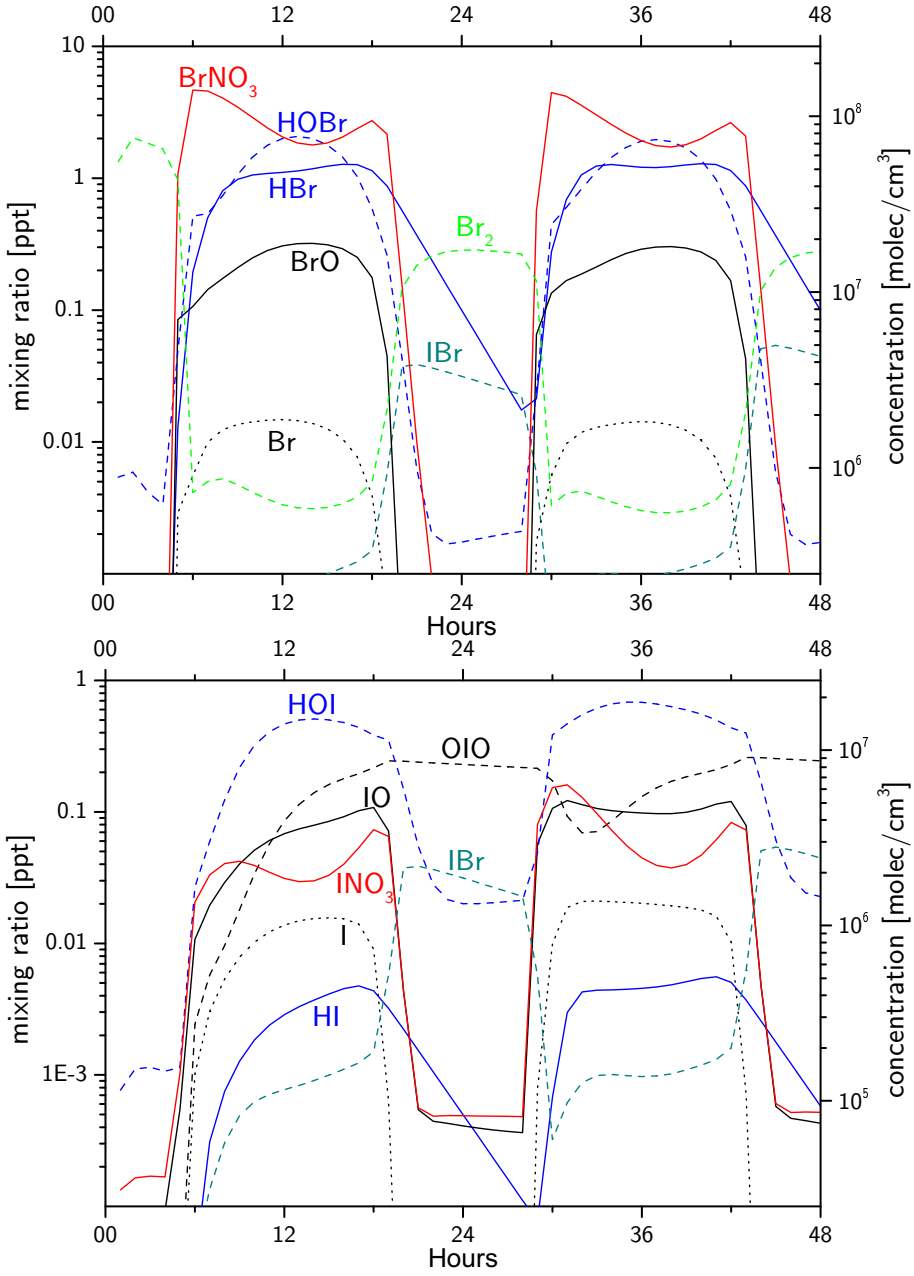

Figure 6.14: *Top: MOCCA results for bromine species at Finokalia. Bottom: Results for the main iodine species as predicted by the model.*

2 ppt of Br_2 are produced, mainly from the oxidation of sea salt bromide by N_2O_5 and NO_3 which are taken up by the aerosol (see reactions 2.39, 2.41 and 2.42 on pages 24 and 25). In the following the (re)cycling processes described in section 2.2.1 take place to yield the diurnal patterns shown. Br_2 is photolyzed at sunrise yielding Br atoms, which destroy ozone in reaction cycles 2.23 and 2.26. However, the most important daytime bromine species at the NO_x levels observed are $BrNO_3$ and HOBr, which are formed by reactions 2.30a and 2.35b of BrO with NO_2 and HO_2, respectively. The minimum of $BrNO_3$ around noon is due to its photolysis according to reaction 2.30b. The daytime maximum level of BrO predicted by the model is 0.3-0.4 ppt. This is a factor of 2 below the minimum detection limit for the LP-DOAS BrO measurements. The main nighttime reservoir species are Br_2 and IBr, while the major reactive bromine sink HBr is only slowly recycled by heterogeneous reactions on the aerosol surface overnight.
Initial iodine is only formed after sunrise due to photolysis of the organic precursor species listed in Table 6.3. The main iodine species during daytime is HOI, indicating the importance of the HO_x cycle (see reactions 2.26 on page 18) for iodine. IO is the most important reactive iodine species at maximum levels between 0.1 and 0.2 ppt in the morning and afternoon hours. OIO rises to maximum levels of 0.3 ppt just after sunset[4]. The mixing ratios for IO and OIO predicted by the model are still a factor of 2.5 and 5, respectively, below the minimum LP-DOAS detection limits during the Crete2000 measurements. INO_3 (formed by reaction 2.30a) is also an important daytime reservoir species at mixing ratios up to 0.2 ppt in the morning. Photolysis (reaction 2.30b) leads to the noontime minimum of INO_3. The main nighttime reservoir species for reactive iodine are OIO, formed by the IO self- and IO-BrO cross-reaction, and IBr, which is formed by the heterogeneous reaction of HOI with bromide on aerosols.
In summary the MOCCA simulation of halogen chemistry in the moderately polluted Mediterranean region shows significant halogen activation. However, the predicted maximum daytime levels of BrO, IO and OIO (nighttime), which were measured by LP-DOAS on Crete, are below the respective detection limits. The standard NO_x and HO_x chemistry was well described by the model run, suggesting strong halogen-NO_x interaction and an important role of the reservoir species XNO_3 (X=Br, I).

6.5 Results from the Hudson Bay Measurements

Some of the most interesting results obtained in this work are based upon the first ground-based observations of BrO and ozone at the Hudson Bay in spring 2001. Hudson Bay was proposed to be a major source region for boundary layer bromine oxide

[4]OIO chemistry is still a major uncertainty in the model, since the possible photolysis reaction yielding $I+O_2$ [*Plane et al.* 2001; *Hebestreit* 2001] is not included. The only loss processes for OIO are reactions with OH and NO.

radicals [*Richter et al.* 1998; *Wagner et al.* 2001], because the region frequently showed enhanced BrO VCDs on the GOME satellite maps. These BrO VCDs were explained by the assumption of boundary layer BrO levels comparable to the ones measured by ground-based instruments in polar regions (typically 20-30 ppt as measured by e.g. *Hausmann and Platt* [1994] at Alert and *Tuckermann et al.* [1997] at Spitsbergen). However, Hudson Bay is located much further south between 55°N and 65°N and can be classified as low Arctic region. Until the measurements were performed in this work there was still distrust in the somewhat indirect measurements from the GOME satellite instrument, because an artefact caused e.g. by cloud or ground albedo effects or anomalies of the stratospheric BrO column (elevated for very low tropopause height) could not be ruled out by the satellite observations.

6.5.1 First Halogen Oxide Measurements at Hudson Bay

Within this work the first direct bromine oxide measurements (shown in Figure 5.4.3) were carried out at Kuujjuarapik on the east coast of Hudson Bay. These measurements unambiguously identified BrO in the Hudson Bay boundary layer (see sample spectrum in Figure 3.4 on page 59) and proved its abundance at levels comparable to previous measurements at high Arctic sites [*Hausmann and Platt* 1994; *Tuckermann et al.* 1997; *Martinez et al.* 1999]. These measurements also represent the southernmost (55°N) field data for Arctic springtime ozone depletion associated with reactive bromine chemistry in the boundary layer. Additionally day/night cycles of the key species involved in surface ozone depletion were measured for the first time in this work. Figure 6.15

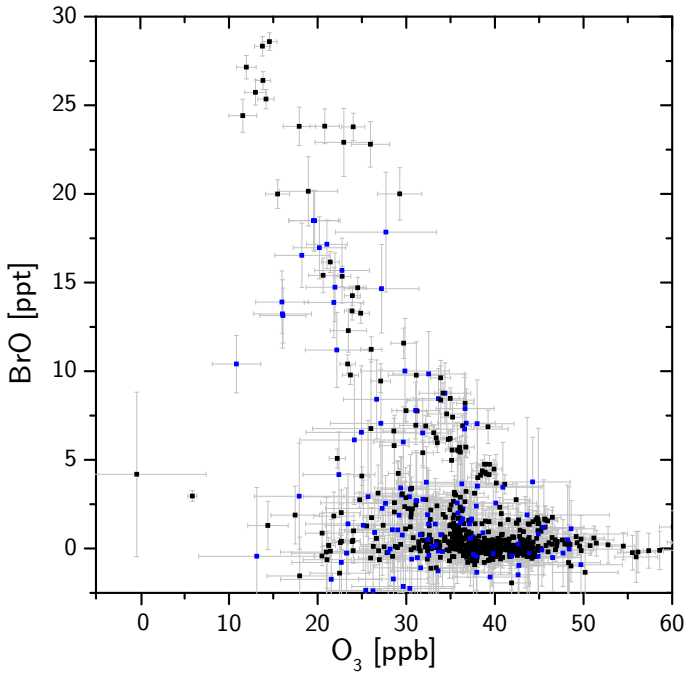

Figure 6.15: *BrO mixing ratios measured at Kuujjuarapik versus O_3. The blue data points indicate measurements from the short lightpath.*

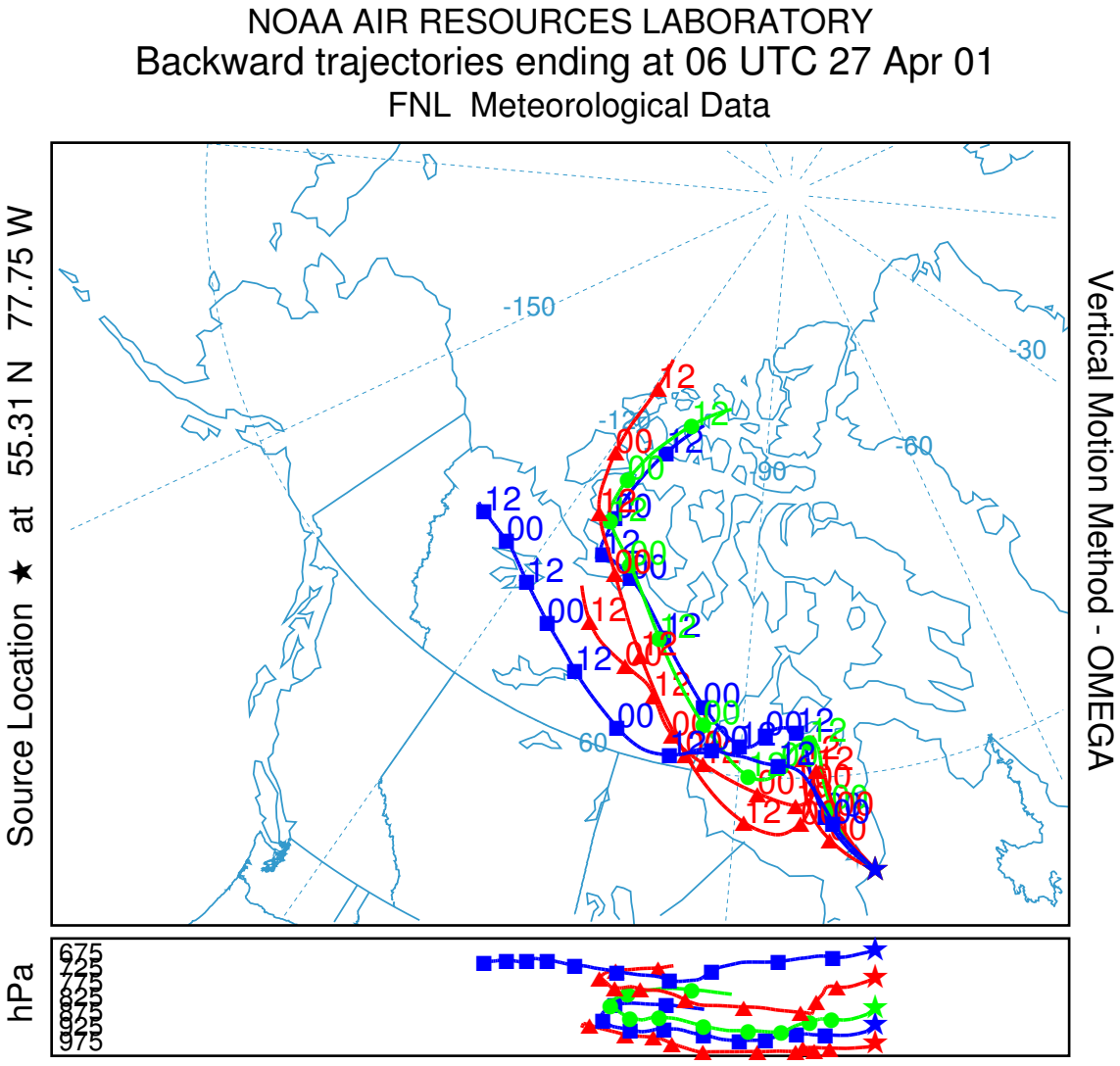

Figure 6.16: *Back trajectories ending at Kuujjuarapik on April 27, 2001, 6h UT. Height levels of 1 m, 500 m, 1 km, 2 km and 3 km are indicated in different colors.*

shows the clear anti-correlation of ozone and BrO for the complete data set obtained at Kuujjuarapik (note also the same Figure 6.10 for the ALERT2000 data). This also proves that bromine oxide is associated with surface ozone depletion involving catalytic cycles at the Hudson Bay. However, during the measurements in spring 2001 ozone depletion periods were generally short (several hours) and only one complete ozone depletion event was monitored starting on April 26 after sunset. This event was associated with strong winds from the north and heavy snowdrift which did not allow active LP-DOAS measurements due to visibilities of less than 1 km. The 5 day back trajectories calculated for this case with the HYSPLIT model [*Draxler* 1999] are shown in Figure 6.16. The trajectories ending at Kuujjuarapik during the night of April 26 to 27, 2001 show that

air masses originating from the high Arctic reached the site. These air masses could be affected by bromine chemistry and ozone destruction for several days leading to complete ozone depletion. The fact that the trajectories for the different height levels are almost parallel to the ground for the 2 days prior to the arrival at Kuujjuarapik indicates, that the vertical exchange was negligible due to stable conditions and the ozone free boundary layer was not replenished with ozone from higher altitudes. Starting at dawn of April 27, 2001 first MAX-DOAS measurements (see section 6.5.4 and Figure 6.22) and, when the visibility allowed measurements on the short lightpath after local noon, also active LP-DOAS measurements proved the influence of reactive bromine chemistry with BrO mixing ratios around 20 ppt.

6.5.2 Day/Nighttime Chemistry of Bromine Oxide

The measurements at Kuujjuarapik at the Hudson Bay also provided the first opportunity to study the photochemical changes in the chemical system involving reactive halogen species, which is responsible for ozone depletion at the surface. At high Arctic sites like Alert (82.5°N) or Ny Ålesund, Spitsbergen (78°N) during spring there is always sunlight available and the diurnal modulations with the changing solar radiation are rather weak. The southernmost study of BrO and springtime Arctic ozone depletion was carried out at Kangerlussuaq, Greenland, which is located just north of the Arctic Circle at 67°N [*Miller et al.* 1997]. *Miller et al.* [1997] also reported that at several sites further south (Edmonton and Goose Bay, Canada, 54°N; Churchill, west coast of Hudson Bay, Canada, 60°N; Iceland, 63°N and Finland, 67°N) no evidence for springtime depletion of surface ozone was found (see also [*Oltmans* 1993]).
The measurements presented here therefore not only represent the first direct measurements of BrO in the boundary layer at the Hudson Bay, but they also prove, that the phenomenon of springtime surface ozone depletion can extend as far south as 55°N in the Hudson Bay region. Since Kuujjuarapik is located at mid-latitudes, during April and May there were about 14 hours of daylight and 10 hours night. About 8 hours were completely dark, so photolysis of any chemical species could be neglected during this time[5]. The sudden changes of solar radiation during sunrise and sunset in combination with active LP-DOAS measurements at high temporal resolution (1-30 min) represent the first field observations adequate to model the photochemical changes of the chemical system involving reactive bromine compounds and ozone chemistry.

[5]maximum solar zenith angles in the first nights of the measurement period were 115°, at the beginning of May minimum SZAs around local noon were 40°.

Case Study April 18-19, 2001

As first example the observation period from noon of April 18 to sunset on April 19, 2001 is shown in Figure 6.17 on an expanded time scale. On April 18, daytime BrO

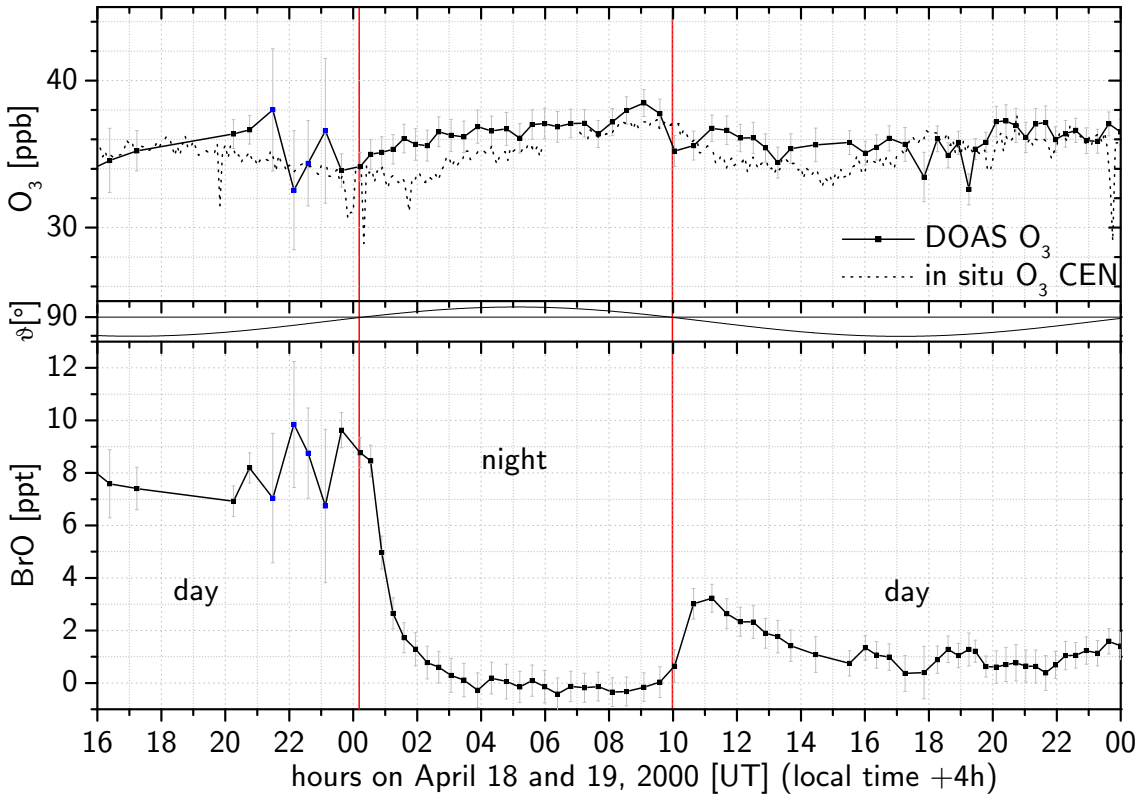

Figure 6.17: *Time series of BrO and ozone mixing ratios observed at Kuujjuarapik on April 18 and 19, 2001. Periods of day and nighttime are indicated, red vertical lines indicate the times of sunrise and sunset.*

levels ranged between 7 and 10 ppt. These BrO levels cause moderate ozone loss rates of $\leq$0.1 ppb/h[6]. The fact that ozone levels on that day are around 35 ppb indicates that the air masses reaching the site have not been subject to ozone depletion chemistry for a longer time, so 'fresh' bromine chemistry and its effects on ozone could be studied. The 5 day back trajectories ending at Kuujjuarapik on April 18, 18h (UT) are shown in Figure 6.18, indicating that the arriving air masses have passed over the frozen Hudson Bay and could be enriched in reactive bromine through the bromine explosion mechanism (see Equations 2.44). As the sun sets on April 18, a rapid decay of BrO from 10 ppt before sunset to zero within 4 hours is visible in Figure 6.17. For the DOAS ozone data before sunset no significant change is visible due to the large error bars. After sunset ozone slowly recovers from 35 to 38 ppb. Also shown in Figure 6.17 is the ozone time series

[6]calculated according to Equation 2.29 for 1 ppt HO_2, neglecting other halogen oxides

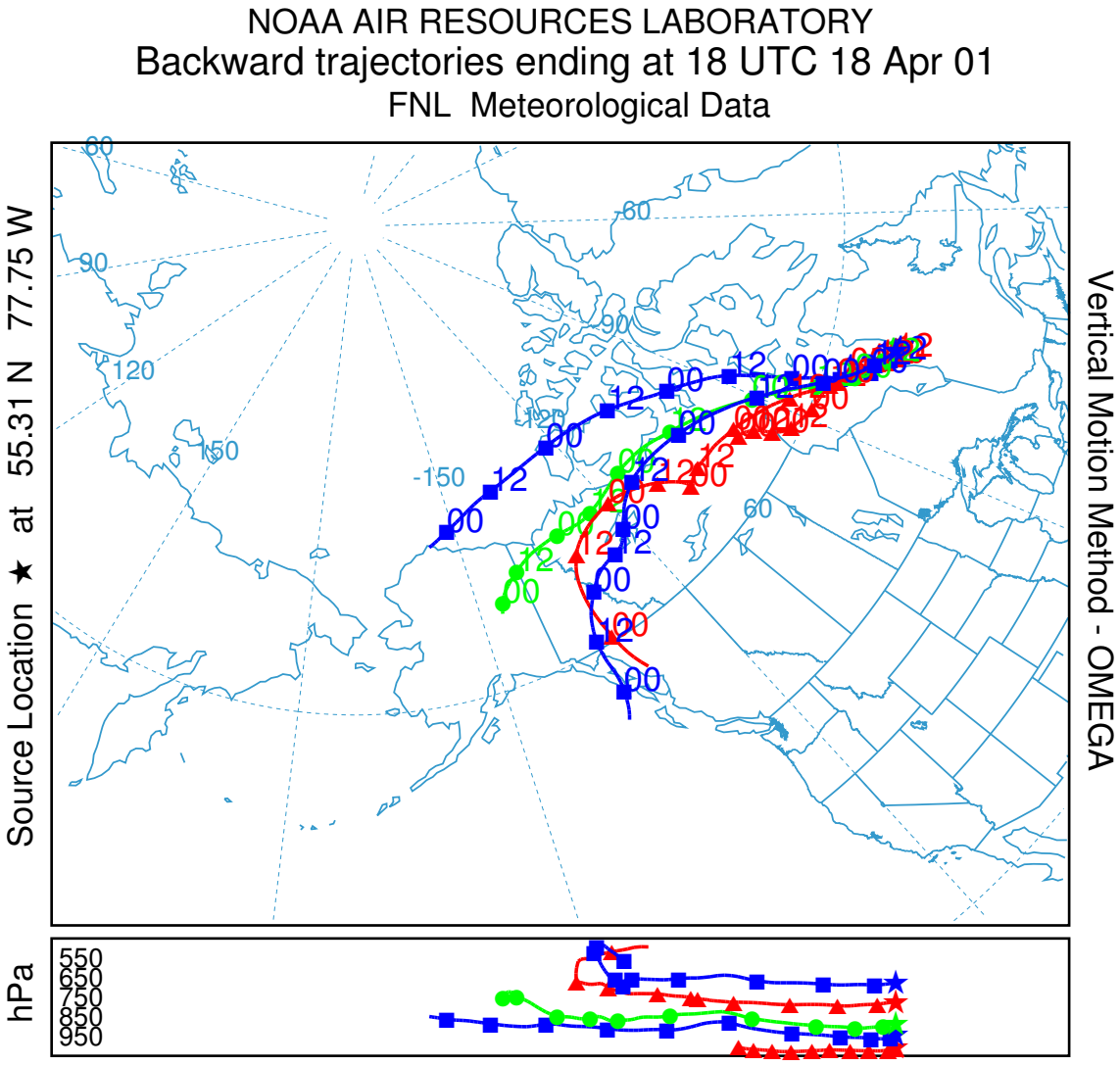

Figure 6.18: *Back trajectories ending at Kuujjuarapik on April 18, 2001, 18h UT.*

measured by the in situ monitor at the Centre d'études nordiques (CEN) in Kuujjuarapik [*Poissant* 2001]. While the DOAS measurements were taken over the Hudson Bay, the CEN is located ∼2 km inland. This may lead to enhanced vertical mixing of air in the boundary layer because of the local topography. A time offset and a more diluted effect of bromine chemistry on ozone would be expected. For this particular case the ozone time series from the CEN indeed lags behind by 1-2 hours and ozone loss rates of maximum 0.25 ppb/h can be derived.

After sunset, the BrO lifetime can be determined to τ_{BrO}=1 hour. The major reaction path for BrO radicals at night is the self reaction (see section 2.3.2), which produces

bromine atoms (85%) and bromine molecules (15%)[7]. Since Br atoms are rapidly converted back to BrO by reaction with ozone, the loss to HBr by reaction with unsaturated hydrocarbons, formaldehyde or peroxy radicals is very slow ($\tau \gtrsim 15000$ s). The lifetime with respect to Br_2 formation is 4800 s at 10 ppt BrO and 260 K, which is only slightly longer than the value of 1 hour derived from the measured BrO decay. Additional loss processes are therefore assumed to play a minor role only, however, the possible cross reactions with small amounts of ClO or IO could lead to additional loss pathways forming the reservoir species BrCl and IBr. HO_2 radicals are believed to be of minor importance at night. If present at significant levels, the reaction with BrO would yield HOBr, which can be recycled heterogeneously on aerosols or the sea ice surface to effectively produce additional Br_2 and BrCl through the reactions listed in cycle 2.44.

After all reactive bromine is converted to nighttime reservoir species, no more BrO can be produced, which is confirmed by the zero levels measured after the decay. As discussed above, Br_2 is believed to be the major nighttime reservoir species for reactive bromine at Kuujjuarapik. At sunrise Br_2 is rapidly photolyzed to yield bromine atoms which produce a morning peak of BrO and destroy ozone. This fact is clearly visible in Figure 6.17. BrO peaks shortly (30 min to 1 hour) after sunrise at levels of 3 ppt. This is in agreement with 1.5 ppt of Br_2 being present just before sunrise. The photolytic lifetime of Br_2 decreases to less than 10 min at SZA=80°, which is reached 1 hour after sunrise. At the same time as BrO shows its sunrise peak, the DOAS ozone data show a small dip from 38 ppb before sunrise to 36 ppb immediately after sunrise. This shows, that photochemical reactions starting at sunrise trigger the catalytic reaction cycles involving bromine. The same effect can be seen in the in situ ozone data measured at the CEN by *Poissant* [2001], but there the ozone decrease is not as sharp. In the following BrO levels decreased to near zero as the wind direction changed from west to south by noon on April 19, so no more air influenced by the sea ice was observed (cf. Figure 5.35).

These measurements represent the first observations of this kind. Compared to previous high latitude observations these unique measurements at mid-latitudes exhibit the key processes responsible for polar tropospheric ozone depletion in springtime on the very short time scale of only a few hours.

Case Study April 21-23, 2001

As a second example the period from sunset of April 21 to the morning hours of April 23, 2001 (shown in Figure 6.19) is considered. During the first night of this period the situation is similar as in the above case. BrO again decreases to zero by midnight. However, in this case BrO rises to values of 10 ppt 1 hour after sunrise. During this time strong northerly

[7] for T=298 K, at lower temperatures the Br_2 yield increases, for 260 K 25% Br_2 are formed.

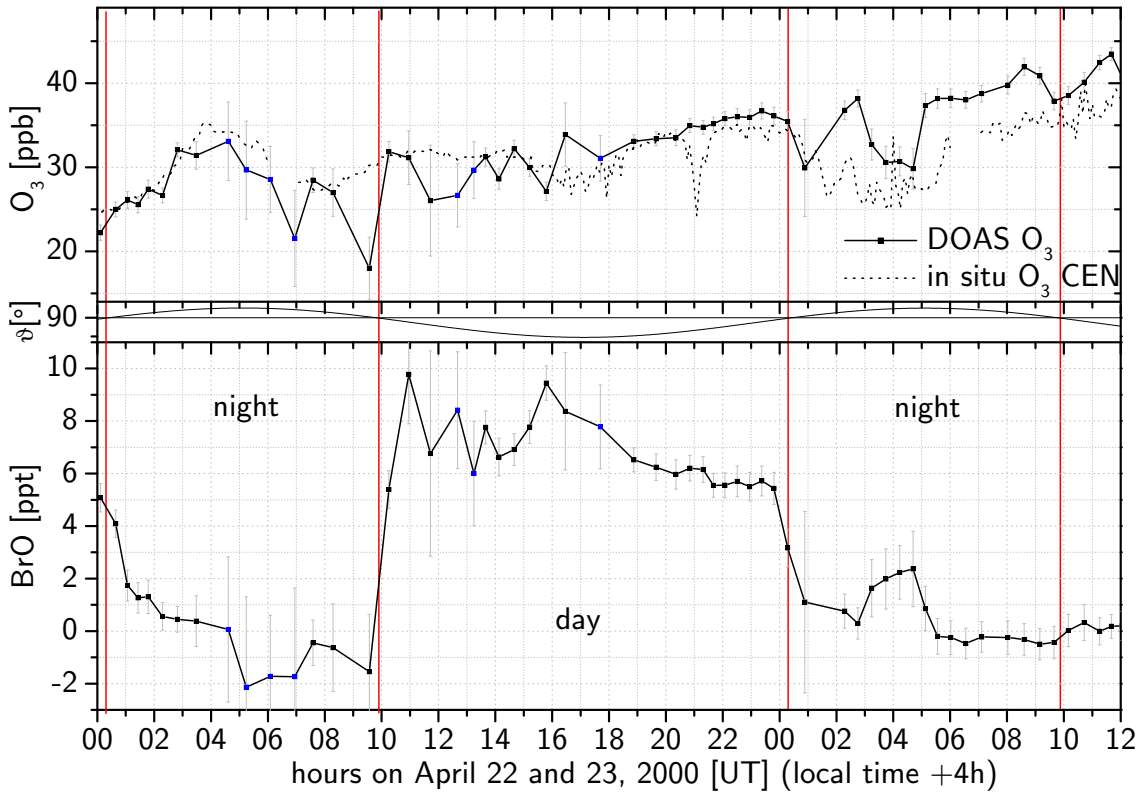

Figure 6.19: *Time series of BrO and ozone mixing ratios observed at Kuujjuarapik on April 22 and 23, 2001. Periods of day and nighttime are indicated, red vertical lines indicate the times of sunrise and sunset.*

winds were associated with snowdrift and low visibility, resulting in comparably high measurement errors for the DOAS data. The strong northerly winds changed to westerlies over the course of the day and the visibility improved. BrO levels remained high over the whole day, but effects on ozone (loss rates of ∼0.1 ppb/h at 10 ppt BrO) were probably masked by the meteorological changes. Particulary in the afternoon the simultaneous increase of ozone and decrease of BrO suggests a transport effect. After sunset on April 22, BrO first decreases to zero, but a small peak of more than 2 ppt BrO coinciding with a decrease in ozone from 40 ppb to 30 ppb is observed just before midnight.

Above the first measurements of BrO at nighttime were discussed and attributed to BrO left from the sunlit daytime due to the relatively long lifetime. The case considered here presents BrO increasing at night, which cannot be explained by commonly assumed chemical reactions. Therefore transport has to be taken into account to explain the observed phenomenon. The corresponding backward trajectories arriving at Kuujjuarapik on April 23 at 4h UT for the height levels 10 m and 500 m are shown in Figure 6.20 (top). The back trajectories show that the air mass observed around midnight at Kuujjuarapik originated from the high Arctic and had been in contact with the Hudson Bay sea ice over the

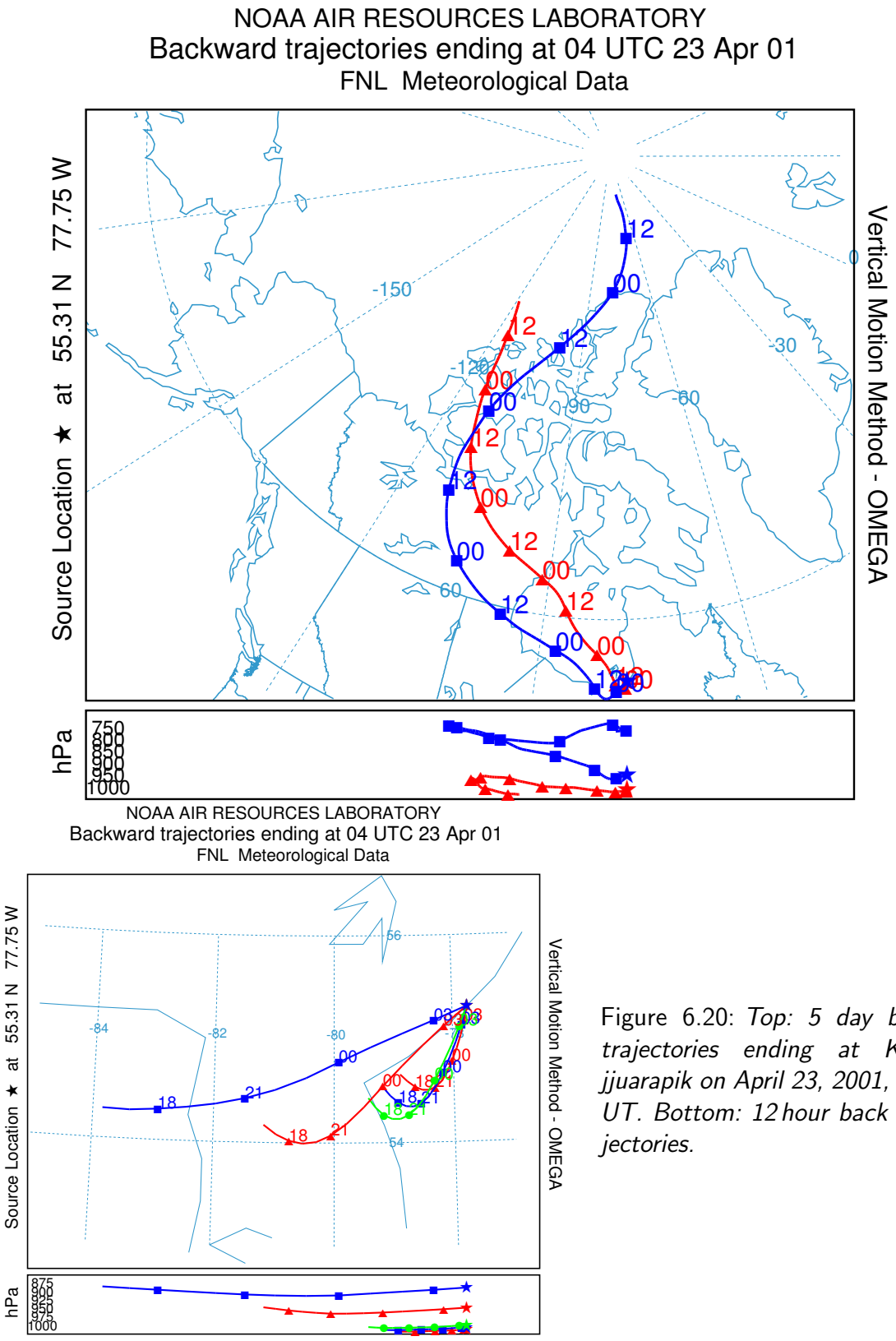

Figure 6.20: *Top: 5 day back trajectories ending at Kuujjuarapik on April 23, 2001, 04h UT. Bottom: 12 hour back trajectories.*

previous days. However, if the last 12 hours before approaching the measurement site are regarded in detail (bottom part in Figure 6.20), the trajectories show, that the observed air mass was approaching from the south. Indeed the weather station at Kuujjuarapik reported southerly winds just for the 2 hours of ozone depletion, easterly winds before and after this period. Therefore a transport effect has very likely caused the observation of BrO increase at nighttime. The observed 2 ppt BrO after 4 hours of darkness can be explained by assuming 30 ppt BrO at sunset, if the BrO self reaction leading to Br_2 formation is considered as the only loss process. Note that the BrO lifetime is very short in the beginning and increases quadratically when the BrO concentration falls. The assumed high levels of BrO before sunset in the airmass observed at midnight at the measurement site are also supported by the fact that significant ozone depletion was simultaneously observed. In summary the observations are most likely due to advection of a bromine rich airmass, which was affected by bromine catalyzed ozone destruction during the previous day.

Comparison of Measured and Modelled Photolysis Frequencies

Photolysis frequencies used for the interpretation of data from Kuujjuarapik were calculated with the model FLUX [*Röth et al.* 1996]. To show that this model correctly describes the average actinic fluxes at Kuujjuarapik, a comparison of the modelled photolysis frequencies with the photolysis frequencies j_{NO_2} of NO_2 measured at Kuujjuarapik by a calibrated filter radiometer is shown in Figure 6.21. The black data points represent all j_{NO_2} values as a function of solar zenith angle. The large scatter of the data is due to changes of the radiative transfer by clouds, fog, albedo changes, etc. The red data points result when only the downwelling actinic flux is considered. This results in a strong underestimation of the j values since due to the high reflectivity of snow at the beginning of the measurements at Kuujjuarapik the ground albedo was near 1, only in May the snow melted and the ground albedo decreased strongly. Besides the FLUX model result for j_{NO_2} and the corresponding NO_2 lifetime (> 1000 s at twilight to < 50 s at noon) also the j values included in the current version of MoccaIce[8] [*Sander et al.* 1997] calculated by the PAPER model [*Landgraf and Crutzen* 1998] are shown. Since the PAPER values were calculated for an albedo of 0 they strongly underestimate the photolysis frequencies. For the modelling studies shown in section 6.5.6 therefore the FLUX model was used to calculate the photolysis frequencies needed to describe the photochemistry in the boundary layer at Kuujjuarapik. Figure 6.21 shows, that the FLUX model also correctly predicts j_{NO_2} at solar zenith angles near 90°, which is essential to model the photochemistry around sunrise and sunset.

[8] **M**odel **O**f **C**hemistry **C**onsidering **A**erosols **I**n **C**old **E**nvironments

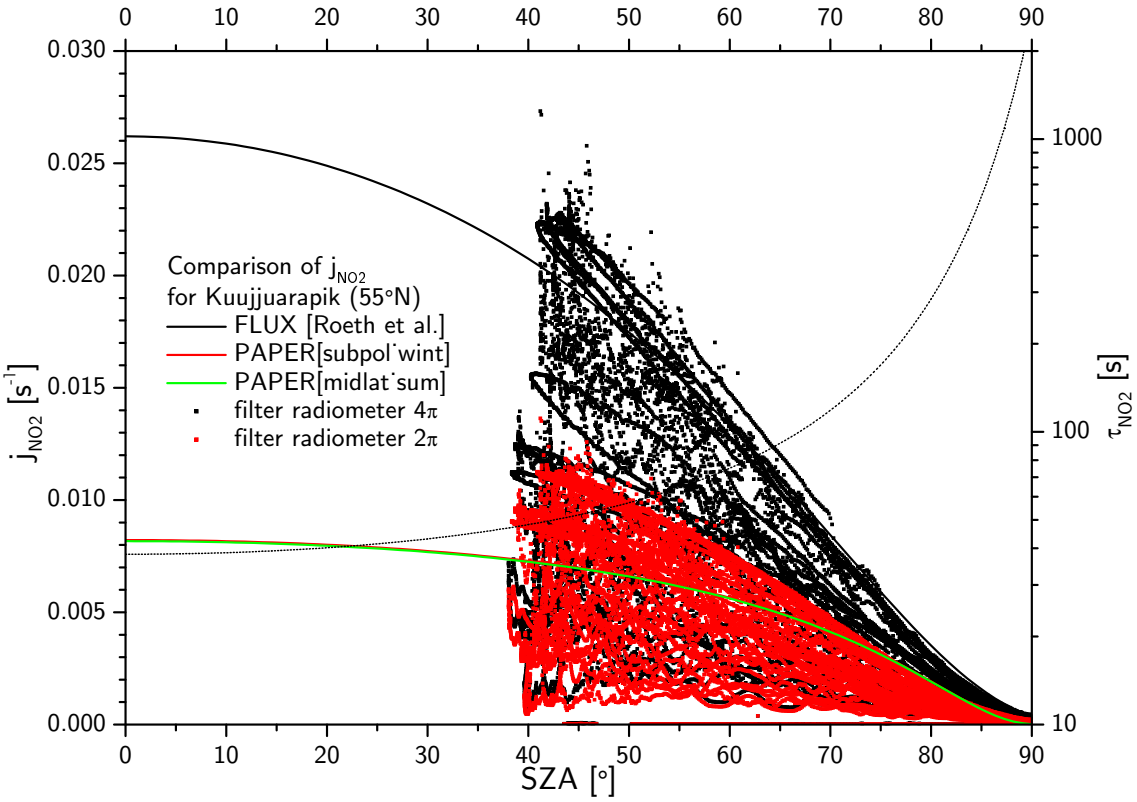

Figure 6.21: *NO_2 photolysis frequencies measured at Kuujjuarapik (black data points include the ground albedo effects, red data points consider the downwelling actinic flux only) and photolysis frequencies calculated by the FLUX model (black line, albedo=1) [Röth et al. 1996] and the PAPER model (green and red lines, albedo=0) [Landgraf and Crutzen 1998]. The black dotted line represents the NO_2 lifetime calculated by the FLUX model.*

6.5.3 Upper Limits of the Halogen Oxides IO, OIO, OBrO and OClO

For the halogen oxides IO, OIO, OBrO, OClO upper limits were derived for the low Arctic boundary layer at Kuujjuarapik, Hudson Bay. The average detection limits listed in Table 5.2 can be regarded as an indication of the upper limit for these species. For particular cases and points of time, however, it is more reliable to take the 2σ or 3σ measurement error as better indication for the upper limit at a given time.

IO was not observed at the Hudson Bay, however, as shown in section 6.3.5, even IO levels of less than 1 ppt, which cannot be ruled out for Kuujjuarapik, can strongly accelerate the O_3 loss due to combined bromine/iodine catalytic cycles and therefore have a significant impact on the ozone levels.

If both IO and BrO were present simultaneously, OIO could have been formed in the IO

self and BrO/IO cross reactions (see Table 2.2). The high detection limit for OIO during the measurements at Kuujjuarapik does not allow to draw any further conclusions.
The production of OBrO in the atmosphere in the IO/BrO cross reaction (see Table 2.2) is very unlikely. *Rowley et al.* [2001] found no indication for OBrO formation in laboratory studies of this reaction and derived an upper limit for the quantum yield of 0.15. OBrO formation in the BrO/ClO cross reaction or the BrO self reaction has not been reported either [*Turnipseed et al.* 1991; *Turnipseed et al.* 1990]. In laboratory studies of the OBrO molecule and absorption cross section (e.g. [*Knight et al.* 2000]) OBrO was produced by discharge in Br_2/O_2/He mixtures. Previous investigations of OBrO in the atmosphere were restricted to the stratosphere. OBrO was proposed at significant levels (20 ppt) in the nighttime stratosphere by *Renard et al.* [1998], however, *Erle et al.* [2000] derived upper limits of 6.4 ppt for the stratosphere at night. For Kuujjuarapik an average upper limit of 5.4 ppt OBrO in the boundary layer was derived.
OClO can be produced by the ClO self reaction as well as in cross reactions with BrO and IO (see Table 2.2). In the stratosphere it has been frequently observed in the polar vortex as an indicator for chlorine activation (e.g. [*Solomon et al.* 1987; *Leue et al.* 2001]). In the troposphere it has not been reported to date. During the measurements at the Hudson Bay OClO has not been identified in any atmospheric absorption spectrum. The average upper limit derived for the boundary layer at Kuujjuarapik was 1.7 ppt. Since the photolytic lifetime of OClO was calculated to less than 40 s shortly after sunrise and 4 s at noon for Kuujjuarapik using the FLUX model [*Röth et al.* 1996], reactive chlorine could still play a minor role during ozone depletion at the Hudson Bay, even though OClO was not observed above 1.7 ppt on average.

6.5.4 Comparison of LP-DOAS and MAX-DOAS Results

For the BrO data measured at the Hudson Bay the first intercomparison of the active LP-DOAS and passive ground-based MAX-DOAS techniques was possible. The LP-DOAS measurements yield average concentrations along the respective lightpath (7.6 km or 1.95 km) at an average altitude of 30 m above the Hudson Bay sea ice surface. The MAX-DOAS measurements on the other hand provide differential slant column densities (dSCD) for elevation angles of α=5°, 10°, 20° and 90°. From these dSCDs boundary layer ΔSCDs can be derived according to equation 6.1. The approximate height of the BrO layer can also be derived as shown in section 6.3.2. In Figure 6.22 the BrO ΔSCDs derived for the Hudson Bay MAX-DOAS measurements are shown in the bottom part (right y-axis). For the high boundary layer BrO events visible in the LP-DOAS data (top part in Figure 6.22) the pattern of the BrO ΔSCD behavior for the low elevation angles (5°, 10° and 20°, shown in different colors in Figure 6.22) is very similar to the one shown in Figure 6.3 for Alert, indicating a BrO layer of ≈1 km at the surface. In order to better

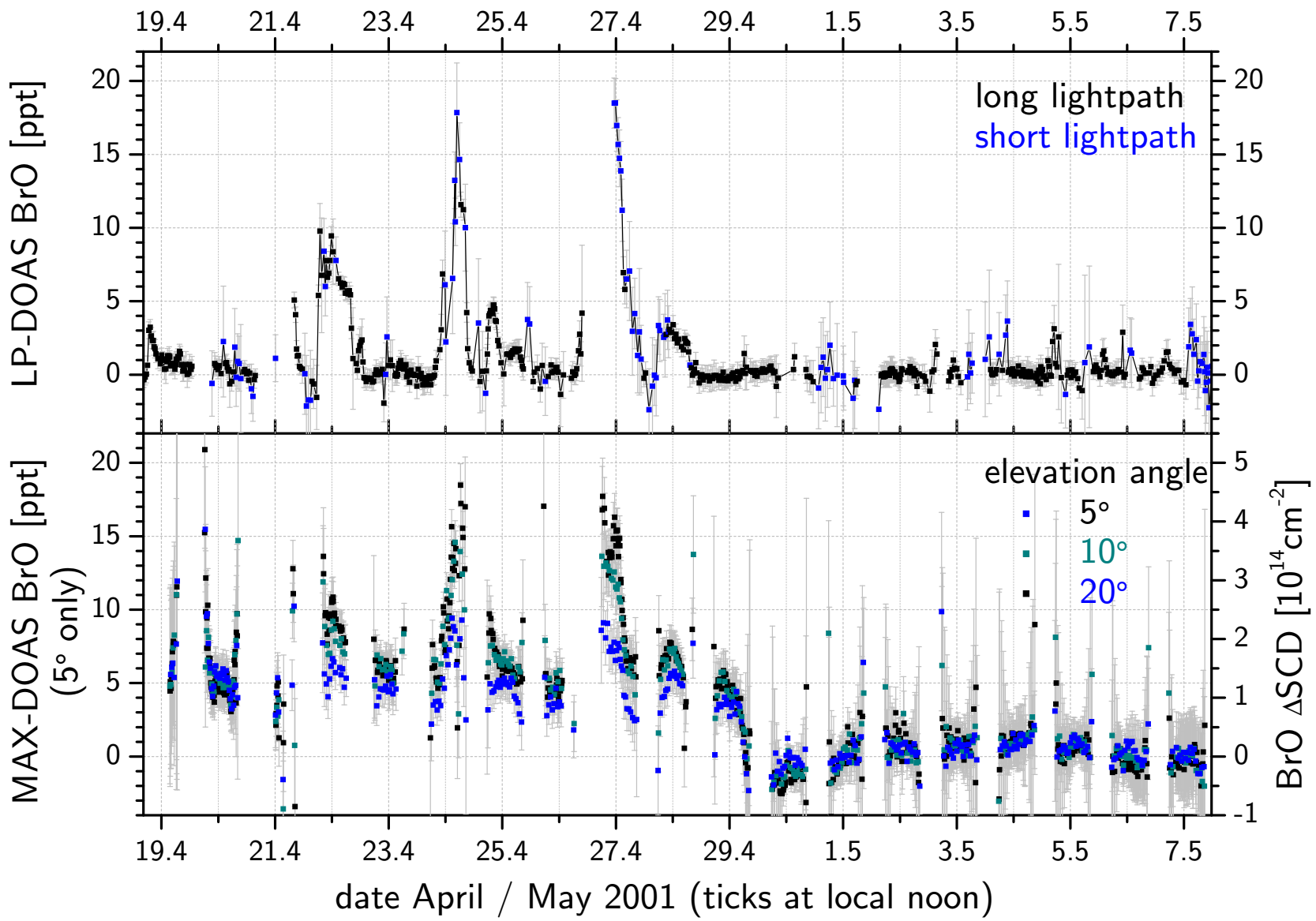

Figure 6.22: *First intercomparison for BrO LP-DOAS (top) and ground-based MAX-DOAS (bottom) measurements at the Hudson Bay. See text for details.*

compare the MAX-DOAS results to the LP-DOAS data, the ΔSCDs for 5° were therefore converted to mixing ratios according to equation 6.2 assuming a BrO layer of 1 km at the surface. For the high BrO events associated with surface ozone depletion (see section 6.5.1) the LP-DOAS and MAX-DOAS BrO mixing ratios agree perfectly both in time and absolute levels. This finding represents the first 'validation' of ground-based MAX-DOAS using the well-established LP-DOAS method and proves that MAX-DOAS measurements can - for boundary layer studies - be applied as substitute for LP-DOAS measurements. Additionally, the MAX-DOAS results provide important information on the vertical BrO profile near the surface. For the days 19.4., 20.4., 23.4., 25.4., 26.4., 28.4. and 29.4.2001, when no or very small surface ozone loss was reported and the LP-DOAS measurements show only small amounts or no BrO, the MAX-DOAS ΔSCD are still elevated and the negligible differences between the 5°, 10° and 20° geometries indicate elevated BrO layers (see section 6.3.2). These elevated BrO layers are likely to have a strong influence on the ozone budget of the polar troposphere during spring and also indicate that vertical mixing of reactive bromine from the boundary layer to the free troposphere is a probable mechanism during polar spring. An important difference between the LP-DOAS and MAX-DOAS methods is that the passive MAX-DOAS relies on the sun as its light source. Therefore measurements are only possible during daytime with limited time resolution during sunrise and sunset. In contrast, active LP-DOAS measurements using an artificial light source provide the possibility of nighttime measurements and high time resolution also during dawn and dusk, when the atmospheric photochemistry involved in the ozone destruction cycles changes rapidly. A major drawback of the LP-DOAS method is, that no measurements are possible during snowdrift and low cloud/fog episodes frequently observed during ozone depletion events in the Arctic, because no light is received from the retro reflectors at low visibilities. MAX-DOAS can provide valuable information during these episodes, e.g. during the Hudson Bay measurements on April 21 and before noon on April 27, when major BrO events were observed and LP-DOAS measurements could not be performed due to visibilities as low as 100 m. The comparison of LP-DOAS and ground-based MAX-DOAS is summarized in Table 6.4.

6.5.5 Comparison of Boundary Layer BrO Data with GOME Maps

In the same way as for the ALERT2000 ground-based BrO data (see section 6.3.4), boundary layer BrO measured by both active LP-DOAS and MAX-DOAS can be compared to satellite measurements of BrO vertical column densities from the GOME instrument. In Figure 6.23 BrO maps for the period of the ground-based MAX-DOAS measurements are shown for the Hudson Bay region. Kuujjuarapik is marked with a blue diamond symbol at the south east coast of Hudson Bay (BrO maps provided by J. Hollwedel, IUP). During the

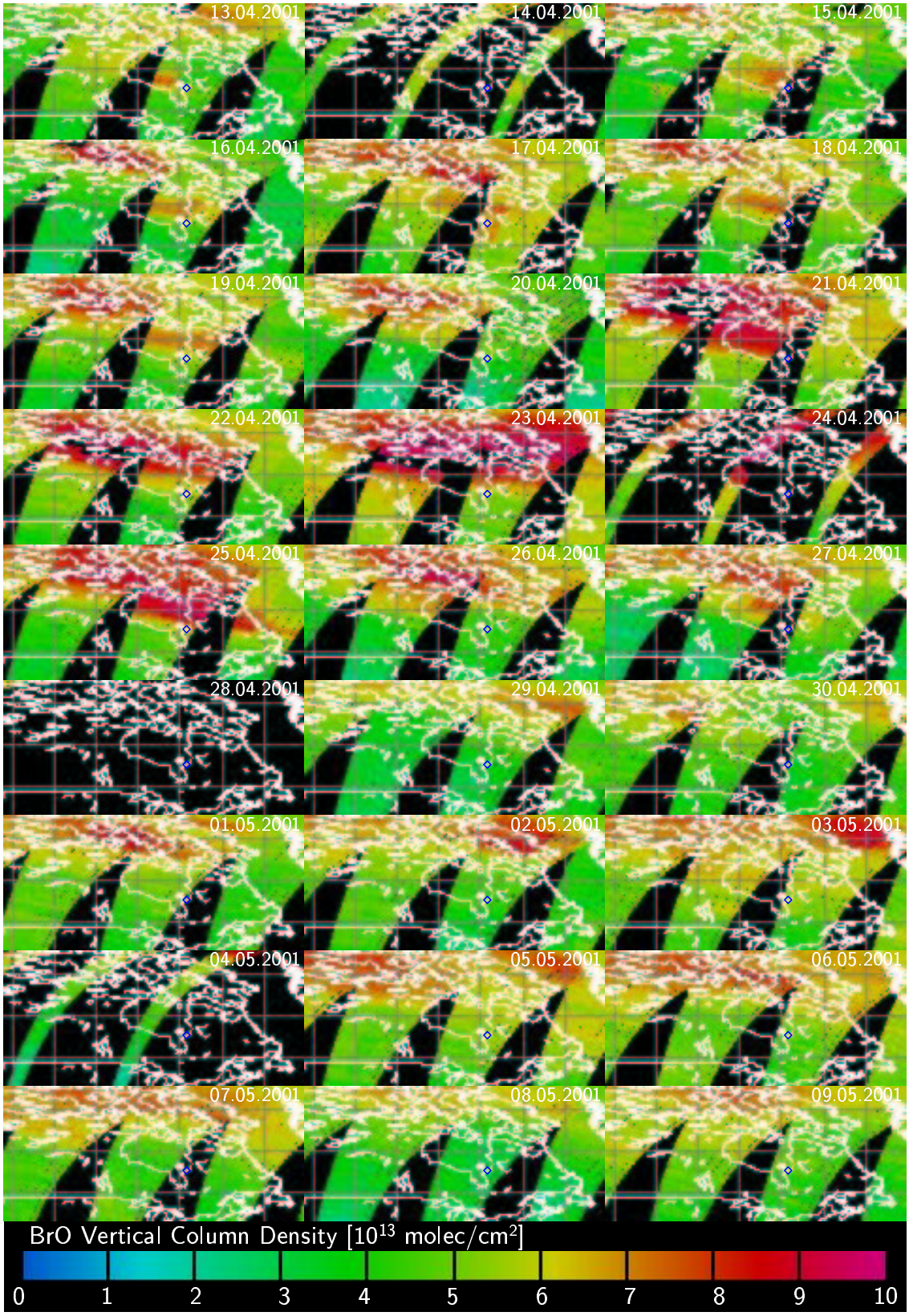

Figure 6.23: *Daily GOME satellite BrO maps during the Hudson Bay campaign: Kuujjuarapik is marked with a blue diamond symbol at the east coast of Hudson Bay. Vertical column densities range between 5×10^{13} molec/cm^2 and 8×10^{13} molec/cm^2 at the station. GOME BrO maps were kindly provided by J. Hollwedel, IUP.*

	LP-DOAS	MAX-DOAS
time resolution	1-30 min	5-60 min[a]
performance at low visibility	short lightpath or not possible	qualitatively correct measurements
light source	artificial (lamp)	sun (daytime)
vertical resolution	only for several lightpaths	500 m-1 km in the BL
accuracy	concentrations ±5-10%[b]	10-20% for ΔSCDs 50-100% for concentrations[c]
experimental effort	high, frequent service	low, works automated

[a]time resolution depends strongly on the measurement loop (number of α's, sequence)
[b]averaged along lightpath
[c]depends on RTM model precision

Table 6.4: *Main characteristics of the LP-DOAS and MAX-DOAS methods.*

first half of the period (upper half of Figure 6.23) Kuujjuarapik was almost daily affected by bromine oxide 'clouds', shown as orange to red patches in the satellite maps. From April 29 to the end of the ground-based measurements GOME did not observe any BrO clouds near Kuujjuarapik. The BrO VCDs during that time allow to derive a seasonal background (containing the stratospheric BrO column and a possible free tropospheric fraction) VCD_{bg} $\approx 4\times10^{13}$molec/cm^2. In order to compare the satellite and ground-based data, this background VCD was added to the boundary layer VCD_{bl} calculated from the boundary layer mixing ratios/ΔSCDs under the assumption of a 1 km homogeneously mixed BrO layer at the surface. The GOME instrument passes above Kuujjuarapik approximately at 10:15h local time each day. In Figure 6.24 the BrO VCDs measured by GOME and the corresponding VCD calculated from VCD_{bg} and VCD_{bl} from the ground-based MAX-DOAS instrument at 10:15h local time are compared. The comparison shows an agreement of both data sets for the majority of days. However, there are also strong deviations visible for a few cases. Especially on April 27 and 29 the GOME data shows VCDs about 2×10^{13}molec/cm^2 smaller compared to the ground-based instrument. In contrast, on April 25 and from May 3 to 6 the GOME VCDs are higher by 1×10^{13}molec/cm^2. The deviations of GOME VCDs can be explained by the following differences between the both measurement platforms:

- snowdrift and low clouds during high BrO events are associated with enhanced absorption paths in the boundary layer to which especially the ground-based instrument is sensitive. In contrast, BrO located close to the surface and interstitial BrO might be shielded from the satellite due to the high albedo of the cloud top (applies to April 27 and 29).

- the spatial averaging of the satellite instrument (320 km×40 km) and no perfect

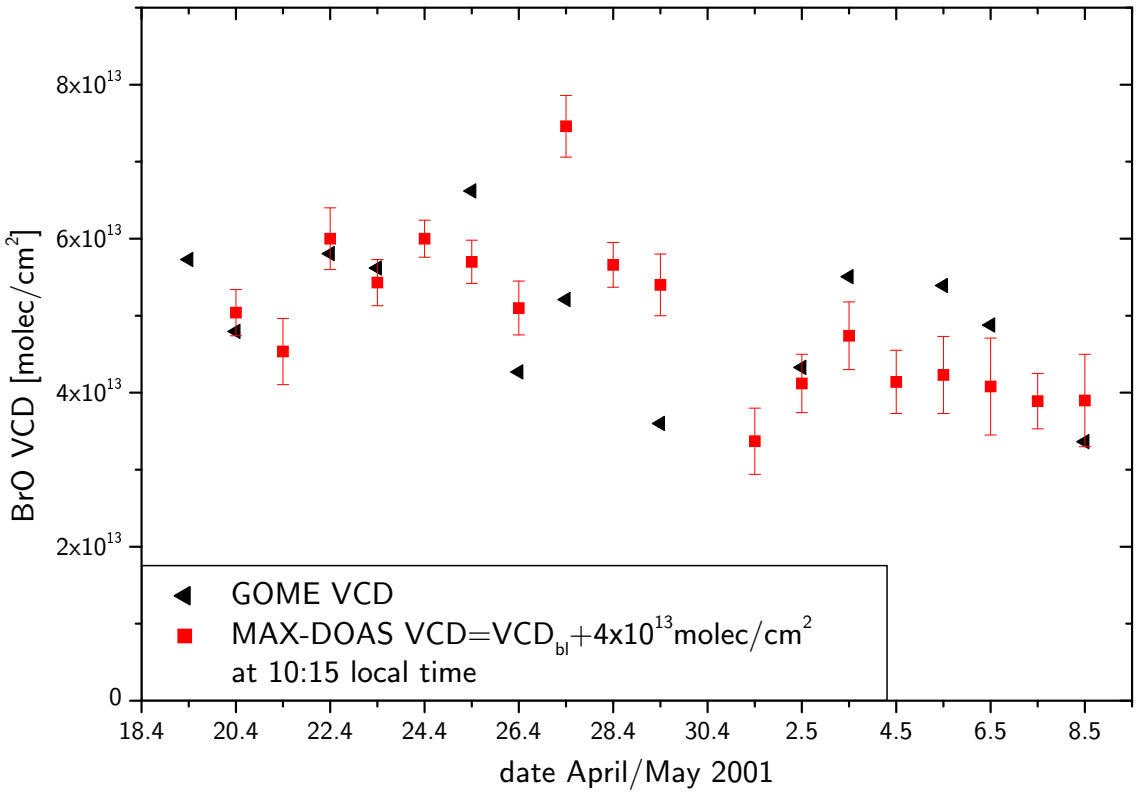

Figure 6.24: *Daily GOME BrO VCDs for the Kuujjuarapik pixel compared to VCDs calculated from the MAX-DOAS ΔSCDs during the Hudson Bay campaign: VCD_{bl} was calculated assuming a 1 km homogeneously mixed surface layer, and a background VCD of 4×10^{13} molec/cm^2 was added to yield total columns. GOME BrO time series provided by J. Hollwedel, IUP.*

temporal coincidence between both measurements may explain deviations of the VCDs in both ways.

- towards the end of the ground-based measurements at the beginning of May the ground albedo of the Kuujjuarapik pixel has changed significantly because the snow at the Hudson Bay coast melted completely. Additionally the surface of the Hudson Bay was covered with a layer of liquid water on top of the ice which also led to a much smaller ground albedo. If this effect is not taken into account correctly, wrong airmass factors may result and the BrO VCDs could be wrong.

- an incorrect or variable VCD_{bg} strongly affects the ground-based data at the beginning of May, since the boundary layer VCD_{bl} was close to zero after May 1^{st}.

As a result it can be summarized, that the GOME BrO VCDs and the ground-based MAX-DOAS measurements agree quite well. The differences found can be explained by

systematic differences between the two measurement platforms. Additionally the differences pointed out in the comparison for Alert (see Table 6.1) should be noted.

6.5.6 Results of a 1D Model to Simulate Day/Nighttime Chemistry of Halogen Oxides at Kuujjuarapik

For the modelling studies presented here, the 1-dimensional model developed by *Lehrer* [1999] was adapted to the conditions at Kuujjuarapik. The model proved to be adequate for modelling the bromine release processes ('Bromine Explosion', see section 2.3.1) which cause the phenomenon of surface ozone destruction in polar spring. It was also found by *Lehrer* [1999] that the high sea salt concentrations of the sea ice surface are needed to explain the observed amounts of bromine found at various sites in the Arctic. Additionally the recycling of the inactive species HOBr and HBr on aerosol surfaces was needed to sustain the high bromine concentrations for a longer time. The model includes the basic gas phase chemistry for HO_x, NO_x, and VOCs, photochemistry as well as chlorine and bromine reactions. Additionally heterogeneous recycling reactions of HOX (X=Cl, Br) and HX on aerosols and primary release processes via the reaction of HOX with sea salt on the sea ice surface are included in the model. The vertical mixing over the boundary layer (assumed vertical extent 1 km) is parameterized for turbulent diffusion between 8 boxes with thicknesses of 100 μm above the sea ice surface logarithmically increasing to 900 m.

The model was adapted for the situation at Kuujjuarapik especially including correct parameterization of the diurnal variation of the photolysis frequencies. The results for j_{NO_2} were compared to the values measured by a calibrated filter radiometer in section 6.5.2 above. Because of the reasonable agreement for j_{NO_2}, the uncertainties of the photolysis frequencies for the other photolyzable compounds is believed to be of minor importance.

The model has already been applied to study the primary release processes when negligible initial bromine was present and to investigate vertical gradients and the effects of vertical mixing [*Lehrer* 1999]. In this work the model was initialized with 60 ppt total bromine at night in order to investigate the day and night chemistry on short time scales of a few days. The initial bromine concentration was chosen such that the daytime maximum values of BrO were in the range of the measurements. Initial amounts of NO_x (5 ppt NO, 5 ppt NO_2) were found to be negligible. The results of the model run for the first four days are shown in Figures 6.25, 6.26 and 6.27. For the comparison with the field measurements at Kuujjuarapik the first three days (72 hours) are adequate. The fourth day represents a situation of complete ozone loss which was not observed during the field measurements at Kuujjuarapik. Ozone is depleted over the course of 4 days from background levels of 40 ppb to less than 1 ppb. It should be noted that ozone depletion always stops over night because photochemistry is needed for efficient catalytic ozone destruction. BrO shows a

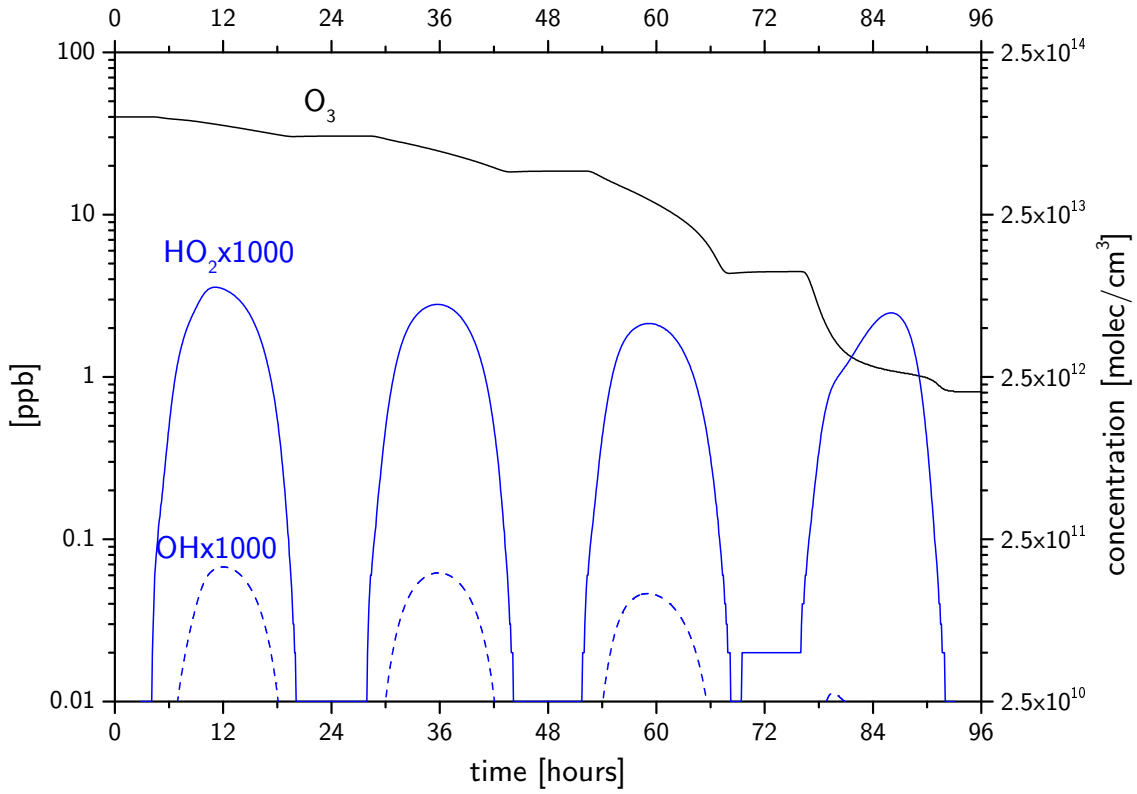

Figure 6.25: *Model results for O_3, HO_2 and OH for the simulation of the Kuujjuarapik situation.*

sharp early morning peak due to photolysis of nighttime reservoir compounds (Br_2 and BrCl) at sunrise. This agrees well with the findings discussed in section 6.5.2. The BrO decrease after sunset from ∼30 ppt at sunset to 0.7 ppt over the course of the night is also in agreement with the observed nighttime decays of BrO with corresponding lifetimes of the order of <1 hour at 30 ppt BrO and >10 hours at 1 ppt BrO derived from the field data. In the model Br_2 is also the predicted major reservoir species during the night at levels up to 20 ppt. This supports the proposed major role of Br_2 as a nighttime reservoir, which is responsible for sunrise peaks of BrO radicals observed at Kuujjuarapik. HOBr, which is always present at high levels until ozone is completely depleted, is efficiently recycled in the model and HBr is the final loss compound for reactive bromine after complete ozone depletion. The almost constant level of HOBr also indicates that the abundance of HO_2 radicals, which are needed to produce HOBr, is not a critical parameter in this case.

For reactive chlorine, the major compound is the interhalogen molecule BrCl, formed mainly by the heterogeneous reaction of HOBr with HCl on aerosols. BrCl builds up in the model simulation to levels of up to 4 ppt over night, so it can produce Br and Cl atoms by photolysis during sunrise. The ClO peaks predicted by the model at sunrise are probably not detectable by DOAS, because the detection limits are of the order of 10 ppt

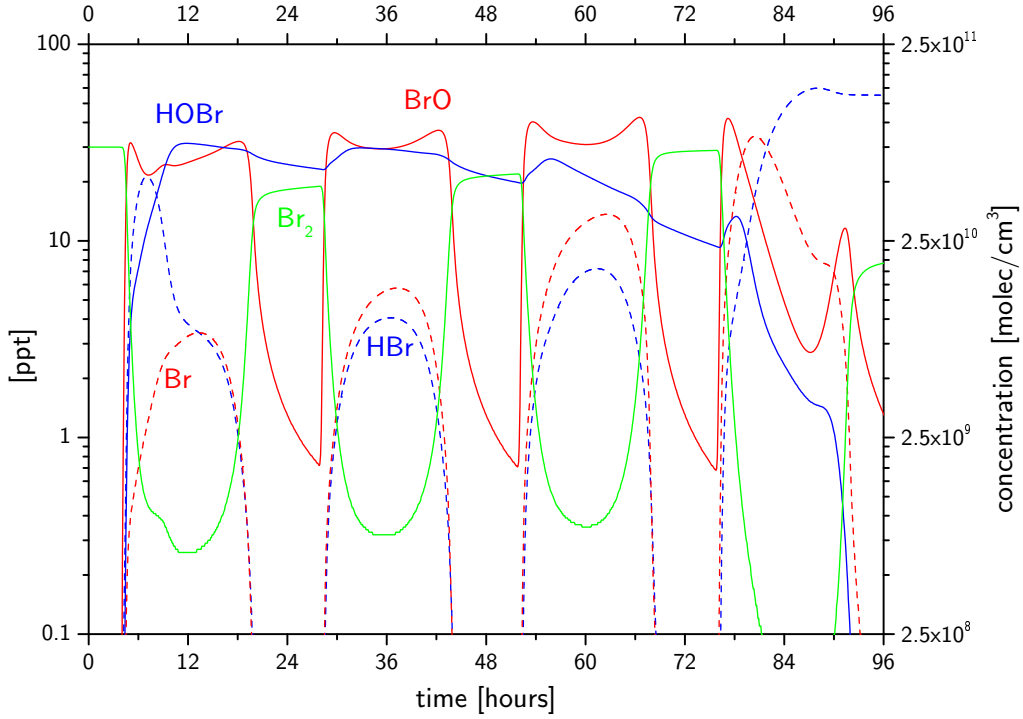

Figure 6.26: *Model results of the major bromine species for the simulation of the Kuujjuarapik situation.*

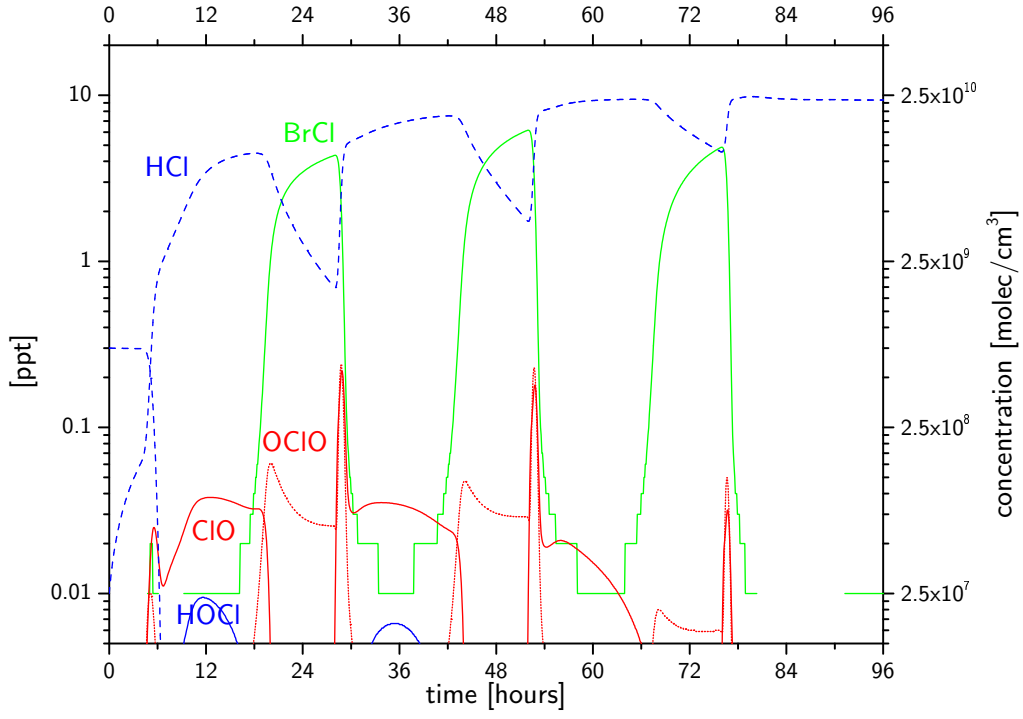

Figure 6.27: *Model results of the major chlorine species for the simulation of the Kuujjuarapik situation.*

[*Tuckermann et al.* 1997]. Maybe chemical amplification can be used to measure the early morning behavior of ClO [*Perner et al.* 1999]. OClO formation is shown by the model to yield highest values at sunrise and sunset, but mixing ratios of ≈2 ppt have to be present to be detectable by DOAS measurements. The main loss of reactive chlorine are reactions with organic compounds (e.g. methane, CH_4) to form HCl. HCl is only lost at night due to recycling processes on aerosols involving HOX (X=Cl, Br).
To summarize, the model simulations strongly support the findings discussed in section 6.5.2 and seems to correctly describe the day/night cycle of bromine and chlorine compounds for the situation at Kuujjuarapik. Iodine chemistry is not yet included in the model, but future applications, e.g. to model the observations at Alert, where IO was first measured simultaneously with BrO in this work, would require iodine and combined iodine/bromine chemistry to be included in the model.

6.6 The Role of BrO as Oxidant for Gas Phase Mercury

The possible role of BrO as oxidizing species for gaseous elemental mercury (GEM) has been proposed by *Boudries and Bottenheim* [2000] (see also section 2.5.2). The measurements shown in this work represent the first simultaneous observations of both Hg^0 and BrO at high time resolution allowing to study the proposed oxidation reaction between the two molecules. The scatter plot in Figure 6.28 shows the anti-correlation between both species for the ALERT2000 field study. At Alert, mercury depletion events (MDE) were

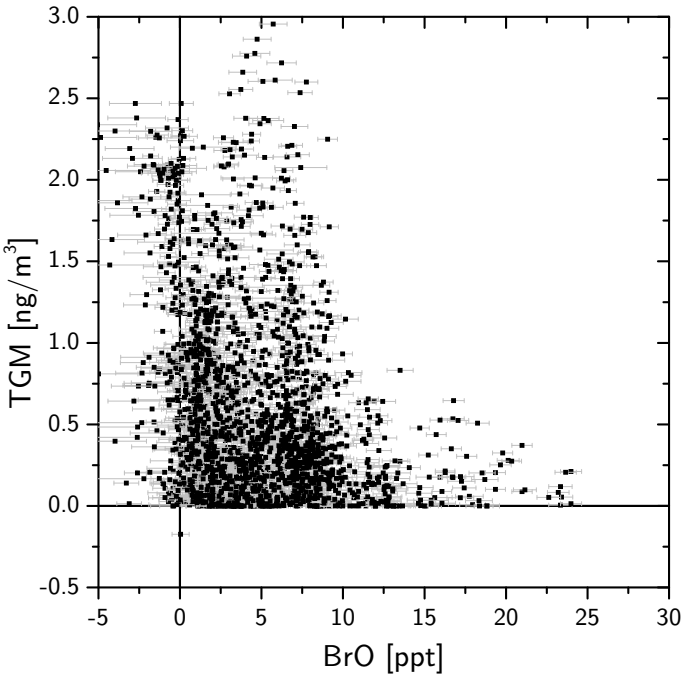

Figure 6.28: *TGM concentrations measured by Steffen et al. [2002] versus MAX-DOAS BrO mixing ratios.*

frequently observed during the period of MAX-DOAS BrO observations at the Ice Camp. The time series shown in Figure 5.24 exhibits a strong decrease in the mercury concentration on April 26, 2000, which is shown on an extended time scale in Figure 6.29. The

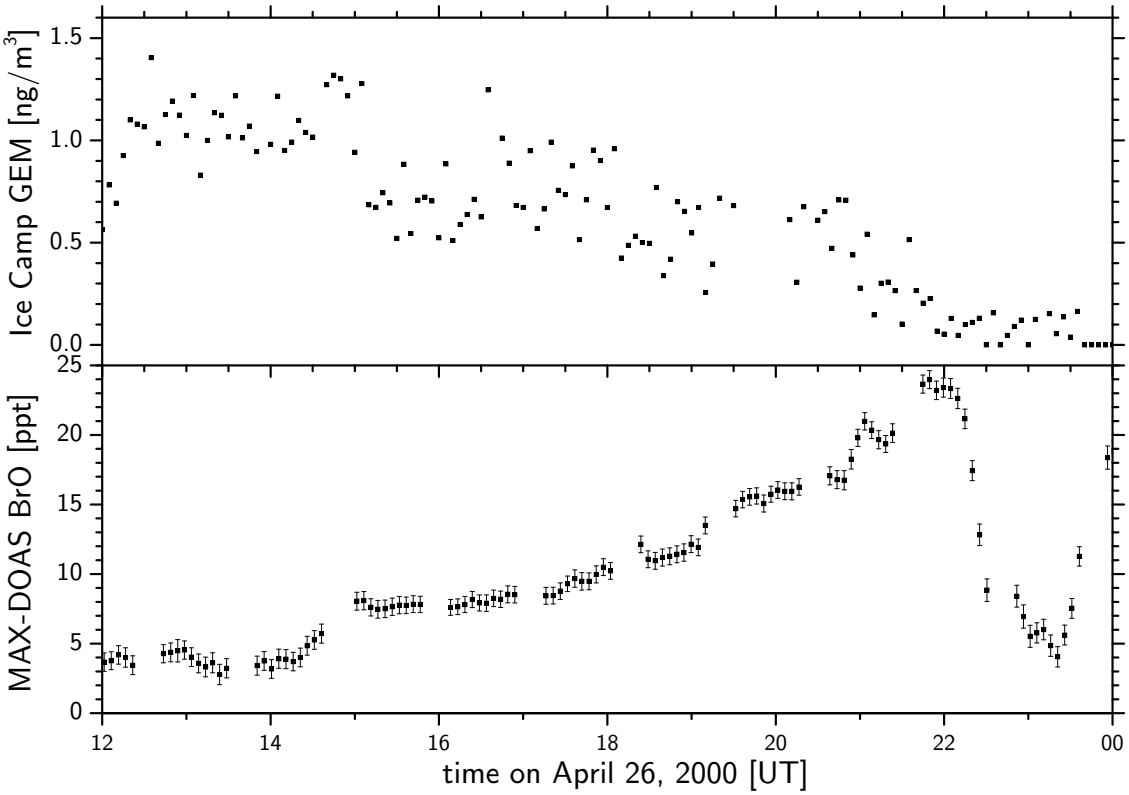

Figure 6.29: *Time series of GEM and BrO at the beginning of the ozone and mercury depletion period.*

1 ng/m^3 Hg, which was still present at 12:00 UT, was completely depleted by 00:00 UT on April 27. Assuming the rate limiting step for this rapid loss of Hg^0 to be the proposed reaction 2.63 of Hg with BrO and neglecting all transport effects, the rate constant k_{Hg+BrO} for this reaction can be estimated to

$$k_{Hg+BrO} = \frac{1}{\tau_{Hg^0} \cdot [BrO]} \tag{6.3}$$

where τ_{Hg^0} is the lifetime of GEM. Assuming an upper limit of 12 hours for τ_{Hg^0} and 6.2×10^8molec/cm^3 (24 ppt) for [BrO], a lower limit for k_{Hg+BrO} can be calculated to 3.7×10^{-14}cm^3/(molec·s). This is already a factor of 2 to 3 faster than the reaction of Hg with OH which was studied by *Sommar et al.* [2001].

For the measurements at Kuujjuarapik, the anti correlation of TGM (as measured by *Poissant* [2001]) and BrO can be seen in Figure 6.30, where TGM concentrations are plotted versus BrO mixing ratios measured by the long path DOAS. At Kuujjuarapik

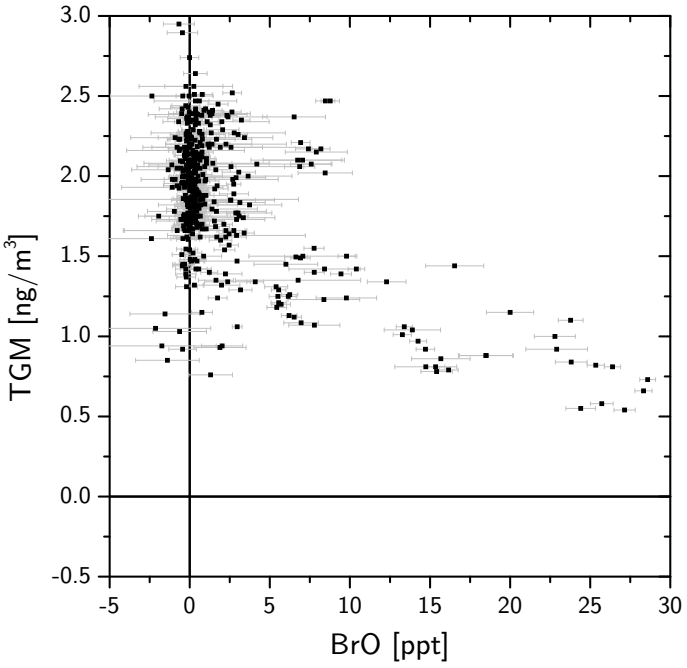

Figure 6.30: *TGM concentrations measured at the CEN by Poissant [2001] versus LP-DOAS BrO mixing ratios. The TGM was averaged over the respective LP-DOAS integration time.*

no complete mercury depletion event was observed during the measurement period (see also the mercury time series shown in Figure 5.46). The mercury depletion rates and corresponding BrO mixing ratios for the MDEs observed at Kuujjuarapik are listed in Table 6.5. At average levels of 2 ng/m^3 Hg^0 or 0.2 ppt the lifetime at Kuujjuarapik is also

$\frac{d[Hg]}{dt}$ [ppt/h]	BrO mixing ratio [ppt]	Date
0.02	25	15.04.2001
0.01	15	16.04.2001
0.02	15	17.04.2001
0.026	5	21.04.2001

Table 6.5: *Mercury depletion rates and corresponding BrO mixing ratios for the mercury depletion events at Kuujjuarapik.*

of the order of 10 hours. The calculation of k_{Hg+BrO} according to Equation 6.3 therefore leads to similar values as inferred above for the ALERT2000 campaign.

6.6.1 Reactive Bromine - Mercury - Interaction

The first simultaneous direct measurements of gaseous mercury and bromine oxide at Alert and Kuujjuarapik support the theory that BrO plays a key role as oxidant of elemental mercury in the gas phase, which was proposed by several authors based on assumptions or indirect measurements [*Boudries and Bottenheim* 2000; *Poissant et al.* 2001; *Lu et al.* 2001]. From the measurements at Alert it seems clear now that during mercury

depletion events Hg^0 is transformed to reactive gaseous mercury (RGM, Hg(II)) in the gas phase [*Steffen et al.* 2002]. For this process very likely BrO is responsible. This is supported by the observed anti-correlation between the direct measurements of both species and the fact that the BrO radical is known to be a strongly oxidizing species. *Steffen et al.* [2002] also found that only part of the Hg^0 lost during MDEs can be recovered from its reactive form Hg(II) in the gas phase. Additionally, accumulation of Hg was found on the snow pack during MDEs. As pointed out by *Lu et al.* [2001], the deposition of significant amounts of mercury in the Arctic environment during spring leads to a massive input of this toxic heavy metal in the Arctic biosphere, which may accumulate in the food chain and therefore influence the health of people living in the Arctic environment.

Chapter 7

Summary and Outlook

In this work, halogen oxide radicals (BrO, IO) were measured at several locations in the high Arctic, for the first time at a low Arctic site in mid-latitudes and in the Indian Ocean mid-latitude marine boundary layer. Besides the well-established active Longpath-DOAS technique, the new Multi-Axis-DOAS technique, developed in this work, was for the first time applied to measure BrO and IO in the boundary layer.
The main results of this thesis are discussed in chapter 6 and are summarized here:

- high levels of BrO radicals (around 30 ppt) have been found in the Arctic boundary layer, correlated to ozone depletion at the surface. This result is in very good agreement with previous measurements by Longpath-DOAS during ozone depletion events in the Arctic. In most cases the largest fraction of the BrO total column was located in a surface layer of approximately 1 km thickness.

- IO was observed in the Arctic boundary layer for the first time at levels of 0.6-0.8 ppt. These measurements represent the first simultaneous observation of both BrO and IO radicals in the Arctic boundary layer, implying that combined bromine/iodine chemistry takes place in the atmosphere leading to strongly accelerated ozone depletion.

- the MAX-DOAS BrO measurements at Alert allowed for the first time to derive information on the vertical profiles of BrO near the ground which helps to understand the dynamic processes involved in surface ozone depletion after polar sunrise. Especially elevated layers of BrO, which might escape detection by other methods, were monitored by MAX-DOAS several times.

- the measurements at the Hudson Bay represent the first ground-based and direct observations of reactive bromine in this low Arctic region. It was also the southernmost location, where Arctic springtime ozone depletion and BrO chemistry was reported to date.

- It was ruled out that the GOME satellite observations of large bromine oxide clouds in the Hudson Bay region during spring is an artefact, caused e.g. by anomalies of the stratospheric column.

- the measurements at the Hudson Bay allowed for the first time to study the day/night behavior of bromine oxide radicals and showed that Br_2 is formed as the major reservoir compound during nighttime. Peaks of BrO in the early morning correlated with ozone destruction during sunrise were for the first time observed on short timescales of a few hours.

- the first simultaneous measurements of BrO in the boundary layer by a traditional Longpath-DOAS instrument and the MAX-DOAS technique developed in this work were also carried out at the Hudson Bay. The very good agreement between both techniques can be regarded as successful validation of MAX-DOAS for ground-based measurements in the boundary layer.

- the observation of mercury depletion events in the high and low Arctic and the first simultaneous BrO measurements showing a strong anti-correlation between both compounds support previous indirect conclusions that BrO is the proposed gas phase oxidant for gaseous elemental mercury. The rate constant for the Hg+BrO reaction was for the first time estimated based on simultaneous measurements of Hg and BrO at high time resolution.

- the first IO measurements in the southern Indian Ocean agree with previous studies at other sites in the coastal remote boundary layer and suggest that IO radicals can be observed in all clean coastal regions where short-lived organic iodine precursors are abundant.

- the upper limits derived from the Longpath-DOAS measurements in the moderately polluted marine boundary layer in the Mediterranean on the Island of Crete suggest, that halogen chemistry plays only a minor role at semi-polluted sites.

It was shown in the course of this thesis that ground-based MAX-DOAS allows the determination of relatively precise concentration levels of absorbers in the boundary layer as well as approximate layer heights and profile shapes with simple instrumentation. The operation of stand alone long term measurements is also possible with the same setup. The airmass factor modelling carried out in this thesis without taking into account clouds and precise aerosol scattering phase functions is only valid for cloud-free and non-snowdrift conditions. However, the MAX-DOAS technique yields qualitatively correct values at high time resolution also during periods of blowing/drifting snow when other optical instruments like Long Path DOAS cannot operate well due to low visibility.
It is planned and tested to operate improved instrumental setups allowing simultaneous

measurements at different elevation angles (or other geometries) rather than the sequential observations employed in this work. This further development should allow the determination of several parameters of the vertical distribution function of absorbers in the troposphere. In addition observations of O_4 and improvements of the model itself will allow more precise radiation transport calculations. Airborne MAX-DOAS (AMAX-DOAS) measurements will be carried out in the near future to investigate BrO in the free troposphere. Further future applications of the MAX-DOAS technique have been discussed at the end of chapter 3 (including the application of the MAX-DOAS technique for other trace gases (e.g. ozone, NO_2), MAX-DOAS measurements to study halogen emissions from salt lakes, volcanic or industrial plumes of pollution, etc.). For this the implementation of the MAX-DOAS geometries in advanced radiative transfer models is needed, which correctly describe the effects of local topography, albedo and clouds/aerosols. Possibly measured O_4 slant columns can serve as input parameters for the RTM calculations to yield better results.

Further instrument development will allow the application of small footprint, lightweight and low power consuming DOAS instruments. Using these new mini-DOAS and micro-DOAS systems simpler and cheaper field measurements will be possible, so the still very limited data set on halogen oxides in the troposphere can be further expanded.

Simultaneous observations with other experimental techniques aimed at measuring reactive halogen species (e.g. chemical amplification, chemical ionization mass spectroscopy for halogens (HALOCIMS), etc.) will further improve the understanding of the chemical reaction schemes involved in atmospheric halogen cycles.

BrO as a gas phase oxidant for gaseous elemental mercury, which is a global pollutant, can lead to significant accumulation of mercury in the polar environments and affect the health of peoples and influence the whole biosphere in these regions. Further laboratory studies to determine the kinetics of the involved reactions as well as field observations to monitor the changes are clearly needed to elucidate the global cycling of atmospheric mercury.

Appendix A

The Etalon-Effect

The Fabry-Perot Etalon-Effect, or short Etalon-Effect, was observed during DOAS measurements by *Stutz* [1991], *Senne* [1996], *Volkamer* [1996] and [*Hönninger* 1999]. It can be explained by multiple reflections on parallel planes in the optical path, which cause interference effects. These interferences can strongly affect spectroscopic measurements due to low and/or high frequency modulations of the intensity with wavelength. Generally multiple reflections between thin layers cause very broadband Etalon structures (e.g. ∼30 nm for the ∼5μm SiO_2 layer on Photo Diode Array detectors [*Stutz* 1991]), whereas narrow spectral structures (as low as 0.03 nm) are associated with reflecting layers of ∼3 mm [*Hönninger* 1999].

Mathematical Description

The intensity modulation for two rays of incident intensity I_0 perpendicular on a plane parallel plate (reflectivity R, thickness d) can be expressed as

$$I(\lambda) = I_0(\lambda)(1 + 2Rcos\frac{2n_1 d}{\lambda}2\pi) \tag{A.1}$$

for one reflection [*Stutz* 1991]. Here n_1 denotes the refractive index of the parallel plate. The light intensity I after passing the plate is therefore cosine-modulated with wavelength. In case of more than one reflection equation A.1 changes to:

$$I(\lambda) = I_0(\lambda)\frac{1}{1 - 2Rcos\frac{2n_1 d}{\lambda}2\pi + R^2} \tag{A.2}$$

For the limit of small R, i.e. single reflection only, equations A.2 and A.1 are equal.
The superposition of two oscillations of similar, but different frequencies leads to a beat. This can originate from two or more plane parallel plates in the optical path, with multiple refections between the reflecting planes. In case of two layers S_1 and S_2, with thicknesses d_1 and d_2 and refractive indices n_1 and n_2, several possible interference patterns are given. The ray, which is reflected once and therefore passes both layers twice has an optical path

difference to the direct ray of δ_1, another ray, which is reflected on the plane between the two layers has the optical path difference δ_2 compared to the direct beam.

$$\delta_1 = 2(n_1 d_1 + n_2 d_2) \tag{A.3}$$

$$\delta_2 = 2 n_2 d_2 \tag{A.4}$$

Therefore, in this simple model three rays interfere, with a normalized total intensity of:

$$I(\lambda) = 1 + \sqrt{R_1 R_2} cos(2\pi \frac{\delta_1}{\lambda}) + \sqrt{R_2 R_3} cos(2\pi \frac{\delta_2}{\lambda}) + R_3 \sqrt{R_1 R_2} cos(2\pi \frac{\delta_1 - \delta_2}{\lambda}) \tag{A.5}$$

Using the formulas given here, the etalon structures described in section 5.4.4 can be explained.

Appendix B

UFS Zugspitze Data Winter 1999/2000

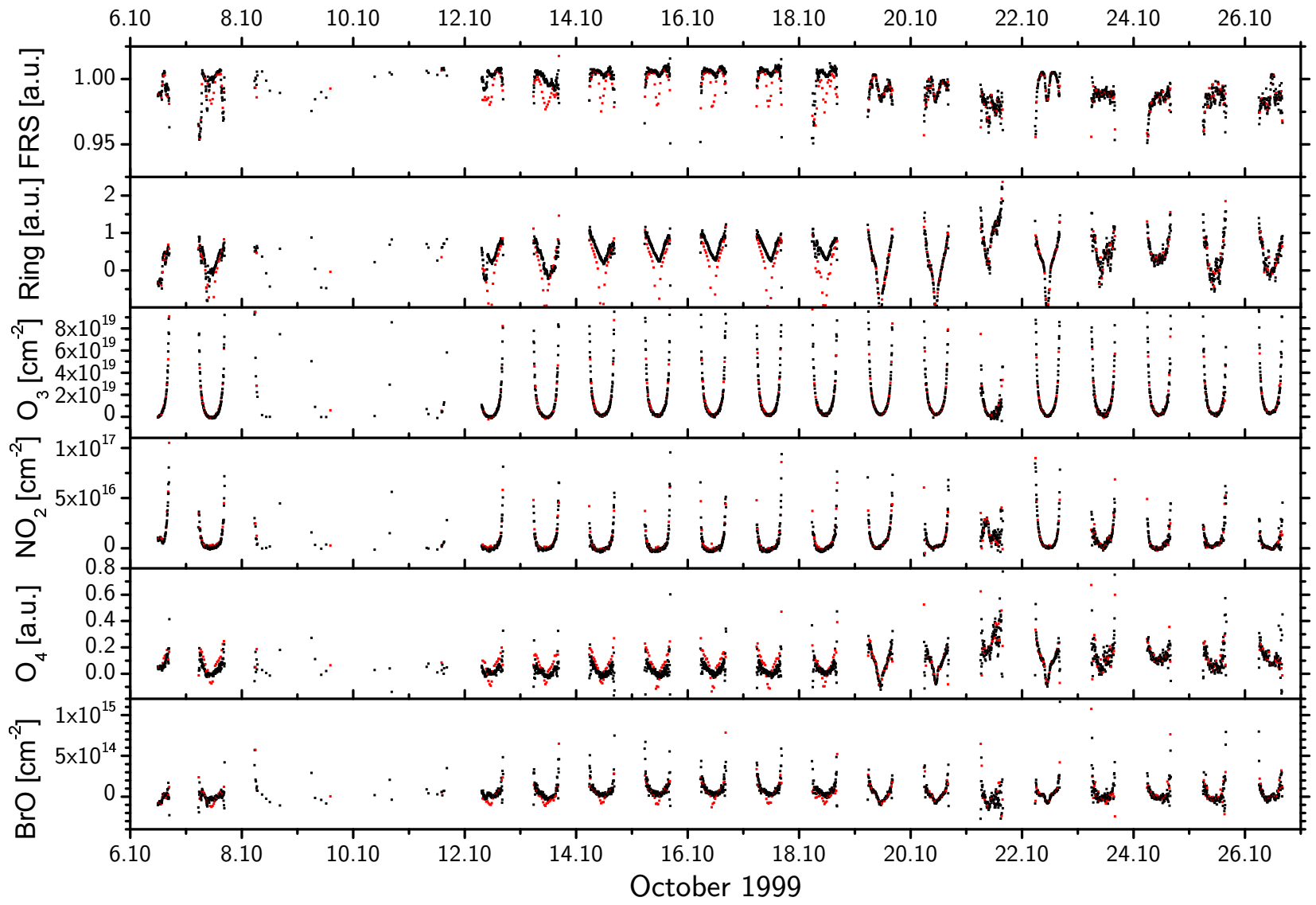

Figure B.1: *DOAS analysis results: Fraunhofer and Ring fit parameters, dSCDs of ozone, NO_2, O_4 and BrO are plotted (red dots: 20° elevation values).*

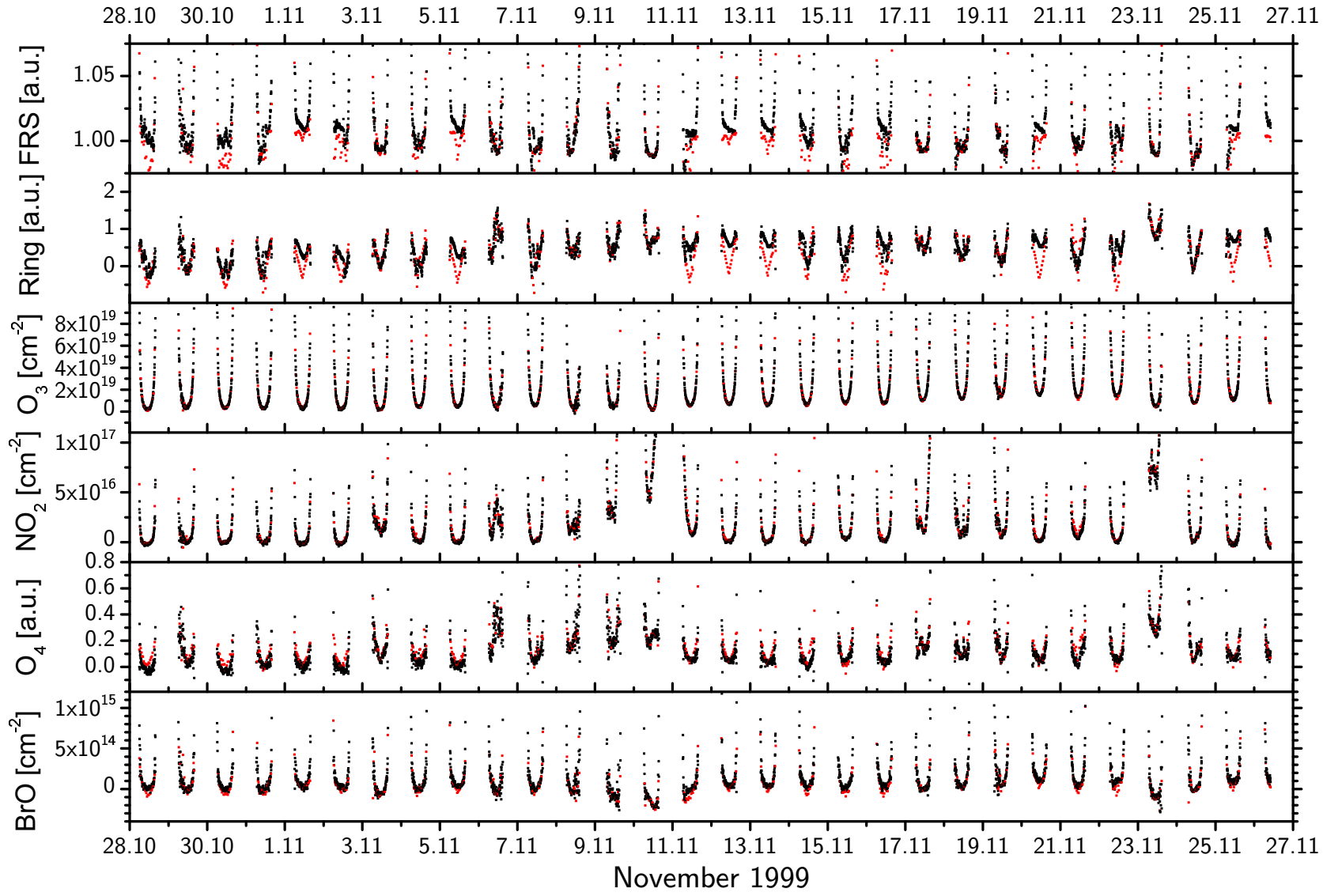

Figure B.2: *DOAS analysis results: Fraunhofer and Ring fit parameters, dSCDs of ozone, NO_2, O_4 and BrO are plotted (red dots: 20° elevation values).*

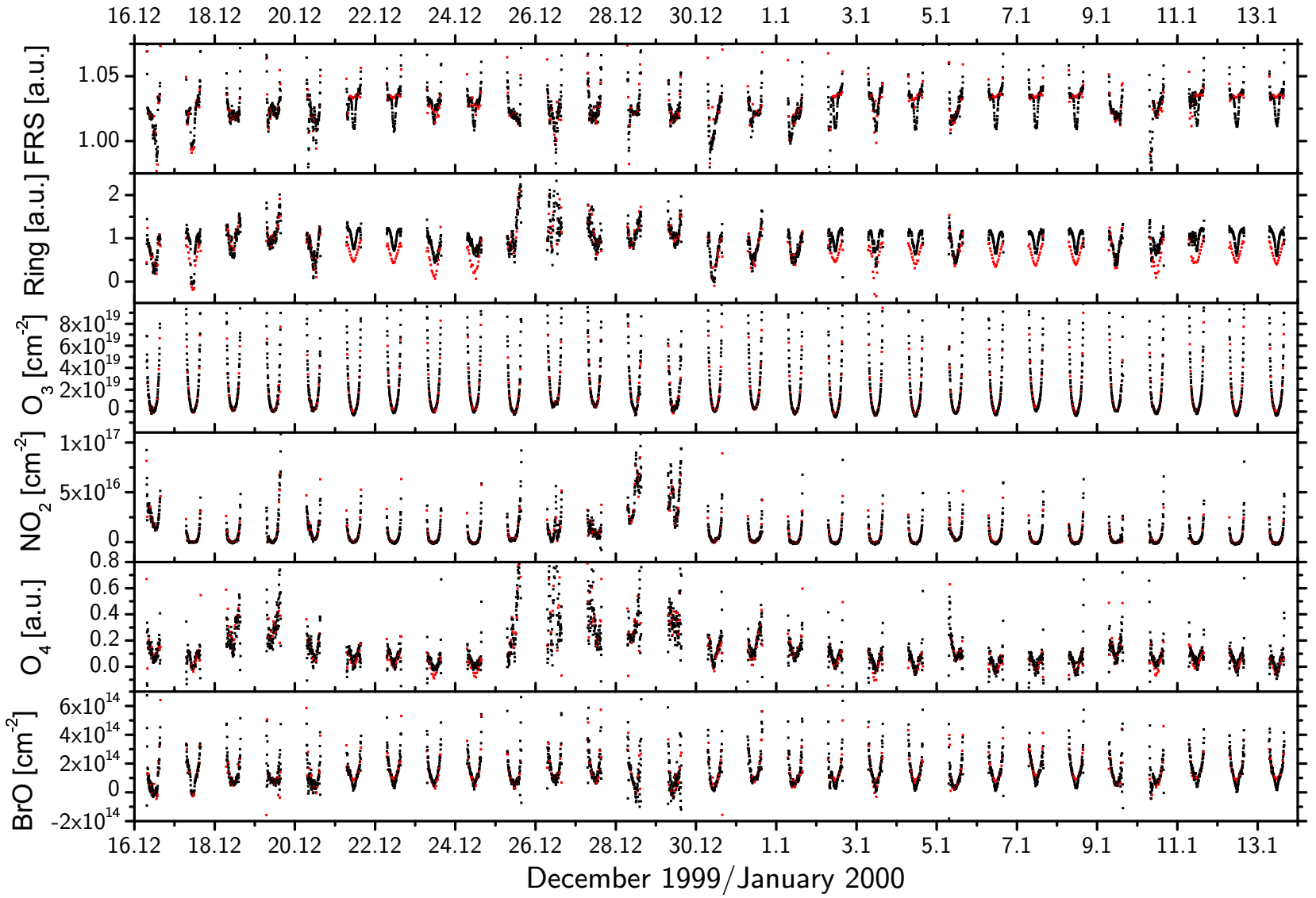

Figure B.3: *DOAS analysis results: Fraunhofer and Ring fit parameters, dSCDs of ozone, NO_2, O_4 and BrO are plotted (red dots: 20° elevation values).*

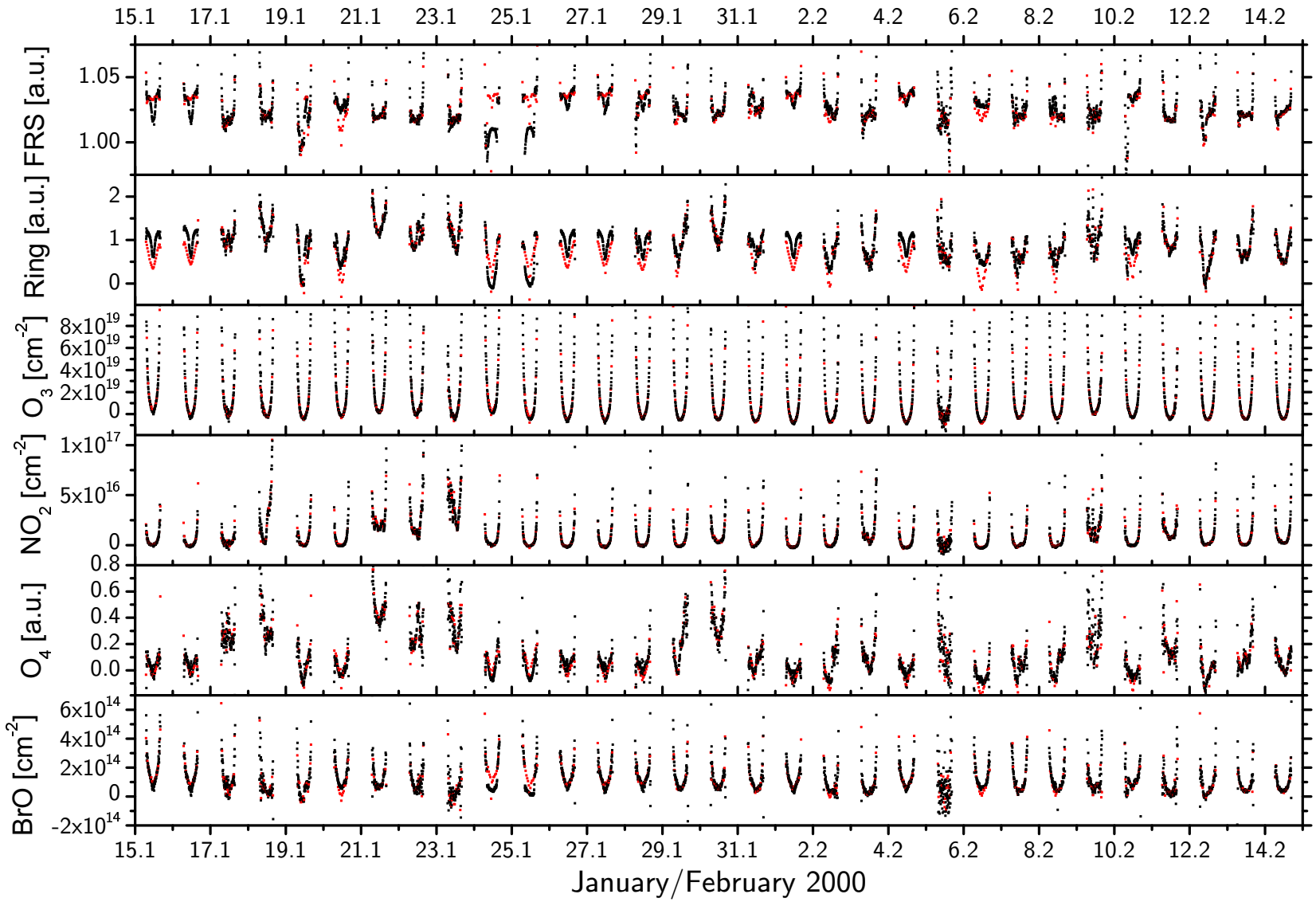

Figure B.4: *DOAS analysis results: Fraunhofer and Ring fit parameters, dSCDs of ozone, NO_2, O_4 and BrO are plotted (red dots: 20° elevation values).*

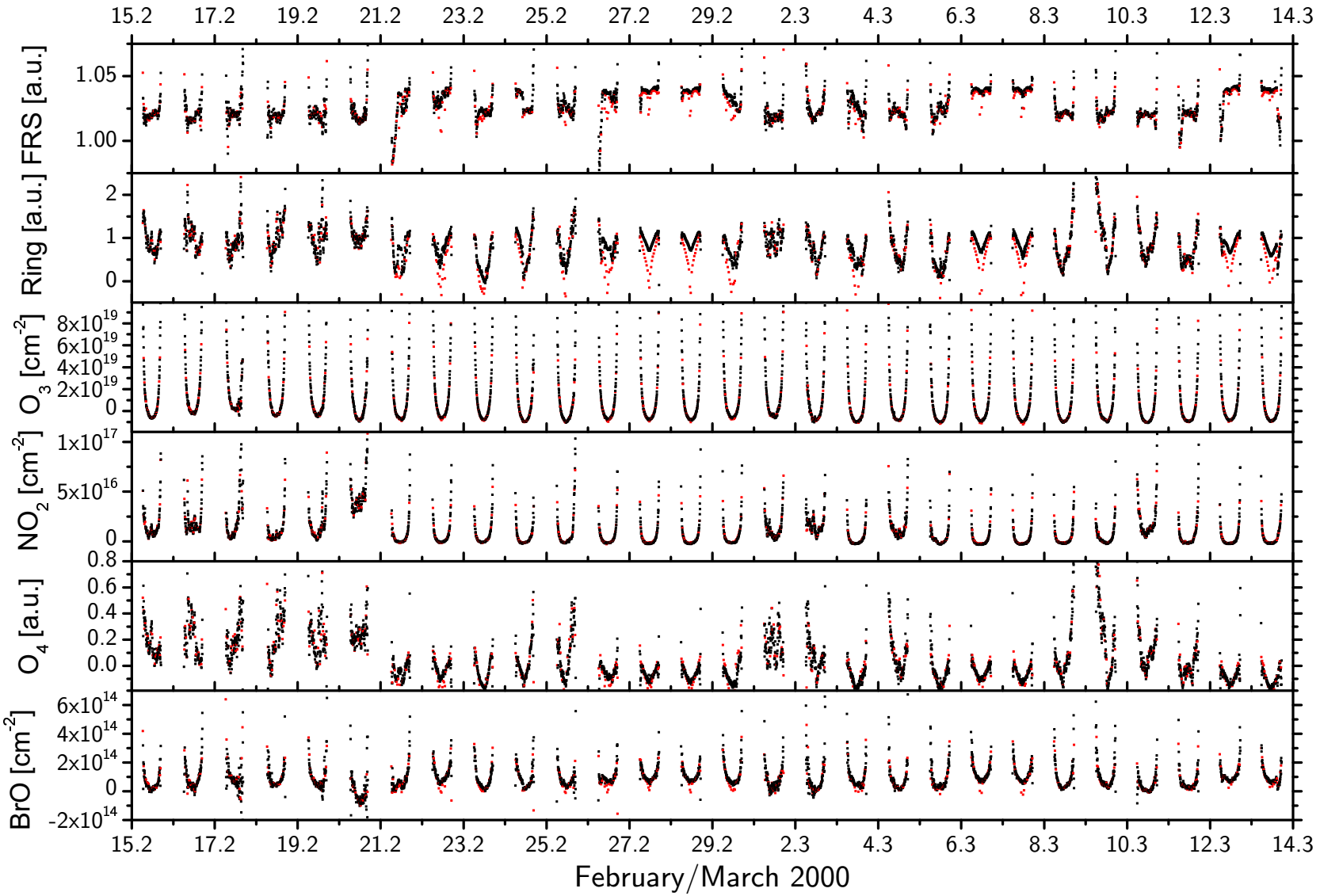

Figure B.5: *DOAS analysis results: Fraunhofer and Ring fit parameters, dSCDs of ozone, NO_2, O_4 and BrO are plotted (red dots: 20° elevation values).*

Appendix C

Data from Marion Dufresne, December 2000

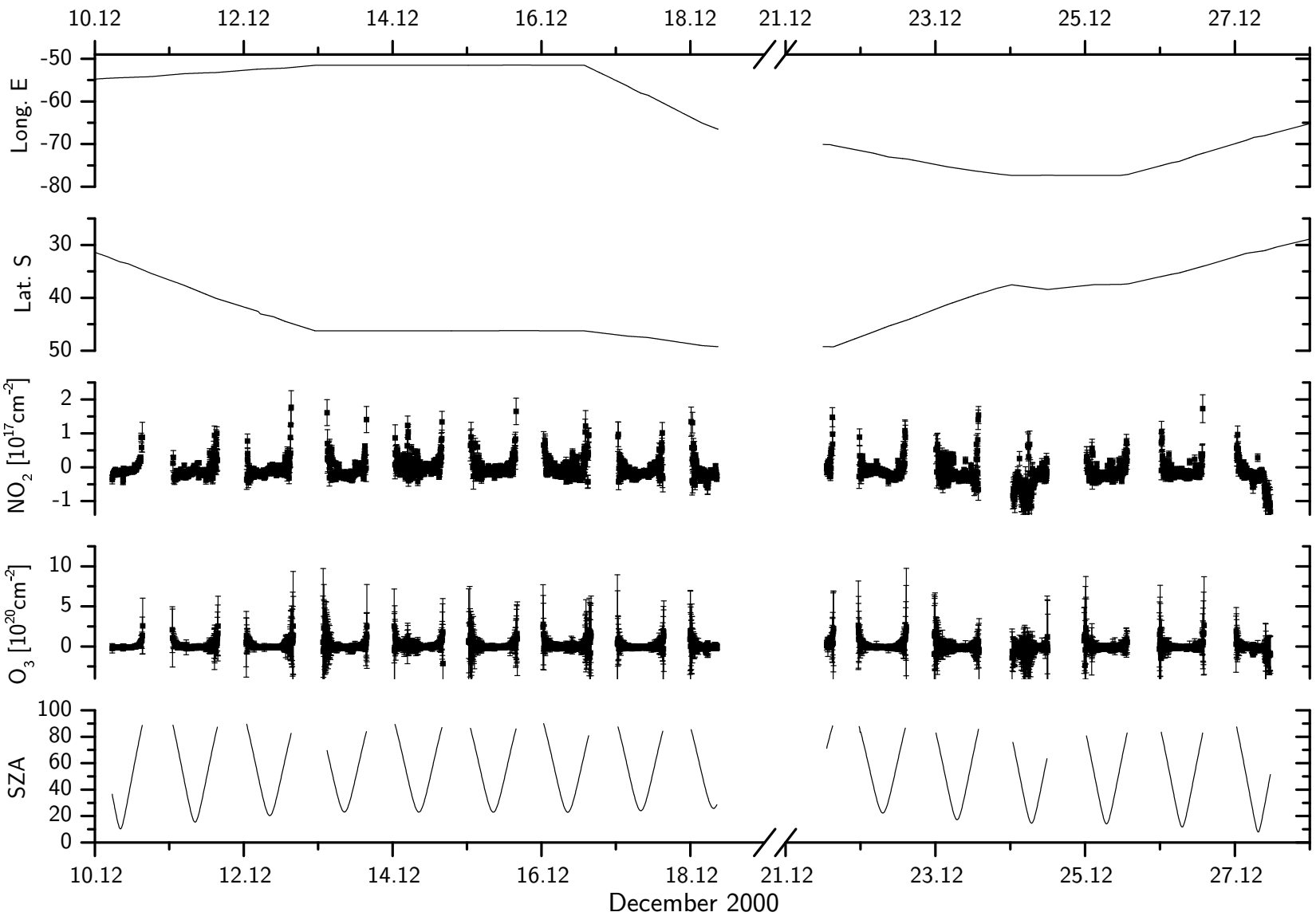

Figure C.1: *DOAS analysis results from shipborne measurements in the southern Indian Ocean: shown are dSCDs of ozone and NO_2, latitude, longitude and SZA are also given.*

Appendix D

5 day Back Trajectories Overview for ALERT2000

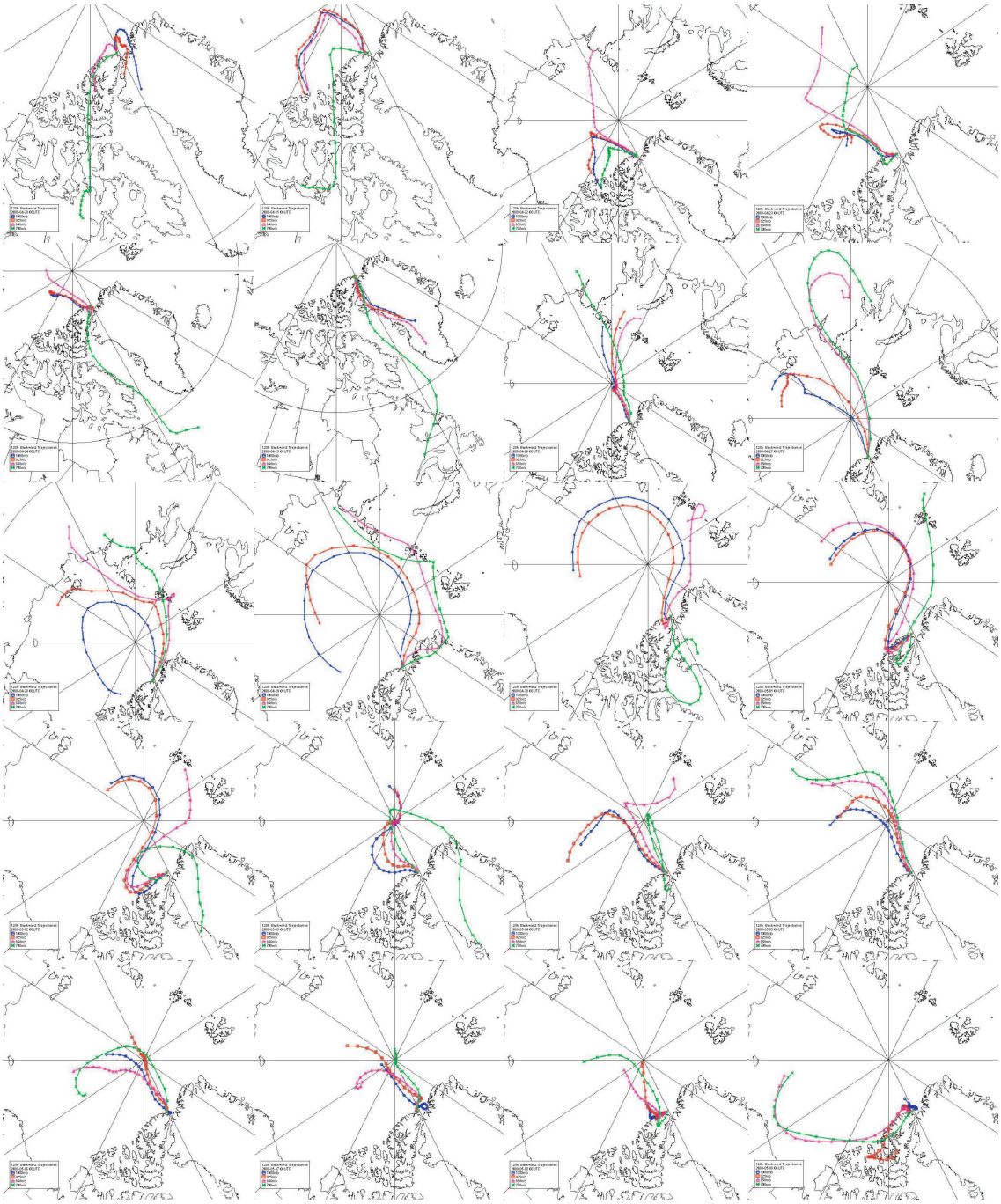

Figure D.1: *5 day back trajectories for ALERT2000. Daily trajectories are shown from April 20, 2000 to May 9, 2000, arriving at Alert at 12h UT.*

Appendix E

MOCCA Simulation Results for Crete2000

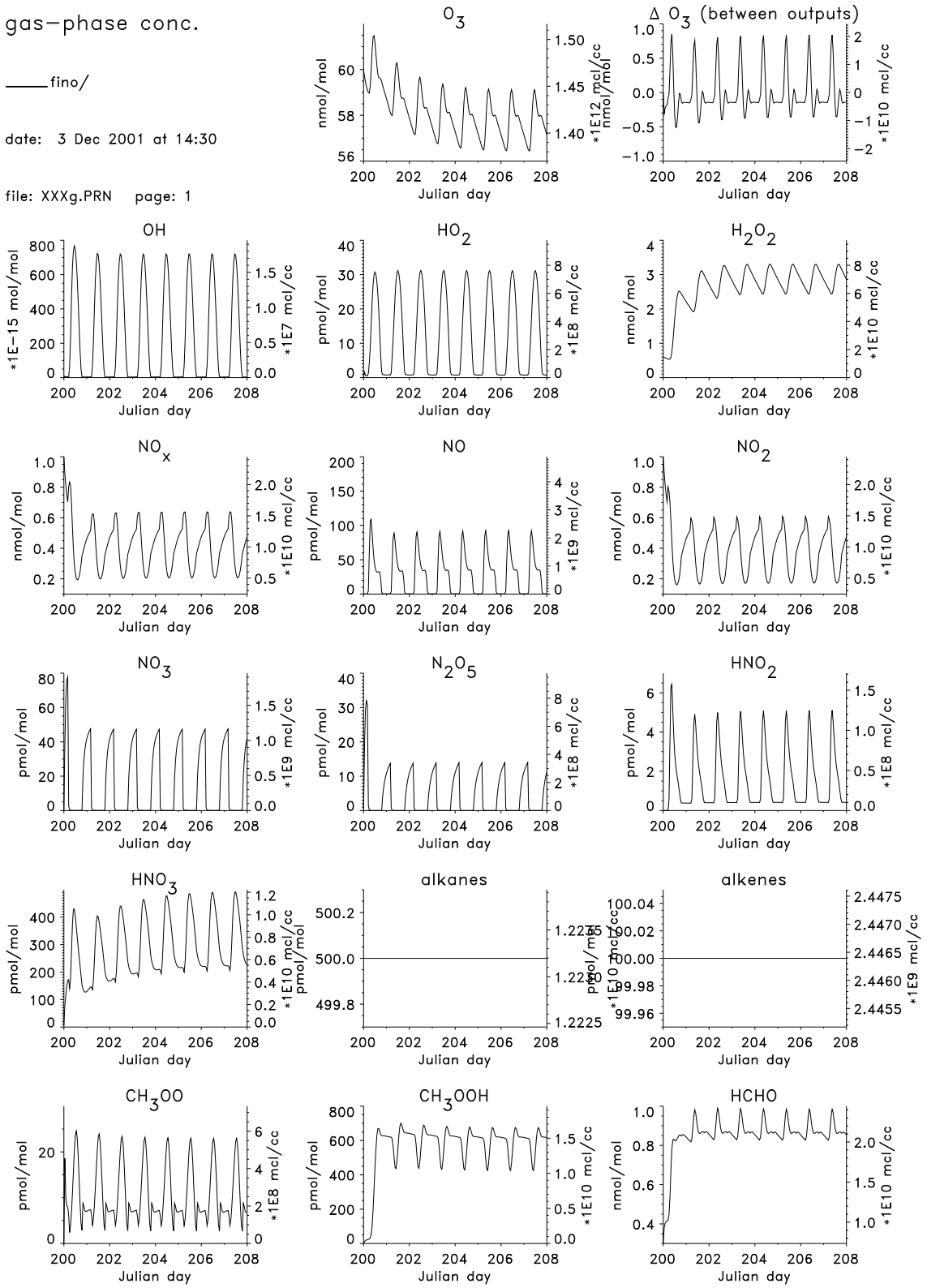

Figure E.1: *8 day time series for the gas phase mixing ratios included in MOCCA.*

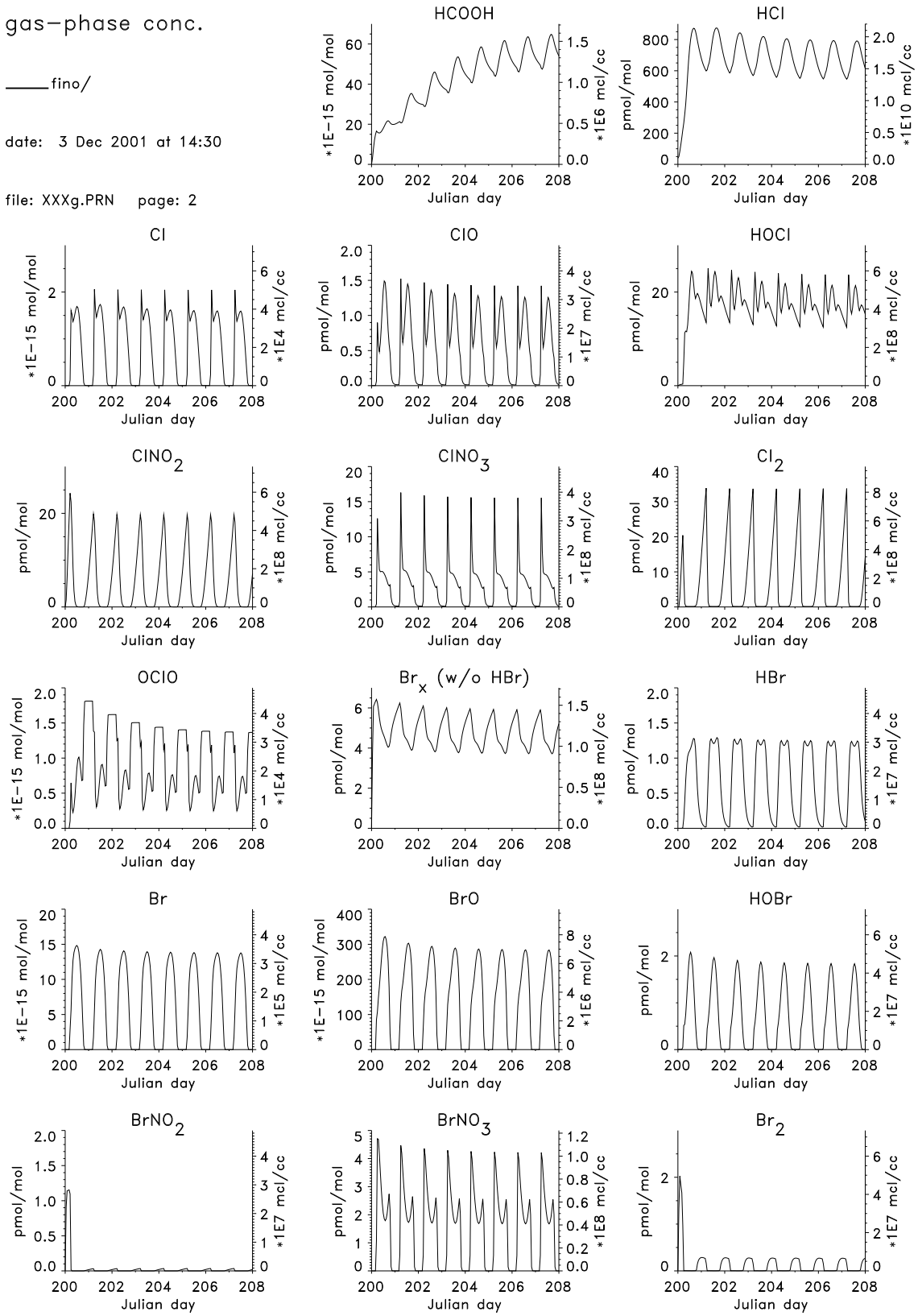

Figure E.2: *8 day time series for the gas phase mixing ratios included in MOCCA.*

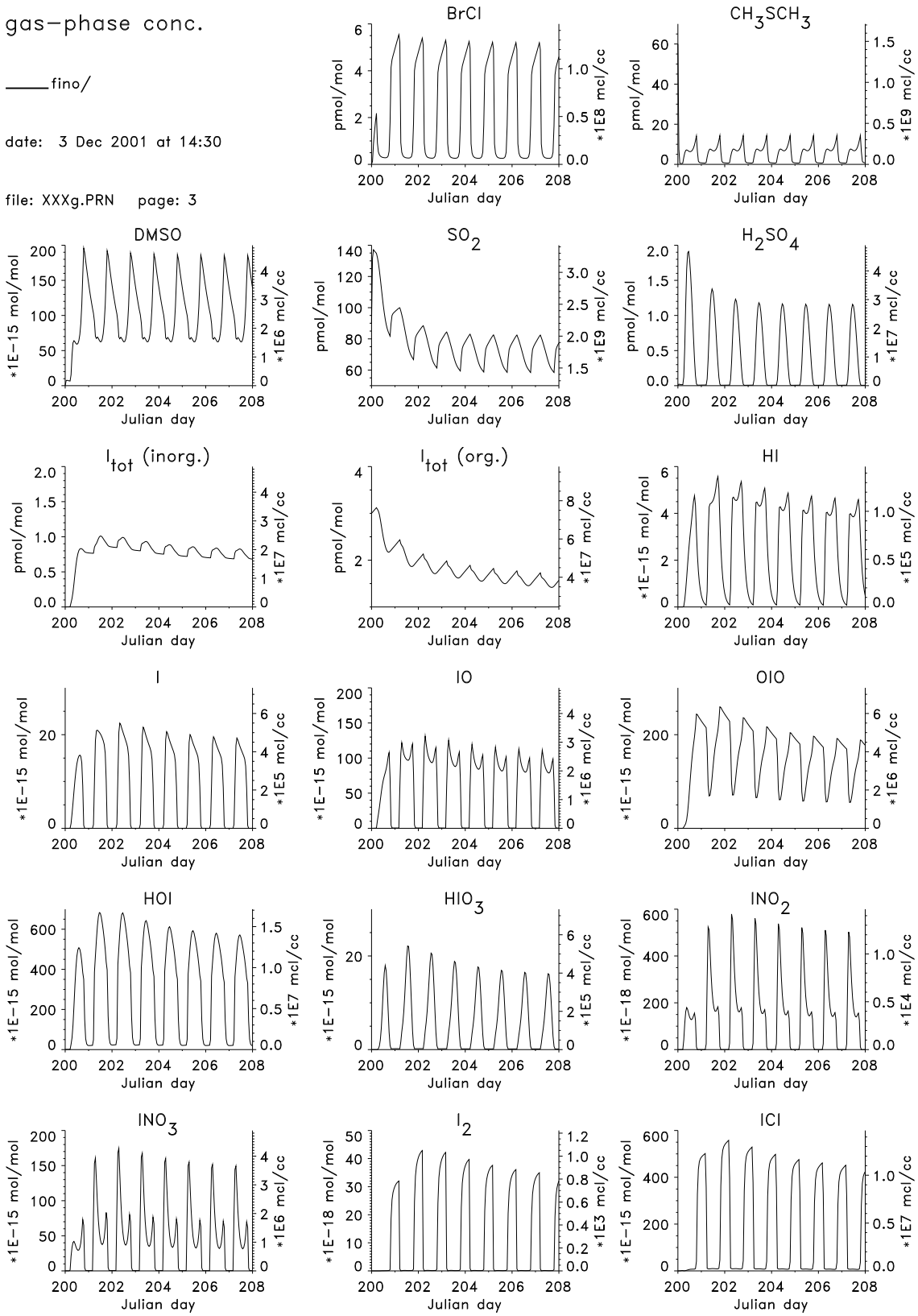

Figure E.3: *8 day time series for the gas phase mixing ratios included in MOCCA.*

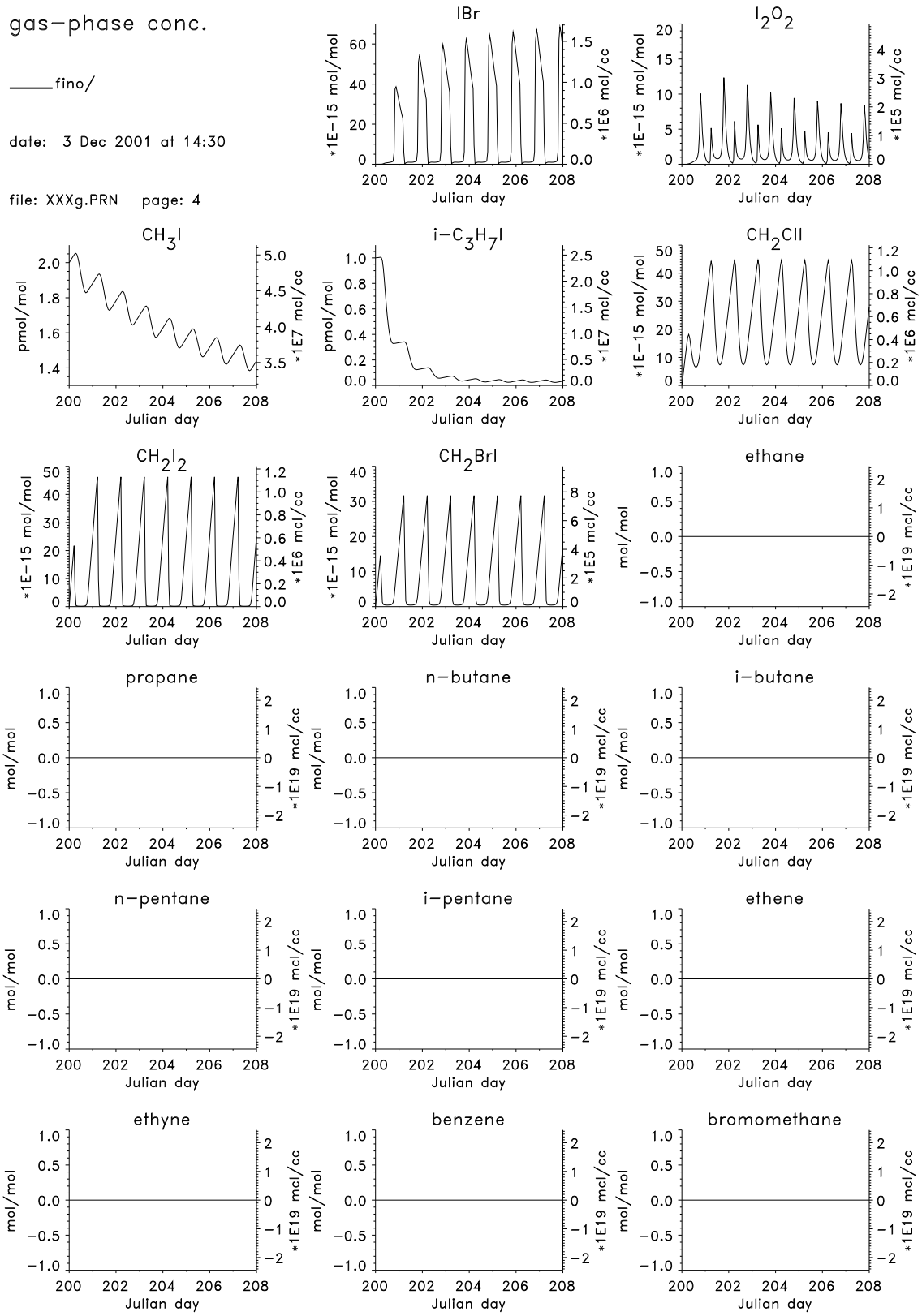

Figure E.4: *8 day time series for the gas phase mixing ratios included in MOCCA.*

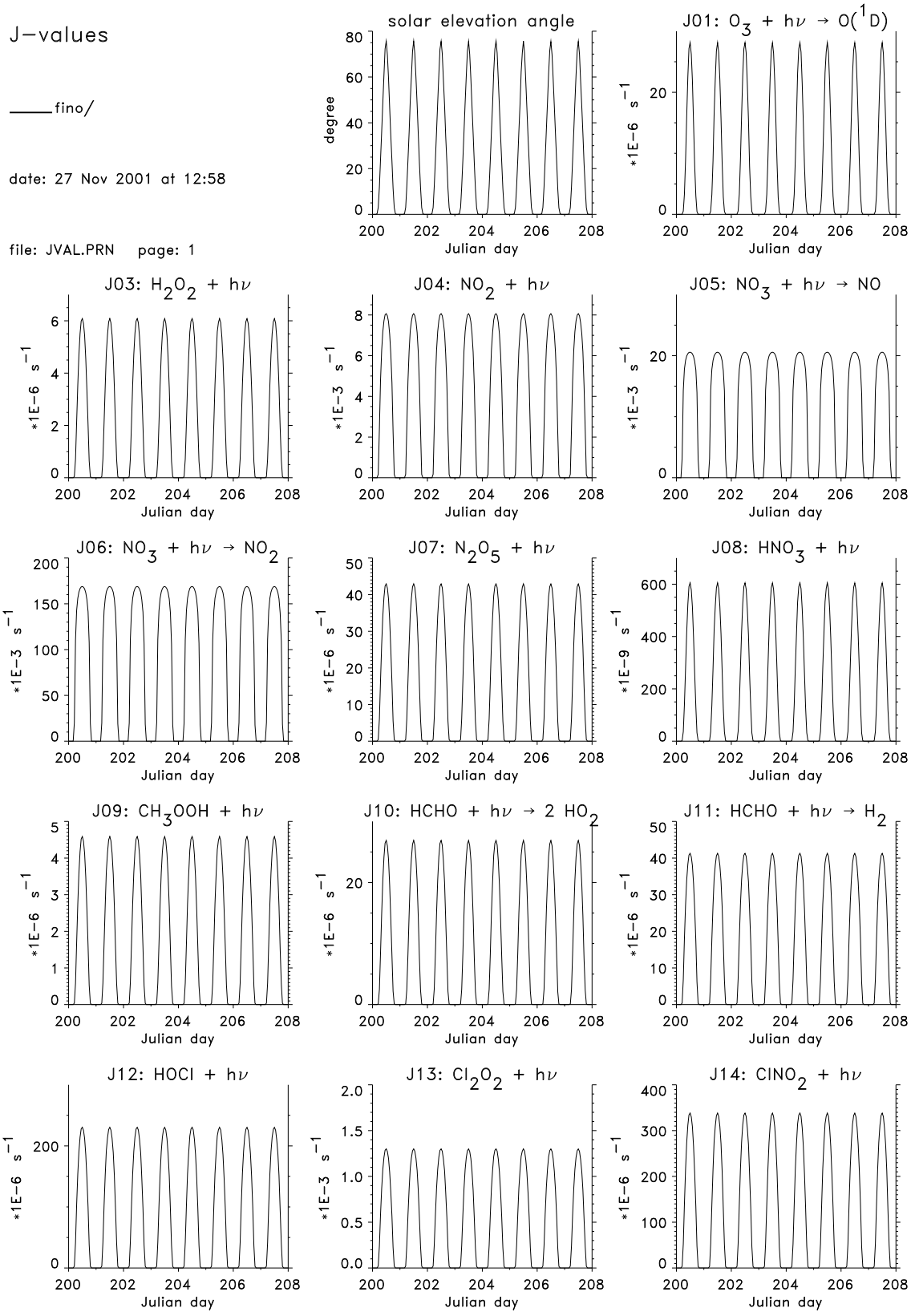

Figure E.5: *8 day time series of the photolysis frequencies of photolyzable species included in MOCCA.*

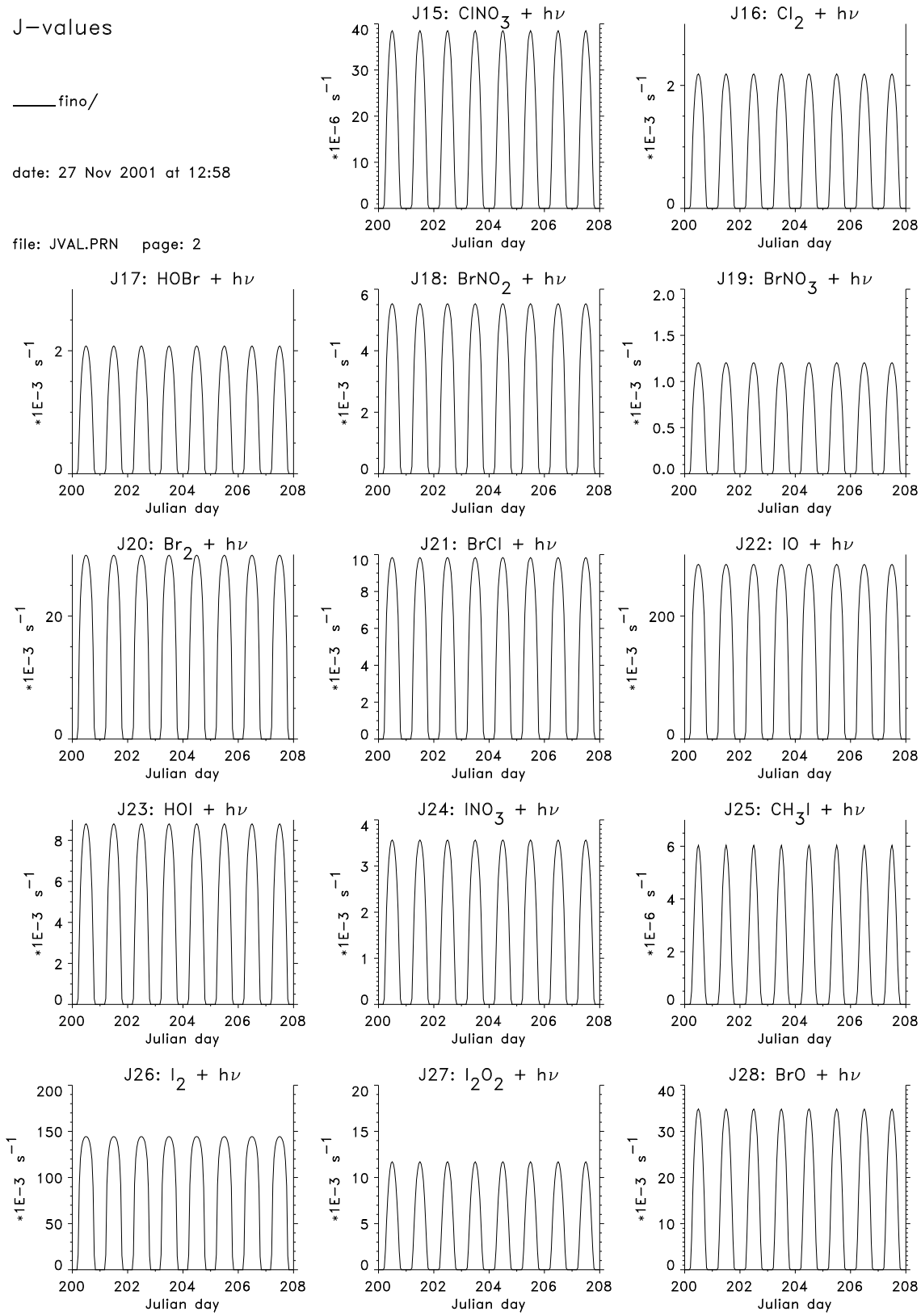

Figure E.6: *8 day time series of the photolysis frequencies of photolyzable species included in MOCCA.*

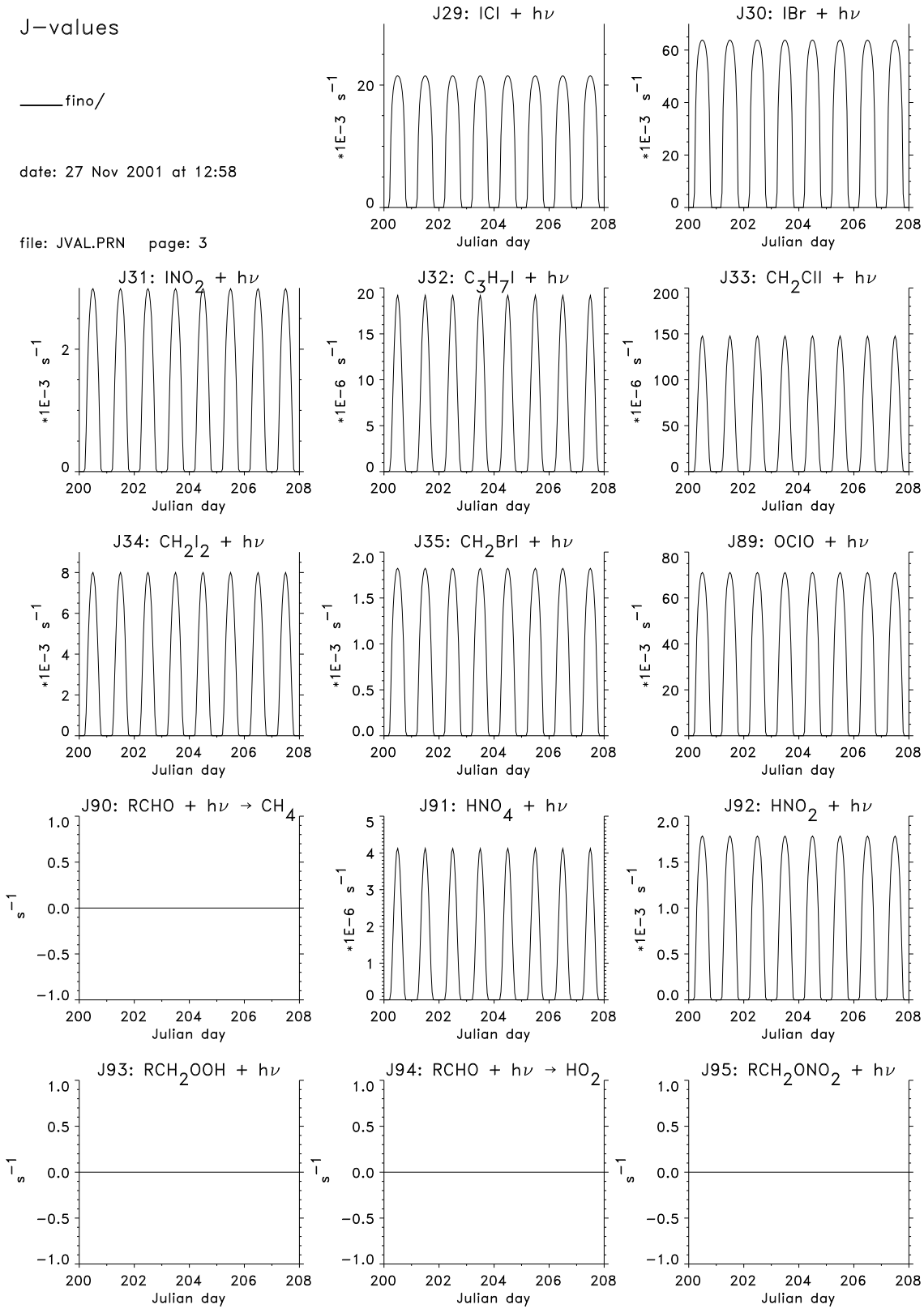

Figure E.7: *8 day time series of the photolysis frequencies of photolyzable species included in MOCCA.*

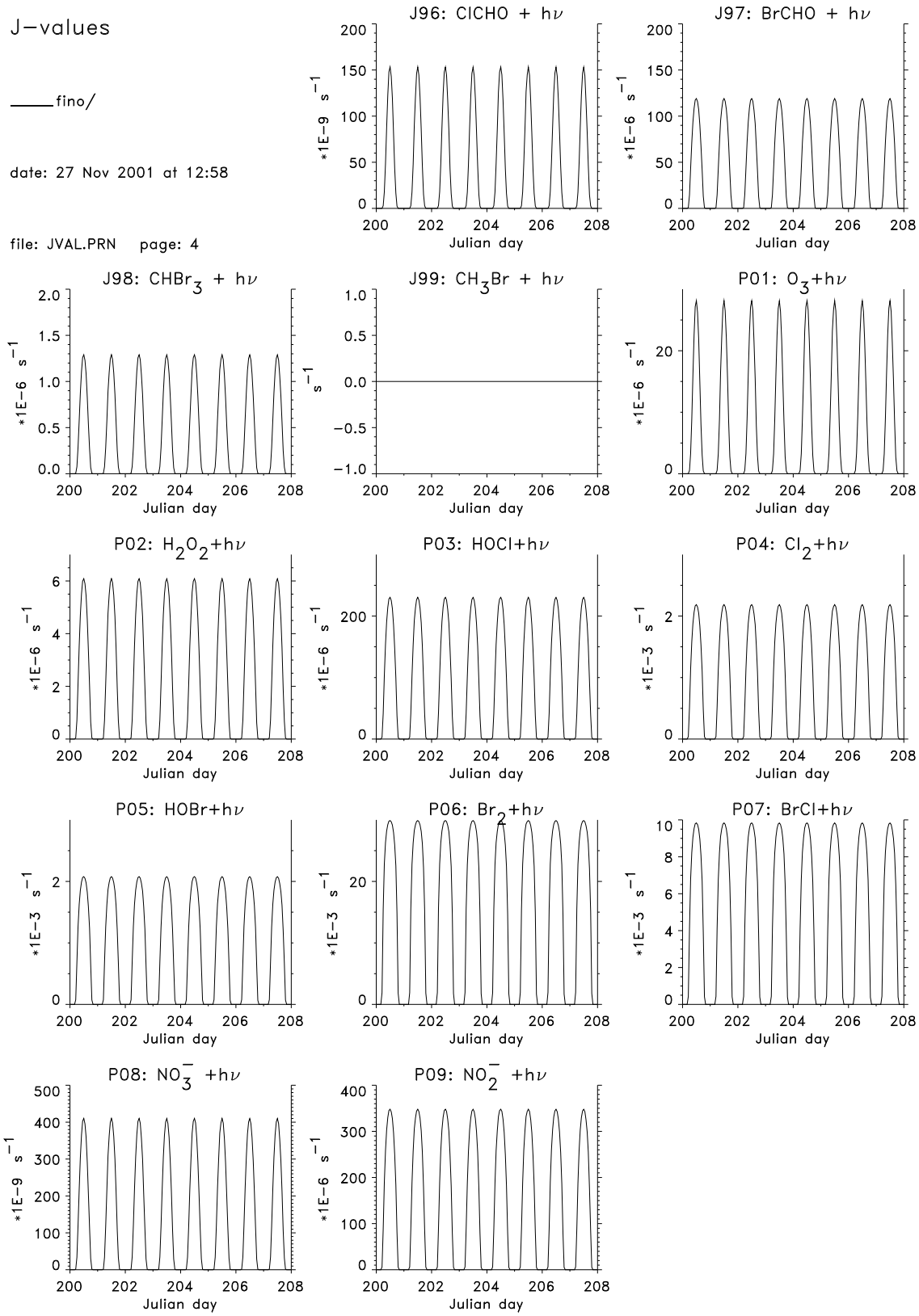

Figure E.8: *8 day time series of the photolysis frequencies of photolyzable species included in MOCCA.*

List of Figures

2.1 Typical O_3 profile . . . 6
2.2 The Chapman cycle . . . 7
2.3 Overview of Global RHS Measurements . . . 15
2.4 O_3 loss rates for different catalytic cycles . . . 19
2.5 Schematic overview of tropospheric halogen chemistry . . . 22
2.6 f-Br Bromine Anti-correlation . . . 28
2.7 Br_2 and BrCl during Polar Sunrise 2000 . . . 29
2.8 Open Leads in the Canadian Arctic . . . 30
2.9 Tropospheric bromine chemistry . . . 33
2.10 Frost flowers on freshly frozen sea ice . . . 34
2.11 Scheme of the tropospheric iodine chemistry . . . 39
2.12 Atmospheric Mercury Budget . . . 41
2.13 Arctic Springtime Depletion of Mercury . . . 44

3.1 DOAS set-up . . . 49
3.2 Absolute and differential cross section . . . 51
3.3 Overview of Differential Absorption Cross Sections . . . 58
3.4 Sample BrO evaluation . . . 59
3.5 Sample Ring Spectrum . . . 64
3.6 Rayleigh scattering phase function . . . 67
3.7 Raman Scattering . . . 68
3.8 Geometry of Scattered Sunlight Observation . . . 71
3.9 Zenith and Off Axis Geometry . . . 78
3.10 Airmass Factor and SCD Change for Off Axis View during Twilight . . . 79
3.11 Off Axis Geometry for Sunrise NO_3 Profiles . . . 81
3.12 Ground-based MAX-DOAS Overview . . . 82
3.13 MAX-DOAS Airmass Factors . . . 85
3.14 Airmass Factor Dependence on Azimuth Angle . . . 86
3.15 Airmass Factor Dependence on the Trace Gas Profile . . . 88
3.16 Airmass Factors for Single and Multiple Scattering . . . 89
3.17 Airmass Factors Dependence on Albedo . . . 90

3.18 Airborne MAX-DOAS 91
3.19 MAX-DOAS Spectra Acquisition 92
3.20 Alpine MAX-DOAS 94
3.21 Salt Lake MAX-DOAS 96
3.22 'COSPEC' type MAX-DOAS 98

4.1 MAX-DOAS setup 100
4.2 LP-DOAS setup 102
4.3 Mini-MAX-DOAS setup 105
4.4 The OceanOptics USB2000 spectrometer 106
4.5 USB2000 grating efficiency 106
4.6 USB2000 Optical Properties 107
4.7 USB2000/ILX511 Dark Current 108
4.8 USB2000/ILX511 Electronic Offset 108
4.9 Portable LP-DOAS setup 109
4.10 Schmidt-Cassegrain telescope 110

5.1 Meteorological Parameters at the Zugspitze 113
5.2 Setup of the DOAS Telescope at the Zugspitze 114
5.3 Sample BrO evaluation from the Zugspitze 116
5.4 Example of Diurnal O_3 and NO_2 dSCD pattern 117
5.5 UFS Results from January 11-14, 2000 118
5.6 UFS Results from March 1-4, 2000 119
5.7 Anomalous Shape of BrO dSCD Diurnal Cycle 120
5.8 Map of the Indian Ocean Measurement Region 121
5.9 Sample Evaluation of OceanOptics Spectra 123
5.10 Sample Days of the BrO Evaluation from the Indian Ocean 124
5.11 The Kerguelen Measurement Site 126
5.12 Overview of the Kerguelen Measurements 127
5.13 Kerguelen IO DOAS Fit 128
5.14 Daylight/Darkness Chart for Alert 129
5.15 Map of Alert and the North Polar Region 130
5.16 Map of the Alert Measurement Site 131
5.17 Picture of the MAX-DOAS Setup at Alert 132
5.18 Meteorological Parameters during ALERT2000 133
5.19 Sample Evaluation of BrO for ALERT2000 135
5.20 Fit Results for ALERT2000 136
5.21 Complete BrO Data from ALERT2000 137
5.22 MAX-DOAS IO Measurements during ALERT2000 139
5.23 Sample IO evaluation for ALERT2000 140

5.24 Ozone, Hg and BrO during ALERT2000 . . . 141
5.25 Vertical Ozone Distribution during ALERT2000 . . . 142
5.26 Map of the Island of Crete . . . 143
5.27 Meteorological Data during the Measurements on Crete . . . 144
5.28 Wind Distribution at Finokalia, Crete . . . 145
5.29 View of the DOAS Lightpaths on Crete . . . 145
5.30 Results of the Halogen Oxide Measurements on Crete . . . 146
5.31 Nitrogen Species measured at Finokalia . . . 147
5.32 NO_3 Evaluation Example . . . 148
5.33 Map of Kuujjuarapik and the Hudson Bay Region . . . 150
5.34 Topography and Lightpaths at the Hudson Bay Site . . . 151
5.35 Meteorological Parameters the Hudson Bay Field Study . . . 152
5.36 Wind Distribution at Kuujjuarapik, Hudson Bay . . . 153
5.37 BrO and O_3 LP-DOAS Measurements at Hudson Bay . . . 154
5.38 Other Halogen Oxides at Hudson Bay . . . 156
5.39 Occurrence of Etalon Structures in Hudson Bay Spectra . . . 157
5.40 Explanation of the Observed Etalon Structures . . . 159
5.41 Episodes of Local Pollution at Hudson Bay . . . 161
5.42 MAX-DOAS Telescope at Kuujjuarapik . . . 162
5.43 MAX-DOAS BrO Measurements at Hudson Bay . . . 164
5.44 In situ and LP-DOAS Ozone Data at Kuujjuarapik . . . 165
5.45 Correlation of in situ and LP-DOAS Ozone . . . 165
5.46 Total Gaseous Mercury at Kuujjuarapik . . . 166

6.1 Boundary Layer BrO Data from ALERT2000 . . . 169
6.2 ΔSCDs for BrO in the Boundary Layer . . . 171
6.3 Comparison of Measured and Modelled BrO Layer Height . . . 172
6.4 ΔSCDs for an elevated BrO layer . . . 172
6.5 Ozone and BrO Mixing Ratios during ALERT2000 . . . 174
6.6 Back Trajectories for Alert . . . 175
6.7 Ozone and BrO during Ozone depletion . . . 176
6.8 Tethersonde Profiles Ice Camp, May 3, 2000 . . . 177
6.9 Tethersonde Profiles Ice Camp, May 6, 2000 . . . 178
6.10 O_3-BrO Anti-Correlation at Alert . . . 179
6.11 GOME Satellite BrO Maps during ALERT2000 . . . 181
6.12 O_3 Loss Rate as Function of [BrO] and [IO] . . . 183
6.13 Ozone, NO_x and HO_x Results for Crete2000 MOCCA Run . . . 185
6.14 Halogen Species for Crete2000 MOCCA Run . . . 186
6.15 O_3-BrO Anti-Correlation at the Hudson Bay . . . 188

6.16 Back Trajectories ending at Kuujjuarapik on April 27, 2001, 6h UT 189
6.17 Day/Night Behavior of BrO and O_3 (I) 191
6.18 Back Trajectories ending at Kuujjuarapik on April 18, 2001, 18h UT 192
6.19 Day/Night Behavior of BrO and O_3 (II) 194
6.20 Back Trajectories ending at Kuujjuarapik on April 23, 2001, 4h UT 195
6.21 Comparison of NO_2 Photolysis Frequencies 197
6.22 LP-DOAS and MAX-DOAS Comparison for BrO 199
6.23 GOME Satellite BrO Maps during the Hudson Bay Campaign 201
6.24 Comparison of GOME and MAX-DOAS BrO Time Series 203
6.25 Model Results for Kuujjuarapik (Ozone and HO_x) 205
6.26 Model Results for Kuujjuarapik (Bromine Species) 206
6.27 Model Results for Kuujjuarapik (Chlorine Species) 206
6.28 Scatter Plot of TGM and MAX-DOAS BrO at Alert 207
6.29 Time Series of GEM Depletion 208
6.30 Scatter Plot of TGM and LP-DOAS BrO at Kuujjuarapik 209

B.1 Zugspitze Data October 1999 218
B.2 Zugspitze Data November 1999 219
B.3 Zugspitze Data December 1999/January 2000 220
B.4 Zugspitze Data January/February 2000 221
B.5 Zugspitze Data February/March 2000 222

C.1 Data from Marion Dufresne, December 2000 224

D.1 Back Trajectories for ALERT2000 226

E.1 Gas Phase Concentrations Modelled for Crete 228
E.2 Gas Phase Concentrations Modelled for Crete 229
E.3 Gas Phase Concentrations Modelled for Crete 230
E.4 Gas Phase Concentrations Modelled for Crete 231
E.5 Photolysis Frequencies Modelled for Crete 232
E.6 Photolysis Frequencies Modelled for Crete 233
E.7 Photolysis Frequencies Modelled for Crete 234
E.8 Photolysis Frequencies Modelled for Crete 235

List of Tables

2.1 Rate constants and photolysis frequencies for RHS 16
2.2 Halogen Oxide Self- and Cross-Reactions 17
2.3 Rate constants for reactions of halogens with RH and O_3 21
2.4 Lifetimes and typical mixing ratio bromo- and iodo-hydrocarbons 26
2.5 Δ H for reaction of X with OH 27
2.6 Physical/chemical properties of important mercury species 40

3.1 Detector Properties 56
3.2 Trace gas cross sections used in this work 60

4.1 Comparison of the employed Xenon arc lamps 104

5.1 Halogen Oxide Detection Limits on Crete 146
5.2 Halogen Oxide Detection Limits at Hudson Bay 156

6.1 Comparison of GOME with ground-based MAX-DOAS measurements . . . 182
6.2 Results for Trace Gases on Crete 184
6.3 Parameters for the Crete MOCCA Run 185
6.4 LP-DOAS/MAX-DOAS Comparison 202
6.5 Mercury Depletion Events at Kuujjuarapik 209

References

Abbatt, J. (1994). Heterogeneous reactions of HOBr with HBr and HCl on ice surfaces at 228K. *Geophys. Res. Lett.,* Vol. 21 (8), 665–668.

Abbatt, J. (1995). Interactions of HBr, HCl, and HOBr with supercooled sulfuric acid solutions of stratospheric composition. *J. Geophys. Res.,* Vol. 100, 14009–14017.

Abbatt, J. and J. Nowak (1997). Heterogeneous interactions of HBr and HOCl with cold sulfuric acid solutions: Implications for Arctic boundary layer bromine chemistry. *J. Phys. Chem. A,* Vol. 101, 2131–2137.

Ackermann, R. (2000). *Auswirkungen von Kraftfahrzeugsemissionen in der urbanen Atmosphäre*. Dissertation, Institut für Umweltphysik, University of Heidelberg.

Albritton, D. L., A. L. Schmeltekopf, and R. N. Zare (1976). An Introduction to the Least-Squares Fitting of Spectroscopic Data. In R. K. Narahari and M. W. Weldon (Eds.), *Molecular Spectroscopy: Modern Research*. Orlando, Florida, USA: Academic Press.

Alicke, B. (2000). *The Role of Nitrous Acid in the Boundary layer*. Dissertation, Institut für Umweltphysik, University of Heidelberg.

Alicke, B., K. Hebestreit, J. Stutz, and U.Platt (1999). Iodine oxide in the marine boundary layer. *Nature,* Vol. 397, 572–573.

Allan, B. J., G. McFiggans, and J. M. C. Plane (2000). Observation of iodine monoxide in the remote marine boundary layer. *J. Geophys. Res.,* Vol. 105, 14363–14369.

Allan, B. J., J. M. C. Plane, and G. McFiggans (2001). Observations of OIO in the remote marine boundary layer. *Geophys. Res. Lett.,* Vol. 28, 1945–1948.

Aranda, A., G. LeBras, G. Verdet, and G. Poulet (1997). The $BrO+CH_3O_2$ reaction: Kinetics and the role in the atmospheric budget. *Geophys. Res. Lett.,* Vol. 24, No. 22, 2745–2748.

Ariya, P., J. Hopper, and G. Harris (1999). C_2-C_7 Hydrocarbon Concentrations in the Arctic Snowpack Interstitial Air: Potential Presence of Actie Br within the Snowpack. *J. of Atm. Chem.,* Vol. 34, 55–64.

Atkinson, R., D. L. Baulch, R. A. Cox, R. F. Hampson, Jr., J. A. Kerr, M. J. Rossi, and J. Troe (1997). Evaluated Kinetic and Photochemical Data for Atmospheric Chemistry: Supplement VI. IUPAC Subcommittee on Gas Kinetic Data Evaluation for Atmospheric Chemistry. *J. Phys. Chem. Ref. Data,* Vol. 26, 521–1011.

Axelson, H., B. Galle, K. Gustavson, P. Ragnarsson, and M. Rudin (1990). A Transmitting / Receiving Telescope for DOAS-Measurements using Retroreflektor Technique. *Techn. Dig. Ser.,* Vol. 4, 641–644.

Barrie, L., J. Bottenheim, R. Schnell, P. Crutzen, and R. Rasmussen (1988). Ozone destruction and photochemical reactions at polar sunrise in the lower Arctic atmosphere. *Nature,* Vol. 334, 138–141.

Barrie, L. and U. Platt (1997). Arctic tropospheric chemistry: and overview. *Tellus,* Vol. 49B, 449–454.

Barrie, L. A., J. W. Bottenheim, and W. R. Hart (1994). Polar Sunrise Experiment 1992 (PSE 1992): Preface. *J. Geophys. Res.,* Vol. 99, No. D12, 25313–25314.

Bates, D. R. and M. Nicolet (1950). Atmospheric hydrogen. *Publ. Astron. Soc. Pac.,* Vol. 62, 106–110.

Bauer, D., T. Ingham, S. A. Carl, G. K. Moortgat, and J. N. Crowley (1998). Ultraviolet-Visible Absorption Cross Sections of Gaseous HOI and Its Photolysis at 355nm. *J. Phys. Chem. A,* Vol. 102, 2857–2864.

Bedjanian, Y., G. LeBras, and G. Poulet (1997). Kinetics and Mechanism of the $IO + ClO$ Reaction. *J. Phys. Chem. A,* Vol. 101, 4088–4096.

Bedjanian, Y., G. Poulet, and G. LeBras (1998). Low pressure study of the reactions of Br atoms with alkenes: reaction with propene. *J. Phys. Chem.,* Vol. 102, 5867–5875.

Behnke, W., C. George, V. Scheer, and C. Zetzsch (1997). Production and decay of $ClNO_2$ from the reaction of gaseous N_2O_5 with NaCl solution: bulk and aerosol experiments. *J. Geophys. Res.,* Vol. 102, 3795–3804.

Beine, H. et al. (2001). NO_x During Background and Ozone Depletion Periods at ALERT: Fluxes Above the Snow Surface. *Atm. Env.,*, in press.

Bevington, P. (1969). *Data Reduction and Error Analysis for the Physical Sciences.* New York: McGraw-Hill.

Bilde, M., T. J. Wallington, C. Ferronato, J. J. Orlando, G. S. Tyndall, E. Estupinan, and S. Haberkorn (1998). Atmospheric chemistry of CH_2BrCl, $CHBrCl_2$, $CHBr_2Cl$, $CF_3CHClBr$ and CBr_2Cl_2. *J. Phys. Chem.,* Vol. 102, 1976–1986.

Bloss, W. J., D. M. Rowley, R. A. Cox, and R. L. Jones (2001). Kinetics and Products of the IO Self-Reaction. *J. of Phys. Chem. A,* Vol. 105, 7840–7854.

Bösch, H. (2002). *Studies of Stratospheric Nitrogen and Iodine Chemistry with Balloon Borne DOAS Measurements.* Dissertation, Institut für Umweltphysik, Universität Heidelberg.

Bottenheim, J. et al. (2002). Dynamics and Vertical Distribution of Ozone in the Arctic Lower Troposphere During Winter and Spring 2000 (ALERT 2000). *Atm. Env.,*, in press.

Bottenheim, J. W., L. A. Barrie, E. Atlas, L. E. Heidt, H. Niki, R. A. Rasmussen, and P. B. Shepson (1990). Depletion of lower tropospheric ozone during Arctic spring: The polar sunrise experiment 1988. *J. Geophys. Res.,* Vol. 95, No. D11, 18,555–18,568.

Bottenheim, J. W., J. D. Fuentes, and J. Arnold (2001). Tethersonde Data, Ice Camp, ALERT2000. *priv. comm.,*.

Bottenheim, J. W., A. C. Gallant, and K. Brice (1986). Measurements of NO_y species and O_3 at 82° N latitude. *Geophys. Res. Lett.,* Vol. 13, 113–116.

Boudries, H. and J. W. Bottenheim (2000). Cl and Br atom concentrations during a surface boudary layer ozone depletion event in the Canadian High Arctic. *Geophys. Res. Lett.,* Vol. 27, No. 1, 517–520.

Brauers, T., M. Hausmann, U. Brandenburger, and H.-P. Dorn (1995). Improvement of Differential Optical Absorption Spectroscopy using Multi-Channel-Scanning-Techniques. *Appl. Opt.,* Vol. 34,21, 4472–4479.

Brosset, C. (1987). The behaviour of mercury in the physical environment. *Water Air and Soil Pollution,* Vol. 34, 145–166.

Brosset, C. and E. Lord (1995). Methylmercury in ambient air. Method of determination and some measurement results. *Water Air and Soil Pollution,* Vol. 82, 739–750.

Burrows, J., U. Platt, K. Chance, M. Vountas, V. Rozanov, A. Richter, H. Haug, and L. Marquard (1996). *Study of the Ring Effect*. Noordivijk, The Netherlands: European Space Agency.

Bussemer, M. (1993). *Der Ring-Effekt: Ursachen und Einfluß auf die spektroskopische Messung stratosphärischer Spurenstoffe*. Diploma thesis, Institut für Umweltphysik, Universit"at Heidelberg.

Butler, J. H. and J. M. Rodriguez (1996). Methyl bromide in the atmosphere. In C. Bell, N. Price, and B. Chakrabarti (Eds.), *The Methyl Bromide Issue*, pp. 28–90. John Wiley, New York.

Carpenter, L., W. Sturges, S. Penkett, P. Liss, B. Alicke, K. Hebestreit, and U. Platt (1999). Observation of short-lived alkyl iodides and bromides at Mace Head, Ireland: links to biogenic sources and halogen oxide production. *J. Geophys. Res.,* Vol. 104, 1679–1689.

Carpenter, L. J. and P. S. Liss (2000). On temperate sources of bromoform and other reactive organic bromine gases. *J. of Geophys. Res.,* Vol. D105, 20539 – 20547.

Chapman, S. (1930). On ozone and atomic oxygen in the upper atmosphere. *Philos. Mag.,* Vol. 10, 369–383.

Cox, R. A., W. J. Bloss, and R. L. Jones (1999). OIO and the atmospheric cycle of iodine. *Geophys. Res. Lett.,* Vol. 26, 1857–1860.

Cox, R. A. and G. B. Coker (1983). Absorption cross section and kinetics of IO in the photolysis of CH_3I in the presence of ozone. *J. Phys. Chem.,* Vol. 87, 4478–4484.

Crutzen, P. J. (1970). The influence of nitrogen oxide on the atmospheric ozone content. *Q.J.R. Meteorol. Soc.,* Vol. 96, 320–327.

Crutzen, P. J. (1973). A discussion of the chemistry of some minor constituents in the stratosphere and troposphere. *Pure Appl. Geophys.,* Vol. 106-108, 1385–1399.

Crutzen, P. J. and P. H. Zimmermann (1991). The changing photochemistry of the troposphere. *Tellus,* Vol. 43AB, 136–151.

Curtis, A. and W. Sweetenham (1987). Facsimile/Chekmat User's Manual. Technical report, Harwell Lab., Computer Science and Systems Division, Oxfordshire, Great Britain.

Czerny, M. and A. Turner (1930). *Z.Phys.,* Vol. 61, 792.

Davies, J. (1970). Correlation Spectroscopy. *Analytical Chemistry,* Vol. 42, 101–112.

DeMore, W., S. Sander, D. Golden, R. Hampson, M. Kurylo, C. Howard, A. Ravishankara, C. Kolb, and M. Molina (1994). Chemical kinetics and photochemical data for use in stratospheric modeling. *NASA JPL Publication,*, 24–26.

DeMore, W. B., S. P. Sander, C. J. Howard, A. R. Ravishankara, D. M. Golden, C. E. Kolb, R. F. Hampson, M. J. Kurylo, and M. J. Molina (1997). Chemical Kinetics and Photochemical Data for Use in Stratospheric Modeling No. 12. *Jet Propulsion Laboratory, Pasadena, Publication 97-4,*.

Dickerson, R. R., K. P. Rhoads, T. P. Carsey, S. J. Oltmans, J. P. Burrows, and P. J. Crutzen (1999). Ozone in the remote marine boundary layer: A possible role for halogens. *J. Geophys. Res.,* Vol. 104, 21385–21395.

Diebel, D., J. Burrows, R. de Beek, R. Munro, B. Kerridge, L. Marquard, U. Platt, and H. Frank (1995). Detailed analysis of the retrieval algorithms selected for the level 1-2 processing of GOME data (Tracegas study). Technical report, ESA contract 10728/94/NL/CM, prepared by SERCO Europe Ltd., Southall, U.K.

Dobson, G. M. B. and D. N. Harrison (1926). Measurements of the amount of ozone in the Earth's Atmosphere and its Relation to other Geophysical Conditions. *Proc. R. Soc. London,* Vol. 110, 660–693.

Draxler, R. R. (1999). HYSPLIT 4 user's guide. NOAA Technical Memorandum ERL ARL-230, NOAA Air Resources Laboratory, Silver Spring, Maryland, U.S.A.

Ebinghaus, R., S. Jennings, W. Schroeder, T. Berg, T. Donaghy, J. Guentzel, C. Kenny, H. Kock, K. Kvietkus, W. Landing, T. Mühleck, J. Munthe, E. Prestbo, D. Schneeberger, F. Slemr, J. Sommar, A. Urba, and Z. Xiao (1999). International field intercomparison measurements of atmospheric mercury species at Mace Head, Ireland. *Atm. Env.,* Vol. 33, 3063–3073.

Edner, H., G. W. Faris, A. Sunesson, and S. Svanberg (1989). Atmospheric atomic mercury monitoring using differential absorption LIDAR technique. *Appl. Opt.,* Vol. 28, 921.

Erle, F., U. Platt, and K. Pfeilsticker (2000). Measurement of OBrO upper limits in the nighttime stratosphere. *Geophys. Res. Lett.,* Vol. 27, No. 15, 2217–2220.

Etzkorn, T. (1998). *Untersuchungen atmosphärisch relevanter Reaktionssysteme mittels Differentieller Optischer Absorptionsspektroskopie.* Dissertation, Institut für Umweltphysik, University of Heidelberg.

Fan, S. and D. Jacob (1992). Surface ozone depletion in Arctic spring sustained by bromine reactions on aerosols. *Nature,* Vol. 359, 522–524.

Farman, J. C., B. G. Gardiner, and J. D. Shanklin (1985). Large losses of total ozone in Antarctica reveal seasonal ClO_x/NO_x interaction. *Nature,* Vol. 315, 207–210.

Fickert, S., J. W. Adams, and J. N. Crowley (1999). Activation of Br_2 and BrCl via uptake of HOBr onto aqueous salt solutions. *J. Geophys. Res.,* Vol. 104, 23719–23727.

Finlayson-Pitts, B. and S. Johnson (1988). The reaction of NO_2 with $NaBr$: Possible source of $BrNO$ in polluted marine atmospheres. *Atmos. Environ.,* Vol. 22, 1107–1112.

Finlayson-Pitts, B. J., M. J. Ezell, and J. N. Pitts (1989). Formation of chemically active chlorine compounds by reactions of atmospheric NaCl particles with gaseous N_2O_5 and $ClONO_2$. *Nature,* Vol. 337, 241–244.

Finlayson-Pitts, B. J., F. E. Livingston, and H. N. Berko (1990). Ozone destruction and bromine photochemistry at ground level in the Arctic spring. *Nature,* Vol. 343, 622–625.

Fish, D. J. and R. L. Jones (1995). Rotational Raman scattering and the Ring effect in zenith-sky spectra. *Geophys. Res. Lett.,* Vol. 22, 811–814.

Fishman, J. and P. Crutzen (1978). The origin of ozone in the troposphere. *Nature,* Vol. 274, 855–858.

Fitzenberger, R., H. Bösch, C. Camy-Peyret, M. Chipperfield, H. Harder, U. Platt, B.-M. Sinnhuber, T. Wagner, and K. Pfeilsticker (2000). First profile measurement of tropospheric BrO. *Geophys. Res. Lett.,* Vol. 27, 2921–2924.

Fleischmann, O. C., M. Hartmann, J. Orphal, and J. P. Burrows (2001). FT measurements of the BrO absorption cross section. *University of Bremen, Institute of remote sensing,*, in preparation.

Foster, K. L., R. A. Plastridge, J. W. Bottenheim, P. B. Shepson, B. J. Finlayson-Pitts, and C. W. Spicer (2001). The Role of Br_2 and BrCl in Surface Ozone Destruction at Polar Sunrise. *Science,* Vol. 291, 471–474.

Frank, H. (1991). *Ein Strahlungstransportmodell zur Interpretation von spektroskopischen Spurenstoffmessungen in der Erdatmosphäre.* Diploma thesis, University of Heidelberg.

Frieß, U. (1997). *Spektroskopische Messungen stratosphärischer Spurenstoffe auf der Neumayer- Station (Antarktis) in den Jahren 1994/95.* Diploma thesis, University of Heidelberg.

Frieß, U. (2001). *Spectroscopic Measurements of Atmospheric Trace Gases at Neumayer-Station, Antarctica.* Dissertation, Institut für Umweltphysik, University of Heidelberg.

Frieß U., M. P. Chipperfield, H. Harder, C. Otten, U. Platt, J. Pyle, T. Wagner, and K. Pfeilsticker (1999). Intercomparison of measured and modelled BrO slant column amounts for the Arctic winter and spring 1994/95. *Geophys. Res. Lett.,* Vol. 26, 1861–1864.

Frieß, U., T. Wagner, I. Pundt, K. Pfeilsticker, and U. Platt (2001). Spectroscopic Measurements of Tropospheric Iodine Oxide at Neumeyer Station, Antarctica. *Geophys. Res. Lett.,* Vol. 28, 1941–1944.

Funk, O. (2000). *Photon Pathlengths Distributions for Cloudy Skies: Oxygen A-Band Measurements and Radiative Transfer Model Calculations*. Dissertation, Institut für Umweltphysik, Universität Heidelberg.

Gäbler, H. E. and K. G. Heumann (1993). Determination of particulate iodine in aerosols from different regions by size fractionating impactor sampling and IDMS. *Intern. J. Environ. Anal. Chem.,* Vol. 50, 129–146.

Gårdfeld, K., X. Feng, J. Sommar, and O. Lindqvist (2001). Total gaseous mercury exchange between air and water at river and sea surfaces in Swedish coastal regions. *Atm. Env.,* Vol. 35, 3027–3038.

Gershenzon, M., S. Iljin, N. Fedetov, and Y. Gershenzon (1999). The mechanism of reactive NO_3 uptake on dry NaX (X = Cl, Br). *Journal of Atmospheric Chemistry,* Vol. 34, 119–135.

Geyer, A. (2000). *The Role of the Nitrate Radical in the Boundary Layer*. Dissertation, Institut für Umweltphysik, University of Heidelberg.

Gomer, T., T. Brauers, F. Heintz, J. Stutz, and U. Platt (1993). *MFC User Manual, Vers. 1.98*. Institut für Umweltphysik, Universität Heidelberg.

Götz, P., F. W., A. R. Meetham, and G. M. B. Dobson (1934). The Vertical Distribution of Ozone in the Atmosphere. *Proc. Roy. Soc.,* Vol. A 145, 416–446.

Grainger, J. and J. Ring (1962). Anomalous Fraunhofer line profiles. *Nature,* Vol. 193, 762.

Gros, V., N. Poisson, D. Martin, M. Kanakidou, and B. Bonsang (1998). Observations and modeling of the seasonal variation of ozone at Amsterdam Island: 1994-1996. *J. Geophys. Res.,* Vol. 103, No. D21, 28103–28109.

Hall, B. (1995). The gas phase oxidation of elemental mercury by ozone. *Water Air and Soil Pollution,* Vol. 80, 301–315.

Harder, H., C. Camy-Peyret, F. Ferlemann, R. Fitzenberger, T. Hawat, H. Osterkamp, M. Schneider, D. Perner, U. Platt, P. Vradelis, and K. Pfeilsticker (1998). Stratospheric BrO profiles measured at different latitudes and seasons: Atmospheric observations. *Geophys. Res. Lett.,* Vol. 25, 3843–3846.

Harder, J. W. and J. W. Brault (1997). Atmospheric measurements of water vapor in the 442-nm region. *J. Geophys. Res.,* Vol. 102, 6245–6252.

Hartley, W. N. (1881). On the absorption of solar rays by atmospheric ozone. *J. Chem. Soc.,* Vol. 39, 111.

Harwood, M., J. Burkholder, M. Hunter, R. Fox, and A. Ravishankara (1997). Absorption Cross Sections and Self-Reaction Kinetics of the *IO* Radical. *J. Phys. Chem. A,* Vol. 101, 853–863.

Haug, H. (1996). *Raman-Streuung von Sonnenlicht in der Erdatmosphäre*. Master's thesis, Institut für Umweltphysik, Ruprecht-Karls-Universität Heidelberg. D467.

Hausmann, M., U. Brandenburger, T. Brauers, and H.-P. Dorn (1997). Detection of tropospheric OH radicals by long-path differential-optical-absorption spectroscopy: Experimantal setup, accuracy, and precision. *J. Geophys. Res.,* Vol. 102, No. D13, 16011–16022.

Hausmann, M., U. Brandenburger, T. Brauers, and H.-P. Dorn (1999). Simple Monte Carlo methods to estimate the spectra evaluation error in differential-optical-absorption spectroscopy. *Appl. Opt.,* Vol. 38, No. 3, 462–475.

Hausmann, M. and U. Platt (1994). Spectroscopic measurement of bromine oxide and ozone in the high Arctic during Polar Sunrise Experiments 1992. *J. Geophys. Res.,* Vol. 99, 25399–25413.

Hebestreit, K. (2001). *Halogen Oxides in the Mid-Latitudinal Planetary Boundary Layer*. Dissertation, Institute für Umweltphysik, University of Heidelberg.

Hebestreit, K., J. Stutz, D. Rosen, V. Matveiv, M. Peleg, M. Luria, and U. Platt (1999). DOAS Mesurements of Tropospheric Bromine Oxide in Mid-Latitudes. *Science,* Vol. 283, 55–57.

Hegels, E., P. J. Crutzen, T. Klüpfel, D. Perner, and P. J. Burrows (1998). Global distribution of atmospheric bromine monoxide from GOME on earth-observing satellite ERS 2. *Geophys. Res. Lett.,* Vol. 25, 3127–3130.

Hermans, C., A. C. Vandaele, M. Carleer, S. Fally, R. Colin, A. Jenouvrier, B. Coquart, and M.-F. Mérienne (1999). Absorption Cross-Sections of Atmospheric Constituents: NO_2, O_2, and H_2O. *Environ. Sci. & Pollut. Res.,* Vol. 6, No. 3, 151–158.

Hermes, T. (1999). *Lichtquellen und Optik für die Differentielle Optische Absorptionsspektroskopie*. Diploma thesis, Institut für Umweltphysik, University of Heidelberg.

Hoff, R. (1992). Differential SO_2 Column Measurements of the Mt. Pinatubo Volcanic Plume. *Geophys. Res. Lett.,* Vol. 19, 175–178.

Hoff, R. and M. Millán (1981). Remote SO_2 mass flux measurements using COSPEC. *JAPCA,* Vol. 31, 381–384.

Hoffmann, T., C. D. O'Dowd, and J. H. Seinfeld (2001). IO homogeneous nucleation: An explanation for coastal new particle formation. *Geophys. Res. Lett.,* Vol. 28, No. 10, 1949–1952.

Holland, H. D. (1978). *The chemistry of the atmosphere and oceans*. New York: John Wiley & Sons.

Hollwedel, J. (2001). Analysis of GOME data for Alert2000 and the Hudson Bay for spring 2001. *pers. comm.,*.

Hönninger, G. (1999). *Referenzspektren reaktiver Halogenverbindungen für DOAS-Messungen*. Diploma thesis, University of Heidelberg.

Hönninger, G. and U. Platt (2002). Observations of BrO and its vertical distribution during surface ozone depletion at Alert. *Atm. Env.,*, in press.

Hönninger, G., I. Pundt, T. Wagner, and U. Platt (2000). MAX-DOAS: An Advanced Instrument for studying Tropospheric Chemistry. *Geophys. Res. Abs.,* Vol. 2.

Horne, D. G., R. Gosavi, and O. P. Strausz (1968). Reactions of Metal Atoms. I. The Combination of Mercury and Chlorine Atoms and the Dimerization of HgCl. *J. of Chem. Phys.,* Vol. 48, No. 10, 4758–4764.

Houzeau, A. (1858). Preuve de la présence dans l'atmosphere d'un nouveau principe gazeux, l'oxygène naissant. *C. R. Acad. Sci. Paris,* Vol. 46, 89.

Huppert, R. (2000). *Theoretische und experimentelle Untersuchungen zum solaren I_0 Effekt*. Diploma thesis, Institut für Umweltphysik, Universität Heidelberg.

Impey, G., C. Mihele, K. Anlauf, L. Barrie, D. Hastie, and P. Shepson (1999). Measurements of Photolyzable Halogen Compounds and Bromine Radicals during Polar Sunrise Experiment 1997. *J. of Atm. Chem.,* Vol. 34, 21–37.

Ingham, T., M. Cameron, and J. N. Crowley (2000). Photodissociation of IO (355 nm) and OIO (532 nm): Quantum Yields for O(^{3}P) and I(^{2}P$_J$) Production. *J. of Phys. Chem. A,* Vol. 104, 8001–8010.

Isaacs, R. G., W.-C. Wang, R. D. Worsham, and S. Goldberg (1987). Multiple Scattering Lowtran and Fascode models. *Appl. Opt.,* Vol. 26, 1272–1281.

Jobson, B., H. Niki, Y. Yokouchi, J. Bottenheim, F. Hopper, and R. Leaitch (1994). Measurements of C_2-C_6 hydrocarbons during the Polar Sunrise Experiment 1992: Evidence for Cl atom and Br atom chemistry. *Journal of Geophysical Research,* Vol. 99 No.D12, 25, 355–368.

Johnston, H. S. (1971). Reduction of stratospheric ozone by nitrogen oxide catalysts from supersonic transport exhaust. *Science,* Vol. 173, 517–522.

Johnston, P. (1996). Making UV/Vis cross sections reference fraunhofer and synthetic spectra. unpublished manuscript.

Jones, A. E., R. Weller, A. Minikin, E. W. Wolff, W. T. Sturges, H. P. McIntyre, S. R. Leonard, O. Schrems, and S. Bauguitte (1999). Oxidized nitrogen chemistry and speciation in the Antarctic troposphere. *J. Geophys. Res.,* Vol. 104, 21355–21366.

Junge, C. E. (1963). Global ozone budget and exchange between stratosphere and troposphere. *Tellus,* Vol. 14, 363–377.

Keeler, G., G. Glinsorn, and N. Pirrone (1995). Particulate mercury in the atmosphere: its significance, transport, transformation and sources. *Water Air and Soil Pollution,* Vol. 80, 159–168.

Keene, W. C., R. Sander, A. P. Pszenny, R. Vogt, P. J. Crutzen, and J. N. Galloway (1998). Aerosol pH in the marine boundary layer: A review and model evaluation. *J. Aerosol Sci.,* Vol. 29, No. 3, 339–356.

Kirchner, U., T. Benter, and R. N. Schindler (1997). Experimental verification of gas phase bromine enrichment in reactions of HOBr with sea salt doped ice surfaces. *Ber. Bunsenges. Phys. Chem.,* Vol. 101, 975–977.

Knight, G., A. R. Ravishankara, and J. B. Burkholder (2000). Laboratory Studies of OBrO. *J. Phys. Chem. A,* Vol. 104, 11121–11125.

Knoll, P., R. Singerand, and W. Kiefer (1990). Improving spectroscopic techniques by a scanning multi channel technique. *Appl.Spectr.,* Vol. 44, 776–782.

Koop, T., A. Kapilashrami, L. Molina, and M. Molina (2000). Phase transitions of sea-salt/water mixtures at low temperatures: Implications for ozone chemistry in the polar boundary layer. *J. Geophys. Res.,* Vol. 105, No. D21, 26393–26402.

Kreher, K. (1991). *Messung der Breitenverteilung (50° N – 70° S) von stratosphärischem Ozon und Stickstoffdioxid mittels optischer Absorptionsspektroskopie*. Diploma thesis, Institut für Umweltphysik, Universität Heidelberg.

Kreher, K., P. V. Johnston, S. W. Wood, and U. Platt (1997). Ground-based measurements of tropospheric and stratospheric BrO at Arrival Heights (78°S), Antarctica. *Geophys. Res. Lett.,* Vol. 24, 3021–3024.

Kromminga, H., S. Voigt, J. Orphal, and J. P. Burrows (1999). UV-visible FT spectra of OClO at atmospheric temperatures. In *Proceedings of the 1st European Symposium on Atmospheric Measurements from Space*. ESA Special Publication.

Landgraf, J. and P. Crutzen (1998). An Efficient Method for Online Calculations of Photolysis and Heating Rates. *J. of Atm. Sci.,* Vol. 55, 863–878.

Lazlo, B., M. Kurylo, and R. Huie (1995). Absorption Cross Sections, Kinetics of Formation, and Self-Reaction of the IO Radical Produced via the Laser Photolysis of $N_2O/I_2/N_2$ Mixtures. *J. Phys. Chem.,* Vol. 99, 11701–11707.

LeBras, G. and U. Platt (1995). A possible mechanism for combined chlorine and bromine catalyzed destruction of tropospheric ozone in the arctic. *Geophys. Res. Lett.,* Vol. 22, 599–602.

Lefer, B., S. Hall, L. Cinquini, and R. Shetter (2001). Photolysis frequency measurements at the South Pole during ISCAT-98. *Geophys. Res. Lett.,* Vol. 28, No. 19, 3637–3640.

Legendre, L., S. F. Ackley, G. S. Dieckmann, B. Gulliksen, R. A. Horner, T. Hoshiai, I. A. Melnikov, W. S. Reeburgh, M. Spindler, and C. W. Sullivan (1992). Ecology of sea ice biota. 2. Global significance. *Pol. Biol.,* Vol. 12, 471–477.

Lehrer, E. (1999). *Polar tropospheric ozone loss*. Ph. D. thesis, University of Heidelberg, Heidelberg, Germany.

Leser, H. (2001). *Untersuchung troposphärischer Spurenstoffe mit Multiaxialer Differentieller Optischer Absorptionsspektroskopie von gestreutem Sonnenlicht (MAX-DOAS)*. Diploma thesis, Institut für Umweltphysik, Universität Heidelberg.

Leue, T. W. C., K. Pfeilsticker, and U. Platt (2001). Monitoring of the stratospheric chlorine activation by GOME OClO measurements in the austral and boreal winters 1995 through 1999. *J. Geophys. Res.,* Vol. 106, 4971–4986.

Levenberg, K. (1944). A Method for the Solution of Certain Non-Linear problems in Least Squares. *Quart. Appl. Math.,* Vol. 2, 164–168.

Lindberg, S., S. Brooks, and C.-J. Lin (2001). Formation of reactive gaseous mercury in the Arctic: Evidence of oxidation of Hg^0 to gas-phase Hg-II compounds after Arctic sunrise. *Water Air and Soil Pollution,*.

Lu, J. Y., W. H. Schroeder, L. A. Barrie, A. Steffen, H. E. Welch, K. Martin, L. Lockhart, R. V. Hunt, G. Boila, and A. Richter (2001). Magnification of atmospheric mercury deposition to polar regions in springtime: the link to tropospheric ozone depletion chemistry. *Geophys. Res. Lett.,* Vol. 28, No. 17, 3219–3222.

Manø, S. and M. Andreae (1994). Emissions of methyl bromide from biomass burning. *Science,* Vol. 263, 1255–1257.

Marquard, L., T. Wagner, and U. Platt (2000). Improved Air Mass Factor Concepts for Scattered Radiation Differential Optical Absorption Spectroscopy of Atmospheric Species. *J. Geophys. Res.,* Vol. 105, 1315–1327.

Marquard, L. C. (1998). *Modellierung des Strahlungstransports in der Erdatmosphäre.* Ph. D. thesis, Institut für Umweltphysik, Ruprecht-Karls-Universität Heidelberg.

Marquardt, D. W. (1963). An Algorithm for Least Squares Estimation of Non-Linear Parameters. *Soc. Indust. Appl. Math,* Vol. 11, 431–441.

Martinez, M., T. Arnold, and D. Perner (1999). The role of bromine and chlorine chemistry for arctic ozone depletion events in Ny Ålesund and comparison with model calculations. *Ann. Geophys.,* Vol. 17, 941–956.

Matveev, V., M. Peleg, D. Rosen, D. S. Tov-Alper, K. Hebestreit, J. Stutz, U. Platt, D. Blake, and M. Luria (2001). Bromine oxide - ozone interaction over the Dead Sea. *J. Geophys. Res.,* Vol. 106, No. D10, 10375–10387.

McElroy, C., C. McLinden, and J. McConnell (1999). Evidence for bromine monoxide in the free troposphere during the Arctic polar sunrise. *Nature,* Vol. 397, 338–341.

McElroy, M. B., R. J. Salawitch, C. S. Wofsy, and J. A. Logan (1986). Reductions of Antarctic ozone due to synergistic interactions of chlorine and bromine. *Nature,* Vol. 321, 759–762.

McFiggans, G., J. M. C. Plane, B. J. Allan, and L. J. Carpenter (2000). A modeling study of iodine chemistry in the marine boundary layer. *J. Geophys. Res.,* Vol. 105, 14371–14385.

Mellouki, A., R. K. Talukdar, A. Schmoltner, T. Gierczak, M. J. Mills, S. Solomon, and A. R. Ravishankara (1992). Atmospheric lifetimes and ozone depletion potentials of methyl bromide (CH_3Br) and dibromomethane (CH_2Br_2). *Geophys. Res. Lett.,* Vol. 19, 2958–2062.

Millán, M., S. Townsend, and J. Davies (1969). *Study of the Barringer refractor plate correlation spectrometer as a remote sensing instrument.* Utias rpt. 146, m.a.sc. thesis, University of Toronto, Toronto, Ontario, Canada.

Miller, H. L., A. Weaver, R. W. Sanders, K. Arpag, and S. Solomon (1997). Measurements of artic sunrise surface ozone depletion events at Kangerlussuaq, Greenland (67°N, 51°W). *Tellus,* Vol. 49B, 496–509.

Misra, A. and P. Marshall (1998). Computational investigations of iodine oxides. *J. Phys. Chem.,* Vol. 102, 9056–9060.

Miyake, Y. and S. Tsnogai (1963). Evaporation of Iodine from the ocean. *J. Geophys. Res.,* Vol. 68, 3989–3993.

Molina, L. T. and M. J. Molina (1987). Production of Cl_2O_2 from the self reaction of the ClO radical. *J. Phys. Chem.,* Vol. 91, 433.

Molina, L. T. and F. S. Rowland (1974). Stratospheric sink for chlorofluromethanes: chlorine atom catalyzed destruction of ozone. *Nature,* Vol. 249, 820–822.

Moortgat, G. K., R. Meller, and W. Schneider (1993). Temperature dependence (256-296K) of the absorption cross-sections of bromoform in the wavelength range 285-360nm. In H. Niki and R. Becker (Eds.), *The Tropospheric Chemistry of Ozone in the Polar Regions*, pp. 359–370. Springer-Verlag, New York.

Mozurkewich, M. (1995). Mechanisms for the release of halogen atom sea-salt particles by free radical reactions. *Journal of Geophysical Research,* Vol. 100, 14199–14207.

Munthe, J., I. Wängberg, N. Pirrone, Å. Iverfeldt, R. Ferrara, R. Ebinghaus, X. Feng, K. Gårdfeld, G. Keeler, E. Lanzillotta, S. Lindberg, J. Lu, Y. Mamane, E. Prestbo, S. Schmolke, W. Schroeder, J. Sommar, F. Sprovieri, R. Stevens, W. Stratton, G. Tuncel, and A. Urba (2001). Intercomparison of methods for sampling and analysis of atmospheric mercury species. *Atm. Env.,* Vol. 35, 3007–3017.

Nagao, I., K. Matsumoto, and H. Tanaka (1999). Sunrise ozone destruction found in the sub-tropical marine boundary layer. *Geophys. Res. Lett.,* Vol. 26, No. 22, 3377–3380.

Nicolet, M. (1984). On the Molecular Scattering in the Terrestrial Atmosphere: An Empirical Formula for its Calculation in the Homosphere. *Planet. Space Sci.,* Vol. 32, No. 11, 1467–1468.

Noxon, J. F. (1975). Nitrogen Dioxide in the Stratosphere and Troposphere measured by Ground-based Absorption Spectroscopy. *Science,* Vol. 189, 547–549.

Noxon, J. F., E. C. Whipple, and R. S. Hyde (1979). Stratospheric NO_2. 1. Observational Method and Behavior at Midlatitudes. *J. Geophys. Res.,* Vol. 84, 5047–5076.

O'Dowd, C. D. (2001). Biogenic coastal aerosol production and its influence on aerosole radiative properties. *J. Geophys. Res.,* Vol. 106, No. D2, 1545–1549.

Oltmans, S. (1993). *Climatology of Arctic and Antarctic tropospheric ozone. In: The tropospheric chemistry of ozone in the polar regions*, pp. 25–40. eds. H. Niki, H. Becker. Berlin: Springer-Verlag.

Oltmans, S. J. and W. D. Komhyr (1986). Surface ozone distributions and variations from 1973-1984 measurements at the NOAA Geophysical Monitoring for Climate Change baseline observatories. *J. Geophys. Res.,* Vol. 91, 5229–5236.

Oum, K. W., M. J. Lakin, and B. J. Finlayson-Pitts (1998). Bromine activation in the troposphere by the dark reaction of O_3 with seawater ice. *Geophys. Res. Lett.,* Vol. 25, No. 21, 3923–3926.

Pacyna, E., J. Pacyna, and N. Pirrone (2001). European emissions of atmospheric mercury from anthropogenic sources in 1995. *Atm. Env.,* Vol. 35, 2987–2996.

Penndorf, R. (1957). Tables of the refractive index for standard air and the rayleigh scattering coefficient for the spectral region between 0.2 and 200 μ and their application to atmospheric optics. *J.Opt. Soc. Am.,* Vol. 47, No. 2, 176–182.

Perner, D., T. Arnold, J. Crowley, T. Klüpfel, M. Martinez, and R. Seuwen (1999). The Measurements of Active Chlorine in the Atmosphere by Chemical Amplification. *J. of Atm. Chem.,* Vol. 34, 9–20.

Perner, D., D. H. Ehhalt, H. W. Paetz, U. Platt, E. P. Roeth, and A. Volz (1976). OH Radicals in the lower Troposphere. *Geophys. Res. Lett.,* Vol. 3, 466–468.

Perner, D. and U. Platt (1979). Detection of Nitrous Acid in the Atmosphere by Differential Optical Absorption. *Geophys. Res. Lett.,* Vol. 6, 917–920.

Petersen, G., Å. Iverfeldt, and J. Munthe (1995). Atmospheric mercury species over central and northern Europe. Model calculations and comparison with observations

from the Nordic Air and Precipitaion Network for 1987 and 1988. *Atm. Env.,* Vol. 29, No. 1, 47–67.

Pfeilsticker, K., F. Erle, O. Funk, L. Marquard, T. Wagner, and U. Platt (1998). Optical path modifications due to tropospheric clouds: Implications for zentih sky measurements of stratospheric species. *J. Geophys. Res.,* Vol. 103, No. D19, 25323–25335.

Pirrone, N., P. Costa, J. Pacyna, and R. Ferrara (2001). Mercury emissions to the atmosphere from natural and anthropogenic sources in the Mediterranean region. *Atm. Env.,* Vol. 35, 2997–3006.

Pirrone, N., G. Keeler, and J. Nriagu (1996). Regional differences in world-wide emissions of mercury to the atmosphere. *Atm. Env.,* Vol. 30, 2981–2987.

Plane, J. M. C., B. J. Allan, and S. H. Ashworth (2001). On the Chemistry of Iodine Oxides in the Marine Boundary Layer. *Geophys. Res. Abs.,* Vol. 3, 6498.

Platt, U. (1978). Dry Deposition of SO_2. *Atmos. Env.,* Vol. 12, 363–367.

Platt, U. (1994). Differential Optical Absorption Spectroscopy (DOAS). In M. W. Sigrist (Ed.), *Monitoring by Spectroscopic Techniques*. New York: John Wiley & Sons, Inc.

Platt, U. (2000). Reactive Halogen Species in the Troposphere - Recent Discoveries. *Water, Air, and Soil Pollution,* Vol. 123, 229–244.

Platt, U. and C. Janssen (1995). Observation and role of the free radicals NO_3, ClO, BrO and IO in the troposphere. *Faraday Discuss.,* Vol. 100, 175–198.

Platt, U. and E. Lehrer (1996). *Arctic Tropospheric Ozone Chemistry, ARCTOC, Final Report of the EU-Project No. EV5V-CT93-0318, Heidelberg.*

Platt, U., L. Marquard, T. Wagner, and D. Perner (1997). Corrections for Zenith Scattered Light DOAS. *Geophys. Res. Letters,* Vol. 24, No. 14, 1759–1762.

Platt, U. and D. Perner (1980). Direct Measurements of Atmospheric CH_2O, HNO_2, O_3, NO_2 and SO_2 by Differential Optical Absorption in the Near UV. *J. Geophys. Res.,* Vol. 85, 7453–7458.

Platt, U., D. Perner, G. W. Harris, A. M. Winer, and J. N. Pitts, Jr. (1980). Detection of NO_3 in the Polluted Troposphere by Differential Optical Absorption. *Geophys. Res. Lett.,* Vol. 7, 89–92.

Platt, U., D. Perner, and H. W. Pätz (1979). Simultaneous Measurement of Atmospheric CH_2O, O_3 and NO_2 by Differential Optical Absorption. *J. Geophys. Res.,* Vol. 84, 6329–6335.

Platt, U. and J. Stutz (1998). *HALOTROP, Results from field, laboratory and modelling studies, Final Report of the EU-Project ENV4-CT95-0019-PL950049, Heidelberg.*

Poissant, L. (2001). Measurements of Mercury and Ozone at Kuujjuarapik. pers. comm.

Poissant, L., M. Amyot, M. Kwan, and Y. Bégin (2001). *Atmospheric mercury transport, oxidation and fallout in northern Qubec (Nunavik): an important potential route of contamination*, Volume ISBN 0-662-30872-7 of *Northern Contaminants Program*, Chapter Synopsis of Research 2000-2001, pp. 125–129. Indian and Northern Affairs Canada.

Pommereau, J. P. and J. Piquard (1994). Observations of the vertical distribution of stratospheric OClO. *Geophys. Res. Lett.,* Vol. 21, 1231–1234.

Ramacher, B., J. Rudolph, and R. Koppmann (1997). Hydrocarbon measurements in the spring Arctic troposphere during the ARCTOC 95 campaign. *Tellus,* Vol. 49B, No. 5, 466–485.

Ramacher, B., J. Rudolph, and R. Koppmann (1999). Hydrocarbon measurements during ozone depletion events: Evidence for halogen chemistry. *J. Geophys. Res.,* Vol. 104, 3633–3653.

Rasmussen, A., S. Kilisholm, J. H. Sø rensen, and I. S. Mikkelsen (1997). Analysis of tropospheric ozone measurements in Greenland. *Tellus,* Vol. 49B, No. 5, 510–521.

Rattigan, O., R. Jones, and R. Cox (1995). The visible spectrum of gaseous OBrO. *Chem. Phys. Lett.,* Vol. 230, 121–126.

Reifenhäuser, W. and K. G. Heumann (1992). Determinations of methyl iodide in the Antarctic atmosphere and the south polar sea. *Atm. Env.,* Vol. 26a, 2905–2912.

Renard, J., M. Pierre, C. Robert, and D. Huguenin (1998). The possible detection of OBrO in the stratosphere. *J. Geophys. Res.,* Vol. 103, 25383–25395.

Richter, A. (1997). *Absorptionsspektroskopische Messungen stratosphärischer Spurengase über Bremen.* 53°*N*. Ph. D. thesis, University of Bremen, Bremen, Germany.

Richter, A., F. Wittrock, M. Eisinger, and J. Burrows (1998). GOME Observations of Tropospheric BrO in Northern Hemispheric Spring and Summer 1997. *Geophys. Res. Lett.,* Vol. 25, 2683–2686.

Rodgers, C. D. (1976). Retrieval of Atmospheric Temperature and Composition From Remote Measurements of Thermal Radiation. *Rev. Geophys.,* Vol. 14, No. 4, 609–624.

Roscoe, H., K. Kreher, and U. Friess (2001). Ozone loss episodes in the free Antarctic troposphere, suggesting a possible climate feedback. *Geophys. Res. Lett.,* Vol. 28, No. 15, 2911–2914.

Röth, E., S. Johänning, H. London, and S. Huber-Thives (1996). Description of a photon flux model to determine photodissociation coefficients. *Berichte des Forschungszentrums Jülich,*.

Rothman, L. S., C. P. Rinsland, A. Goldman, S. T. Massie, D. P. Edwards, J. M. Flaud, A. Perrin, C. Camy-Peyret, V. Dana, J. Y. Mandin, J. Schroeder, A. McCann, R. R. Gamache, R. B. Wattson, K. Yoshino, K. V. Chance, K. W. Jucks, L. R. Brown, V. Nemtchinov, , and P. Varanasi (1998). The HITRAN Molecular Spectroscopic Database and HAWKS (HITRAN Atmospheric Workstation): 1996 Edition. *J. Quant. Spec. and Rad. Transf.,* Vol. 60, 665–710.

Rowley, D. M., W. J. Bloss, R. A. Cox, and R. L. Jones (2001). Kinetics and Products of the IO+BrO Reaction. *J. of Phys. Chem. A,* Vol. 105, 7855–7864.

Rudich, Y., R. Talukdar, and A. R. Ravishankara (1996). Reactive uptake of NO_3 on pure water and ionic solutions. *J. of Geophys. Res.,* Vol. D101, 21023 – 21031.

Sander, R. and P. J. Crutzen (1996). Model study indicating halogen activation and ozone destruction in polluted air masses transported to the sea. *J. Geophys. Res.,* Vol. 101, 522–532.

Sander, R., Y. Rudich, R. v. von Glasow, and P. Crutzen (1999). The role of $BrNO_3$ in marine tropospheric chemistry: A model study. *Geophys. Res. Lett.,* Vol. 26, No. 18, 2857–2860.

Sander, R., R. Vogt, G. W. Harris, and P. J. Crutzen (1997). Modeling the chemistry of ozone, halogen compounds, and hydrocarbons in the Arctic troposphere during spring. *Tellus,* Vol. 49B, 522–532.

Sander, S. P. (1986). Temperature dependence of the NO3 absorption spectrum. *J. Phys. Chem.,* Vol. 90, 4135–4142.

Sanders, R. W., S. Solomon, M. A. Carroll, and A. L. Schmeltekopf (1988). Ground based Measurements of O_3, NO_2, OClO and BrO during the Antarctic Ozone Depletion Event. In R. D. Bjokov and P. Fabian (Eds.), *Ozone in the Atmosphere, Quadrennial Ozone Symposium 1988*, pp. 65–70. Hampton, Va.: Deepak Publishing.

Sanders, R. W., S. Solomon, J. P. Smith, L. Perliski, H. L. Miller, G. H. Mount, J. G. Keys, and A. L. Schmeltekopf (1993). Visible and Near-Ultraviolet Spectroscopy at McMurdo Station Antarctica, 9. Obeservations of OClO from April to October 1991. *J. Geophys. Res.,* Vol. 98, No. D4, 7219–7228.

Schall, C. and K. Heumann (1993). GC determination of volatile organoiodine and organobromine compounds in seawater and air samples. *Fresenius Z. Anal. Chem.,* Vol. 346, 717–722.

Schauffler, S. M., E. L. Atlas, D. R. Blake, F. Flocke, R. A. Lueb, J. M. Lee-Taylor, V. Stroud, and W. Travnicek (1999). Distribution of brominated organic compounds in the troposphere and lower stratosphere. *J. Geophys. Res.,* Vol. 104, 21513–21535.

Schönbein, C. (1840). Recherches sur la nature de l'odeur qui se manifeste dans certaines actions chimiques. *C. R. Acad. Sci. Paris,* Vol. 10, 706.

Schroeder, W. H., k. G. Anlauf, L. A. Barrie, J. Y. Lu, A. Steffen, D. R. Schneeberger, and T. Berg (1998). Arctic springtime depletion of Mercury. *Nature,* Vol. 394, 331–332.

Schroeder, W. H. and J. Munthe (1998). Atmospheric Mercury - An Overview. *Atm. Env.,* Vol. 32, No. 5, 809–822.

Schweizer, F., P. Mirabel, and C. George (1999). Heterogenious Chemistry of Nytryl Halides in Relation to Tropospheric Halogen Activation. *J. of Geophys. Res.,* Vol. 34, 101–117.

Seisel, S. and M. Rossi (1997). The heterogeneous Reaction of HONO and HBr on Ice and on Sulfuric Acid. *Ber. Bunsenges. Phys. Chem.,* Vol. 101, 943.

Senne, T. (1996). *Weiterentwicklung einer Apparatur zur spektroskopischen Bestimmung stratosphärischer Spurenstoffe und Messung eines Nord/Süd-Breitenschnittes von stratosphärischem Ozon und NO_2*. Diploma thesis, Institut für Umweltphysik, Universität Heidelberg.

Sioris, C. E. and W. F. J. Evans (1999). Filling in of Fraunhofer and gas-absorption lines in sky spectra as caused by rotational Raman scattering. *Appl. Opt.,* Vol. 38, No. 12, 2706–2713.

Slemr, F. and E. Langer (1992). Increase in global atmospheric concentrations of mercury inferred from measurements over the Atlantic Ocean. *Nature,* Vol. 355, 434–437.

Slemr, F., G. Schuster, and W. Seiler (1985). Distribution, speciation, and budget of atmospheric mercury. *J. Atmos. Chem.,* Vol. 3, 407–434.

Smith, J. and S. Solomon (1990). Atmospheric NO_3: 3. Sunrise Disappearance and the Stratospheric Profile. *J. Geophys. Res.,* Vol. 95, No. D9, 13819–13827.

Smith, J., S. Solomon, R. Sanders, H. Miller, L. Perliski, J. Keys, and A. Schmeltekopf (1993). Atmospheric NO_3: 4. Vertical Profiles at Middle and Polar Latitudes at Sunrise. *J. Geophys. Res.,* Vol. 98, No. D5, 8983–8989.

Solberg, S., N. Schmidbauer, A. Semb, F. Stordal, and O. Hov (1996). Boundary layer ozone depletion as seen in the Norwegian Arctic. *J. Atmos. Chem.,* Vol. 23, 301–332.

Solberg, S., N. Schmidtbauer, A. Semb, and F. Stordal (1996). Boundary-LayerOzone Depletion as Seen in the Norwegian Arctic in Spring. *J. of Atmos. Chem.,* Vol. 101 No.D1, 1907–1917.

Solomon, S., R. R. Garcia, F. S. Rowland, and D. J. Wuebbles (1986). On the depletion of Antarctic ozone. *Nature,* Vol. 321, 755–758.

Solomon, S., H. G. Mount, R. W. Sanders, and A. L. Schmeltekopf (1987). Visible spectroscopy at McMurdo station, Antarctica 2. Observations of OClO. *J. Geophys. Res.,* Vol. 92, 8329–8338.

Solomon, S., A. L. Schmeltekopf, and R. W. Sanders (1987). On the interpretation of zenith sky absorption measurements. *J. Geophys. Res.,* Vol. 92, 8311–8319.

Sommar, J., K. Gårdfeld, D. Strömberg, and X. Feng (2001). A kinetic study of the gas-phase reaction between the hydroxly radical and atomic mercury. *Atm. Env.,* Vol. 35, 3049–3054.

Steffen, A., W. Schroeder, J. Bottenheim, J. Narayan, and J. Fuentes (2002). Atmospheric Mercury Concentrations: Measurements and Profiles near Snow and Ice Surfaces in the Canadian Arctic during Alert2000. *Atm. Env.,*, in press.

Stoiber, R. and A. Jepsen (1973). Sulfur dioxide contribution to the atmosphere by volcanoes. *Science,* Vol. 182, 577–578.

Stolarski, R. S. and R. Cicerone (1974). Stratospheric chlorine: a possible sink for ozone. *Can. J. Chem.,* Vol. 52, 1610–1615.

Sturges, W. T., R. C. Schnell, S. Landsberger, S. J. Oltmans, J. M. Harris, and S.-M. Li (1993). Chemical and meteorological influences on surface ozone destruction at Barrow, Alaska, during spring 1989. *Atmos. Environ.,* Vol. 27A, No. 17/18, 2851–2863.

Stutz, J. (1991). *Charakterisierung von Photodiodenzeilen zur Messung stratosphärischer Spurenstoffe.* Diploma thesis, Institut für Umweltphysik, Universität Heidelberg.

Stutz, J. (1996). *Messung der Konzentration troposhärischer Spurenstoffe mittels Differentieller-Optischer-AbsorptionsSpektroskopie: Eine neue Generation von Geräten und Algorithmen.* Ph. D. thesis, Institut für Umweltphysik, Ruprecht-Karls-Universität Heidelberg. D455.

Stutz, J., K. Hebestreit, B. Alicke, and U. Platt (1999). Chemistry of halogen oxides in the troposphere: comparison of model calculations with recent field data. *J. Atmos. Chem.,* Vol. 34, 65–68.

Stutz, J., E. S. Kim, U. Platt, P. Bruno, C. Perrino, and A. Febo (1999). UV-visible Absorption Cross-Section of Nitrous Acid. *J. Geophys. Res.,* Vol. 105, No. D11, 14585–14592.

Stutz, J. and U. Platt (1992). Problems in Using Diode Arrays for Open Path DOAS Measurements of Atmospheric Species. *Proc. EOS/SPIE Symp. Berlin, Optical Methods in the Atmospheric Chemistry,* Vol. 1715, 329–340.

Stutz, J. and U. Platt (1996). Numerical Analysis and Estimation of the Statistical Error of Differential Optical Absorption Spectroscopy Measurements with Least-Squares methods. *Appl. Opt.,* Vol. 35, No. 30, 6041–6053.

Stutz, J. and U. Platt (1997). Improving long-path differential optical absorption spectroscopy with a quartz-fiber mode mixer. *Applied Optics,* Vol. 36, No. 6, 1105–1115.

Tang, T. and J. C. McConnel (1996). Autocatalytic release of bromine from Arctic snow pack during polar sunrise. *Geophys. Res. Lett.,* Vol. 23, 2633–2636.

Tellinghuisen, J. (1973). Resolution of the visible-infrared absorption spectrum on I_2 into three contributing transitions. *J. Chem. Phys.,* Vol. 58, 2821–2834.

Thomas, V., J. Bedford, and R. Cicerone (1997). Bromine emissions from leaded gasoline. *Geophys. Res. Lett.,* Vol. 24, No. 11, 1371–1374.

Toumi, R. (1994). *BrO* as a sink for dimethylsulfide in the marine atmosphere. *Geophys. Res. Lett.,* Vol. 21, 117–120.

Tuckermann, M., R. Ackermann, C. Gölz, H. Lorenzen-Schmidt, T. Senne, J. Stutz, B. Trost, W. Unold, and U. Platt (1997). DOAS-observation of halogen radical-catalysed Arctic boundary layer ozone destruction during the ARCTOC campaign 1995 and 1996 in Ny-Alesund, Spitsbergen. *Tellus,* Vol. 49b, 533–555.

Turnipseed, A., J. Birks, and J. Clavert (1990). Kinetics and temperature dependence of the BrO+BrO reaction. *J. of Phys. Chem.,* Vol. 94, 7477–7482.

Turnipseed, A., J. Birks, and J. Clavert (1991). Kinetics and temperature dependence of the BrO+ClO reaction. *J. of Phys. Chem.,* Vol. 95, 4356–4364.

Van de Hulst, H. (1981). *Light scattering by small particles.* New York: Dover publication.

Van Roozendael, M., S. R. Alliwell, P. V. Johnston, A. Richter, M. V. Roozendael, T. Wagner, D. W.Arlander, J. P. Burrows, D. J. Fish, R. L. Jones, K. K. Tørnkvist, J. C. Lambert, K. Pfeilsticker, and I. Pundt (1999). Analysis for BrO in zenith-sky spectra - an intercomparison exercise for analysis improvement. *J. Geophys. Res.,*. in preparation.

van Roozendael, M., D. W. Arlander, J. Burrows, M. Chipperfield, C. Fayt, F. Hendrick, C. Hermans, P. Johnston, R. Jones, K. Kreher, J.-C. Lambert, N. Tahrin, D. Newnham, K. Pfeilsticker, U. Platt, J.-P. Pommereau, I. Pundt, A. Richter, B. Sinnhuber, A. South, K. Tørnkvist, and T. Wagner (2000). Lessons learned from 2 years of coordinated multi-platform UV-visible observations of atmospheric bromine monoxide. *Proceedings of the Quadrennial Ozone Symposium, Hokkaido University, Sapporo, Japan,*, 157–158.

Vogt, R., P. J. Crutzen, and R. Sander (1996). A mechanism for halogen release from sea-salt aerosol in the remote marine boundary layer. *Nature,* Vol. 383, 327–330.

Vogt, R., R. Sander, R. von Glasow, and P. J. Crutzen (1999). Iodine chemistry and its role in halogen activation and ozone loss in the marine boundary layer: a model study. *J. Atmos. Chem.,* Vol. 32, 375–395.

Voigt, S., J. Orphal, and J. P. Burrows (1999). UV-visible absorption cross-sections of NO_2 and O_3 at atmospheric temperatures and pressures by FTS. In *Proc. of the 1st Europ. Symp. Atmos. Meas. from Space (ESAMS-99), ESA-ESTEC, Noordwijk, The Netherlands, ESA WPP-161*, Volume 2, pp. 443–465.

Volkamer, R. (1996). *Absorption von Sauerstoff im Herzberg I System und Anwendung auf Aromatenmessungen am EUropean PHOto REactor (EUPHORE).* Diploma thesis, Institut für Umweltphysik, Universität Heidelberg.

von Friedeburg, C. (1999). *Optimierung der NO_3-Höhenprofilermittelung mittels Differentieller Streulichtspektroskopie.* Diploma thesis, Institut für Umweltphysik, Universität Heidelberg.

von Friedeburg, C. (2001). Evaluation of MAX-DOAS spectra for the Highway campaign 2001. *pers. comm.,*.

von Friedeburg, C., T. W. A. Geyer, N. Kaiser, B. Vogel, H. Vogel, and U. Platt (2001). Derivation of Tropospheric NO_3 Profiles Using Off-axis-DOAS Measurements During Sunrise and Comparison with Simulations. *J. Geophys. Res.,*, accepted.

von Friedeburg, C., T. Wagner, A. Geyer, and B. V. U. Platt (2001). Nitrate Radical formation during the Solar Eclipse of 1999 over Southern Germany. *in prep.,*.

Wagner, T. (1999). *Satellite observations of atmospheric halogen oxides.* Ph. D. thesis, University of Heidelberg, Heidelberg, Germany.

Wagner, T., M. Bruns, J. Burrows, S. Fietkau, F. Finocchi, K.-P. Heue, G. Hönninger, U. Platt, I. Pundt, A. Richter, R. Rollenbeck, C. von Friedeburg, F. Wittrock, and P. Xie (2001). The AMAXDOAS Instrument and its Application for Sciamachy Validation. *Proceedings of the 15^{th} ESA Symposium on Rocket and Balloon Programmes and Related Research, Biarritz, France, 28-31 May 2001,*, 471.

Wagner, T., C. Leue, M. Wenig, K. Pfeilsticker, and U. Platt (2001). Spatial and temporal distribution of enhanced boundary layer BrO concentrations measured by the GOME instrument aboard ERS-2. *J. Geophys. Res.,* Vol. 106, No. D20, 24225–24235.

Wagner, T. and U. Platt (1998). Satellite mapping of enhanced BrO concentrations in the troposphere. *Nature,* Vol. 395, 486.

Wahner, A., A. R. Ravishankara, S. P. Sander, and R. R. Friedl (1988). Absorption cross section of BrO between 312 and 385 nm at 298 and 223 K. *Chemical Physics Letters,* Vol. 152, No. 6, 507–512.

Wayne, R., G. Poulet, P. Biggs, J. Burrows, R. Cox, P. Crutzen, G. Haymann, M. Jenkin, G. L. Bras, G. Moortgat, U. Platt, and R. Schindler (1995). Halogen oxides: radicals, sources and reservoirs in the laboratory and in the atmosphere. *Atmos. Environ., Special Issue,* Vol. 29, 2675 – 2884.

Weaver, A., S. Solomon, R. W. Sanders, K. Arpag, and H. L. Miller (1996). Atmospheric NO_3 5. Off-axis measuements at sunrise: Estimates of tropospheric NO_3 at 40°N. *J. Geophys. Res.,* Vol. 101, No. D13, 18605–18612.

Wennberg, P. (1999). Bromine explosion. *Nature,* Vol. 397, 299–300.

Wessel, S. (1996). *Troposphärische Ozonvariationen in Polargebieten.* Ph. D. thesis, University of Bremen, Bremen, Germany.

Wessel, S., S. Aoki, P. Winkler, R. Weller, A. Herber, and H. Gernandt (1998). Tropospheric ozone depletion in polar regions - A comparison of observations in the Arctic and Antarctic. *Tellus,* Vol. 50B, No. 1, 34–50.

Wiscombe, W. J. (1980). Improved Mie scattering algorithms. *Appl. Opt.,* Vol. 19, 1505–1509.

Wittrock, F., R. Müller, A. Richter, H. Bovensmann, and J. P. Burrows (2000). Measurements of iodine monoxide (IO) above Spitsbergen. *Geophys. Res. Lett.,* Vol. 27, 1471–1474.

Xie, P. H., D. Arlander, C. Friedeburg, M. Hofmann, J. Lee, J.Lösch, K. Mettendorf, U. Platt, T. Wagner, and I. Pundt (2001). Motorway traffic emission measurements by three dimensional DOAS Tomography. *Poster presented at the POET International workshop: Emissions of chemical species and aerosols into the atmosphere, June 19-22, Paris, France,.*

Yvon, S. and H. Butler (1996). An improved estimate of the oceanic lifetime of atmospheric CH_3Br. *Geophys. Res. Lett.,* Vol. 23, 53–56.

Zhou, X., H. J. Beine, R. E. Honrath, J. D. Fuentes, W. Simpson, P. B. Shepson, and J. W. Bottenheim (2001). Snowpack Photochemical Production of HONO: a Major Source of OH in the Arctic Boundary Layer in Springtime. *Geophys. Res. Lett.,* Vol. 28, No. 21, 4087.

Acknowledgements

Here, I would like to thank all those people, who have continuously supported me during the course of this thesis and who have helped in the successful completion of this work.

Herrn Prof. Dr. Ulrich Platt danke ich für die Ermöglichung dieser Arbeit und die interessante Thematik. Durch seine Vorschläge und Anregungen gab er mir immer wieder die Impulse, die mich in meiner Arbeit voranbrachten und zu ihrem Gelingen beitrugen.

Herrn Prof. Dr. Konrad Mauersberger danke ich für die freundliche Übernahme der Begutachtung dieser Arbeit.

Dr. Dieter Perner danke ich für die Unterstützung während dieser Arbeit, insbesondere für die Initiierung der Messungen auf der Zugspitze.

Allen Freunden und Kollegen in meiner Arbeitsgruppe danke ich besonders für das hervorragende Arbeitsklima. Besonders zu nennen sind Hans, der durch seine Ausstrahlung permanent guter Laune jede Situation rettete und die MAX-DOAS Messungen and der Hudson Bay voll unter Kontrolle hatte, inklusive Knick, Knack und Dauerknick. Dank an Oliver für zwei unvergeßliche Meßkampagnen, die nicht nur tolle Ergebnisse brachten, sondern auch touristisch interessant waren, von unvermeidlichem Raki bis zu VTTs und Mermaids. Vielen Dank an Kai, Björn, Nicole, Hartmut, Christoph, Andi, Ralf, Hansjörg, Thomas (wat), Udo, Jutta, Kai-Uwe, Pinhua, Rainer, Klaus, Thomas (Scholli), Richard, Oli Funk und wen ich noch vergessen habe. Alle haben für abwechslungsreiche Mittags- und Kaffeepausen gesorgt. Vielen Dank an Jochen Stutz, für alle Tips und Anregungen während meiner Diplomarbeitszeit und während SOS99 in Nashville.

Der IUP-Werkstatt danke ich besonders für die umgehende Bearbeitung diverser "ganz dringender" Aufträge, ohne die keine der Meßkampagnen in dieser Arbeit möglich gewesen wäre.

Dem Personal auf dem Schneefernerhaus danke ich für die Unterstützung während der DOAS-Messungen und der Fraunhofer Management Gesellschaft für die finanzielle Unterstützung durch ein BMBF-Stipendium.

I wish to thank all the people involved in the Alert2000 polar sunrise experiment for the great teamwork, interesting discussions, and entertaining evenings. Thanks to Jan Bottenheim and Paul Shepson for coordinating and leading the whole study. Special

thanks to Al Gallant for his tireless support and running the Ice Camp. Sandy, with additional thanks for the mercury data, Jim Milne, the two Marc/k Lill(e)ys, Amy, Martin, Ann Louise and the French guys made the campaign at Alert an unforgettable experience.

I would also like to thank Rolf Sander for providing the MOCCA source code and for introducing me in the main features of the model.

I also wish to thank the EL CID people Jean, Nikos, Mihalis, Haido and Florence for the help and great atmosphere during the field campaigns on Crete and at the Hudson Bay.

The French Polar Institute (IFRTP) I thank for the opportunity to explore the French Islands in the Indian Ocean. Thanks also to Benji for the support during the "LP-DOAS in one day" measurements at Kerguelen. Special thanks also to the crew and the cooks on Marion Dufresne for the excellent French cuisine which saved me from getting seasick.

I also wish to thank Claude Tremblay for the invaluable and friendly support during the measurements at Kuujjuarapik, for providing a measurement site and taking care of all little problems arising during a field campaign. Special thanks also to Laurier Poissant for seeking out Kuujjuarapik as a measurement site, for the interesting discussions and of course for providing the mercury data. Thanks also to André for the right meal in every situation.

Ein herzliches Dankeschön gilt meinen Eltern, die mich in meinem Studium und meinen Entscheidungen stets unterstützten und ein wichtiger Rückhalt waren.

Der größte Dank aber gehört meiner allerliebsten Anita, die mich zu jeder Zeit voll unterstützte, Nachsicht in Zeiten der einsetzenden Zerstreuung hatte, mich nach langen Meßkampagnen wieder an den Alltag gewöhnte und mich in der Zeit des Zusammenschreibens unermüdlich mit allem Lebensnotwendigen versorgt hat.